NANYANG
TECHNOLOGICAL
UNIVERSITY
SINGAPORE

VANADIUM-BASED ANODE MATERIALS (Li_3VO_4 AND VS_4) FOR LITHIUM ION BATTERIES

YANG GUANG

Interdisciplinary Graduate School
Energy Research Institute @ NTU

2018

VANADIUM-BASED ANODE MATERIALS (Li_3VO_4 AND VS_4) FOR LITHIUM ION BATTERIES

YANG GUANG

INTERDISCIPLINARY GRADUATE SCHOOL

A thesis submitted to the Nanyang Technological University
in partial fulfilment of the requirement for the degree of
Doctor of Philosophy

2018

Statement of Originality

I hereby certify that the work embodied in this thesis is the result of original research and has not been submitted for a higher degree to any other University or Institution.

31 July 2018

Yang Guang

Authorship Attribution Statement

Chapter 4 is published as **Yang, G**.; Zhang, B.; Feng, J.; Lu, Y.; Wang, Z.; Aravindan, V.; Aravind, M.; Liu, J.; Srinivasan, M.; Shen, Z.; Huang, Y., Morphology-controlled lithium storage in Li_3VO_4 anodes. **Journal of Materials Chemistry A 2018,** *6*, 456-463.

The contributions of the co-authors are as follows:

- A/Prof Huang, Prof Madhavi, and Prof Shen provided the initial project direction and edited the manuscript drafts.
- I prepared the manuscript drafts. The manuscript was revised by Prof Liu and Prof Huang.
- I co-designed the study with Dr Feng and Dr Aravindan and performed all the laboratory work at the School of Materials Science and I also analyzed the data.
- All microscopy except TEM, including sample preparation, was conducted by me in the Facility for Analysis, Characterization, Testing and Simulation.
- Mr Zhang and Dr Wang assisted in the collection of TEM and HRTEM images.
- Mr Lu assisted in the collection of part of the electrochemical performance data.

Chapter 5 is published as **Yang, G.**; Feng, J.; Zhang, B.; Aravindan, V.; Peng, D.; Cao, X.; Yu, H.; Madhavi, S.; Huang, Y., Solvothermal synthesis of Li_3VO_4: Morphology control and electrochemical performance as an anode for lithium-ion batteries. **International Journal of Hydrogen Energy** 2017, 42, 22167-22174.

The contributions of the co-authors are as follows:

- Prof Huang, Prof Shen, and Prof Madhavi suggested the materials area.
- I wrote the drafts of the manuscript. The manuscript was revised together with Prof Huang and Liu.
- I performed almost all the materials synthesis, collected X-ray diffraction patterns and visible light spectra, and conducted data evaluation.
- Mr Zhang performed the TEM and HRTEM testing.

- Mr Cao, Yu, and Peng conducted part of the XRD date testing.

Chapter 6 is published as **Yang, G.**; Zhang, B.; Feng, J.; Wang, H; Ma, M.; Huang, K; Liu, J; Madhavi, S.; Shen, Z.; Huang, Y., High crystallinity urchin-like VS_4 anode for high-performance lithium-ion storage. **ACS Applied Materials & Interfaces** 2018, 10, 14727-14734.

The contributions of the co-authors are as follows:

- Prof Huang, Prof Shen, and Prof Madhavi suggested the materials area.
- I wrote the drafts of the manuscript. The manuscript was revised together with Prof Huang and Liu.
- Miss Ma and Mr Huang provided some suggestions for the manuscript.
- I performed almost all the materials synthesis, collected X-ray diffraction patterns and visible light spectra, and conducted data evaluation.
- Mr Zhang performed the TEM and HRTEM testing.

31 July 2018

Yang Guang

Abstract

Tremendous attention has been paid to the development of high energy and power lithium-ion batteries (LIBs) used in electric vehicles. Unfortunately, the commercial graphite anode material has inadequate energy and power density. In addition, safety hazard such as formation of lithium dendrites further hinders its widespread utilization and application. Recently, Li_3VO_4 (denoted as LVO) anode has been reported as a promising insertion type material to replace graphite due to its higher theoretical capacity (395 mAh g^{-1}) and cycling stability. Furthermore, it has an appropriate voltage window of 0.5–0.8 V vs. Li^+/Li. This allows greater security since safety issues are commonly associated with the formation of Li dendrites that happens below 0.1 V vs. Li^+/Li. Apart from LVO, vanadium sulfide VS_4 is another promising anode material with a high theoretical specific capacity of 1196 mAh g^{-1}. Until now, significant progress has been made to improve the electric/ionic conductivity and cycling stability of both LVO and VS_4. However, good understanding the relationship between materials morphological structure properties and electrochemical characteristics is still lacking. Therefore, the main objective of this thesis is to investigate the morphological effect, along with the effect of compositing LVO and VS_4 with carbon on the electrochemical performance.

Work I. LVO materials with a series of morphologies from spherical-assembly, nanorod, flower-shape to bulk-shape are successfully synthesized. These diversity structures and/or morphologies provide ideal models to correlate structural features with electrochemical performance and identify the Li^+ storage mechanism. The electrochemical performance degrades in the order of nanorods, sphere, flower, and bulk. LVO nanorods demonstrate the best performance benefiting from their small particle size, large surface area, and high crystallinity. The calculated Li^+ ion diffusion coefficients further support the good performance. Further improvement in electrochemical performance is achieved via carbon coating. However, the cycling stability is still not satisfactory.

Work II. From the first work, the cycling performance of sphere-assembly LVO shows better cycling stability compared to LVO nanorods, despite its poorer specific capacity. As such, hierarchical structure LVO with small primary particle size is hypothesized to improve the stability while maintaining a high specific capacity. In the second work, LVO microspheres exhibit surpassing electrochemical performance compared to LVO rods. Thus, this work concludes the importance of small primary particle size in obtaining high specific capacity. Also, it shows that hierarchical structure favors cycling stability.

Work III. Another vanadium-based anode, vanadium sulfide, was explored as anode material because of its higher theoretical capacity and electrical conductivity compared to lithium vanadium oxide. VS_4 with a variety of special morphologies are prepared and compared systematically. According to this study, electrochemical performance degrades in the order of urchin-VS_4 > octopus-like VS_4 > sea grass-like VS_4 > flower-like VS_4. Urchin-VS_4 with high crystallinity demonstrates the best performance, suggesting that high crystallinity is necessary in achieving high specific capacity. This is further supported by their superior kinetic parameters such as diffusional coefficients and charge transfer resistance. Furthermore, more kinetic information is derived from the EIS measurements under different state-of-charge (SOC).

Work IV. One key challenge of VS_4 lies in its poor electrical conductivity. Work IV is just focusing on this topic through compositing VS_4 with rGO. One-dimensional VS_4 nanowires directly grown on rGO via a facile solvothermal method is presented and rarely been reported in literature. Compared to pristine VS_4, the composite shows enhanced electrochemical performance. In addition, VS_4 with different amounts of rGO (5, 15, and 35 wt% rGO) were also synthesized and compared systemically. The 15 wt% rGO @ VS_4 demonstrates the best performance due to the appropriate amount of rGO.

In summary, firstly, the electrochemical performance of LVO can be enhanced by reducing the particles size and using hierarchical structure design concept. Secondarily, crystallinity and morphologies are important for VS_4 material to achieve high electrochemical performance. Thirdly, compositing active material with carbonaceous material like carbon or rGO could be an effective way to improve the performance. The work provides insight and valuable guidance for future material design especial vanadium-based oxide or sulfide in the field of LIBs.

Lay Summary

The lithium-ion battery mentioned here refers specifically to a rechargeable lithium-ion secondary battery, not a disposable battery. Lithium-ion batteries are present in every corner of our lives. Applications include mobile phones, tablet computers, notebook computers, smart watches, mobile power supplies (rechargeable treasures), emergency power supplies, razors, electric bicycles, electric vehicles, electric buses, tourist and sightseeing vehicles, drones, and other types of power tools. As a carrier of electrical energy and a source of power for many devices, it can be said that without the lithium-ion battery, the current world can not function well (unless we want to go back a few decades ago without electronic devices). In addition, with the increasing depletion of oil resources, the pollution emission problem from traditional vehicles is becoming more and more severe. The demand for the development of clean electric vehicles is becoming more and more urgent. The existing commercial negative electrode material graphite cannot meet the requirements, either from point of view that the amounts of charge storable by the devices, or from the fast charging speed. Therefore, searching for novel materials that can store more energy is urgently needed.

Lithium vanadate and vanadium sulfide can store more energy theoretically. In addition, vanadium is a cheap material and abundantly reserve on earth, avoiding the challenge of shortage in the future. However, the current research is mainly focused on improving electrical conductivity through compositing with various carbonaceous materials or synthesizing certain morphologies. There is a lack of systematic research on these two materials, especially the effect of morphology or particle size on their electrochemical performance. Therefore, lithium vanadate and vanadium sulfides with different morphologies were synthesized during this Ph.D. period. Emphasis is placed on the investigation of the effect of materials' morphology on their electrochemical performance. Meanwhile, lithium storage mechanism has also been studied. By measuring the diffusion coefficient of lithium ions and charge transfer resistance, an in-depth understanding of the effects of different morphology on lithium ion diffusion can be achieved. In addition, carbon coated lithium vanadium vanadate and vanadium sulfide composited graphene have also been successfully prepared. To the best of our knowledge, vanadium sulfide nanowires grown on graphene are rarely reported. The comparison between the bare material and composites is made in terms of morphologies and electrochemical performance. The composites demonstrate surpassing performance. This suggests the importance of improving the electrical conductivity.

In summary, this study is very meaningful, timely, and can provide invaluable guidance for the future design of anode materials for lithium-ion battery application, especially vanadium-based materials.

Acknowledgments

The author would like to express her deepest gratitude to main supervisor Prof Huang Yizhong and co-supervisors Prof Shen Zexiang and Prof Madhavi Srinivasan, for their valuable guidance and support:

Assoc. Professor Huang Yizhong
Prof. Madhavi Srinivasan
Mr. Zhang Bowei
Dr. Wang Zhiqiang
Dr. Shubha Nageswaran
Ms. Ma Mingbo
Mr. Edison Eldho
Dr. Li Chaojiang
Ms. Foo Shini
Mr. Peng Dongdong
Ms. Rao Yuhan
Laboratory technicians in FACTS Lab, Inorganic Lab, and Consumable Stores (NTU, MSE)

Prof Shen Zexiang
Dr. Feng Jianyong
Dr. Liu Jilei
Dr. Rohit Satish
Mr. Huang Tan
Ms. Guo Ziqi
Ms. Wang Huanhuan
Mr. Cao Xun
Dr. Hao Shiji
Ms. Astorga Solangeelizabeth

My families and my dearest friends

I am grateful and fortunate to know each of you. Thanks for your valuable companionship and understanding whenever I am facing difficulties or being demotivated. I am tremendously appreciative of your constant patience, support, encouragement, guidance, inspiration, and insightful comments during this dissertation. It would not have been possible to finish this thesis without you.

Table of Contents

Table Captions

Figure Captions

Abbreviations

LIB	Lithium-Ion Battery
CV	Cyclic Voltammetry
GDC	Galvanostatic Discharge Charge
TGA	Thermogravimetric Analysis
FTIR	Fourier Transform Infrared Spectroscopy
XRD	X-ray Diffraction
SEM	Scanning Electron Microscopy
TEM	Transmission Electron Microscopy
HRTEM	High-Resolution Transmission Electron Microscopy
PXRD	Powder X-ray Diffraction
SAED	Selected Area Electron Diffraction
SEI	Solid Electrolyte Interface
XPS	X-ray Photoelectron Spectroscopy
FFT	Fast Fourier Transform
EC	Ethylene Carbonate
DEC	Diethylene Carbonate
EV	Electric Vehicle

Chapter 1

Introduction

This chapter introduces the background and problem lithium-ion batteries (LIBs) are facing. Then, the brief literature review provides information regarding previous works as well as the research niche. Finally, the research objectives, sub-objectives, and dissertation of the different chapters are penned down in detail.

1.1 Hypothesis/Problem Statement

Energy consumption of the world is increasing sharply. However, 80 % of the energy consumed today still comes from non-renewable energy sources (e.g., fossil fuel and gasoline), which leads to global warming, pollution, and climate change problems [1, 2]. Non-renewable energy, as its name suggests, are exhaustible and difficult to reproduce. As such, great efforts have been made to find alternative energy sources and technologies. Renewable energies such as solar energy, tidal energy, or wind energy, are forms of clean sustainable energy. However, most renewable energy such as solar energy, wind energy, and tidal energy, are intermittent in nature. Providing appropriate storage technologies for such intermittent energies is therefore of great importance. Among the varied energy conversion and storage systems, batteries and capacitors are promising in applications such as utility, transport, and portable devices. This explains the growing demand for Li-ion batteries (LIB) in recent years since LIBs possess high energy density, low self-discharge rate, and long cycling life.

Despite the strong demand for LIB, technology development still needs to be upgraded towards high energy density and power density to fulfill the requirements. For instance, electric vehicles require energy density larger than 40 kWh [3]. To fulfill such requirements, tuning the constituents of LIB (i.e., anode, cathode, separator, and electrolyte) and improving battery management system are necessary. Since the research of cathode materials like $LiFePO_4$ is quite mature, anode material will be focused on my research. Graphite is a commonly used anode material proposed by Sony in 1991 due to its cheap and non-toxic features. However, it has a relatively low specific capacity of 372 mAh g^{-1}. Meanwhile, its working voltage is also low of 0.1 V vs. Li^+/Li. Such low voltage could cause lithium plating upon the high current operation, which is one major setback for graphitic materials. Intense research has been conducted to find a better alternative to graphite. Conversion and alloy type materials are well-known alternatives because of their high specific capacities [4-6]. However, conversion type materials exhibit large voltage hysteresis, volume variation, relatively higher redox potential and poor cycling stability [7]. On the other hand, alloy type materials suffer from cyclability problem due to the huge volume change during charging/discharging process; for instance, Si has a volume change of more than 300 % during cycling [8], which generate high mechanical stress which eventually results in the detachment of active material from the current collector and drastic capacity fading [9]. Besides graphite, $Li_4Ti_5O_{12}$ as another intercalation type material known for its low volume change and high reversibility. However, the high insertion potential (about 1.5 V vs. Li^+/Li) and low capacity (~150 mAh g^{-1}) of $Li_4Ti_5O_{12}$ severely restrict its application [10]. Therefore, continuous effort is necessary for exploring anodes with high capacity and suitable potential for future LIB applications. Recently, Li_3VO_4 (denoted as LVO) anode with β polymorph has been reported as a promising insertion type material to replace graphite and $Li_4Ti_5O_{12}$. Up to two moles of Li can be accommodated by LVO, giving a theoretical capacity of ca. 395 mAh g^{-1}, which is higher than that of $Li_4Ti_5O_{12}$ [11]. Besides its high capacity, LVO also has an appropriate voltage window (0.5–0.8 V vs. Li^+/Li), allowing the avoidance of safety issue related to the formation of lithium dendrites and guarantees high voltage of the full cell [12, 13]. These advantages make LVO a promising anode material among the current studied materials. Intensive research has been conducted on LVO to improve its battery performance. However, the electronic conductivity and ionic conductivity are the hindrance to release its full capacity. As such, extensive amounts of efforts have been placed in designing materials that provide express pathways for both ions and electrons. Common ways to improve the ionic conductivity are compositing or coating with conductive materials, reducing particle size, and doping; while electrical conductivity can be improved through surface modification, particle size controlling and doping. The detailed strategies will be discussed in literature review section.

vanadium-based material (VS_4) is another promising anode material due to its small bandgap of ~1.0 eV [14]. This suggests that VS_4 has relatively good electrical conductivity in comparison to metal oxides. Furthermore, it has a long chain structure, which allows storage of Li^+ ions between the chains. A high theoretical specific capacity of 1196 mAh g^{-1} makes VS_4 a potential anode material for a lithium-ion battery [15]. In spite of its many advantages, insufficient research has been conducted on VS_4 due to its challenging synthesis procedure [16]. In addition, the electronic conductivity of VS_4 must also be improved to allow successful usage in battery application. Also, fundamental studies such as the effect of morphologies on the electrochemical performance are also lacking.

Hypothesis

As mentioned early, LVO is a promising anode material due to its high specific capacity and a suitable lithium insertion voltage range (~0.7 V). However, it has some shortcomings like low electronic conductivity and volume change. Electronic conductivity affects the charge transfer resistance while drastic volume change results in degradation of cycling stability. Currently, intensive work has been focused on improving LVO performance through reduction of particle size [17, 18], synthetic optimization [17, 19-21], surface modification [12, 22, 23], and hybridizations [24-29]. Another factor that could significantly influence the electrochemical performance is morphologies of materials. For example, hollow LVO with various shell thickness is prepared, and different electrochemical performances are obtained [30]. Sphere-like and platelet-like LVO materials are developed via an aerosol spray approach and show very different electrochemical capabilities [31]. All these examples clearly demonstrate that morphologies play a significant role in the electrochemical performance. Therefore, the study of the effect of morphologies on the electrochemical performance, especially in systematically way, seems relevant and important for guiding the design of advanced LVO or other vanadium-based materials. On the other hand, synthesis of LVO with classic morphologies (e.g. nanorod or microspheres) could also provide ways to improve the electrochemical performance. Such classic morphologies have been proved viable in other materials. For instance, Si nanowires directly grown on current collector show excellent cycling stability and high specific capacity. The authors attributed the good performance to the 1D structure, which allows better accommodation of large volume change, meanwhile, its 1D structure provides an efficient pathway for electrons transportation [32]. 1D MFe_2O_4 (M = Co, Zn, Ni) nanorods prepared via a hydrothermal method also demonstrate superior electrochemical performance. This is due to the shortened diffusion path and reduced strain generated upon charging/discharging process provided by the 1D structure [33]. Many other materials like $LiFePO_4$ [34], SnO_2 [35], GeO_2 [36] with 1D structure all shows prominent electrochemical performance. Thus, the first hypothesis is the assumption of 1D LVO could enhance the electrochemical performance.

Another promising morphology is hierarchical nano-micro structure, in which the primary nano-sized particles could shorten the lithium diffusion path; meanwhile, the micro-sized secondary particles could stabilize the structure during cycling. Many research works like hierarchical porous $LiNi_{1/3}Co_{1/3}Mn_{1/3}O_2$ nano-/micro spheres [37], V_2O_5 [38], $Li_4Ti_5O_{12}$ [39], $CuBi_2O_4$ [40] etc. have proven the feasibility of improved electrochemical performance. Thus, the second hypothesis is that hierarchical LVO can enhance electrochemical performance.

Apart from LVO, VS_4 is another promising vanadium-based anode material for LIB application. However, little research has been conducted on VS_4 because of its difficulty in synthesis. As mentioned before, morphologies have great influence on the electrochemical performance of the lithium-ion battery; investigating the effect of VS_4 morphologies could be an interesting work. Moreover, synthesis of VS_4 with special morphologies may help boost the electrochemical performance. One promising structure is urchin-like structure. The urchin-like structure has a 3D morphology with multiple long nanowires emanating from the core. This may make the material exhibit superior performance as it combines porosity and large surface area. Furthermore, the nanowires not only provide shortened diffusion length and large interfacial area between active material and electrolyte, but also enhance porosity allowing large volume change upon charging and discharging process. Many materials have been synthesized in urchin-like morphologies [41-47]. Such morphology has been taken advantage to produce good electrochemical performance [48]. Similarly, applying urchin-like morphology to VS_4 could improve the performance by maintaining the cycling stability via alleviating the large volume change during cycling. Therefore, the third hypothesis is that the urchin-like VS_4 could improve the electrochemical performance.

Graphene is frequently used as a substrate to support metal oxide, sulfide, or phosphides due to its high mechanical stability and superior electronic conductivity. On one hand, the good mechanical stability can provide the electrode a buffer space to accommodate the volume change during discharging/charging process. The high electronic conductivity can improve the overall electronic conductivity of the electrode. Intensive research has been conducted to enhance the electrochemical performance of anode materials by compositing them with graphene. Particularly, directly growing active material with special structures such as 0D nanoparticles, 1D nanowires or nanorods, 2D nanosheet or nanoplates, and 3D flowers could enhance the performance of active material. This method has been proved feasible in many other material such as nanopillar Sn/graphene [49], Sn@CNT nanorods/graphene [50], Sn@carbon nanocables/graphene [51], 1D Co_3S_4 nanotubes/graphene [52]. Thus, the fourth hypothesis is that VS_4 with special morphologies like nanowires can grow on rGO with improved LIB electrochemical performance.

1.2 Objectives and Scope

The overall objective of the thesis is to study the two vanadium-based anode material (LVO and VS_4). To explore the possibility of these two anode materials for next-generation LIB application by improving their electrochemical performance, investigating the effect of morphologies on performance is imperative. In addition, the effect of carbon compositing with active material will also be studied through this thesis. Specifically, the sub-objectives are enumerated as below:

1.2.1 Investigate the effect of the morphologies of LVO and VS_4 on battery performance

Material nanostructuring can be classified into 0D nanoparticles, 1D nanotubes or wires, 2D nanosheets or belts, and 3D hierarchical, porous, or hollow structures. All these structures could lead to different battery performances. This is because of the exposed different planes, different particle size, void between the particles, and other factors as long as the Li-ion diffusion length and specific surface area are affected. For instance, LTO with 10 nm nanocrystals demonstrates better rate and capacity performance compared to the larger-size crystals [53]. The aspect ratio of 1D structure could also affect the electrochemical performance. For instance, TiO_2 with higher aspect ratio shows better battery performance at high current rates [54]. As such, nanocrystals with different exposed planes also show different performance. For example, exposed (001) facets of TiO_2 nanosheets is desirable because these facets have higher reactivity compared to other facets [55]. Alcohol is commonly used together with water to synthesize materials with various morphologies. The parameters (e.g., dielectric constant, boiling point, steric hindrance, and viscosity) are changed with alcohols. Thus, usage of various alcohols or addition of alcohol could be a simple and effective way to synthesize materials with novel morphologies.

1.2.2 Evaluate the electrochemical performance of carbon coated LVO and rGO@VS_4

Metal oxide or sulfides are normally mixed with carbonaceous materials like carbon, graphene, or CNT to improve the battery performance. The reasons can be attributed to the robust carbon matrix which allows volume accommodation and enhanced electronic conductivity. In this segment, amorphous carbon coated LVO and rGO@VS_4 nanowires will be demonstrated.

1.2.3 Unravel the underlying mechanism using comprehensive characterization techniques

To understand the distinct differences in electrochemical performance, characterization tools such as SEM, TEM, XRD, and BET are utilized to perform a comprehensive characterization on the materials. Also, EIS and CV testing are conducted to study the Li^+ ion kinetics, which could be correlated with the physical structures. The kinetic parameters such as Li^+ diffusion coefficient and charge transfer resistance are compared to understand the effect of morphologies on performance better.

1.3 Dissertation Overview

The thesis studies the effect of morphologies of LVO and VS_4 on the electrochemical performance for LIB application. Moreover, novel LVO nanostructures such as LVO nanorod, LVO microsphere, urchin-VS_4, and nanowire VS_4 grown on rGO are synthesized. Their effect on electrochemical performances is compared with other morphologies counterparts systematically.

Chapter 1 provides a rationale for selection of LVO and VS_4. Several research gaps involving LVO and VS_4 are also identified. Thereafter, the hypothesis, objectives, and scope are outlined, followed by listing the novelty and contributions of this thesis to the scientific communities.

Chapter 2 reviews the literature concerning lithium-ion battery anode materials, starting from the three working mechanisms depicting the interaction of lithium-ion with anode materials, to the selection process for LVO and VS_4. Furthermore, the advantages and shortcoming of LVO and VS_4 are also discussed in detail. The recent research activities on these two anode materials are thoroughly reviewed. This part serves as a guide to the gaps in knowledge that the whole thesis will be addressing.

Chapter 3 discusses the methodology of research works in this thesis. The synthesis methods and characterization tools are explained in detail. The principles underlying the synthesis/characterization are also discussed. Detailed battery assembly procedures are also presented.

Chapter 4 elaborates the first major set of results. Effect of LVO morphologies on the performance is investigated. Furthermore, the effect of carbon coating on LVO nanorod is studied.

Chapter 5 elaborates the second major set of results. This chapter investigates the effect of morphologies of LVO on the performance. In comparison to nanorod, microsphere LVO shows better performance. Moreover, the effect of carbon coating on LVO microsphere is investigated.

Chapter 6 elaborates the third major set of results which is to investigate the urchin-like VS_4 on the electrochemical performance. It is compared with other VS_4 having various morphologies. The morphologies and performance are correlated from a kinetic point of view.

Chapter 7 elaborates the fourth major set of results which is to further improve the performance of VS_4. This chapter shows the synthesis procedure of nanowire VS_4 directly grown on rGO via a simple one-step solvothermal reaction.

Chapter 8 concludes the whole project and draws together the threads of the whole thesis. The objectives of chapter 1 are achieved and the original hypothesis is verified. All the key findings and contributions are discussed. In addition, some outstanding questions and recommendations for future works are proposed, followed by the reconnaissance works that did not warrant a whole chapter.

1.4 Findings and Outcomes/Originality

This research led to several novel outcomes by:

1. Establishing a synthesis method to synthesize nanorod and microsphere LVO.
2. Correlating morphologies with electrochemical performance of LVO and VS_4, identifying the key structural/morphological parameters that determine Li^+ ion storage, which provides a fundamental guidance for designing vanadium-based materials.

3. Demonstrating the synthesis of VS_4 nanowires in-situ grown on rGO via a facile one-step solvothermal synthesis method. This is reported for the first time.

References

[1] W.B. Group, 2012: World Bank Publications.

[2] D.J. Wuebbles, A.K. Jain, Fuel Process. Technol., 71 (2001) 99-119.

[3] M. Lowe, S. Tokuoka, T. Trigg, G. Gereffi, Center of Glob., (2010).

[4] C. Yuan, H. Wu, Y. Xie, X.W.D. Lou, Angew Chem Int Ed, 53 (2014) 1488-1504.

[5] X.l. Huang, R.z. Wang, D. Xu, Z.l. Wang, H.g. Wang, J.j. Xu, Z. Wu, Q.c. Liu, Y. Zhang, X.b. Zhang, Adv Funct Mater, 23 (2013) 4345-4353.

[6] D. Ma, Z. Cao, H. Wang, X. Huang, L. Wang, Energy Environ. Sci., 5 (2012) 8538-8542.

[7] H.K. Liu, Z.P. Guo, J.Z. Wang, J. Mater. Chem., 20 (2010) 10055-10057.

[8] E.M. Erickson, C. Ghanty, D. Aurbach, J. Phys. Chem. Lett., 5 (2014) 3313-3324.

[9] A.L. Michan, M. Leskes, C.P. Grey, Chem. Mater., 28 (2016) 385-398.

[10] Z. Yang, D. Choi, S. Kerisit, K.M. Rosso, D. Wang, J. Zhang, G. Graff, J. Liu, J. Power Sources, 192 (2009) 588-598.

[11] C. Zhang, H. Song, C. Liu, Y. Liu, C. Zhang, X. Nan, G. Cao, Adv. Funct. Mater., 25 (2015) 3497-3504.

[12] Z. Liang, Z. Lin, Y. Zhao, Y. Dong, Q. Kuang, X. Lin, X. Liu, D. Yan, J. Power Sources, 274 (2015) 345-354.

[13] S. Ni, J. Zhang, J. Ma, X. Yang, L. Zhang, X. Li, H. Zeng, Adv. Mater. Interfaces, 3 (2016) 1500340.

[14] C.S. Rout, B.-H. Kim, X. Xu, J. Yang, H.Y. Jeong, D. Odkhuu, N. Park, J. Cho, H.S. Shin, Journal of the American Chemical Society, 135 (2013) 8720-8725.

[15] X. Xu, S. Jeong, C.S. Rout, P. Oh, M. Ko, H. Kim, M.G. Kim, R. Cao, H.S. Shin, J. Cho, Journal of Materials Chemistry A, 2 (2014) 10847-10853.

[16] C. Zhang, C. Liu, X. Nan, H. Song, Y. Liu, C. Zhang, G. Cao, ACS Applied Materials & Interfaces, 8 (2016) 680-688.

[17] C. Zhang, C. Liu, X. Nan, H. Song, Y. Liu, C. Zhang, G. Cao, ACS Appl. Mater. Interfaces, 8 (2015) 680-688.

[18] S. Ni, X. Lv, J. Ma, X. Yang, L. Zhang, J. Power Sources, 248 (2014) 122-129.

[19] W.T. Kim, Y.U. Jeong, Y.J. Lee, Y.J. Kim, J.H. Song, J. Power Sources., 244 (2013) 557-560.

[20] Y. Shi, J.-Z.Z. Wang, S.-L.L. Chou, D. Wexler, H.-J.J. Li, K. Ozawa, H.-K.K. Liu, Y.-P.P. Wu, Nano Lett., 13 (2013) 4715-4720.

[21] J. Liu, P.J. Lu, S. Liang, J. Liu, W. Wang, M. Lei, S. Tang, Q. Yang, Nano Energy, 12 (2015) 709-724.

[22] Y. Dong, Y. Zhao, H. Duan, P. Singh, Q. Kuang, H. Peng, J. Power Sources, 319 (2016) 104-110.

[23] S. Hu, Y. Song, S. Yuan, H. Liu, Q. Xu, Y. Wang, J. Power Sources, 303 (2016) 333-339.

[24] J. Zhang, S. Ni, T. Kang, J. Tang, X. Yang, L. Zhang, J. Mater. Chem. A, 4 (2016) 14101-14105.

[25] D. Zhao, M. Cao, ACS Appl. Mater. Interfaces, 7 (2015) 25084–25093.

[26] Q. Li, J. Sheng, Q. Wei, Q. An, X. Wei, P. Zhang, L. Mai, Nanoscale, 6 (2014) 11072-11077.

[27] Q. Li, Q. Wei, J. Sheng, M. Yan, L. Zhou, W. Luo, R. Sun, L. Mai, Adv. Sci., 2 (2015) 1500284.

[28] S. Ni, X. Lv, J. Ma, X. Yang, L. Zhang, Electrochim. Acta, 130 (2014) 800-804.

[29] S. Ni, J. Zhang, J. Ma, X. Yang, L. Zhang, J. Mater. Chem. A, 3 (2015) 17951-17955.

[30] Q. Li, Q. Wei, Q. Wang, W. Luo, Q. An, Y. Xu, J. Mater. Chem. A, 3 (2015) 18839-18842.

[31] P. Tartaj, J.M. Amarilla, M.B. Vazquez-Santos, Chem. Mater., 28 (2016) 986-993.

[32] C.K. Chan, H. Peng, G. Liu, K. McIlwrath, X.F. Zhang, R.A. Huggins, Y. Cui, Nature nanotechnology, 3 (2008) 31.

[33] N. Wang, H. Xu, L. Chen, X. Gu, J. Yang, Y. Qian, Journal of Power Sources, 247 (2014) 163-169.

[34] V.S. Saji, Y.-S. Kim, T.-H. Kim, J. Cho, H.-K. Song, Physical Chemistry Chemical Physics, 13 (2011) 19226-19237.

[35] S. Chen, Y. Xin, Y. Zhou, F. Zhang, Y. Ma, H. Zhou, L. Qi, Journal of Materials Chemistry A, 2 (2014) 15582-15589.

[36] W. Wei, F. Jia, P. Qu, Z. Huang, H. Wang, L. Guo, Nanoscale, 9 (2017) 3961-3968.

[37] Z. Chen, J. Wang, D. Chao, T. Baikie, L. Bai, S. Chen, Y. Zhao, T.C. Sum, J. Lin, Z. Shen, Scientific reports, 6 (2016) 25771.

[38] H.-E. Wang, D.-S. Chen, Y. Cai, R.-L. Zhang, J.-M. Xu, Z. Deng, X.-F. Zheng, Y. Li, I. Bello, B.-L. Su, Journal of colloid and interface science, 418 (2014) 74-80.

[39] L. Shen, C. Yuan, H. Luo, X. Zhang, K. Xu, Y. Xia, Journal of Materials Chemistry, 20 (2010) 6998-7004.

[40] H. Yin, M.-L. Cao, X.-X. Yu, C. Li, Y. Shen, M.-Q. Zhu, RSC Advances, 7 (2017) 13250-13256.

[41] Y. Dong, D. Li, C. Gao, Y. Liu, J. Zhang, Journal of Materials Chemistry A, (2017).

[42] X.Q. Zhang, Y.C. Zhao, C.G. Wang, X. Li, J.D. Liu, Journal of materials …, (2016).

[43] J. Liang, K. Xi, G. Tan, S. Chen, T. Zhao, P.R. Coxon, Nano Energy, (2016).

[44] K. Zhang, M. Park, L. Zhou, G.H. Lee, W. Li, Advanced Functional …, (2016).

[45] X. Wu, J. Guo, M.J. McDonald, S. Li, B. Xu, Y. Yang, Electrochimica Acta, (2015).

[46] D. Li, C. Feng, H.K. Liu, Z. Guo, Scientific reports, (2015).

[47] A.K. Mondal, D. Su, Y. Wang, S. Chen, Q. Liu, Journal of Alloys and …, (2014).

[48] W. Fang, H. Zhao, Y. Xie, J. Fang, J. Xu, Z. Chen, Acs Appl Mater Inter, 7 (2015) 13044-13052.

[49] L. Ji, Z. Tan, T. Kuykendall, E.J. An, Y. Fu, V. Battaglia, Y. Zhang, Energy & Environmental Science, 4 (2011) 3611-3616.

[50] Y. Zou, Y. Wang, Acs Nano, 5 (2011) 8108-8114.

[51] B. Luo, B. Wang, M. Liang, J. Ning, X. Li, L. Zhi, Advanced Materials, 24 (2012) 1405-1409.

[52] N. Mahmood, C. Zhang, J. Jiang, F. Liu, Y. Hou, Chemistry-A European Journal, 19 (2013) 5183-5190.

[53] J.M. Feckl, K. Fominykh, M. Döblinger, D. Fattakhova- Rohlfing, T. Bein, Angew. Chem. Int. Ed, 51 (2012) 7459-7463.

[54] Y. Tang, Y. Zhang, J. Deng, D. Qi, W.R. Leow, Angew. Chem. Int. Ed, 126 (2014) 13706-13710.

[55] J.S. Chen, X.W.D. Lou, Chem. Sci., 2 (2011) 2219-2223.

Chapter 2

Literature Review

This chapter begins with the introduction of background for lithium-ion battery and the related working principles. Then, the categorization of anode materials is outlined, and their working mechanism is explained. This is followed by the justification of Li_3VO_4 *and* VS_4 *for Phd study. In addition, the properties such as crystal structures, electrical and ionic conductivities are also discussed. The preparation and current research progress, strengths, drawbacks, and strategies for improving/ameliorating on* Li_3VO_4 *and* VS_4 *reported in the literature are summarized and compared. The last section shows the research niche concerning about the morphological and carbon coating effect on* Li_3VO_4 *and* VS_4*. The contents and objective of my PhD study are listed.*

2.1 Overview

Energy for centuries has been generated mainly by non-renewable fossil fuels such as petroleum oil, coal, and natural gas. However, negative effects of using fossil fuels such as inevitable exhaustion of fossil fuels and environmental pollution have raised peoples' awareness. Consequently, replacing the current fossil fuels with clean and renewable energies is imperative [1, 2]. However, renewable energies such as solar, wind and tidal energy tend to intermittent in nature. Reliable energy storage and conversion systems with high conversion efficiency are required to store such clean energy.

As one type of energy storage and conversion devices, the rechargeable battery has been developed for the portable electric devices and electric vehicles, catering to the need of this information-rich and mobile society. The first rechargeable battery was called lead acid battery and invented in 1859 with Pb and PbO_2 as electrodes, which is now still applicable in today's automobiles [3]. Later in the last century, a few other batteries such as NiCd, NiMH, and LIB (lithium-ion batteries) have been gradually brought into the commercial market [4]. Among them, LIB is of particular interest because of its high energy density (ca. 250-400 Wh kg^{-1}) with long cycling and lighter weight (Figure 2.1) [5]. Besides that, its operating voltage (~3.7 V) is high and self-discharge is low [3, 6]. All these make LIB be promising electrochemical energy storage devices.

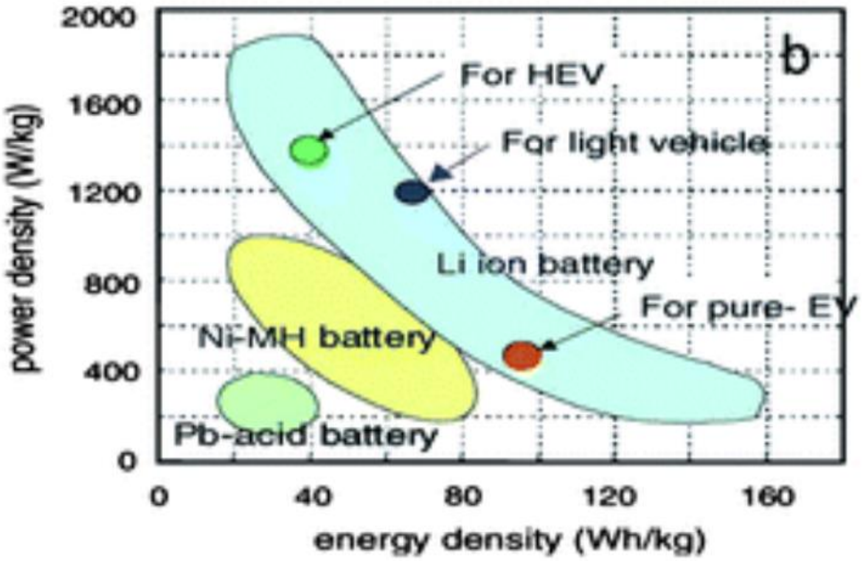

Figure 2.1 Advantages of LIB in the rechargeable batteries matrix (x-axis indicated energy density, expressed in Wh Kg^{-1}, and y-axis indicates power density, expressed in h kg^{-1}) [2]. (Reprinted with permission from RSC)

2.2 Basic principles of LIBs

Similar to other batteries systems, LIB stores electrical energy through an electrochemical reaction, in which the energy could be extracted when the external load is connected [7, 8]. The basic LIB consists of four components, a cathode, anode, electrolyte, and separator. The common used commercial cathode materials are layered oxides like $LiCoO_2$, spinel $LiMn_2O_4$ and Olivine materials like $LiFe(PO_4)$. In contrast, the anode materials commercially viable till today mainly consists of carbonaceous materials like graphite. The active cathode and anode material are normally intermixed with carbon to improve its electrical conductivity and PVDF to ensure active materials stick to the aluminum or copper foil current collector. Consequently, the cycling stability and performance can be enhanced. The electrolyte is to provide ionic conductive medium allowing Li or other alkali ions to shuttle between cathode and anode in discharging and charging process, meanwhile electrically separate cathode and anode to prevent the short circuit. Different alkali ion batteries use different electrolyte; Lithium salts (like $LiPF_6$ or KPF_6, $liClO_4$, and $KClO_4$) dissolved in carbonate-based solvents (PC, EC, DEC) are used for lithium-ion battery and potassium ion batteries. These organic electrolytes are chosen due to their relatively large potential window compared to aqueous-type batteries. The separator is either microporous polymeric membrane or woven glass fibers that need to be wetted with electrolyte before usage. A key function of the separator is separating cathode and anode electrically, at the same time allowing the conduction of ionic species through them. Here, commercial anode graphite and cathode material $LiCoO_2$ are used as an example to explain the working mechanism (Figure 2.2).

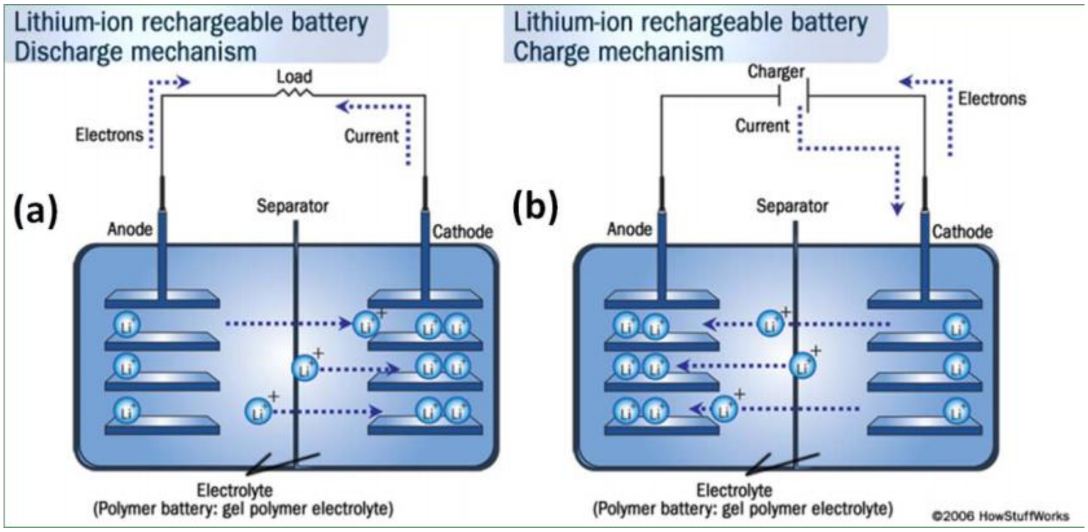

Figure 2.2 Schematic diagram of LIB working mechanism during (a) discharging and (b) charging [9].

Half-cell reaction for the cathode part ($LiCoO_2$) during charging [10]:

$$LiCoO_2 \leftrightarrow Li_{1-x}CoO_2 + xLi^+ + xe^{-1} \quad (1)$$

In contrast, half-cell reaction for the anode part (graphite) during charging:

$$6C + xLi^+ + xe^{-1} \leftrightarrow LiC_6 \quad (2)$$

The electrochemical energy stored in Li-ion batteries is *via.* a rocking chair mechanism which can be elucidated in a full-cell equation 1. Lithium ions migrate from $LiCoO_2$ host to graphite, accompanying the oxidizing Co^{3+} to Co^{4+} during discharging process. To maintain the charge neutrality, electrons move through the external circuit from $LiCoO_2$ host to graphite. The charging process is just opposite.

$$LiCoO_2 + 6C \leftrightarrow Li_{1-x}CoO_2 + Li_xC_6 \quad (3)$$

LIBs are advised to operate in the certain temperature ranges, typically, from 15 to 60 ºC. If the operating temperature is below 15 ºC, the reaction kinetic will be slow; higher temperature than 60 ºC will degrade the electrolyte and affect the battery lifetime [6, 11]. Besides working temperature, the working potential range also plays an important role. The overall potential is limited by the decomposing voltage limit of organic electrolyte and lower limited by alkali metal plating potential [12]. The lifetime and the net capacity of a Li-ion cell also depend on this reaction occurring reversible with minimal loses.

Specific capacity is a key parameter to measure the quantity of charge could be stored for a certain electrode material. Theoretical specific capacity is calculated based on the following equation:

$$\text{Specific capacity (mAh g}^{-1}\text{)} = \frac{zF}{M} X \frac{1000}{3600} \qquad (4)$$

Where z is the number of electrons generated during a redox reaction, F is the Faraday constant 96485 C mol^{-1}, M is the molar mass of the electrode material. According to the above equation, the specific capacity is determined by the molar mass of active material as well as a number of Li^+ ions involved in the reaction, which is correlated with the reaction mechanism. Another important parameter is coulombic efficiency, which is obtained from the ratio of the discharge capacity and charge capacity. The coulombic efficiency reflects the reversibility and charge loss during each charge/discharge cycle.

$$\text{Coulombic efficiency} = \frac{Discharge\ capacity}{Charge\ capcity} \qquad (5)$$

Coulombic efficiency will ideally be 100% if there is no capacity loss. However, it is much often less than 100% due to some parasitic side reactions that irreversibly consume Li or K ions from electrolyte or the other electrode materials. Rate cyclability is also a key parameter to measure the battery performance as different current density or C rate. 1C rate means charge/discharge a battery using 1h at a certain current density. For example, an electrode material with a capacity of 100 mAh g^{-1} needs a 100 mA g^{-1} current to discharge/charge for 1h, in contrast, it needs a current of 1000 mA g^{-1} for an electrode material with a capacity of 1000 mAh g^{-1}. With the increase in current density, the capacity drops because of the diffusion/kinetic limitations and the morphology, structure and reaction mechanism with alkali ions are also influence the capacity drops [13].

2.3 Classification of anode materials

As mentioned before, the specific capacities of electrode materials are dependent on materials types (Figure 2.3). Anode materials generally can be divided into three types: insertion-type, alloying-type, and conversion-type anode materials [13]. These three type materials have their advantages and drawbacks. The commercially used graphite anode belongs to insertion type anode material with a theoretical capacity of 372 mAh g^{-1}. This is a relatively low capacity compared to conversion- and alloy-type anode materials. However, insertion-type materials have low volume changing during charging/discharging process, which helps keep the integration of materials and maintain the long cycling life of the battery. Commercial graphite material also has a safety hazard related to the lithium plating, especially at high current rates. Lithium plating could lead to dendrites formation and short-circuit the battery [14, 15]. Thus, much attention has been paid to exploit alternative anode to replace graphite anodes. The new anode materials are expected to have high specific capacity, environmentally friendly, superior cycling stability, cheap and lower working voltage. Conversion-type anode materials have high reversible capacities but are accompanied by large polarization, large volume change and sloping voltage profile, which is associated with their reaction mechanism involving the bond breaking and forming process [6]. Similar to conversion-type, alloying-type anode material has high specific capacity with low operating potential [16]. However, the huge volume change leads to the short life of the battery. Despite many difficulties ahead, it is worth it to invest in investigating the next generation of anode materials.

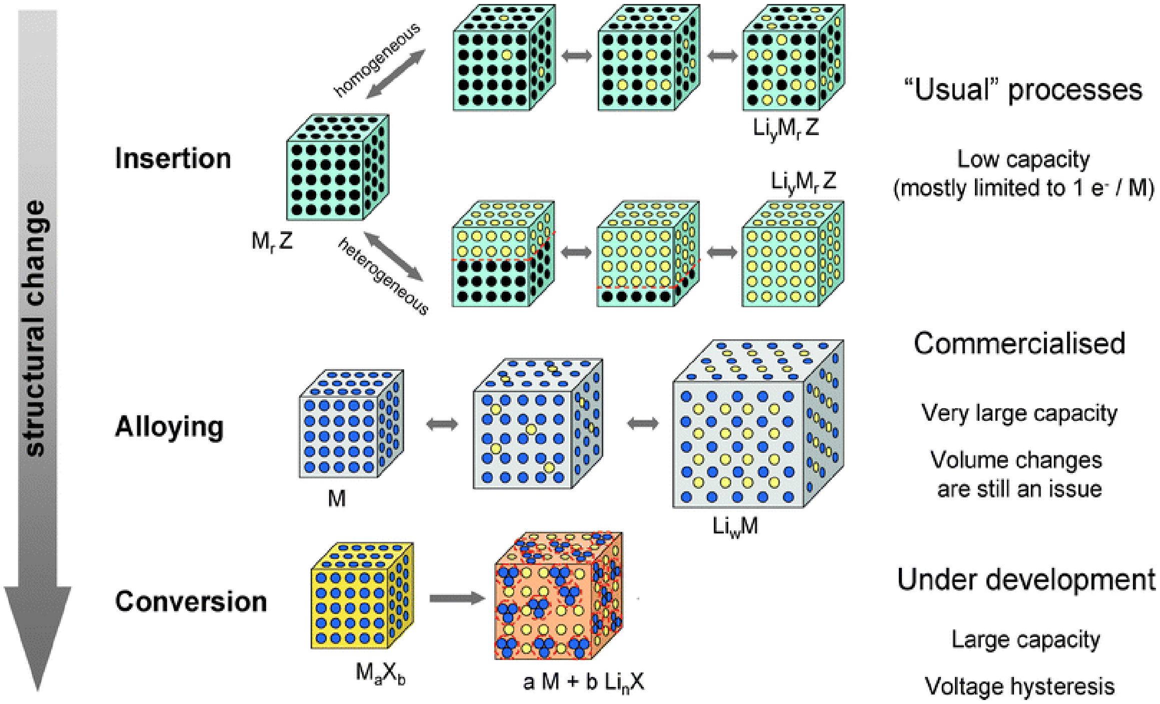

Figure 2.3 Schematic representing anode materials with different reaction mechanism [13].

2.3.1 Anodes by intercalation

Insertion type materials are characterized by their small volume change and flat working voltage plateau. Intercalation sites are required to accommodate the alkali ions like Li^+ or K^+. During the insertion/deinsertion process, a minor volume change happens to the host materials and the reversibility and cycling stability can be ensured [17, 18]. One typical example is $LiCoO_2$ and graphite; both can host Li ions in a 2D planes. Li ions shuttle between $LiCoO_2$ and graphite electrodes. This 'rocking chair' theory was first proposed by Armand and Scrosati et al. [19]. Apart from graphite, various insertion-type materials have also been investigated as new anodes for LIB, such as oxides (Ti-based, carbon-based, Nb-based and V-based) and chalcogenides (TiS_2) [19]. One typical insertion-type anode is TiO_2. It exists in several polymorphs (e.g. rutile [20], anatase [20], brookite [21], and TiO_2-B [22]). Spinel $Li_4Ti_5O_{12}$ was also a promising candidate because of the excellent reversibility with almost zero volume change during cycling process. Furthermore, its high working voltage of 1.5 V make it a safer choice compared to graphite. However, its capacity is only capped at 175 mAh g^{-1} [23]. Nb_2O_5 also presents in several polymorphs and orthorhombic structure is the most commonly studied one [24, 25]. The insertion-type materials are attractive owing to their rapid intercalation property.

2.3.2 Anodes by alloy/dealloy

Asides from intercalation mechanism, anode materials that undergo alloying reaction mechanism is also of great interests. Dey et al. showed a series of metallic or semimetallic elements that own very large capacity. They can react with lithium to form alloy or intermetallics upon discharging process (e.g., Group 13, 14, 15 and 16 elements) [26]. Nanocrystalline metal can be reformed after dealloying in charging process [23]. The theoretical capacities and compatibilities of alloy-based materials with lithium can be speculated from the phase diagrams (Figure 2.4). For instance, Si can alloy with 4.4 Li and Sn with 4.4 Li. Thus, Si has a theoretical capacity of ~4200 mAh g^{-1} and Sn has a capacity of ~960 mAh g^{-1}. Mg and Al gained less focus compared with other elements because they have a layer of native oxide that decreases Li^+ diffusion kinetics. Although the alloy-type anode materials have much higher capacities than that of graphite, they demonstrate poor capacity retention arising from the excessive volumetric change in active materials upon cycling. For example, $Li_{4.4}Si$ suffers a 400% lattice volume expansion after being alloyed [27, 28]. The large volume change brings high stresses generation or cracking of the active material, finally leads to poor cycling stability. This shortcoming impedes the commercial application of alloy/dealloy-based anode materials. Several strategies have been proposed to address this issue including nano-synthesis and morphology control strategies [27, 29] or compositing with carbonaceous materials [30]. Sony previously invented and improved Sn-Co-C anode material for Nexelion commercial LIB in 2005. This material has a high reversible capacity of 500 mAh g^{-1} and good stability benefiting from the non-active metal Co [31]. The Co not only effectively relieves the volume expansion, while enhancing electrical conductivity [23, 32]. Nevertheless, the further study of substitution of Co is necessary due to the toxicity and cost of Co [33, 34].

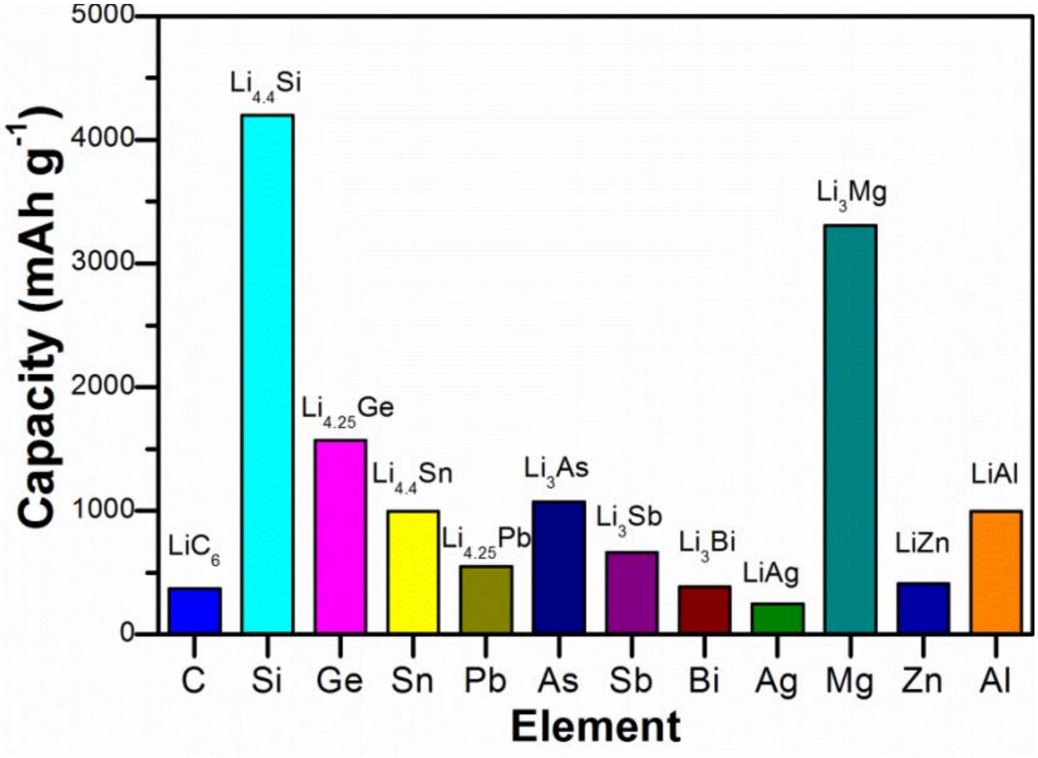

Figure 2.4 Common alloying-based elements and comparison of their specific capacities [23, 35].

2.3.3 Anodes by conversion

The last type of Li storage mechanism is conversion reaction. These type anode materials also have high specific capacity in the ranges of ca. 400-1000 mAh g^{-1} and most transition metal oxides fall in this category. This mechanism is commonly seen in some other materials, such as metal sulfides, nitrides, fluorides, phosphides, etc. [34, 36]. The high capacity comes from their reaction with more than one Li ion per unit compound [37]. In spite of the obtained high capacity, the large capacity brings along conversion type materials with extensive volume change, structural damage, and resulting in poor cycling performance. During lithiation process, the compound converts to metallic nanocrystals and embeds within the Li$_n$X matrix. The overall reaction for transition metal compound could be summarized in equation 6:

$$M_cX_d + d.nLi^+ \leftrightarrow cM + dLi_nX \qquad (6)$$

Where n is the redox number of anionic X^{n-}, M is the transition metal, X is O, S, P, N etc, the reaction redox potential is determined by ionicity of M-X. Initially, the reaction of TMOs was perceived to be irreversible because of the formation of inactive Li$_2$O. It was not until Poizot et al. proposed that the CoO reacts with Li metal to form Co and Li_2O during 1st discharge, and then they react back to nanocrystalline CoO in the subsequent charge process [37]. What needs to be emphasized here is the importance of nanoscaling of TMOs, because nano-scale material has enough chemical reactivity to return to metal oxide after reaction with lithium [38, 39]. In addition, nano-scale materials can provide a large surface area and shortened diffusion pathway, which will increase the electrochemical kinetics [36, 40, 41]. The main downside of the conversion type materials is the voltage hysteresis that affects the energy efficiency. Another drawback is its low operating voltage (<0.5 V vs. Li^+/Li), which lower than the SEI formation voltage. This could lead to the formation of thick SEI and eventually affect the lithium ion transportation [39, 40].

2.4 Li_3VO_4

Lithium-ion batteries (LIBs) have high energy densities and long cycle life, and these advantages allow them to have wide applications, such as electronic devices, electric cars and hybrid electric cars, and other energy storage devices. These applications, in turn, promoted a better development of lithium-ion batteries [42]. The conventional commercialized intercalation-type graphite anode materials are insufficient to meet the needs of the next-generation LIBs, especially in electric cars applications. That is because graphite has the disadvantages of low theoretical specific capacity and safety problem. The safety issue is embodied in the generation of lithium dendrites, especially in the case of high current densities. The dendrites can pierce through the separator, causing the battery to short circuit and eventually cause a fire. Therefore, much effort has been devoted to finding alternative anode materials with high theoretical specific capacity, good rate capability and long life [42, 43]. Another classic anode material is spinel $Li_4Ti_5O_{12}$ (LTO), which has superb cycling stability and safety although with a relatively low theoretical capacity (175 mAh g^{-1}). The excellent cycling stability is attributed to the very small volume change of the host material during battery cycling process [2]. Its excellent safety is reflected in its operating voltage, which is far higher than lithium dendrite formation voltage. However, such high voltage will sacrifice the full cell voltage and energy density seriously [24]. Recently in 2013, Li and co-workers [44] first discovered that Li_3VO_4 (LVO) can be used in lithium-ion batteries, and the operating voltage is between 0.5 and 1 V vs. Li/Li$^+$ and high capacity (394 mAh g^{-1}). On one hand, its capacity is higher than that of commercial graphite. Its working voltage is neither high nor low, which is in an appropriate voltage range. These features not only avoid the formation of lithium dendrites, but also ensure reasonable working window and full battery energy density. Its inherent advantages make it a very promising anode material for further commercial applications.

LVO exists into two polymorphs, namely, β and γ phase. Its γ form is stable at high temperature while β form generally stable at low temperature [45]. The γ form is more favorable for LIB application due to its higher ionic conductivity. Unfortunately, it is not stable at room temperature and transforms to β form LVO when cooling down [46] (Figure 2.5). Therefore, most of the research is focused on β-form LVO. The β form LVO falls into the orthorhombic structure category in the space group Pnm21. Its unit cells consist of VO_4 and LiO_4 tetrahedrons, which are corner connected to one another to form a lattern-like structure. This structure is very conducive for Li$^+$ ions to insert or de-insert [47]. The possible insertion mechanism of LVO can be depicted using the following equation:

$xLi^+ + Li_3VO_4 + xe^{-1} \leftrightarrow Li_xVO4$

The exact amount of insertable Li$^+$ is still debatable. Initially, Ni's group [48] proposed that two Li$^+$ could be inserted into LVO accompanied by the reduction from V^{5+} to V^{3+}, which was examined and proved by the XPS. However, another view concerning the maximum Li$^+$ has been given by Liang and co-workers [47]. Their synthesized carbon – coated LVO showed a capacity of 542 mAh g^{-1}, equivalent to ca. 2.77 Li$^+$, surpassing its theoretical capacity (394 mAh g^{-1}). Galvanostatic intermittent titration technology (GITT) combining with computational results deduced that the maximum of Li$^+$ could be three rather than two. Kim et al. [49] also agreed with that conclusion through examining the intermediates upon discharge/charge using XPS. Up to now, no definitive conclusion has been drawn. A computational study showed that the third Li$^+$ occurs at 0.14 V with a volume change of 20% [50]. Anyway, although the exact number of insertable Li$^+$ is unclear, LVO is still competitive compared to LTO and graphite in terms of the capacity (Table 2.1).

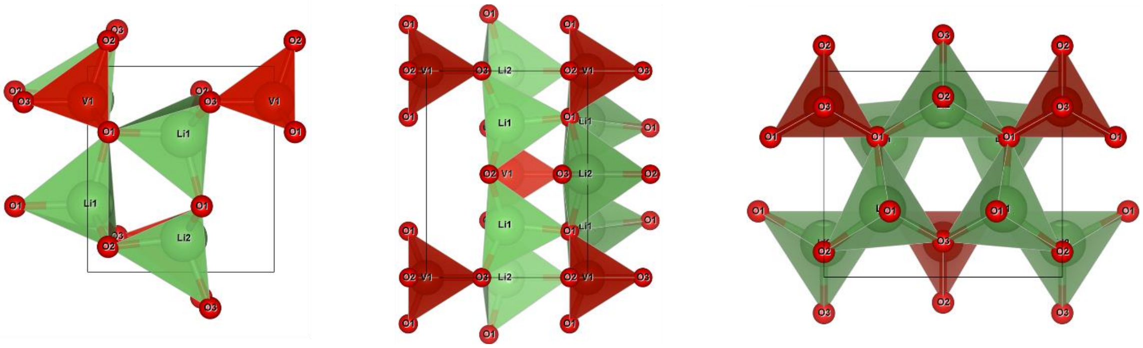

Figure 2.5 Schematic structure of β form LVO, projected along a, b, c-axis.

Table 2.1 The strengths and drawbacks for LTO and LVO

Material	Voltage (V)	Capacity (mAh g^{-1})	Electronic conductivity (S cm^{-1})	Diffusivity (cm^2 s^{-1})	Advantages	Common issues
Li_3VO_4	0.8-1	394	10^{-6} [51]	10^{-13} [52]	Low voltage Prevent lithium dendrite High capacity	Low electronic conductivity Poor rate capability
$Li_4Ti_5O_{12}$	1.55	175	$8x10^{-13}$ [51]	10^{-15} [53]	Good cycling stability Stable structure	High voltage Low capacity

2.4.1 Strengths of Li_3VO_4

1.1.1 Higher capacity than graphite

Graphite as a commonly used commercial anode material for LIBs faces some problems that have been discussed previously. Its relatively low working potential leads to Li-plating at a high current rate, which results in short circuit for the battery [54]; on the other hand, its theoretical capacity is limited to 372 mAh g^{-1}. In comparison, LVO has a higher capacity of 394 mAh g^{-1} and suitable intercalation potential of 0.5 to 1 V, which prevents lithium plating. Di et al. reported that LVO nanoparticles embedded in hierarchically porous carbon network, showed a capacity of 381 mAh g^{-1} after 300 cycles at a current density of 0.2 A g^{-1}. It retained a high reversible capacity of 275 mAh g^{-1} even at a rate as high as 4 A g^{-1}, after 500 cycles [55]. With the improvement of synthesis method, the capacity of LVO nowadays can achieve around 600 mAh g^{-1}. Such a capacity is even competitive with conversion and alloying type anode material. Moreover, the structure of LVO characterized by XRD is proved going through a reversible change during charging and discharging cycle, and this ensures the good long-term cycling stability [56, 57].

1.1.2 Proper working potential

Li_3VO_4 has an orthorhombic crystal structure with $P2_1nm$ space group. Oxygen atoms are hexagonal close-packed with cations occupying the tetrahedral sites. While octahedral sites are empty and available for Li^+ ion insertion, which contributes its high ionic conductivity [58]. A proper working potential window of 0.5~1.0 V vs. Li/Li^{+1} was found for Li_3VO_4 [44]. This is because if the reduction potential of a negative electrode is below 0.4 V vs. Li/Li^+, there will be a great possibility that the higher polarization at high current density will result in voltage approaching 0 V, leading to the reduction of Li^+, causing lithium plating. Non-homogeneous Li plating may form Li dendrites which probably shorten the cell and causing safety hazard [59]. The slightly higher working potential of Li_3VO_4 makes it a safe anode material. In addition, the moderately high working potential also ensures the full-cell voltage and energy.

2.4.2 Drawbacks and strategies to improve

1.2.1 Poor electrical conductivity

Although LVO is an ionic conductor, it has a bandgap of 4 eV, which makes it a poor electronic conductor [54]. Such poor intrinsic conductivity can seriously affect the electrochemical properties, especially at high rate rates. The coulombic efficiency is also reduced due to the high polarization arising from the poor electrical conductivity.

1.2.1.1 Ways to improve - Compositing with conductive materials

The approach includes incorporation Li_3VO_4 with conducting additives. Conductive additives can be carbonaceous materials (graphite, amorphous carbon, CNT, graphene), conducting polymers (PPY, PANI, etc.), or metallic compounds (Au, Cu, etc.). Such a composite can increase the external electronic and ionic conductivity at the same time. The conducting materials provide a pathway for electrons within the electrode materials. Meanwhile, the incorporation of conducting materials could reduce the ion diffusion length. For instance, a carbon nanotube (CNT)@TiO_2 core-shell structure was reported with porous TiO_2 small particles on the surface, whereby the CNTs in the core could provide sufficiently fast electron conduction [60]. Meanwhile, the CNT could prevent the active material TiO_2 from aggregation and agglomeration. These agglomerated clusters increase the diffusion length of ions and cause the overall ionic pathway to be easily blocked. All these examples prove that compositing can improve the external electronic conductivity.

1.2.1.2 Ways to improve - Coating with conductive materials

Carbon coating is another very common method for improving the electrical conductivity of electrode materials. For instance, carbon-coated $LiMn_2O_4$ nanoclusters were prepared by Cho and colleagues [61]. The carbon is connected to form a network. It is demonstrated that this composite shows ultrahigh rate performance when tested as anodes for LIBs. Metallic materials, like Au, Ag, etc. are also commonly used conductive additives for coating on active materials. For instance, Au enveloped cobalt oxide nanowires with the help of virus were synthesized. They showed improved electrochemical performance at a high current density in comparison to the pristine Co_3O_4 [62].

1.2.1.3 Ways to improve - Reducing particle size

Nanostructuring strategies for fabricating active materials with 0D nanoparticles or quantum dots, 1D nanotubes or nanowires, 2D sheets or belts, and 3D hierarchical porous or core-shell or hollow structures have been adopted. These peculiar structures can shorten the diffusion lengths and enhance the transportation rates of electrons or Li^+ ions [63]. For instance, hierarchical LTO clusters with high mesoporous structure demonstrated not only battery performance, but also supercapacitor performance. It even works at a high rate of 400 C, owing to its large specific surface area of 205 m^2 g^{-1} and small particle size [64].

1.2.1.4 Ways to improve - Doping

Doping is the introduction of homogeneous/heterogeneous, metal/non-metal ions, or vacancies into raw materials. The purpose is to make it more electrically conductive by the deficiency/excess of electrons, thus improving the battery performance. For example, the introduction of into LTO nanowires was prepared by heat-treating LTO in a hydrogen atmosphere. The resulting Ti^{3+} doped LTO nanowires demonstrated a capacity of three times higher compared with pristine LTO nanowires [65]. Beyond that, black anatase TiO_2 by a similar method showed a high specific capacity of 152 mAh g^{-1} at a very rate of 100 C [66].

1.2.2 Low Li ion conductivity

For Li_3VO_4, it has a Li^+ ion diffusivity ca. 10^{-13} cm^2/s. However, organic electrolytes normally have a good Li-ion conductivity of more than 0.1 S cm^{-1}, which is a few orders magnitude higher compared to anodes/cathodes materials, good enough for ultrafast ion transport [67]. Therefore, the ionic conductivity of the electrode material needs to be improved to match with the electrolyte.

1.2.2.1 Ways to improve – surface modification

Similar to carbon encapsulation to improve the electrical conductivity, ionic conductivity of active material can be improved by coating high ionic conductivity materials. For example, the rutile TiO_2 coated LTO nanosheets demonstrated excellent rate capacity, especially at high current rate of 60C, the capacity of coated LTO is ca. 11 times higher compared to pure LTO nanosheets. Such good rate performance can be attributed to high ionic conductivity from rutile TiO_2 which enhanced the performance of overall material [68]. Aside from coating with another material, surface off-stoichiometry ($LiFe_{0.9}P_{0.95}O_{4-\delta}$)

modification on LFP provided an fast ion transportation on the surface, eventually, a capacity of above 100 mAh g^{-1} was achieved even at a high current rate of 197 C [69].

1.2.2.2 Ways to improve - Reducing particle size

Nanostructuring can enhance both electronic and ionic transportation. For example, Chen and co-workers reported that the electrochemical performance is dependent on the nanotubular aspect ratio. It was found that the battery behaves like capacitors with low charge transfer resistance [70].

1.2.2.3 Ways to improve - Doping

Doping technique is also commonly used to change the lattice atomic arrangement or expand lattice and thus improve the Li ion diffusion of Li^+ ions. A.Veluchamy et al. [71] reported that boron-doped $LiMn_2O_4$ shows increased D_{Li} measured by current pulse relax method. Apart from spinel structure, olivine structured LFP was doped and the structure was changed by Mn^{2+} [72]. Zinc-doped LFP ($LiZn_{0.01}Fe_{0.99}PO_4$) was prepared and demonstrated higher lithium ion diffusion rate due to the pillar effect of the doped Zn atoms [73].

1.2.3 Relatively low capacity

1.2.3.1 Ways to improve - Compositing with other high capacity materials

Insertion-type anode materials normally have high cycling stability but lower capacities. In contrast, alloying and conversion type materials have higher capacities but poor cycling stability. Synergic effect of their composite has been investigated. In some of the reports, Sn [74], SnO_2 [75], CuO [76] and Fe_2O_3 [77], Si [78] were used to be mixed with LTO and improvement in specific capacity was noted.

Table 2.2 Comparison of Li_3VO_4 (1C =400 mA g^{-1}) electrochemical performances from literature

Synthesis methods	Final product	1st charge capacity (mAh g^{-1})	Reversible capacity/Nth cycle/current density	Ref
Ultrasonic spray pyrolysis	Spherical particles with size 0.2-2 μm	400/0.2C	250/100/0.2C	[79]
Solution-based precipitation	Individual particles 1- 4 μm	245/0.2C 229/0.5C 249/1C	196/100/0.2C 184/100/0.5C 185/100/1C	[24]
SSR + Ball mill + CVD carbon coating	Spherical particle 300-500 nm with 8nm carbon, 5% carbon content	315/20 mA g^{-1}	250/50/20 mA g^{-1}	[80]
Sol gel method citric acid	Particle size 100 nm with 3.2 nm carbon coating 6.1% weight	480/0.18C	365/40/0.8C	[81]
Hydrothermal + annealing	250 nm porous	481/0.25C	396/100/0.25C	[48]
Hydrothermal + annealing	300 nm nanoparticles	472/150 mA g^{-1}	460/100/150 mA g^{-1} 264/2200/2 A g^{-1}	[82]
Carbon coated solid-state reaction	Particle size <1μm 3 nm carbon coating	490/350 mA g^{-1}	398/80/350 mA g^{-1}	[83]
Carbon coated solid-state reaction	Irregular shaped particle size 500 nm 6.67% carbon weight	547/0.2C	480/100/400 mA g^{-1} 291/100/4A g^{-1}	[47]
Hydrothermal + immersion with Ni foam	LVO film with cracks on the Ni surface	531/0.3C	378/100/0.3C	[84]
Hydrothermal + annealing	Particle size 40 nm embed in nanoflakes 15.6 % weight N doped Graphene	429/150 mA g^{-1} 200/2 A g^{-1}	476/100/150 mA/g 193/900/2 A/g	[85]
Hydrothermal + annealing	100 nm on 0.5-20 mm graphite 0.09 g graphite	427/156 mA g^{-1}	468/100/156mAg^{-1}	[86]

Hydrothermal + dry at 70C	Hollow LVO entangled with CNT,400 nm width, 800 nm length and thickness 50-80 nm particle size	355/0.1 A g^{-1} 290/2 A g^{-1}	250/2000/2 A g^{-1}	[87]
One pot hydrothermal + wash and dry	Graphene wrapped LVO Loading Graphene 10.5% weight	420/20 mA g^{-1}	378/50/20 mA g^{-1} 300/50/ 800 mA g^{-1} 250/50/ 4 A g^{-1}	[88]
Oil bath method	Hollow shell LVO/rGO Thickness 10-300 nm by adjusting ratio of water and EG in solvent	387/0.5 C	257/1500/ 10 C	[89]
Hydrothermal + SSR	Ultrathin LVO nanoribbon/graphene sandwich-like structures	406/0.2 C	453/200/0.2 C 299/1000/10 C	[90]

2.5 VS_4

In recent years, chalcogenides are attracting much attention for the battery applications due to their high capacities comparable to those of metal oxides, and relatively good electrical conductivity [91, 92]. Moreover, the diverse crystal structures of transition metal sulfides including 1D, 2D, and 3D structures provide us enormous opportunities to explore advanced materials for LIB [93]. Among the transition metal sulfides, VS_4 is outstanding because of its unique chain-like structure and high sulfur content, which endows it distinctive electrochemical behaviors. VS_4 was discovered in 1906, published in 1907 by Hillebrand [94]. It was not until Allmann et al. presented its crystal structure in 1964 [95]. VS_4 has a monoclinic structure with a=6.78, b=10.42, and c=12.11. S_2^{2-} dimer and V atoms are connected to form chains (Figure 2.6). Thus, it can be described as $V^{4+}(S_2^{2-})^2$. The chains are bonded by weak van der Waals force and an interchain distance is ca. 0.583 nm, much larger than the radiuses of Li^+ (0.76 Å), Na^+ (1.02 Å), and K^+ (1.38 Å). Another advantage of VS_4 is low cost because of the abundance in the earth, giving it superiority for practical energy storage application. Nevertheless, little research has reported this material due to the difficulty in synthesizing pure VS_4.

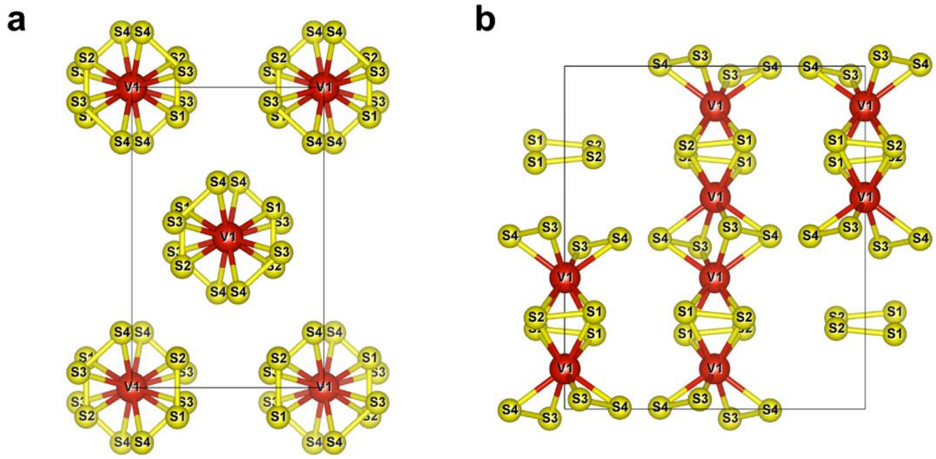

Figure 2.6 Structure of VS_4: (a) View from c axis (b) View from a axis.

2.5.1 Advantages and drawbacks of VS_4

Compared to the theoretical capacity of graphite (372 mAh g^{-1}), the theoretical capacity of VS_4 is 1196 mAh g^{-1}. In addition, VS_4 with low-cost material make it one of promising anode materials for LIB and other alkali ion batteries. Of course, the drawbacks of VS_4 also cannot be ignored. First, the electrical conductivity and ionic conductivity of VS_4 still need improvement when used as anode materials for LIB. Second, a large volume change is caused in the active material during the charging and discharging process, which would generate an excessive stress to material and crumble the material, sometimes even peel the electrode material off the current collector.

2.1.4.2 Strategies to ameliorate the drawbacks of VS_4

Similar to LVO, the electrical and ionic conductivity of VS_4 can be improved through compositing or coating with other conductive material, reducing the particle size and/or doping. VS_2/graphene nanocomposites were prepared for lithium-ion battery cathode application and demonstrated excellent high rate capability. Such good electrochemical performance is credited to the exceptional interaction between VS_2 and graphene that reducing the electrical resistance. Meanwhile, the graphene acted as a template or buffer matrix for the volume change and high-speed ion diffusion [96]. VS_4/graphene nanocomposite for LIB anode [97], 3D VS_4/graphene for LIB anode [98], and VS_4/rGO for NIB anode [99] all have demonstrated its effectiveness of compositing with graphene. Aside from composting with graphene, coating with conductive polymer has been proven to be an effective approach to improve the electrochemical performance. The polymer coating can enhance the electrical conductivity and suppress the dissolution of polysulfide [100]. Another drawback of VS_4 is the large volume change upon charging/discharging process. As mention earlier, graphene and conductive polymer not only improve the electrical/ionic conductivity, but also provide a porous structure or hold the material to accommodate the volume change.

2.6 Questions to answer based on literature

Based on the literature review, for the LVO, the research is much focus on reducing the particle size, enhancing the electrical conductivity and ionic conductivity. The particle size can be reduced by using various synthesis methods, such as hydrothermal [101, 102], impregnation [103, 104], solvothermal [56, 105, 106], solution-based [55, 107], electrospinning [108], template synthesis [109], ultrasonic spray pyrolysis [110, 111], ultracentrifugation [112], aerosol-assisted synthesis [113], and freeze-drying method [114]. The intrinsic electrical conductivity and ionic conductivity of LVO can be improved by doping with different elements (Mo^{6+} [115], Si^{4+} [46], Ti^{4+} [116], Ni^{2+} [117], N^{3-} [118], Cr^{6+} [119], Cu^{2+} [120], oxygen vacancies [121, 122]). A γ-LVO can be prepared by doping Si^{4+}, in which the γ-LVO only exists at high temperature. The electrochemical performance of two phases (γ- and β- LVO) are compared in terms of their rate capability and cycling performance [46]. Besides this, the extrinsic electrical conductivity could be enhanced by coating with electrically conductive materials, like carbon [82, 123], graphene [124], expanded graphite [125], metal Ni [126]. The capacity loss of LVO upon Li insertion/extraction was also investigated [50, 127, 128]. In order to improve it specific capacity, composting with MoS_2 is also demonstrated [129].

Morphologies and particle size are important parameters affecting electrochemical performance. For instance, commercial rutile form of TiO_2 with particle sizes ranges from 15 nm, 30 nm to 300 nm were compared in terms of their specific capacity and rate capabilities. It has been shown that 15 nm TiO_2 has a highest discharge/charge capacity of 378 mAh g^{-1}, along with a stable reversible capacity of 200 mAh g^{-1}, compared to the 300 nm TiO_2, whose capacity is only 50 mAh g^{-1} [130]. In contrast, J.W. Kang et al. synthesized anatase TiO_2 with various particle sizes in the range 5-50 nm. The smallest TiO_2 exhibits the worst electrochemical performance, which was attributed to the disordered crystal lattice with many defects that could hinder Li diffusion. On the other hand, if the particle size exceeds the optimal size, then produces too long diffusion length, hindering Li diffusion [131]. Mesoporous and nanowire SnO_2 were prepared via a template method using KIT-6 and SBA-15 hard templates [132]. Mesoporous SnO_2 exhibits a better capacity retention, which is associated with its mesopores accessible to the electrolyte. Furthermore, Chen Xu and co-workers prepared C@FeS nanosheets, C@FeS nanospheres, and C@FeS nanoplates via a 1-Dodecanethiol assisted solution-based synthesis method [133]. Nanosheets display the best Li storage properties with high capacities and especially at high current rates. Thus, based on examples mentioned above, the morphologies indeed play a significant role in tuning the electrochemical performance in LIBs applications. Regarding LVO, though much progress has been achieved, special morphologies like those that nanorods have not been reported before. Moreover, the effects of morphologies on the electrochemical performances as well as the reasons behind are still blank in this area.

For the VS_4, the research is mainly going on improving its electrical conductivity and buffering the volume changing during charging/discharging process. However, special morphologies like an urchin and 1D nanowires have rarely been reported. A systematic study of the effect of morphologies on the electrochemical performance is needed to improve the material further. In addition, graphene is normally composited with other metal oxides/sulfides to improve the overall conductivity and accommodate the volume change of the electrode material. Other research groups have reported VS_4/graphene. However, VS_4 with special morphologies anchored on rGO is rarely reported. All these works are imperative to have a better fundamental understanding of these materials before putting into practical applications.

2.7 PhD in context of literature

This work will address the questions posed in the preceding section. Synthesis of Li_3VO_4 with special morphologies using the solvothermal method, and the effect of morphologies and nanostructuring for Li_3VO_4 will be systematically investigated. Furthermore, syntheses of VS_4 with peculiar morphologies are also investigated as well as their morphologies effect on the electrochemical performance in LIBs. Their kinetic parameters like diffusion coefficients will be calculated and compared, along with the EIS comparison measured at different cycles or voltages in the 1st discharge/charge process. Finally, the VS_4 nanowires in-situ grown on rGO will be prepared, and the electrochemical performance will be analyzed.

References

[1] F. Cheng, J. Liang, Z. Tao, J. Chen, Advanced Materials, 23 (2011) 1695-1715.

[2] V. Etacheri, R. Marom, R. Elazari, G. Salitra, D. Aurbach, Energy & Environmental Science, 4 (2011) 3243-3262.

[3] M. Winter, R.J. Brodd, in, ACS Publications, 2004.

[4] J.-M. Tarascon, M. Armand, Issues and challenges facing rechargeable lithium batteries, in: Materials For Sustainable Energy: A Collection of Peer-Reviewed Research and Review Articles from Nature Publishing Group, World Scientific, 2011, pp. 171-179.

[5] A. Patil, V. Patil, D.W. Shin, J.-W. Choi, D.-S. Paik, S.-J. Yoon, Materials research bulletin, 43 (2008) 1913-1942.

[6] M. Reddy, G. Subba Rao, B. Chowdari, Chemical reviews, 113 (2013) 5364-5457.

[7] M. Armand, J.-M. Tarascon, nature, 451 (2008) 652.

[8] J.B. Goodenough, K.-S. Park, Journal of the American Chemical Society, 135 (2013) 1167-1176.

[9] N. Omar, M. Daowd, P.v.d. Bossche, O. Hegazy, J. Smekens, T. Coosemans, J.v. Mierlo, Energies, 5 (2012) 2952-2988.

[10] M. Smith, R.E. Garcia, Q.C. Horn, Journal of The Electrochemical Society, 156 (2009) A896-A904.

[11] E. McCalla, A.M. Abakumov, M. Saubanère, D. Foix, E.J. Berg, G. Rousse, M.-L. Doublet, D. Gonbeau, P. Novák, G. Van Tendeloo, Science, 350 (2015) 1516-1521.

[12] K. Luo, M.R. Roberts, R. Hao, N. Guerrini, D.M. Pickup, Y.-S. Liu, K. Edström, J. Guo, A.V. Chadwick, L.C. Duda, Nature chemistry, 8 (2016) 684.

[13] M.R. Palacin, Chemical Society Reviews, 38 (2009) 2565-2575.

[14] H. Buqa, D. Goers, M. Holzapfel, M.E. Spahr, P. Novák, Journal of The Electrochemical Society, 152 (2005) A474-A481.

[15] T. Tran, J. Feikert, R. Pekala, K. Kinoshita, Journal of applied electrochemistry, 26 (1996) 1161-1167.

[16] M. Dahbi, N. Yabuuchi, K. Kubota, K. Tokiwa, S. Komaba, Physical chemistry chemical physics, 16 (2014) 15007-15028.

[17] N. Li, G. Zhou, F. Li, L. Wen, H.M. Cheng, Advanced Functional Materials, 23 (2013) 5429-5435.

[18] N. Li, G. Liu, C. Zhen, F. Li, L. Zhang, H.M. Cheng, Advanced Functional Materials, 21 (2011) 1717-1722.

[19] M. Winter, J.O. Besenhard, M.E. Spahr, P. Novak, Advanced materials, 10 (1998) 725-763.

[20] D. Dambournet, I. Belharouak, K. Amine, Chemistry of materials, 22 (2009) 1173-1179.

[21] R. Buonsanti, V. Grillo, E. Carlino, C. Giannini, T. Kipp, R. Cingolani, P.D. Cozzoli, Journal of the American Chemical Society, 130 (2008) 11223-11233.

[22] V. Etacheri, J.E. Yourey, B.M. Bartlett, Acs Nano, 8 (2014) 1491-1499.

[23] C.-M. Park, J.-H. Kim, H. Kim, H.-J. Sohn, Chemical Society Reviews, 39 (2010) 3115-3141.

[24] W.-T. Kim, Y.U. Jeong, Y.J. Lee, Y.J. Kim, J.H. Song, Journal of Power Sources, 244 (2013) 557-560.

[25] A.L. Viet, M. Reddy, R. Jose, B. Chowdari, S. Ramakrishna, The Journal of Physical Chemistry C, 114 (2009) 664-671.

[26] A. Dey, Journal of The Electrochemical Society, 118 (1971) 1547-1549.

[27] C.K. Chan, R. Ruffo, S.S. Hong, Y. Cui, Journal of Power Sources, 189 (2009) 1132-1140.

[28] U. Kasavajjula, C. Wang, A.J. Appleby, Journal of Power Sources, 163 (2007) 1003-1039.

[29] L. Ji, Z. Lin, M. Alcoutlabi, X. Zhang, Energy & Environmental Science, 4 (2011) 2682-2699.

[30] H. Chen, Z. Dong, Y. Fu, Y. Yang, Journal of Solid State Electrochemistry, 14 (2010) 1829-1834.

[31] J. Hassoun, S. Panero, G. Mulas, B. Scrosati, Journal of Power Sources, 171 (2007) 928-931.

[32] J. Vaughey, M. Thackeray, D. Shin, C. Wolverton, Journal of The Electrochemical Society, 156 (2009) A536-A540.

[33] J.M. Christensen, Science of the total environment, 166 (1995) 89-135.

[34] R. Malini, U. Uma, T. Sheela, M. Ganesan, N. Renganathan, Ionics, 15 (2009) 301-307.

[35] W.-J. Zhang, Journal of Power Sources, 196 (2011) 877-885.

[36] J. Cabana, L. Monconduit, D. Larcher, M.R. Palacin, Advanced Materials, 22 (2010).

[37] P. Poizot, S. Laruelle, S. Grugeon, L. Dupont, J. Tarascon, Nature, 407 (2000) 496.

[38] P.G. Bruce, B. Scrosati, J.M. Tarascon, Angewandte Chemie International Edition, 47 (2008) 2930-2946.

[39] B. Scrosati, Nature nanotechnology, 2 (2007) 598.

[40] Y.G. Guo, J.S. Hu, L.J. Wan, Advanced Materials, 20 (2008) 2878-2887.

[41] H. Li, P. Balaya, J. Maier, Journal of the Electrochemical Society, 151 (2004) A1878-A1885.

[42] Y. Chen, X. Li, K. Park, J. Song, J. Hong, L. Zhou, Y.-W. Mai, H. Huang, J.B. Goodenough, Journal of the American Chemical Society, 135 (2013) 16280-16283.

[43] G. Yang, H. Cui, G. Yang, C. Wang, Acs Nano, 8 (2014) 4474-4487.

[44] H. Li, X. Liu, T. Zhai, D. Li, H. Zhou, Advanced Energy Materials, 3 (2013) 428-432.

[45] A. West, F. Glasser, Journal of Solid State Chemistry, 4 (1972) 20-28.

[46] C. Liao, Y. Wen, Z. Xia, R. Qin, X. Liu, Y. Yu, B. Shan, T. Zhai, H. Li, Advanced Energy Materials, (2017).

[47] Z. Liang, Z. Lin, Y. Zhao, Y. Dong, Q. Kuang, X. Lin, X. Liu, D. Yan, Journal of Power Sources, 274 (2015) 345-354.

[48] S. Ni, X. Lv, J. Ma, X. Yang, L. Zhang, Journal of Power Sources, 248 (2014) 122-129.

[49] W.-T. Kim, B.-K. Min, H.C. Choi, Y.J. Lee, Y.U. Jeong, Journal of The Electrochemical Society, 161 (2014) A1302-A1305.

[50] M.E. Arroyo-de Dompablo, P. Tartaj, J.M. Amarilla, U. Amador, Chemistry of Materials, 28 (2016) 5643-5651.

[51] Y.H. Rho, K. Kanamura, M. Fujisaki, J.-i. Hamagami, S.-i. Suda, T. Umegaki, Solid State Ionics, 151 (2002) 151-157.

[52] J. Liu, P.-J. Lu, S. Liang, J. Liu, W. Wang, M. Lei, S. Tang, Q. Yang, Nano Energy, 12 (2015) 709-724.

[53] C.-L. Wang, Y. Liao, F. Hsu, N. Tai, M. Wu, Journal of The Electrochemical Society, 152 (2005) A653-A657.

[54] A. Manthiram, J. Phys. Chem. Lett., 2 (2011) 176-184.

[55] D. Zhao, M. Cao, ACS Applied Materials & Interfaces, 7 (2015) 25084-25093.

[56] Q. Li, Q. Wei, J. Sheng, M. Yan, L. Zhou, W. Luo, R. Sun, L. Mai, Adv. Sci., 2 (2015) 1500284.

[57] C. Zhang, C. Liu, X. Nan, H. Song, Y. Liu, C. Zhang, G. Cao, ACS Appl. Mater. Interfaces, 8 (2015) 680-688.

[58] Y. Shi, J.-Z.Z. Wang, S.-L.L. Chou, D. Wexler, H.-J.J. Li, K. Ozawa, H.-K.K. Liu, Y.-P.P. Wu, Nano letters, 13 (2013) 4715-4720.

[59] I. Plitz, A. DuPasquier, F. Badway, J. Gural, N. Pereira, A. Gmitter, G.G. Amatucci, Applied Physics A, (2005).

[60] F.-F. Cao, Y.-G. Guo, S.-F. Zheng, X.-L. Wu, L.-Y. Jiang, R.-R. Bi, L.-J. Wan, J. Maier, Chemistry of Materials, 22 (2010) 1908-1914.

[61] S. Lee, Y. Cho, H.K. Song, K.T. Lee, Carbon- Coated Single- Crystal LiMn2O4 Nanoparticle Clusters as Cathode Material for High- Energy and High- Power Lithium- Ion Batteries, (2012).

[62] K.T. Nam, D.-W. Kim, P.J. Yoo, C.-Y. Chiang, N. Meethong, P.T. Hammond, Y.-M. Chiang, A.M. Belcher, science, 312 (2006) 885-888.

[63] J. Wang, N. Yang, H. Tang, Z. Dong, Q. Jin, M. Yang, D. Kisailus, H. Zhao, Z. Tang, D. Wang, Angewandte Chemie, 125 (2013) 6545-6548.

[64] J.M. Feckl, K. Fominykh, M. Döblinger, D. Fattakhova- Rohlfing, T. Bein, Angewandte Chemie International Edition, 51 (2012) 7459-7463.

[65] L. Shen, E. Uchaker, X. Zhang, G. Cao, Advanced Materials, 24 (2012) 6502-6506.

[66] S.-T. Myung, M. Kikuchi, C.S. Yoon, H. Yashiro, S.-J. Kim, Y.-K. Sun, B. Scrosati, Energy & Environmental Science, 6 (2013) 2609-2614.

[67] Y. Tang, Y. Zhang, W. Li, B. Ma, X. Chen, Chemical Society Reviews, (2015).

[68] Y.-Q. Wang, L. Gu, Y.-G. Guo, H. Li, X.-Q. He, S. Tsukimoto, Y. Ikuhara, L.-J. Wan, Journal of the American Chemical Society, 134 (2012) 7874-7879.

[69] B. Kang, G. Ceder, Nature, 458 (2009) 190-193.

[70] Y. Tang, Y. Zhang, J. Deng, D. Qi, W.R. Leow, Angewandte …, (2014).

[71] A. Veluchamy, Solid State Ionics, 143 (2001) 161-171.

[72] T. Nakamura, K. Sakumoto, M. Okamoto, S. Seki, Y. Kobayashi, T. Takeuchi, M. Tabuchi, Y. Yamada, Journal of Power Sources, 174 (2007) 435-441.

[73] H. Liu, Q. Cao, L.J. Fu, C. Li, Y.P. Wu, H.Q. Wu, Electrochemistry …, (2006).

[74] A. Sivashanmugam, S. Gopukumar, R. Thirunakaran, C. Nithya, S. Prema, Materials Research Bulletin, 46 (2011) 492-500.

[75] Y.-Y. Wang, Y.-J. Hao, Q.-Y. Lai, J.-Z. Lu, Y.-D. Chen, X.-Y. Ji, Ionics, 14 (2008) 85-88.

[76] J. Zhu, G. Yang, J. Zhao, Q. Wang, H. Yang, Synthesis and Electrochemical Properties of Li₄Ti₅O₁₂/CuO Anode Material for Li-Ion Batteries, 279 (2011).

[77] M. Chen, W. Li, X. Shen, G. Diao, ACS applied materials & interfaces, 6 (2014) 4514-4523.

[78] C. Chen, R. Agrawal, C. Wang, Nanomaterials, 5 (2015) 1469-1480.

[79] V.R. Channu, R. Holze, E.H. Walker Jr, S. Wicker Sr, R.R. Kalluru, Q.L. Williams, W. Walters, Int. J. Electrochem. Sci, 5 (2010) 1355-1366.

[80] G. Shao, L. Gan, Y. Ma, H. Li, T. Zhai, Journal of Materials Chemistry A, 3 (2015) 11253-11260.

[81] Z. Liang, Y. Zhao, L. Ouyang, Y. Dong, Q. Kuang, X. Lin, X. Liu, D. Yan, Journal of Power Sources, 252 (2014) 244-247.

[82] S. Ni, J. Zhang, J. Ma, X. Yang, L. Zhang, Journal of Materials Chemistry A, 3 (2015) 17951-17955.

[83] Z. Liang, Y. Zhao, Y. Dong, Q. Kuang, X. Lin, X. Liu, D. Yan, Journal of Electroanalytical Chemistry, 745 (2015) 1-7.

[84] S. Ni, X. Lv, J. Ma, X. Yang, L. Zhang, Electrochimica Acta, 130 (2014) 800-804.

[85] S. Ni, J. Zhang, J. Ma, X. Yang, L. Zhang, Journal of Power Sources, 296 (2015) 377-382.

[86] S. Ni, X. Lv, J. Zhang, J. Ma, X. Yang, L. Zhang, Electrochimica Acta, 145 (2014) 327-334.

[87] Q. Li, J. Sheng, Q. Wei, Q. An, X. Wei, P. Zhang, L. Mai, Nanoscale, 6 (2014) 11072-11077.

[88] Y. Shi, J.-Z. Wang, S.-L. Chou, D. Wexler, H.-J. Li, K. Ozawa, H.-K. Liu, Y.-P. Wu, Nano Letters, 13 (2013) 4715-4720.

[89] Q. Li, Q. Wei, Q. Wang, W. Luo, Q. An, Y. Xu, C. Niu, C. Tang, L. Mai, Journal of Materials Chemistry A, 3 (2015) 18839-18842.

[90] J. Liu, P.J. Lu, S. Liang, J. Liu, W. Wang, M. Lei, S. Tang, Q. Yang, Nano Energy, 12 (2015) 709-724.

[91] J. Xiao, L. Wan, S. Yang, F. Xiao, S. Wang, Nano Lett., 14 (2014) 831–838.

[92] H. Chen, J. Jiang, L. Zhang, H. Wan, T. Qi, D. Xia, Nanoscale, 5 (2013) 8879-8883

[93] Y. Zhou, J. Tian, H. Xu, J. Yang, Y. Qian, Energy Storage Mater., 6 (2017) 149-156.

[94] W.F. Hillebrand, J. Am. Chem. Soc., 29 (1907) 1019-1029.

[95] R. Allmann, I. Baumann, A. Kutoglu, H. Rösch, E. Hellner, Naturwissenschaften, 51 (1964) 263-264.

[96] W. Fang, H. Zhao, Y. Xie, J. Fang, J. Xu, Z. Chen, ACS Appl. Mater. Interfaces, 7 (2015) 13044-13052.

[97] X. Xu, S. Jeong, C. Rout, P. Oh, M. Ko, H. Kim, M. Kim, R. Cao, H. Shin, J. Cho, J. Mater. Chem. A, 2 (2014) 10847-10853.

[98] Q. Li, Y. Chen, J. He, F. Fu, J. Lin, W. Zhang, J. Alloys Compd., 685 (2016) 294-299.

[99] R. Sun, Q. Wei, Q. Li, W. Luo, Q. An, J. Sheng, D. Wang, W. Chen, L. Mai, ACS Appl. Mater. Interfaces, 7 (2015) 20902–20908.

[100] Y. Zhou, Y. Li, J. Yang, J. Tian, H. Xu, J. Yang, W. Fan, ACS Appl. Mater. Interfaces, 8 (2016) 18797-18805.

[101] X. Jin, B. Lei, J. Wang, Z. Chen, K. Xie, F. Wu, Y. Song, D. Sun, F. Fang, Journal of Alloys and Compounds, 686 (2016) 227-234.

[102] Y. Shi, Y. Zhang, L. Liu, Z. Zhang, J. Wang, S. Chou, J. Gao, H.D. Abruña, H. Li, H. Liu, Journal of Solid State Electrochemistry, 21 (2017) 2547-2553.

[103] L. Shen, H. Lv, S. Chen, P. Kopold, P.A. van Aken, X. Wu, J. Maier, Y. Yu, Advanced Materials, (2017) 1700142.

[104] L. Shen, S. Chen, J. Maier, Y. Yu, Advanced Materials, 29 (2017).

[105] G. Yang, B. Zhang, J. Feng, Y. Lu, Z. Wang, V. Aravindan, M. Aravind, J. Liu, M. Srinivasan, Z. Shen, Journal of Materials Chemistry A, (2018).

[106] G. Yang, J. Feng, B. Zhang, V. Aravindan, D. Peng, X. Cao, H. Yu, S. Madhavi, Y. Huang, International Journal of Hydrogen Energy, 42 (2017) 22167-22174.

[107] J. Zhang, S. Ni, J. Ma, X. Yang, L. Zhang, Journal of Power Sources, 301 (2016) 41-46.

[108] R. Qin, G. Shao, J. Hou, Z. Zheng, T. Zhai, H. Li, Science Bulletin, 62 (2017) 1081-1088.

[109] Y. Yang, J. Li, J. Huang, J. Huang, J. Zeng, J. Zhao, Electrochimica Acta, 247 (2017) 771-778.

[110] Y. Yang, J. Li, D. Chen, J. Zhao, Journal of The Electrochemical Society, 164 (2017).

[111] Y. Yang, J. Li, X. He, J. Wang, D. Sun, J. Zhao, Journal of Materials Chemistry A, 4 (2016) 7165-7168.

[112] E. Iwama, N. Kawabata, N. Nishio, K. Kisu, J. Miyamoto, W. Naoi, P. Rozier, P. Simon, K. Naoi, ACS nano, 10 (2016) 5398-5404.

[113] P. Tartaj, J.M. Amarilla, M.B. Vazquez-Santos, Chemistry of Materials, 28 (2016) 986-993.

[114] S. Ni, J. Zhang, J. Ma, X. Yang, L. Zhang, X. Li, H. Zeng, Advanced Materials Interfaces, 3 (2016) n/a-n/a.

[115] Y. Dong, H. Duan, K.-s. Park, Y. Zhao, ACS Applied Materials & Interfaces, (2017).

[116] C. Mu, K. Lei, H. Li, F. Li, J. Chen, The Journal of Physical Chemistry C, 121 (2017) 26196-26201.

[117] C. Zhang, K. Wang, C. Liu, X. Nan, H. Fu, W. Ma, Z. Li, G. Cao, NPG Asia Materials, 8 (2016) e287.

[118] B. Dong, R. Jarkaneh, S. Hull, N. Reeves-McLaren, J.J. Biendicho, A.R. West, Journal of Materials Chemistry A, 4 (2016) 1408-1413.

[119] V. Massarotti, D. Capsoni, M. Bini, P. Mustarelli, G. Chiodelli, C.B. Azzoni, P. Galinetto, M.C. Mozzati, The journal of physical chemistry. B, 109 (2005) 14845-14851.

[120] K. Wang, H. Fu, Z. Li, M. Xia, X. Liang, R. Qi, G. Cao, X. Lu, ChemElectroChem.

[121] K. Wang, C. Zhang, H. Fu, C. Liu, Z. Li, W. Ma, X. Lu, G. Cao, Chemistry-A European Journal, 23 (2017) 5368-5374.

[122] L. Chen, X. Jiang, N. Wang, J. Yue, Y. Qian, J. Yang, Advanced Science, 2 (2015).

[123] F. Wang, Z. Liu, X. Yuan, J. Mo, C. Li, L. Fu, Y. Zhu, X. Wu, Y. Wu, Journal of Materials Chemistry A, 5 (2017) 14922-14929.

[124] K. Huang, Q. Ling, C. Huang, K. Bi, W. Wang, T. Yang, Y. Lu, J. Liu, R. Zhang, D. Fan, Journal of Alloys and Compounds, 646 (2015) 837-842.

[125] S. Hu, Y. Song, S. Yuan, H. Liu, Q. Xu, Y. Wang, C.-X. Wang, Y.-Y. Xia, Journal of Power Sources, 303 (2016) 333-339.

[126] S. Ni, J. Zhang, X. Lv, X. Yang, L. Zhang, Journal of Power Sources, 291 (2015) 95-101.

[127] C. Liao, Y. Wen, B. Shan, T. Zhai, H. Li, Journal of Power Sources, 348 (2017) 48-56.

[128] L.L. Zhou, S.-Y. Shen, X.-X. Peng, L.N. Wu, Q. Wang, C.-H. Shen, T.-T. Tu, L. Huang, J.-T. Li, S.-G. Sun, ACS Appl. Mater. Interfaces, 8 (2016) 23739-23745.

[129] Y. Liu, M. Zhang, Y. Liu, M. Xue, B. Li, X. Tao, Materials Letters, 196 (2017) 209-212.

[130] C. Jiang, I. Honma, T. Kudo, H. Zhou, Electrochemical and solid-state letters, 10 (2007) A127-A129.

[131] J. Kang, D. Kim, V. Mathew, J. Lim, J. Gim, J. Kim, Journal of the Electrochemical Society, 158 (2011) A59-A62.

[132] H. Kim, J. Cho, Journal of Materials Chemistry, 18 (2008) 771-775.

[133] C. Xu, Y. Zeng, X. Rui, N. Xiao, J. Zhu, W. Zhang, J. Chen, W. Liu, H. Tan, H.H. Hng, ACS nano, 6 (2012) 4713-4721.

Chapter 3

Experimental Methodology

In this chapter, all experimental procedures employed in the materials synthesis of my PhD work are summarized. The principle and details of selected synthesis methods, as well as the characterization methodologies of materials, are presented. Then, the device fabrication of nanostructured LVO and VS_4 for LIB anode application are also included. Moreover, the rationale behind the selection of the various techniques employed for synthesizing and characterizing the desired materials was enumerated in this chapter. Structural and electrochemical characterization techniques will be discussed in detail.

3.1 Rationale for selection

The main aim of the thesis is to synthesize LVO and VS_4 with special morphologies as well as the effect of morphologies on the final electrochemical performance of LIB. We also discussed the advantages and drawbacks of LVO and VS_4 for LIB application in the previous chapter, as well as the possible methods to overcome the limitations. Before selecting of proper synthesis techniques, the following factors need to consider:

1. Homogenous mixing of precursors.
2. The time required for synthesis.
3. Morphological control.
4. The possibility of scaling up.
5. Environmental impact.

Keeping in mind the above considerations, two different synthesis techniques were chosen namely solvothermal/hydrothermal method and sol-gel synthesis method. In order to synthesize LVO and VS_4 with special morphologies and a series of morphologies, a hydrothermal/solvothermal method is preferred compared to conventional solid-state reaction or other synthesis methods because of its easier morphological control characteristic. Moreover, well-crystallized products can be obtained via the hydrothermal/solvothermal method. Compositing VS_4 with carbon-based material has shown to be an excellent way for enhancing the electrochemical performance. C_{60}, MWCTN, SWCNT, hard carbon, graphite, etc. are the commonly used carbon materials for composting. Graphene stands out owing to its high electrical conductivity, tensile etstrength and high surface area. Although some papers reported VS_4/rGO nanocomposites, growing VS_4 with special morphologies such as 1D structure is still challenging. The hydrothermal method could be a way to achieve VS_4 nanowire growing on rGO.

3.2 Materials Synthesis

Voluminous literature on synthesis of anode materials has been reported [1-9]. Here, hydrothermal synthesis, sol-gel synthesis and solid-state synthesis employed in this thesis are illustrated based on the principles and advantages/disadvantages in details.

3.2.1 Hydrothermal/solvothermal synthesis

Hydrothermal techniques are one of the most commonly used synthesis methods to make various nanomaterials. It refers to a reaction conducted at an appropriate temperature and pressure in an enclosed container. The temperature is usually above 100 ºC, while pressure is in the range of 1~100 MPa. The solvent can be either aqueous or organic solvents. The temperature and pressure make the solvent in subcritical or supercritical conditions. Hydrothermal synthesis indicates the solvent is water, while solvothermal synthesis has organic solvent like alcohol or amine as a solvent. Hydrothermal/solvothermal method can be classified into pressurized or non-pressurized types. In pressurized type, a critical point called supercritical point occurs when a solvent is at specific values of temperature and pressure. For water, the supercritical point is 374 ºC and 22.1 MPa. At this point or above the temperature and pressure, the water owns both liquid and gas characteristics. The viscosity and dielectric constant drops. All these could affect the morphology and phase of the synthesized product.

Principle

The solvent properties dramatically change under supercritical conditions. Supercritical fluids have high diffusivity comparable to the gas phase and high solubility as the liquid phase. The dielectric constant of water drops from 78 to below 10, when the condition changes from room temperature to supercritical condition. It becomes non-polar and can dissolve organic easily, but inorganic solubility decreases fast (Figure 3.1). These factors could contribute to the rate of reaction and nanoparticle formation [10, 11].

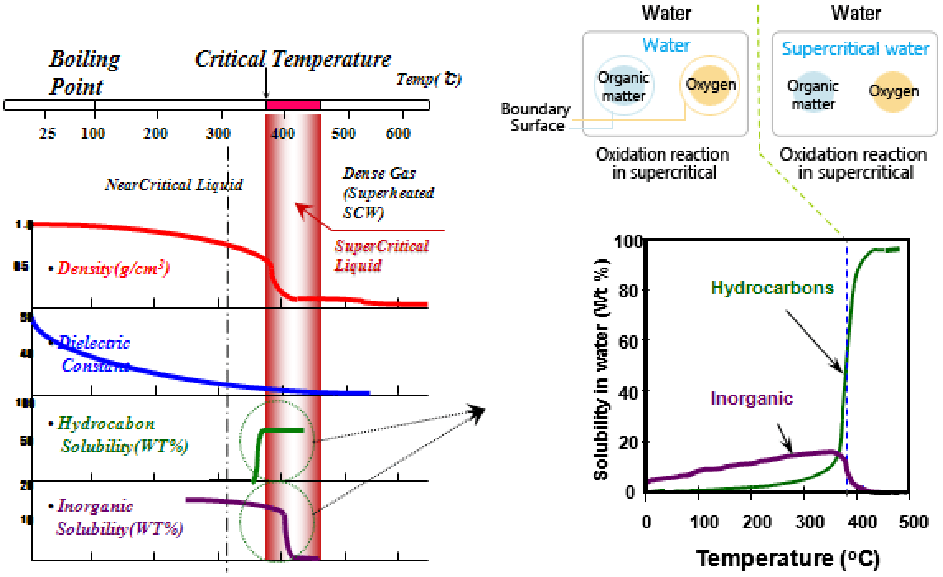

Figure 3.1 Character of supercritical water [12].

As mentioned earlier, a hydrothermal/solvothermal method is a promising method to synthesize metal oxide nano-sized particles with various morphologies. The shapes or morphologies of nanomaterials can be controlled by tuning each step of the reaction. In general, the hydrothermal reaction includes two steps: nucleation and growth (Figure 3.2). The nucleation stage can be classified into homogeneous and heterogeneous nucleation. In this thesis, only homogeneous nucleation was used because no other materials were introduced during the reaction. Many parameters like concentration of solute and reaction temperature, affect the nucleation rate. During this stage, the solution becomes supersaturating solution when the concentration exceeds the critical concentration limit. Supersaturation solution generates a large number of nuclei rapidly accompanying the continuously consuming the solute concentration. The reaction temperature also provides high energy to overcome the nucleation barrier. Aggregation/agglomeration or Ostwald Ripening may occur on the preformed nuclei. The number of particles is reduced until equilibrium is reached. During the growth stage, if the reaction is thermodynamically controlled, pseudo-spherical, and isotropic nanoparticles are usually formed; while anisotropic shapes are formed in the kinetic-controlled process. In other words, experimental parameters like supersaturation, temperature, surfactants and PH values can be played around to control the final morphologies [13-15].

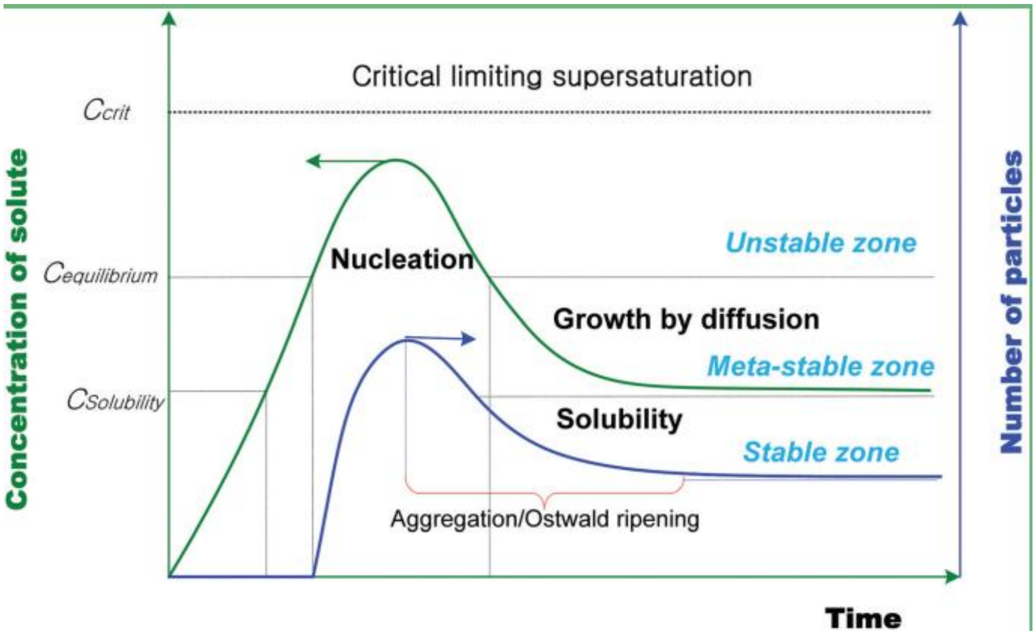

Figure 3.2 Scheme for nucleation and growth as well as the variation of number of particles [15].

Advantages

1. Shape and morphology of nanomaterials can be controlled very well.
2. Products are well-crystallized.
3. The combination with other technique like sol-gel is possible to create hybrid structures.
4. Easy setup

Disadvantages

1. A safety issue is a problem for hydrothermal techniques.
2. The morphology cannot be predicted.

3.2.2 Sol-gel method

The sol-gel method is one of the most commonly used wet chemical synthesis methods for the synthesis of metal and metal oxides. A sol is a stable dispersion of colloidal particles or polymer in a solvent. This sol-gel process involves the evolution of sol to an integrated network (gel). A gel is a semi-rigid mass formed when the solvent of sol evaporates and leave behind the 3D network consisting of particles or ions. The precursors are usually metal alkoxides, such as $Si(OCH_2CH_3)_4$.

Principle

In the sol-gel process, metal alkoxides/chlorides are used as starting precursors (Figure 3.3). They form a clear solution with the solvent and then undergo hydrolysis and polycondensation reaction to form a sol. Then, gelation steps occur and result in the formation of a gel by polycondensation and polyesterification reaction. At this stage, water and other volatile liquids exist in the gel [16, 17]. Based on the way of removing the solvent, the gel could become the xerogel, aerogel, and cryogel. Aerogel can be obtained by removing the solvent via supercritical drying. This is because the conventional drying could result in the loss of porous structure arising from the liquid-vapor interfacial tension [18]. For the supercritical drying, N_2 and CO_2 are the typical supercritical solvents. The gel is processed with pressure and heat, high porosity, a homogeneous nanocrystalline product with the high surface area can be obtained [19]. This is because the solvent in the gel is exchanged by supercritical solvent prior to drying step. Sometimes, hydrophobic solvent like toluene or benzene is introduced into the precursor and is found increase the surface area of the final product due to the reduction of gel pores [20]. On the other hand, if the gel is dried by evaporation, the pore structure will shrink and resulting in signification reduction of pore volume due to the increasing capillary forces. The obtained product has less porous powder and called xerogel. Cryogel is produced when the gel undergoes the freeze-drying process. The gel is quickly frozen first, and then the solvent sublimates under vacuum.

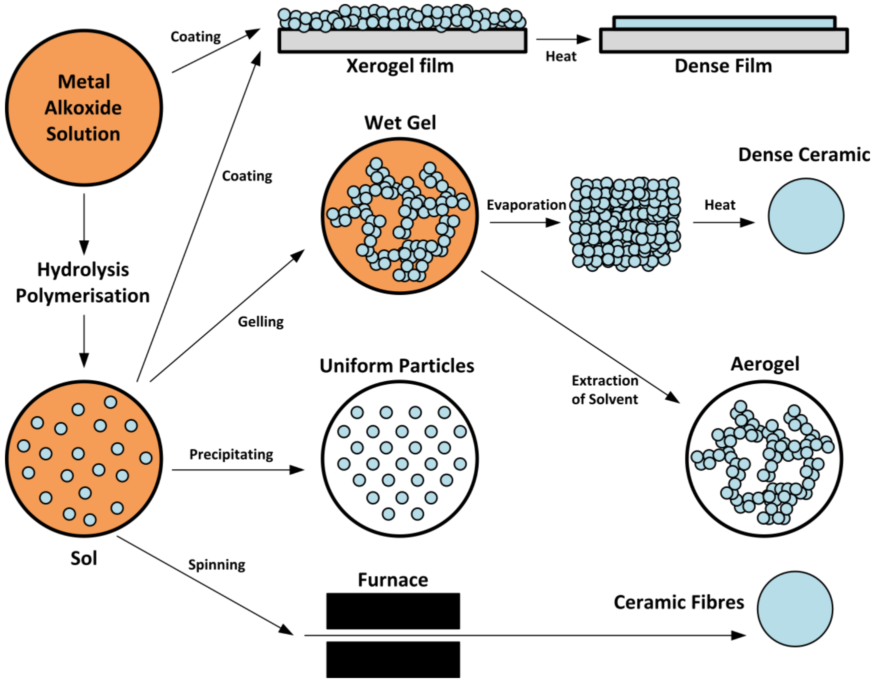

Figure 3.3 Schematic procedures and applications of sol-gel method [21].

The starting point of the sol-gel process is the hydrolysis of alkoxides (Si, Ti, Al, Sn, et al. Eq). After this, polycondensation process occurs and form the branched oligomers with a metal oxo based skeleton, residual hydroxo, and alkoxy groups: oxolation and olation, respectively. Olation indicates the formation of hydroxyl bridges, while oxolation represents the formation of oxygen bridges in condensation process (see below reactions). Olation usually reacts faster compared to that of oxolation. All these reactions contribute the formation of the metal oxo 3D structure. In other words, a series of parameters like the reactivity of precursors, property of solvent, PH value, reaction temperature, and precursor concentration all could affect the final structure and morphologies.

$\equiv$M-OR + H_2O → $\equiv$M-OH + HOR (Hydrolysis)

$\equiv$M-OH + RO-M$\equiv$ → $\equiv$M-O-M$\equiv$ + HOR (Condensation)

$\equiv$M-OH + HO-$\equiv$M → $\equiv$M-$(OH)_2$-M$\equiv$ → $\equiv$M-O-M$\equiv$ + H_2O (Addition)

where M is metal or semimetal and R refers to alkyl group. The sol-gel process is a very flexible synthesis method and a variety of applications can be expected (Figure 3.3). Thin film can be made by dip coating or spin coating on substrate, and fibres could be prepared by adjusting the viscosity of gel and draw into ceramic fibres.

Here in this thesis, metal oxide powders are synthesized by sol-gel with the subsequent calcination process.

Advantages

1. This method can produce high purity multicomponent products because the precursors are well mixed in atomic level.
2. Low sintering temperature is enough, usually 200-600 ºC.
3. Porous structure can be synthesized.
4. Flexible system and can produce powder and thin film

Disadvantages

1. Sometimes the metal alkoxide precursors are expensive.
2. The obtained particle size sometimes not uniform.

3.2.3 Solid state synthesis

The solid-state technique is a high-temperature reaction, where a solid material reacts with another solid (solid-solid reaction), or a liquid (solid-liquid reaction) or a gas (solid-gas reaction). The material can turn into gas or melt during the reaction. Solid/gas reaction gives a better contact compared to the solid/solid reaction. The solid/solid reaction is the most common approach to synthesize solid-state materials. Sometimes, the reactants are well mixed and pelletized to ensure the good contact, which is important for ions diffusion through the ongoing reaction. The oxygen and pressure level can also be adjusted to obtain the desired products. Solid-state synthesis method does not offer the same homogeneity during precursor mixing like wet synthesis methods and no morphological control. Nevertheless, it is capable to scale up and often employed as a baseline to compare with other synthesis methods because solid-state synthesis method is an industry used method.

Principle

Solid/solid state synthesis is the most common type solid-state technique and is used in this thesis (Figure 3.4). In a typical procedure, firstly, the reactant precursors should be homogeneously mixed by hand grinding or ball milling. It is preferred that the precursors have a small particle size and narrow size distribution in order to avoid the incomplete reaction. The reaction happens at the interface of the solids and form product nuclei. Smaller reactant size gives more surface area to the reaction and accelerates the reaction process. During the reaction, the grown product layer on the material surface slows down the ions diffusion from the other solids. Thus, the rate of reaction will be decreased. Smaller particle size can enhance the reaction rate. In addition, the good compaction between particles is also necessary to ensure the reaction is complete and pure final product phase. Secondly, at room temperature, the reactants hardly react unless the high temperature is provided to give enough energy for ions to diffuse. The exact temperature and pressure are based on the phase diagram. The maximum reaction temperature should be less than 2/3rd of the melting point of any reactants and minimum reaction temperature larger than 1/3rd using empirical Tarman rule [22]. Solid-state reaction is generally very slow due to it is limited by the diffusion, driven thermodynamically by a concentration gradient. After that, the mixed reactants are heat-treated and the product is obtained. Lastly, the procedure of grinding and heat treatment is repeated for a few times to ensure the final product is in pure phase. To get fine product particles, ball milling can be employed to break the large particles.

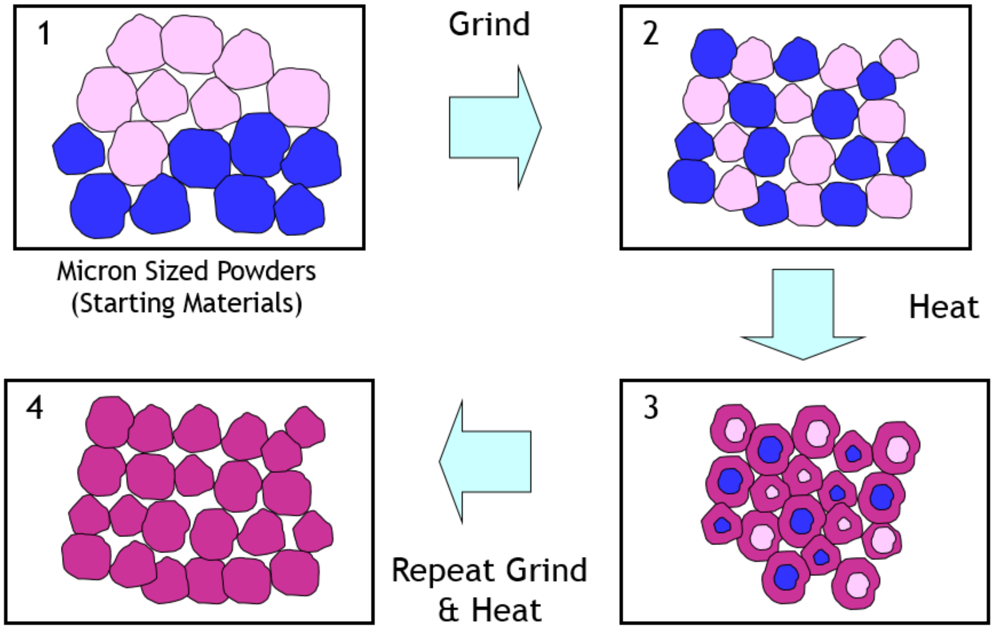

Figure 3.4 Schematic of solid/solid-state reaction procedure.

Advantages:

1. Cost is low and not many steps involved.
2. Mass production is attainable.

Shortcoming

1. Particle size distribution is wide.
2. Nanoparticle size is difficult to achieve.
3. The high temperature is involved.
4. Morphology cannot be controlled.
5. The too high temperature may lead to sublimation of precursors and impurity may appear.
6. Reaction kinetics cannot be controlled.

3.3 Characterization Methodologies

The electrochemical performance and behaviors are evaluated by galvanostatic charge-discharge (GCD), cyclic voltammetry (CV), and impedance spectroscopy (EIS). To understand the reasons behind, characterization techniques are selected to explain the performance. FESEM, TEM, and BET are used to characterize the morphologies and structures, where pore size and size distributions are extracted. Subsequently, phase purity and lattice parameter are determined by X-ray diffraction. The subsequent sections would discuss each of the physical characterization techniques and performance evaluation techniques in detail.

3.3.1 Field emission scanning electron microscope (FESEM)

FESEM (JEOL7600F) as one of the most versatile instruments for microstructure analysis uses a focused beam of electrons to scan the surface of the sample. There is some interaction between the applied electron beam and the sample surface, which generating different responses, such as secondary electrons, a scattering of electrons, X-rays etc (Figure 3.5). These signals generated from the interaction are collected by the equipped detectors. Secondary electrons are collected to produce an image of the surface morphologies of our samples. While X-rays are collected to produce elemental mapping or elements ratio, which will be further discussed in next EDX section. Secondary electrons are low energy electrons that come from conduction/valence band electrons. These loosely bond electrons are easily knocked off from the specimen. The secondary electron detector is special and only allow the low electron to pass through. The collected secondary electrons are subsequently processed and generate images. The detection of secondary electrons is very sensitive to the topology of the sample. More secondary electrons are collected from the higher surface compared to lower parts. Thus, the brightness will be different in various areas and consequently provide contrast for the surface. To enhance the resolution, probe size can be adjusted. Nevertheless, too small probe size would generate fewer electrons, and the contrast will be compromised.

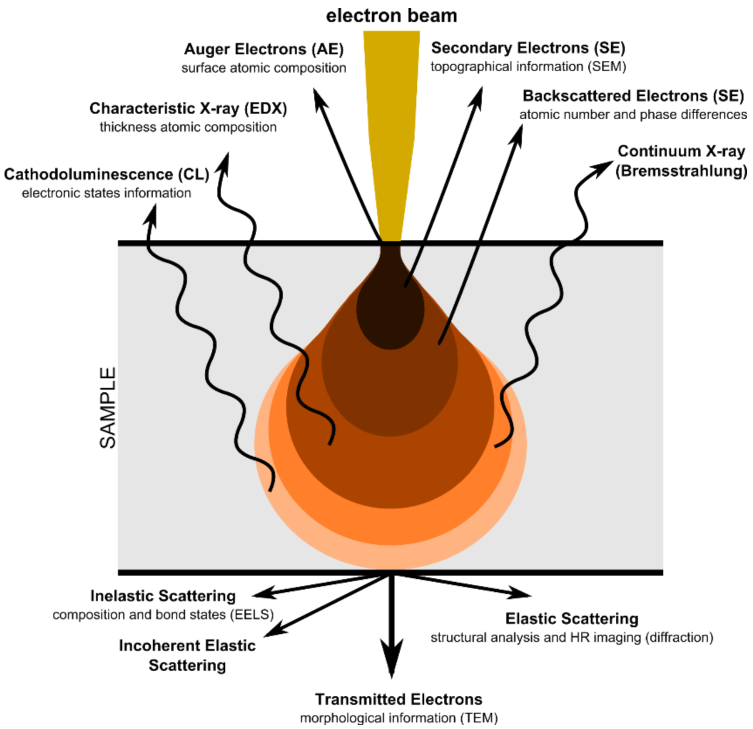

Figure 3.5 Various signals from the interactions between electron beam and specimen [23].

In my experiment, prior to imaging, the samples were firstly coated with platinum with ca. 10~15 nm thickness to prevent the too much charging during SEM. The working distance is set to 6 cm with the accelerating voltage at 5 kV.

3.3.2 Transmission electron microscope (TEM)

Different from FESEM, TEM employs a beam of electrons with high acceleration rate that could go through the specimen. These passing through electrons are collected and used to produce an image. This mechanism is similar to a light microscope, except TEM uses high-speed electrons instead of light. The wavelength is inversely proportional to voltage, and minimum resolvable distance is proportional to wavelength. As a result, the resolution is up to 0.2 nm allowing TEM resolve rows of atoms. One requirement for TEM sample is that the sample must be prepared thin enough for an electron to shine through. The sample also should be stable upon the strong electron beam shining on it. Despite its limitations on the sample, TEM is a powerful tool to analyze the morphologies and crystal structure of the sample.

TEM operates in two different modes: imaging mode and a diffraction mode (Figure 3.6). In imaging mode, it has a bright field and dark field image. They both use a small objective aperture. Bright field images are formed when the small objective aperture and optic axis are concentric to exclude scattered electrons. The thicker part of the sample will appear darker due to the stronger blockage of electrons. Regarding the dark field image, the small objective aperture is misaligned with the optic axis to allow the scattered electrons passing through and form the image. The mode transfers to diffraction by tuning the intermediate lens strength. The selected area diffraction (SAD) aperture is inserted during diffraction mode to allow elastically scattered electrons passing through. The elastically scattered electrons from a different part of the sample are focused into points, thus forming an initial diffraction pattern at the back focal plane where the objective lens located. Only the points lie on the surface of Ewald sphere will be shown in the diffraction pattern, similarly adhering the Bragg's law.

In this thesis, JEOL 2100F TEM microscope was employed to study both the morphological and crystallographic properties. Samples were first dispersed into ethanol first without too dense, and then a drop of the diluted prepared solution was dropped on the copper grid. After the sample on the grid dried, it can be loaded to the TEM sample holder.

Since TEM was operated at 200 kV, the morphologies are identified using imaging mode. While HRTEM and diffraction mode is to examine the crystal planes and inter-plane distances.

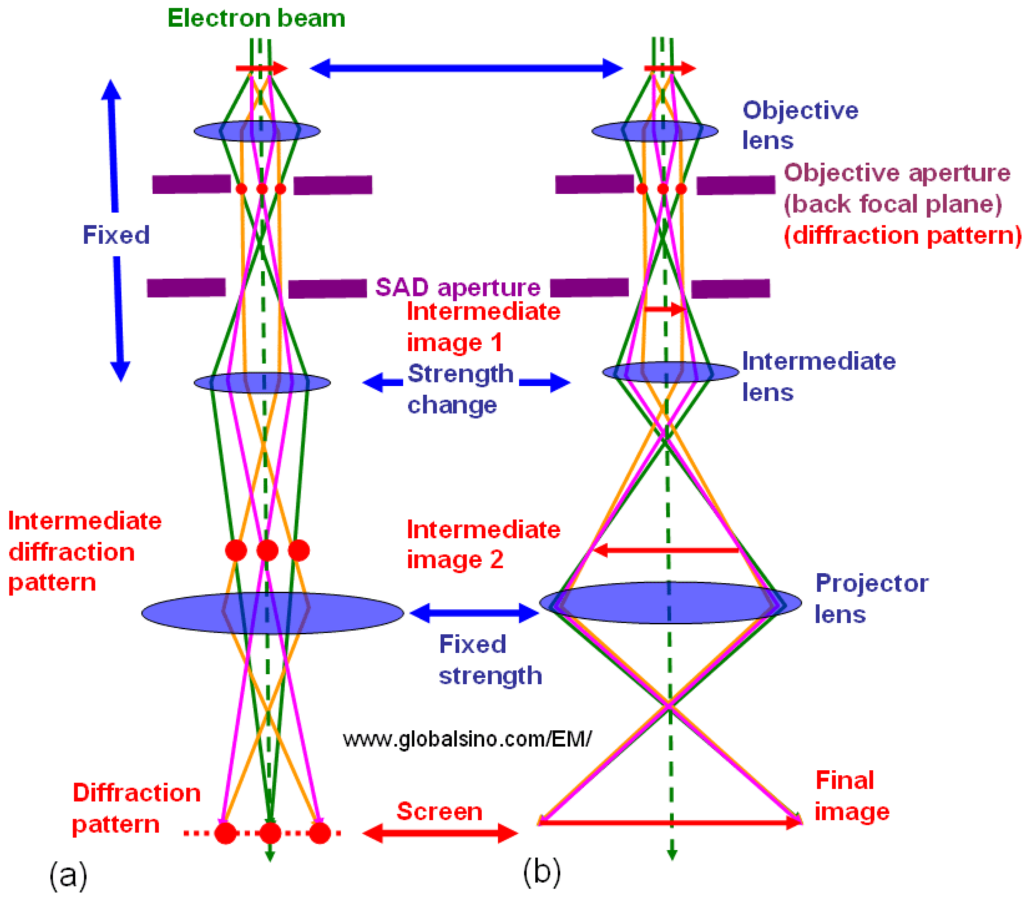

Figure 3.6 (a) Diffraction mode and (b) Imaging mode of TEM [24].

3.3.3 Energy dispersive x-ray spectroscopy (EDX)

As mentioned in the preceding part, TEM and FESEM are usually equipped with EDX instrument. EDX can be used to identify elements presents and provide a quantitive measurement of the elements. It works at higher voltage compared to SEI to provide the beam electrons with enough energy to kick out the innermost shell electrons in the sample (Figure 3.7). The kick out inner shell electrons are momentarily excited to a higher state but drop back into the original state with the emission of x-ray. Since each element has a unique electronic structure, the energy of the emitted x-ray will differ. Thus, this method is used as a fingerprint method to identify the elements. The intensity of the x-ray can be measured and is correlated to the number of interested elemental atoms. One limitation of this method is that if the elements have similar electronic structure, we may face difficulty in identifying them.

Elemental compositions of the samples were analyzed by EDS equipped with FESEM 7600 or TEM 2100F. For EDX-FESEM, the working distance of 15 cm and accelerating voltage of 20 kV were selected.

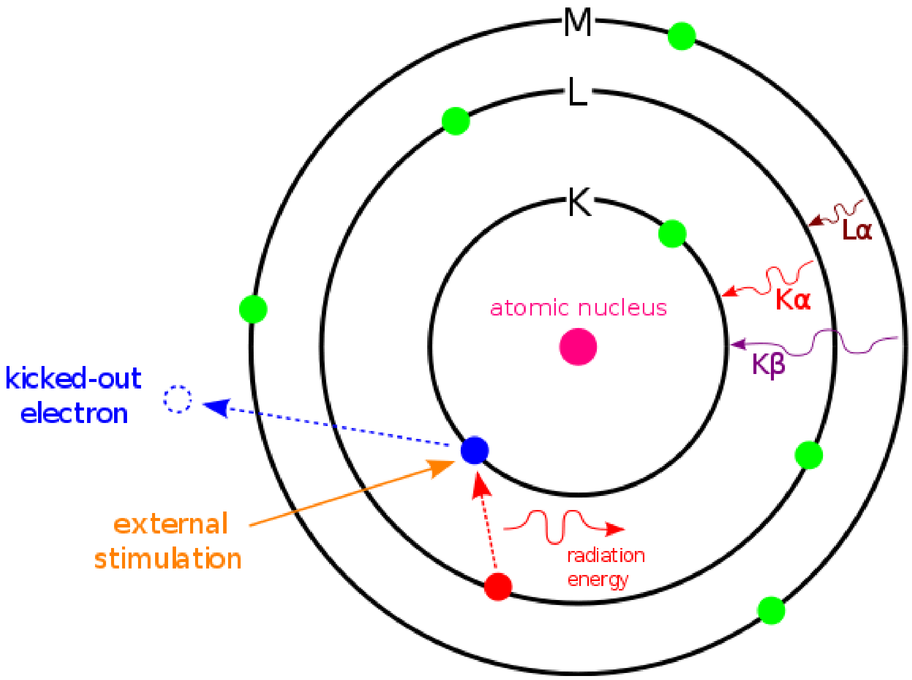

Figure 3.7 EDX working principle [25].

3.3.3 Powder x-ray diffraction (XRD)

X-ray diffraction (XRD) is one of the commonly used instruments to study the crystalline materials. The reason that x-rays were utilized as the probe is its proper wavelength of 0.1-10 nm, which is close to the size of interplane distances of atoms. Synchrotron x-ray diffraction uses an x-ray wavelength ca 0.7276 Å, while our normal powder XRD is 1.5418 Å. Even though its energy is less than that of the synchrotron, routinely studying the crystal structures of common material is enough. X-ray is produced from a cathode ray tube and then become a monochromatic and collimated radiation through slit filtering. Such x-rays illuminate the sample and are reflected by crystal lattice. The reflected x-rays interfere with each other in different ways. Some x-rays are canceled out due to the x-ray wave phases are just opposite while some are reinforced, which are called constructive interference. The condition for constructive interference is that the scattered x-rays must satisfy the Bragg's law (Figure 3.8).

$$n\lambda=2d\sin\theta$$

Where λ is wavelength of incident x-ray, d is inter-planar spacing between the adjacent planes, and θ is the angle between the incident beam and crystal plane.

The intensity and peak position of x-ray diffraction depends on the type of atoms and the atomic arrangement within the crystal structure. Thus, this technique can be used to fingerprint materials. In this thesis, the structural information of all the samples was characterized Bruker D8 Advance with Cu Kα radiation, λ = 1.54 Å. The step size is 0.05° coupled with a recording time of 1 s/step. XRD machine was collimated with a 2.5° soller, 1° divergence, a secondary graphite monochromator, and 0.3 mm receiving slits with a scintillation counter. After acquiring the data and plotting into XRD pattern, fitting with ideal patterns was performed to generate lattice parameters, crystallite size, etc. One of the fitting methods is Rietveld refinement, which uses fundamental parameters peak shape profile in TOPAS**.**

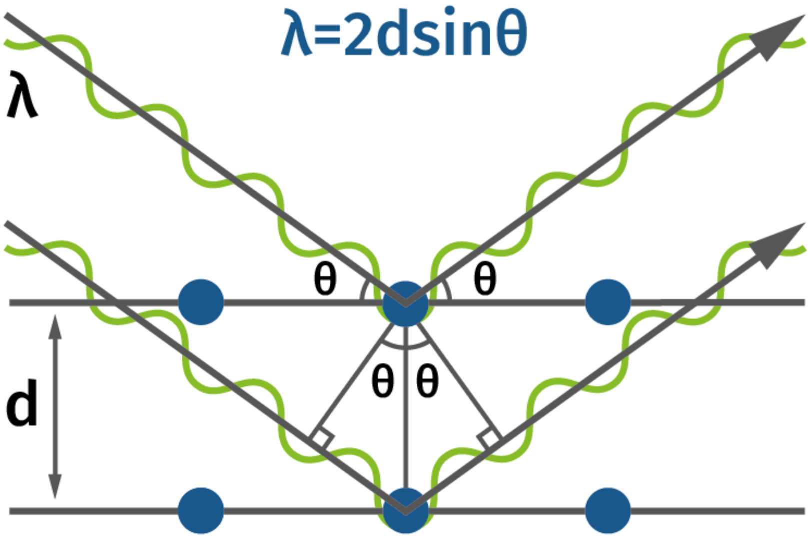

Figure 3.8 X-ray diffraction from crystal with Bragg's law [26].

3.3.4 Fourier transform infrared spectroscopy (FTIR)

Fourier transform infrared spectroscopy (FTIR) is one preferred method of IR and offers a valuable opportunity to detect the existence of certain functional groups in the sample. The sample can be both organic and inorganic. When IR radiation impinges the sample, some of the radiation is absorbed by the sample, while others are transmitted. The absorbed IR radiation depends on the molecular bonds as well as their surrounding bonds. The bonds will absorb the IR radiation if the frequency of molecular bonds movement matches the certain frequency of IR radiation. Since each molecular bond has its unique types of movement, thus a fingerprint method to identify the materials can be provided. Molecular bonds movements can be vibration, stretching, rocking, twisting, etc. If a dipole is created during molecular-associated movement, it is possible that this dipole could absorb certain frequency IR. Therefore, the dipole is necessary for IR to identify. For example, O_2, Cl_2 cannot be identified due to no dipole moment exists. Another advantage of FTIR is its ability to analyze a wide variety of samples, such solid, liquid, and gases by using different modes (transmission and reflection).

In this study, a Perkin Elmer Frontier Infrared spectrometer was utilized to investigate the purity of LVO and VS_4, as well as the functional groups on their surface after the hydrothermal reaction. The samples were prepared by mixing 100 mg KBr and ca. 0.2 mg active material and then subjected to pelletizing to form a translucent disk. The frequency range of 4000-400 cm^{-1} at a resolution of 2 cm^{-1} was chosen for analysis.

3.3.5 Raman spectroscopy

Raman spectroscopy is another most common vibrational spectroscopies used to provide information on the molecular fingerprint of materials [27]. This technique utilizes laser light to irradiate a spot on the sample, and generate an infinitesimal amount of inelastically scattered light (also namely Raman scattered light), which is then detected by the CCD detector of Raman. The Raman scattered light is account for only 0.000001% of the total scattered light. Over 99% of the scattered radiation is called Rayleigh scattering, which has the same frequency as the incident beam. In contrast, Raman scattered light has an either higher or lower frequency, but the Raman contains much information as to the energies of molecular vibration, chemical bonds, molecular structure, and environment where the atoms reside.

Different from FTIR that depends on a change in dipole moment, Raman arises from molecular vibration causing a change in polarizability. That means a distortion of electron cloud around the molecule is induced when Raman scattering occurs. Raman is sensitive to a homo-nuclear molecule, such as C-C, C=C, and C≡C. FTIR is sensitive to hetero-nuclear molecular bonds, OH is a typical example. On the contrary, H_2O has a very weak Raman signal. Furthermore, unlike FTIR which measures the absolute wavelength, Raman measures the relative frequencies (namely wavenumber) at which sample scatters radiation. In the Raman spectra, the shape of the peak is important and closely related to crystallinity and types of functional group (Figure 3.9). For example, the position of the peak is linked to molecular structure, and a shift even for the same vibrational modes could be observed due to the change in the nearby environment surrounding the functional group. The Raman spectroscopy can be used for identifying an unknown substance, identifying polymorphs, tracking changes in molecular structures, tracking a change in crystallinity, evaluating the magnitude of residual stress, and investigating the orientation of molecules.

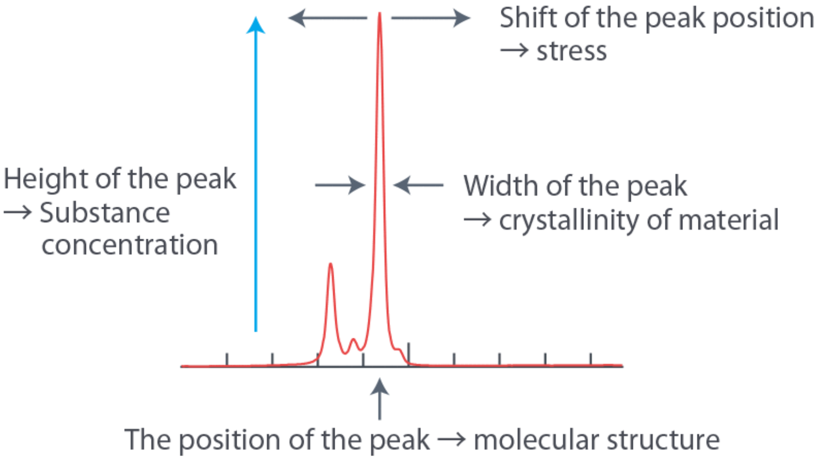

Figure 3.9 Explanation of Raman spectra [28].

3.3.6 BET measurement

The Brunauer-Emmett-Teller (BET) method is one of the most common techniques to characterize porous materials allowing for the determination of the surface area, pore size distribution, and pore volume of samples. There are six types of adsorption isotherms. The BET method is only applicable to type II (non-porous powders) and type IV (mesoporous with pores in the range of 1.5-100 nm). Its testing is conducted at a constant temperature, typically in N_2, 77K, and an adsorption isotherm is plotted by measuring the amount of gas adsorbed over a wide range of pressure. Conversely, desorption isotherms are obtained by measuring the amount of gas as pressure is released. BET is an extension of the Langmuir theory because it concerned with multiple layer adsorption of adsorbate, while Langmuir surface area is a model of monolayer adsorption, which this hypothesis is never fulfilled. Langmuir surface area is always larger than that of BET surface area because multilayer adsorption is treated as monolayer adsorption in BET method.

$$\frac{1}{v[\left(\frac{p_0}{p}\right)-1]}=\frac{(c-1)}{v_m c}\left(\frac{p}{p_0}\right)+\frac{1}{v_m c}$$

$$C=1+\frac{slope}{inercept}$$

Where v is volume of gas adsorbed at pressure equilibrium p, p_0 is the saturation pressure, v_m is the monolayer adsorbed gas, c is the BET constant, representing the surface interaction energy and usually the value of C is in between 100-200, if it is greater than 200, there are micropores present; below 100 indicates strong adsorbent/adsorbate interaction. The surface area is calculated based on the following equation:

$$S_{BET}=a.\frac{p_0\, v_M}{R.273K}N_a$$

Where N_a is the Avogadro number, a is the area of N_2 molecule (16.2Å^2). The above equation can be further simplified to:

$$S_{BET}=\frac{4.355}{slope+inercept}$$

It would be very interesting to study the process of BET measurements, anandd the main steps in the process of BET measurement are listed below (Figure 3.10):

1. Degas the sample. The sample must be degassed before determination of the adsorption/desorption isotherms over the BET region. The purpose of degassing is to remove the moistures of alien gas adsorbate in the pores of sample. Sometimes a temperature of 110 C is necessary to help remove the moisture, and the temperature is

also subjective to the utmost temperature the sample can withstand. Once the sample is cooling down, it should be reweighed to take into consideration of the moisture mass loss.

2. Evacuate the sample and reference tubes.
3. Dead-volume measurement. After evacuating the sample, another type of gas He is pumped inside to tube. The dead-volume is measured and are used to correct the quantity of adsorbate. Sample and reference tube should have similar dead-volume. Normally, glass rod or beads are used to reduce the dead-volume.
4. Evacuate the dead-volume gas.
5. Adsorption of the gas. The N_2 gas is admitted into both the sample and reference tubes in a slow continuous flow manner. At this stage, adsorption of N_2 on the samples occurs, the pressure inside the sample tube falls arising from the equilibration of adsorbed N_2 and the rest N_2. The amount of adsorbed N_2 can be calculated based on the difference between the amount of admitted gas and the non-adsorbed N_2. P0 is the saturation pressure, which can be measured initially for an empty tube. The isotherm for adsorption is plotted over the range of P/P0.
6. Desorption of the gas. Desorption is required to calculated other quantities like pore volume and distribution.

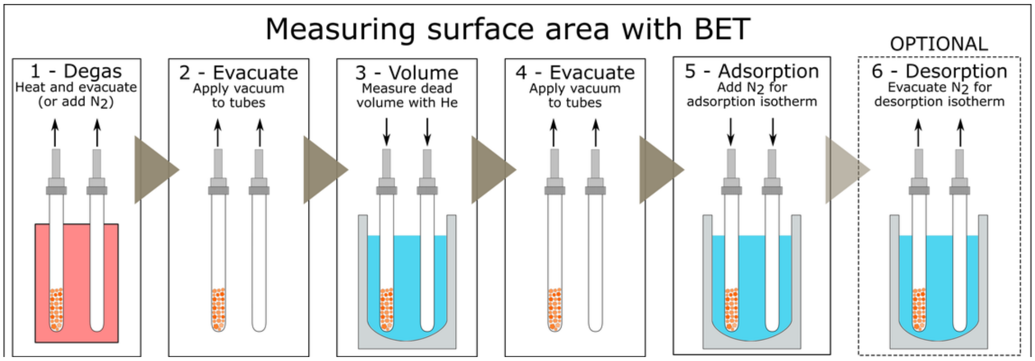

Figure 3.10 The procedures of BET measurement [29].

In this study, the surface area of the samples was tested in Liquid nitrogen using Micromeritics, ASAP 3020. Prior to measurement, all samples were degassed under vacuum for overnight.

3.3.7 Thermogravimetric analysis (TGA)

TGA analysis was employed to measures the weight loss of a material, either over a range of temperature or isothermally over a range of time, in an atmosphere of air, nitrogen, helium or in a vacuum. All sorts of materials like metal, inorganic, organic can be analyzed. The temperature ranges from room temperature to 1000 C, but the exact temperature range depends on the sample. Normally TGA can go up to 1000C, but a temperature of 900 C is a routinely used maximum temperature. The range of sample weight is 1~150 mg. The preferred sample weight is more than 10 mg, and weight change sensitivity is 0.01 mg. It is worth noting that the sample loaded inside the Pt cannot be too high, at the risk of dropping. Samples should be as small as possible to ensure the temperature of the interior sample remains close to the measured temperature. In this work, to determine the decomposition temperature of materials and carbon content of the composites, the samples testing were conducted utilizing TA Instrument Q500. The mass of applied sample is ca. 15 mg, in the temperature from room temperature to 800 °C with a heating rate of 10 °C min^{-1}, in either Nitrogen or synthetic air atmosphere.

3.3.8 2016 coin cell fabrication

The electrochemical performances of all the samples were evaluated in a 2016-coin cell. It is a two-electrode set up with active material as working electrode and lithium metal as the counter electrode. The active material is commonly mixed with PVDF binder (Kynar) and conductive carbon (i.e., Super P) in a ratio of 7:1:2. NMP is used as a solvent to dissolve PVDF and disperse other components to generate a slurry. Conductive carbon serves to provide electrical conductivity for the otherwise electrically insulative LVO or VS_4. The PVDF binder holds the active material and conductive carbon together and adheres them to current collector. The current collector for anode material is etcher copper and has uniform thickness density. Thus, the current collectors punched out from the entire roll are supposingly have same or similar weight.

In this work, electrodes were prepared by mixing 70 wt% of active materials, 20 wt% of Super P (Timcal) and 10 wt% of the binder (Kynar) in N-methyl-pyrrolidinone (NMP, Sigma Aldrich) to form a homogenous slurry. Following the coating of slurry on etched copper foil via doctor blade technique (thickness ~ 25-40 µm), the samples are dried below 80 °C in vacuum. Higher temperature may lead to thermal fracture due to the rapid contraction of electrode with the quick water evaporation. After drying in vacuum for 12h, the samples are pressed between twin rollers with a pressure of ~500 psi to improve the inter-particle contact and the adhesion between active material and current collector. Subsequently, electrodes are then cut into from an electrode preparation die with a diameter of 16 mm and each electrode disk contains 1-2 mg of active material.

Thereafter, for the lithium-ion battery testing, the electrodes were assembled in an argon-filled glovebox (MBraun, Germany) with oxygen and water content less than 1 ppm. Lithium metal served as a counter electrode, Celgard 2400 as the separator and 1 M solution of LiPF6 dissolved in ethylene carbonate/diethylene carbonate (EC: DEC = 1:1 by volume, Charslton Technologies Pte Ltd.) was used as the electrolyte.

3.3.9 Cyclic voltammetry (CV)

The CV experiments were performed using Solartron 1470E in the voltage window range from 0.01 to 3.0 V. The scanning rate is normally set to either 0.2 mV s^{-1} or 0.1 mV s^{-1}, which is affected by the active materials tested. In the half-cell testing, cathodic peaks in lithiation process are related to the reduction reaction, whereas anodic peaks in the delithation process correspond to the oxidation reaction.

3.3.10 Galvanostatic cycling

Galvanostatic cycling means the cell charge/discharge at a constant current with a certain potential range. Herein, regard to our materials, a voltage range of 0.1-3 V is chosen for LVO and 0.01-3.0 V for VS_4. The testing is conducted using Neware battery tester at room temperature under different current densities ranges from 0.1 to 2 A g^{-1}. A minimum of 100 cycles at certain current densities was tested to verify the cycling stability of materials.

3.3.11 Electrochemical impedance spectroscopy (EIS)

EIS is used to study the various processes that may occur on the active material. An altering small current is applied to a steady state system, and the corresponding current responses are observed. The electrical, charge transfer resistance and ionic conductivity in the bulk materials can be evaluated. The electrical resistance can be measured at the high-frequency range, while charge transfer resistance and diffusion in bulk are measured at mid-frequency and low-frequency ranges. The impendence measurements are conducted before, in the middle and after the cycling to monitor certain process happens at which state of charge. For instance, the formation of solid electrolyte interface normally occurs at around 0.6 V, where the impedances can reflect such formation process. In this study, EIS was tested in the frequency range of 100 MHz–0.1 Hz with a bias voltage of 10 mV.

3.4 Overview of Methodologies

In summary, in order to synthesize LVO with VS_4 with special morphologies, and investigate the relationships between morphologies and the electrochemical performance when used as LIB anode materials, hydrothermal synthesis method was chosen due to its ability to achieve various morphologies. Many parameters like using of surfactant, hydrothermal time, temperature, precursor concentration and different solvent for the hydrothermal could be adjusted to synthesize a material with various morphologies. After obtaining the material with a series of morphologies, physical and structural characterization are followed by, FESEM and TEM are employed to characterize the morphologies, while TEM can be used to investigate the phase. Another technique that can characterize the phase purity and lattice parameters is XRD. The surface area and pore size distribution were characterized by BET testing. Thermogravimetric analysis was employed to identify optimum temperature for calcination and carbon content of the samples. After characterization of physical and structure, the electrochemical performance as anode material for LIBs is tested and investigated. The performance is correlated with the morphologies.

3.5 Material synthesis

3.5.1 Carbon coated Li_3VO_4 nanorod

Single-crystal Li_3VO_4 nanorods (denoted as LVO-ROD): 0.234 g NH_4VO_3 and 0.245 g LiOH monohydrate were mixed in 10 mL DI water first, and then stirred until the chemical fully dissolved. After that, 20 ml ethanol was added to the above transparent solution. Subsequently, the above solution was transferred to a 45 ml autoclave and heated at 180 °C for 4 hrs. Finally, the obtained product was centrifuged and washed four times with methanol, which was then dried at 80 °C in vacuum overnight.

Spherical-assembly shaped, large single-crystal flower structure and bulk-shape Li_3VO_4 (denoted as LVO-SPHERE, LVO-FLOWER, and LVO-BULK): these Li_3VO_4 structures were obtained by simply replacing ethanol with other alcohols (Methanol, Propanol, and Butanol). For the carbon coating process on LVO-ROD, 200 mg LVO-ROD powder was added to 4 mL of poly(vinylpyrrolidone) (PVP Molecular Weight 29K) / EtOH solution (25 mg/mL). This slurry was then ground until dry. The resulting powder was heated at 500 °C for 2 h in Ar atmosphere to pyrolyze PVP forming a carbon-based amorphous coating. It is noteworthy that methanol instead of water was used to wash LVO because LVO is soluble in water.

3.5.2 Carbon coated Li_3VO_4 microsphere

First, 2 mmol NH_4VO_3 and 6 mmol $LiOH{\cdot}H_2O$ were dissolved in 15 mL DIW, and continuously stirred until a homogeneous solution was obtained. Then, 15 mL EtOH was then added to the above transparent solution followed by transferring it to a 45 ml Teflon lined autoclave and maintained for 4 h at 180 °C. Finally, the obtained product was centrifuged and washed 4 times with methanol to form Li_3VO_4 powder, which was dried in vacuum at 80 °C overnight. To investigate the morphology changes with varying volume ratio of solvent components, LVO was prepared with the volume ratio of EtOH and DIW from 30:0, 20:10, 15:15, 10:20, and 0:30 (denoted as 30-0, 20-10, 15-15, 10-20, and 0-30, respectively). The total volume of solvent is 30 mL. For the carbon coating process on 15-15, 100 mg LVO powder was added to 2 mL of a poly(vinylpyrrolidone) (PVP molecular weight 29 K) in EtOH solution (25 mg/mL). This slurry was then stirred until it became dry. The resulting powder was heated at 500 °C for 2 h in Ar atmosphere to form the carbon-based amorphous coating over the surface of LVO particles. It is worth mentioning that methanol was used instead of water to wash LVO since LVO is soluble in water.

3.5.3 Urchin-like VS_4

Urchin-like VS_4 with single-crystal long legs (denoted as urchin-VS_4): 7.5 mmol thioacetamide (TAA) was dissolved in 30 mL methanol first, and then 1.5 mmol NH_4VO_3 was introduced into the above solution. The solution was stirred to mix the precursors well and then transferred into a Teflon-lined stainless-steel autoclave with a capacity of 45 mL. The autoclave was sealed and heated at 160 °C for 24 hrs. Finally, the obtained product was centrifuged and washed three times with water and ethanol, respectively. The obtained VS_4 powder was vacuumed dried at 80 °C overnight.

Hierarchical microflower VS_4, octopus-like structure VS_4, and sea grass-like structure VS_4 (flower-VS_4, octopus-VS_4, and sea grass-VS_4): they were prepared by changing of solvent from methanol to ethanol, propanol, and butanol, respectively.

3.5.4 In-situ grown VS_4 nanowires on rGO

Urchin-like VS_4 with single-crystal long legs (denoted as urchin-VS_4): 7.5 mmol thioacetamide (TAA) was dissolved in 30 mL methanol, followed by 1.5 mmol NH_4VO_3 into the above solution. The solution was then stirred to produce a homogeneous mixture before being transferred into a Teflon-lined stainless-steel autoclave with a capacity of 45 mL. The autoclave was sealed and heated at 160 °C for 24 hrs. The obtained product was centrifuged and washed three times with water and ethanol. Finally, VS_4 powder was vacuumed dried at 80 °C overnight.

Nanowire VS_4 in-situ grown on rGO with various loading (5rGO@VS_4, 15rGO@VS_4, and 35rGO@VS_4): theoretically, 268 mg VS_4 could be obtained for each reaction. Thus, 14 mg, 47 mg and 150 mg vacuum-dried GO were added into the reaction with 15 mins ultrasonication to attain 5 wt% GO 15 wt% GO and 50 wt% GO (denoted as 5rGO@VS_4, 15rGO@VS_4, and 35rGO@VS_4) respectively.

References

[1] J. Chen, S. Wang, M.S. Whittingham, Journal of Power Sources, 174 (2007) 442-448.

[2] S. Balaji, D. Mutharasu, N.S. Subramanian, K. Ramanathan, Ionics, 15 (2009) 765.

[3] J.-M. Tarascon, N. Recham, M. Armand, J.-N. Chotard, P. Barpanda, W. Walker, L. Dupont, Chemistry of Materials, 22 (2009) 724-739.

[4] X. Feng, C. Shen, X. Fang, C. Chen, Journal of Alloys and Compounds, 509 (2011) 3623-3626.

[5] J.-H. Lim, H. Bang, K.-S. Lee, K. Amine, Y.-K. Sun, Journal of Power Sources, 189 (2009) 571-575.

[6] A. Van Bommel, J. Dahn, Journal of The Electrochemical Society, 156 (2009) A362-A365.

[7] V. Aravindan, J. Sundaramurthy, P.S. Kumar, Y.-S. Lee, S. Ramakrishna, S. Madhavi, Chemical Communications, 51 (2015) 2225-2234.

[8] Y. Tanaka, Q. Zhang, F. Saito, Powder technology, 132 (2003) 74-80.

[9] S.-H. Park, S.-T. Myung, S.-W. Oh, C.S. Yoon, Y.-K. Sun, Electrochimica acta, 51 (2006) 4089-4095.

[10] W.F. Bleam, Reviews of Geophysics, 31 (1993) 51-73.

[11] H. Hayashi, Y. Hakuta, Materials, 3 (2010) 3794-3817.

[12] I. AUTOCLAVE., in, 2014.

[13] T.-D. Nguyen, Nanoscale, 5 (2013) 9455-9482.

[14] H. Zhang, M. Jin, Y. Xiong, B. Lim, Y. Xia, Accounts of chemical research, 46 (2012) 1783-1794.

[15] Z. Wu, S. Yang, W. Wu, Nanoscale, 8 (2016) 1237-1259.

[16] J. Gopalakrishnan, Chemistry of Materials, 7 (1995) 1265-1275.

[17] W. Xuewen, Z. Zhiyong, Z. Shuixian, Materials Science and Engineering: B, 86 (2001) 29-33.

[18] C.L. Carnes, P.N. Kapoor, K.J. Klabunde, J. Bonevich, Chemistry of materials, 14 (2002) 2922-2929.

[19] K.J. Klabunde, J. Stark, O. Koper, C. Mohs, D.G. Park, S. Decker, Y. Jiang, I. Lagadic, D. Zhang, The Journal of Physical Chemistry, 100 (1996) 12142-12153.

[20] S. Utamapanya, K.J. Klabunde, J.R. Schlup, Chemistry of Materials, 3 (1991) 175-181.

[21] WIKIPEDIA., in, 2018.

[22] G. Cao, Nanostructures & nanomaterials: synthesis, properties & applications, Imperial college press, 2004.

[23] W. COMMONS., in, 2017.

[24] Globalsino., in, 2018.

[25] WIKIPEDIA., in, 2018.

[26] stresstech., in, 2018.

[27] D.D. Le Pevelen, NIR FT-Raman A2 - Lindon, John C, in: G.E. Tranter, D.W. Koppenaal (Eds.) Encyclopedia of Spectroscopy and Spectrometry (Third Edition), Academic Press, Oxford, 2017, pp. 98-109.

[28] Nanophoton., in, 2016.

[29] A. Connelly., in, 2017.

Chapter 4

Carbon-coated Li_3VO_4 nanorods

Li_3VO_4 (LVO) anode materials with controllable morphologies from spherical-assembly, single-crystal nanorods, flower shape, to bulk-shape were designed via solvothermal approach using different alcohols (i.e., ethanol, methanol, propanol, and butanol). XRD, SEM, BET, Raman and FTIR and galvanostatic charge/discharge measurements were carried out to correlate the structure/morphology with their electrochemical characteristics. Experimental results reveal that both structure and morphology play important roles in the Li^+ ion storage of LVO, which degrades in the sequential order from nanorods, sphere, flower to bulk. The LVO nanorods are hierarchical and have a small particle size, high specific surface area, and high crystallinity, thus exhibit the largest Li^+ ion diffusion coefficient and best electrochemical performance among the four electrodes. Moreover, carbon that is coated over single-crystal LVO nanorods further enhances the Li^+ ion storage. It is reasonable that the carbon-coated LVO nanorods deliver a high reversible capacity of 440 mAh g^{-1} at 0.1 A g^{-1} with good cycling stability and demonstrate great practical application. In addition, the results promote a better fundamental understanding of the Li^+ ion storage behavior in LVO and provide insight in guiding the optimal design of LVO and other vanadium-based electrode materials.

---

*This section published substantially in **Yang, G** et al. Journal of Materials Chemistry A 2018, 6, 456-463.

4.1 Introduction

The sharp proliferation of electric automotive and regenerative electric energy storage system (EES) drives the search of high-performance power sources that have high energy density and power density. Stable Li^+ ion intercalation chemistry of graphite ensures the success of LIBs over the past decades. However, challenges facing graphite anode such as limited specific capacity (372 mAh g^{-1}) and safety issue related to Li dendrite formation upon Li^+ ion intercalation at low potential (close to 0 V), especially at high rates, promote urgent demands for novel anode alternatives with both large capacities and more positive intercalation voltages (*vs*. Li^+/Li) [1, 2]. Spinel $Li_4Ti_5O_{12}$ has been exploited since it operates with zero strain, high reversibility, and good rate performance [3-7]. Nevertheless, its low specific capacity (~150 mAh g^{-1}) and relatively high operating potential (about 1.5 V *vs*. Li^+/Li) sacrifices the overall cell performance. In addition to insertion type anodes [8, 9], conversion-type anodes (*i.e*., transition metal oxide and metal sulfides, etc.) [10, 11], and alloying-type anodes (*e.g*., Si and Sn-based materials) [10-12] have been also investigated. The conversion-type anodes generally deliver a specific capacity of 2-3 times of that of graphite, which is because the theoretical value is determined by the oxidation state of metal ions [13]. However, they suffer from poor kinetics, low energy efficiency and large polarization associated with the energy barrier to trigger the cleavage of the metal-oxygen and/or sulfur bonds [10]. The alloying-type anodes can deliver ultra-high capacities but at the expense of huge volume change and poor cycling performance. Given the improved specific capacity and appropriate intercalation potential, intercalation-type anodes are intrinsically attractive from the perspective of highly reversible Li^+ insertion/extraction and negligible volume change upon cycling.

More recently, Zhou *et al* reported such a material, β-Li_3VO_4 (LVO), with high reversible capacity (394 mAh g^{-1}, based on $Li_3VO_4 + xLi^+ + xe^- \leftrightarrow Li_{3+x}VO_4$, $0 \leq x \leq 2$) and suitable Li^+ ion intercalation potential (0.5 V ~ 1.0 V, *vs*. Li^+/Li) [14]. The orthorhombic LVO exhibits a hollow lantern-like 3D framework consisting of a regular array of corner-shared VO_4 tetrahedra and LiO_4 tetrahedrons, which provides lots of empty sites and intercalation channels for Li^+ ion [15]. Moreover, the high ionic conductivity of LVO (10^{-4} ~10^{-6} s cm^-

^{1}) [16, 17] ensures fast Li^+ ion diffusion. *Ex-situ* XRD results revealed that the insertion of Li^+ into LVO starts with a solid-solution step and follows with a two-phase reaction [15]. Theoretical calculations also showed that the reversible phase transformation from Li_3VO_4 to Li_5VO_4 is energetically favorable (with a biphasic reaction at 0.7 V, *vs*. Li^+/Li) upon 2 Li insertion/extraction process [18]. Nonetheless, for one more Li insertion, this process is difficult as manifested by the low predicated voltage (0.14 V, *vs*. Li^+/Li) and the major structural rearrangements (20% volume variation) [18]. However, experimental results demonstrate the practical feasibility of the third Li insertion although the underlying mechanism is still unclear. For example, a high reversible specific capacity of 540 mAh g^{-1} (about 2.7 Li) was reported for Li_3VO_4/C composite at a current density of 150 mA g^{-1} [19]. The carbon-coated LVO prepared by solid-state method delivers a reversible capacity of 547.1 mAh g^{-1} based on GITT tests and *in-situ* XRD characterizations [15]. Further work has also shown that the synthesis method, crystallinity and the morphology greatly affect the electrochemical properties of electrode materials [20]. For example, micro-sized LVO (0.8-2.0 μm) prepared by solid-state method delivers the first discharge and charge capacity of 345 and 258 mAh g^{-1}, respectively [21]. These values rise up to 469 and 326 mAh g^{-1} for hollow cuboid LVO synthesized by a sol-gel method [22], and 624 and 481 mAh g^{-1} for nano-sized LVO (10-100 nm) produced by a hydrothermal method [23]. Reduction of particle size and improving the intrinsic/extrinsic electronic conductivity have been the main performance improvement approaches for LVO. These approaches can be achieved through synthetic optimization [24], morphology tailoring [22, 25, 26], surface modification [15, 27, 28], in-situ growing on electric substrate [29] and/or electrode hybridization [30-34] Despite significant progresses have been made so far, LVO is still far from practical applications due to its low electronic conductivity in comparison to its high ionic conductivity and the lack of understanding in i) a comprehensive relationship between materials structure properties with electrochemical characteristics, and ii) the fundamental electrochemistry.

Herein, we synthesized a series of LVO with controlled morphologies from spherical-assembly, single-crystal nanorods, flower shape, to bulk by a solvothermal approach using different alcohols. To investigate the morphology effect on the anodes, XRD, SEM, FITR, Raman CV and galvanostatic charge/discharge were employed to examine their physical properties with electrochemical characteristics. The results reveal that single-crystal LVO nanorods show the best performance in terms of rate performance and cyclability. This enhanced electrochemical performance can be ascribed to i) the high surface area of the porous rod-shaped structure that offers favorable ion diffusion and electron transfer, and ii) the small particle size that reduces the diffusion length. Moreover, further improvement in the electrochemical performance was achieved using carbon coating on the single-crystal LVO nanorods. The as-prepared LVO/C delivers a high reversible capacity of 430 mA g^{-1} at a current of 100 mA g^{-1}, along with good rate performance and cycling stability.

4.2 Experimental procedures

4.2.1 Material synthesis

The details are seen in Chapter 3.5.

4.2.2 Materials Characterization

The powder X-ray diffraction patterns were collected in Bruker D8 Advance using Cu Kα radiation. The morphologies of synthesized samples were characterized using scanning electron microscopy (SEM, JEOL JSM-7600, Japan) and high-resolution Transmission electron microscopy (HRTEM, JEOL JEM-2100F). Raman spectra were obtained using a WITecCRM200 Raman system (WITec, Germany).

4.2.3 Electrochemical Characterization

The electrochemical performance of LVO was evaluated by assembling 2016 coin cells in an argon-filled glovebox (MBraun, Germany) with oxygen and water content less than 1 ppm. The electrodes were prepared by mixing 70 wt. % active materials, 10 wt. % binder (PVDF Kynar), and 20 wt. % Super P (Timcal) in a weight ratio of 7:1:2 in N-methyl-pyrrolidinone (NMP, Sigma Aldrich). The typical electrode was dried at 60 °C for 2 h and

120 °C for 10 h in a vacuum oven before being assembled into a coin cell in the glovebox. The mass loading was about 1 mg cm^{-2}. Lithium foil served as a counter electrode, and Celgard 2400 was used as the separator. The electrolyte was composed of 1 M solution of $LiPF_6$ dissolved in ethylene carbonate/diethylene carbonate (EC: DEC = 1:1 by volume, Charslton Technologies Pte. Ltd.). The specific capacity for Carbon coated LVO-ROD sample is calculated based on the total weight of LVO and amorphous carbon. Electrochemical impedance spectroscopy (EIS) and cyclic voltammetry (CV) measurements were performed using Solartron Instrument. The frequency of EIS measurement was carried out from 100 KHz to 0.01 Hz with an AC signal of 10 mV amplitude.

4.3 Results and discussion

4.3.1 Synthesis and characterization of LVO with four different morphologies

LVO with different morphologies (Figure 4.1) was synthesized in Methanol, Ethanol, Propanol, and Butanol solvothermal solvents. Spherical shape, nanorod shape, flower- like shape and bulky LVO were obtained. In the text below, these products are simply illustrated as LVO-SPHERE, LVO-ROD, LVO-FLOWER, and LVO-BULK, respectively. LVO-SPHERE is a microspherial-assembled cluster. LVO-ROD shows hierarchical structure consisting of rods with diameter range from 50-100 nm. Flower-shape LVO composes of primary particles with the size around 1 µm, while LVO-BULK appears large crystals with the size around 7 µm. Table 4.1 lists all these products along with their corresponding particle sizes.

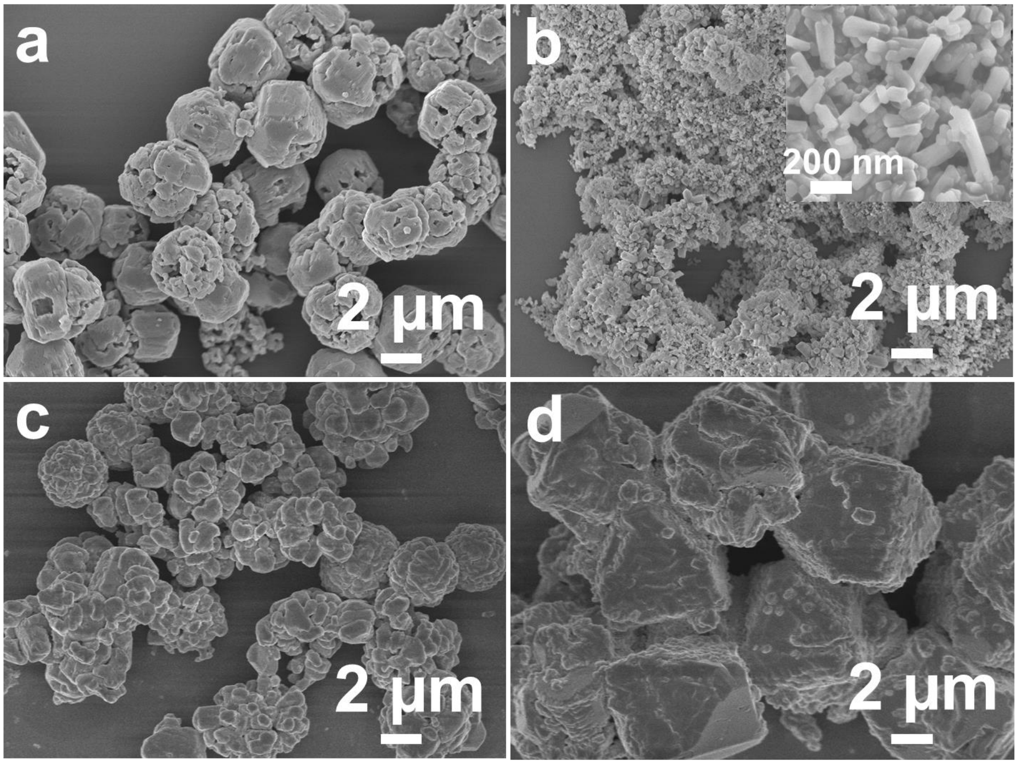

Figure 4.1 Morphology and Structure. SEM images of: (a) LVO-SPHERE; (b) LVO-ROD; (c) LVO-FLOWER; (d) LVO-BULK; all the SEM images show the same magnification.

Powder-XRD results reveal that all samples are a pure phase and determined to be LVO phase (JCPDS NO. 38-1247) (Figure 4.2). LVO-ROD shows the broadest peak in the XRD pattern indicating the smallest crystallite size, in good agreement with the SEM result. The Rietveld refined XRD patterns of the samples are shown in Figure 4.3. The refined crystallographic parameters are presented in Table 4.2. The lattice volume of LVO-ROD is largest among all these samples, which allows the fastest diffuse of Li ions leading to the highest Li-ion diffusion coefficient.

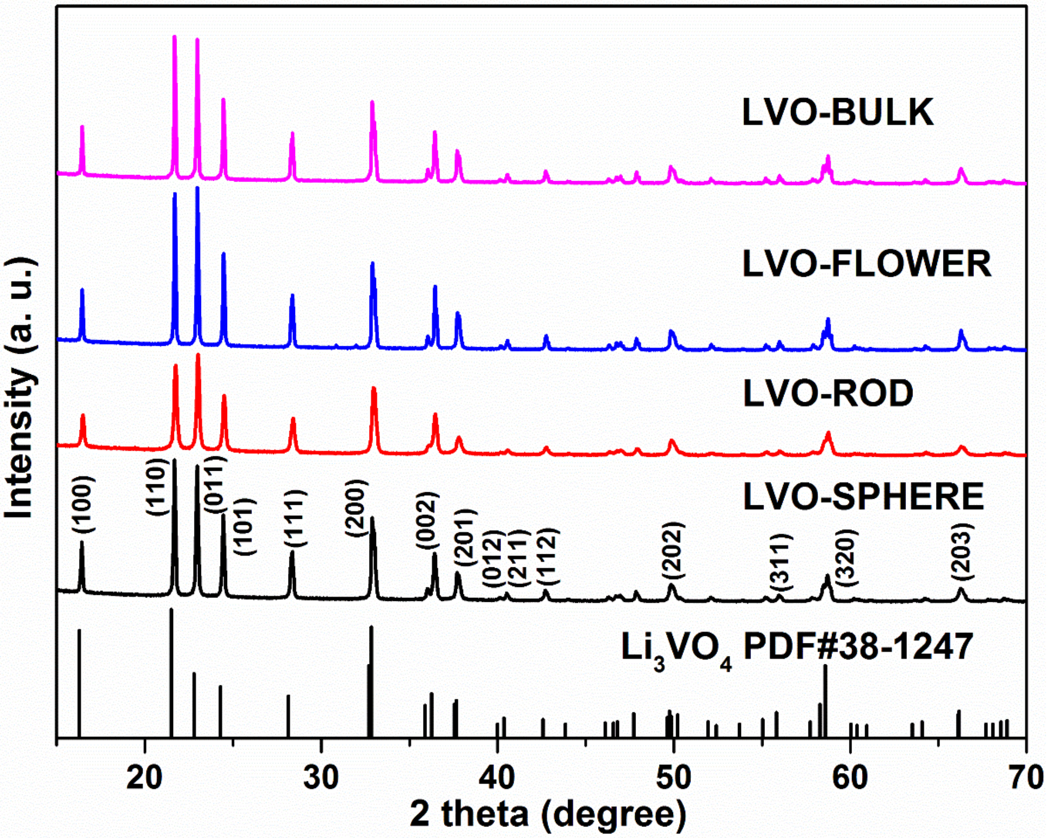

Figure 4.2 XRD patterns of LVO-SPHERE, LVO-ROD, LVO-FLOWER, and LVO-BULK.

Table 4.1 LVO samples particle size, BET surface area and pore volume

Sample	Particle size	S_{BET} calculated (m^2/g)	Pore volume (cm^3/g)
LVO-SPHERE	Primary:100–1000 nm Secondary: 4 μm	1.35	0.004828
LVO-ROD	Dia: 50-100 nm Length: 100-500 nm	10.49	0.059163
LVO-FLOWER	Primary: 0.5-1 μm Secondary: 5 μm	0.94	0.003664
LVO-BULK	7 μm	0.05	0.000396

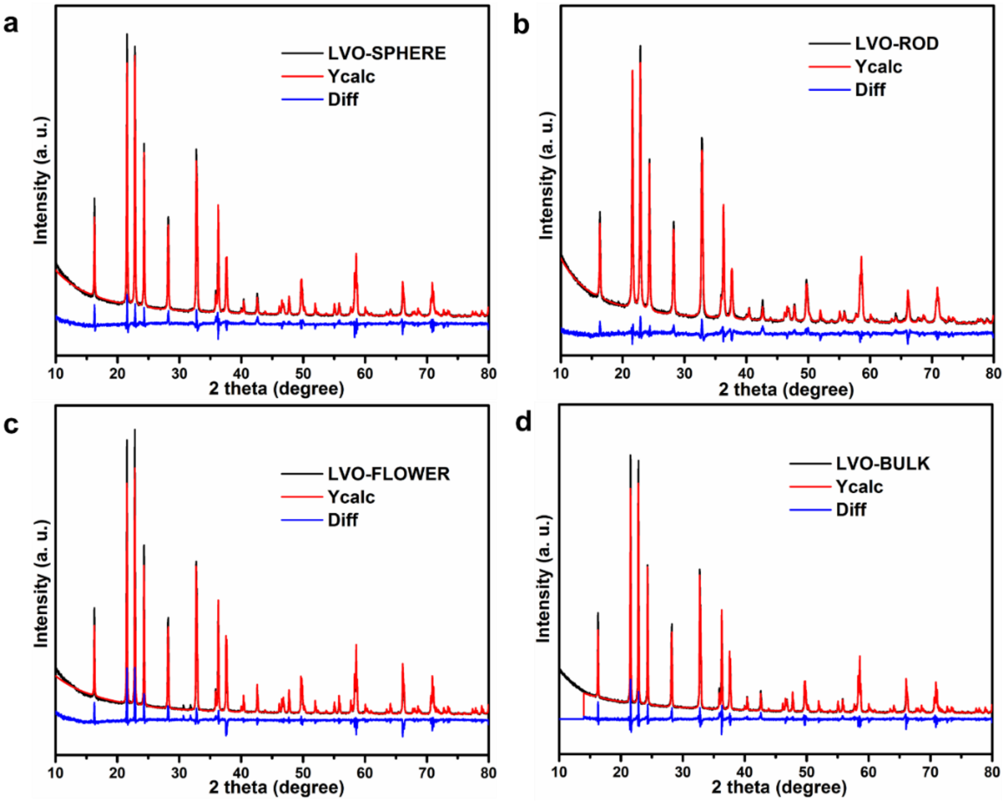

Figure 4.3 Rietveld refinement of the XRD data for (a) LVO-SPHERE, (b) LVO-ROD, (c) LVO-FLOWER, (d) LVO-BULK.

Table 4.2 Lattice parameters of the samples

Sample	**a(Å)**	**b(Å)**	**c(Å)**	**V(Å^3)**	**Rwp**
LVO-SPHERE	6.3265376	5.4496384	4.9527315	170.75702	5.13
LVO-ROD	6.3268489	5.4523261	4.9571351	171.00155	2.86
LVO FLOWER	6.32673	5.449300	4.950601	170.67820	7.78
LVO-BULK	6.3273897	5.4490063	4.9528472	170.76420	6.54

Raman and Fourier transform infrared (FTIR) spectroscopies were used to further investigate the structural features of the samples. In Figure 4.4a, the peak at 819 cm^{-1} is attributed to symmetric stretching of VO_4^{3-}, whereas the peak at 791 and 785 is assigned to asymmetric stretching of VO_4^{3-}. The peak at 328 cm^{-1} is generated by the VO_4 vibration. Almost identical spectra collected from all the samples indicate that no impurity phases are present [26, 35, 36]. Figure 4.4b shows the FTIR spectra of the samples and the assignment of these peaks are summarized in Table S2. Both peaks at 3433 and 1637 cm^{-1} are attributed to the moisture inside the samples. The peak at around 1420 cm^{-1} is associated with the amorphous carbon, which may come from the synthesis process using alcohol as solvents [32]. Another small peak at around 2344 cm^{-1} is related to the adsorption of CO_2 on the sample surface [37]. The main peaks located at 851, 806 and 466 are assigned to the symmetric, asymmetric stretching of V-O, and symmetric stretching of V-O-V, respectively [38, 39]. The peak around 851 cm^{-1} is different for all the four samples, which is due to the different particle sizes as well as the different preferred crystallographic orientation formation under different preparation conditions as described in XRD section [40-42].

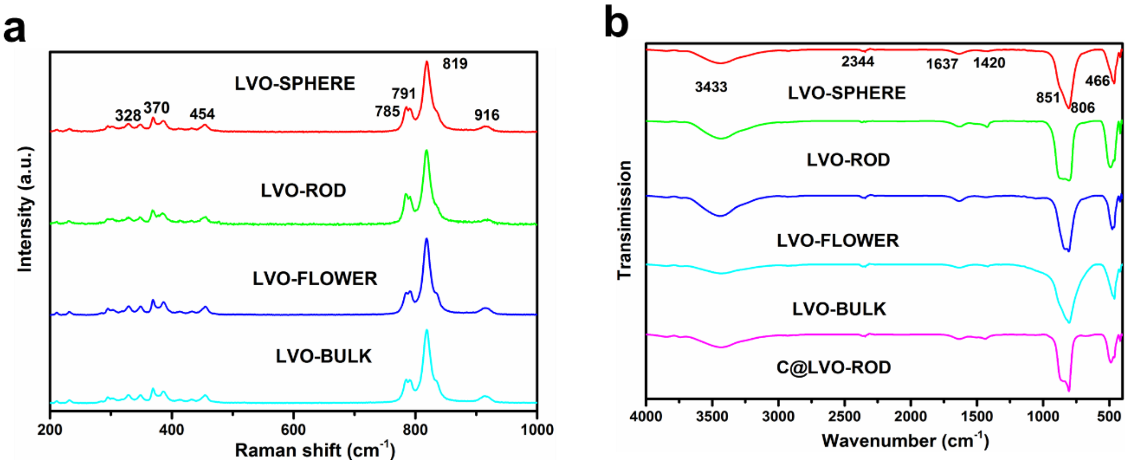

Figure 4.4 (a) Raman and (b) FTIR spectra for (a) LVO-SPHERE, (b) LVO-ROD, (c) LVO-FLOWER, (d) LVO-BULK.

Figure 4.5 shows a representative TEM image of a single nanorod. Uniform lattice fringes have been identified from SAED pattern. The lattice fringes are measured to be 0.41 nm, which correspond to the d-spacing of the (110) plane of Li_3VO_4. Moreover, the distinct periodic dots in SAED patterns (Figure 4.5) suggest its single-crystal feature. HRTEM image and the corresponding fast-Fourier transform (FFT) from another rod also demonstrate that the rods are a single crystal. The TEM image and the corresponding EDX elemental mapping images of V and O indicate the presence and uniform distribution of element V and O across the nanorod.

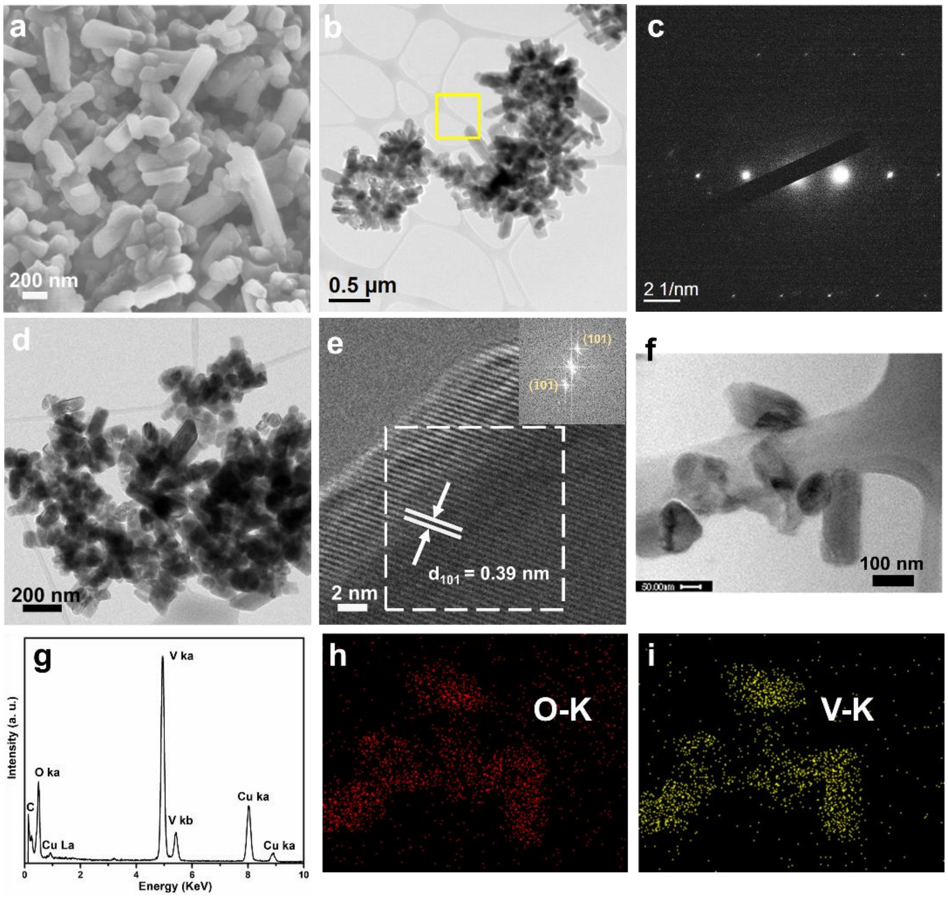

Figure 4.5 (a, b, d) TEM image and (c, e) HRTEM image of LVO-ROD, the inset shows the corresponding FFT image, (f) TEM image of LVO-ROD, (g) EDX spectrum, and elemental mapping images of h) O and (i) V for LVO-ROD in (f).

4.3.2 Comparison of electrochemical performance of four LVOs and mechanism study

The electrochemical performance of LVO-SPHERE, LVO-ROD, LVO-FLOWER, and LVO-BULK were investigated and compared. Typical cyclic voltammetry (CVs) curves of LVO-ROD for the first three cycles are illustrated in Figure 4.6. The reduction peak at around 0.28 V in the first cathodic scan is resulted by the SEI (solid electrolyte interface) formation and/or side reactions. This cathodic peak is broader compared to some literature; one possible explanation could be the small particle size and special nanorod morphologies [43]. A small reduction peak at around 1.4 V comes from decomposition of electrolyte [44, 45]. CV curves overlap well from the 2nd cycle onwards, indicating the good reversibility and cycling stability. Two dominant reduction peaks around 0.87, 0.54 V appear in the subsequent cycles, which are correlated with the multistep insertion of lithium ions to Li_3VO_4 accompanied by the phase change to $Li_{3+x}VO_4$ [11, 15, 29, 46]. The oxidation peak around 1.35 V demonstrates the delithiation process with the oxidation from $Li_{3+x}VO_4$ to LVO. Similar redox reactions were also identified for LVO-SPHERE, LVO-FLOWER, and LVO-BULK.

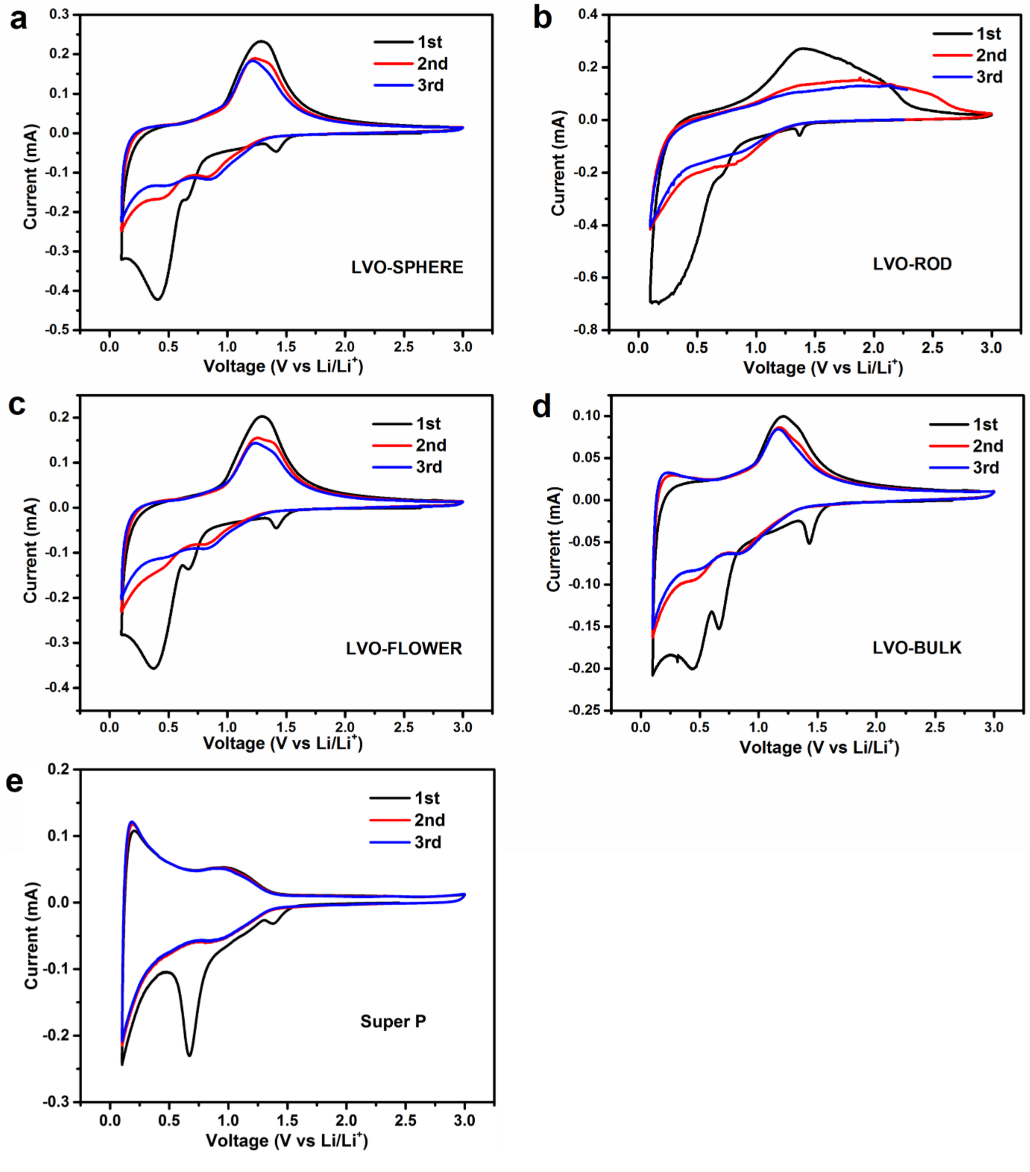

Figure 4.6 First three CVs of (a) LVO-SPHERE, (b) LVO-ROD, (c) LVO-FLOWER, (d) LVO-BULK, (e) Super P carbon additives with a scan rate of 0.2 mV s^{-1} in the voltage range of 0.1-3 V vs Li/Li^+.

GDC profiles (Figure 4.7) in the first cycle deliver three voltage plateaus at 1.4 V, 0.75 V and 0.6 V, which correspond to the irreversible reactions but are not observed in the second cycle, in good agreement with the CV results. The LVO-ROD electrode produces an initial discharge capacity of 550 mAh g^{-1} and first charge capacity of around 370 mAh g^{-1} with the first-cycle coulombic efficiency of 67.28%. The capacity loss is mostly due to the irreversible reactions including the decomposition of electrolyte and the formation of the SEI film, as identified from the shape difference between the discharge profiles of the first and second cycles. The electrochemical performance of LVO-ROD is superior over that of LVO-SPHERE, LVO-FLOWER, and LVO-BULK, probably due to its large surface area and high electron transportation. More discussion will be given later.

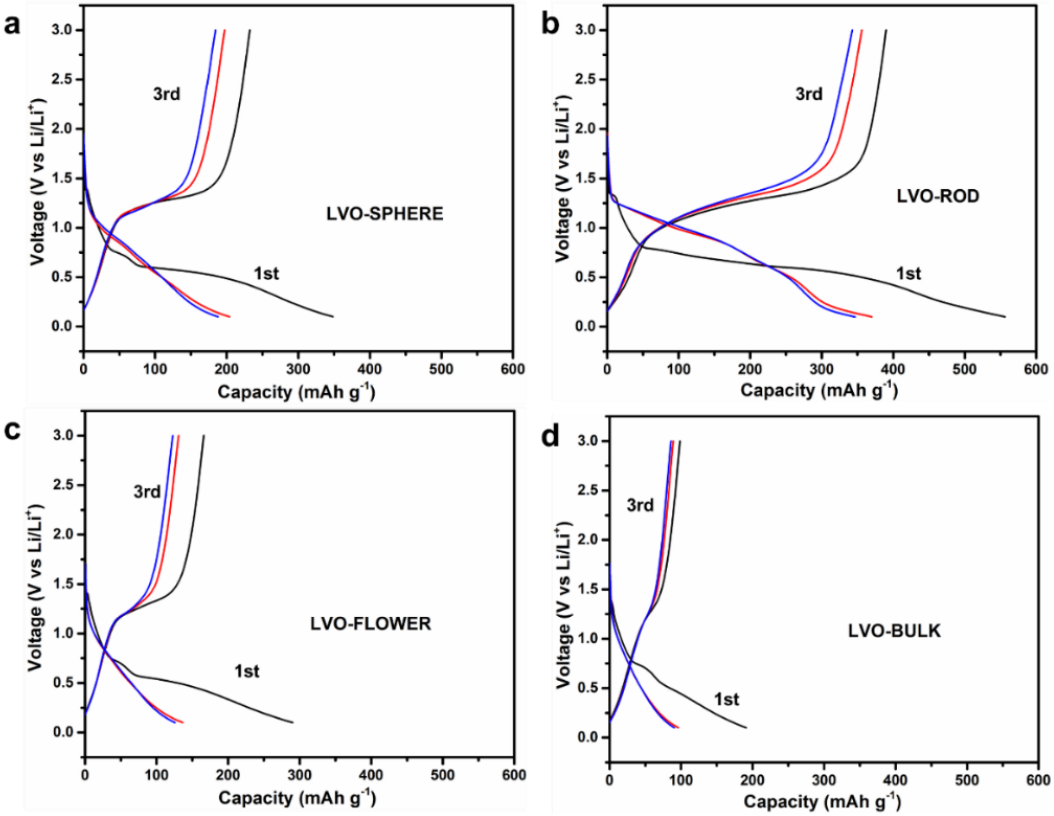

Figure 4.7 First three galvanostatic discharge-charge profiles at a current rate of 0.1 A g^{-1} in the voltage range of 0.1-3 V vs Li/Li^+ for (a) LVO-SPHERE, (b) LVO-ROD, (c) LVO-FLOWER, (d) LVO-BULK.

Moreover, the LVO-ROD exhibits enhanced rate performance compared with other LVO samples (Figure 4.8). For example, a discharge capacity of 150 mAh g^{-1} can be achieved even at a high current density of 4000 mA g^{-1}. Particularly, a high capacity of 280 mAh g^{-1} can be still produced when the current density reduces back to 100 mA g^{-1}. Such excellent cycling performance is also well illustrated in Figure 4.8, in which the LVO-based electrodes show a trivial decrease in specific capacities upon cycling. A capacity of 250 mAh g^{-1} (at 100 mA g^{-1}) is retained till 100 cycles for LVO-ROD, with a capacity retention of 72%. The LVO-SPHERE, LVO-FLOWER, and LVO-BULK deliver smaller specific capacities but shows reasonable cycling stability, suggesting that LVO is a promising anode for LIBs.

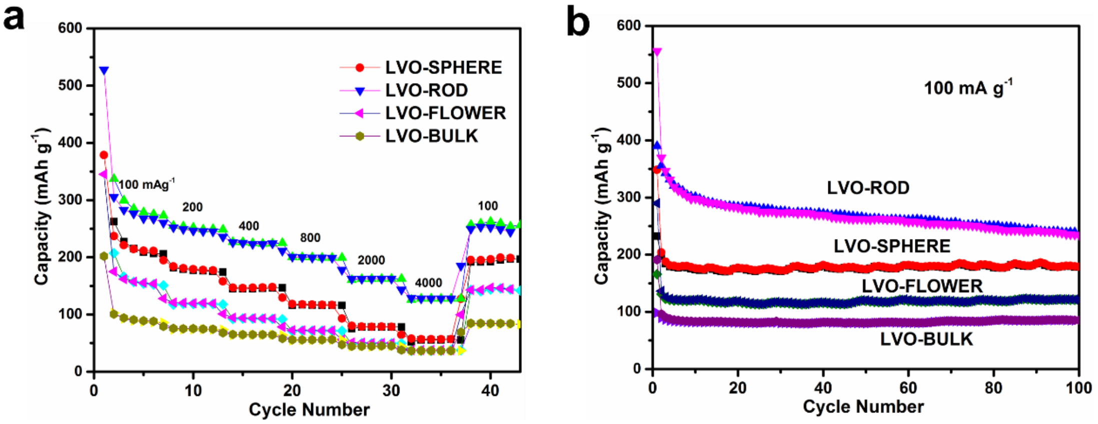

Figure 4.8 Lithium storage behavior (c) Comparative rate performance and (d) cycling performance of LVO-SPHERE, LVO-ROD, LVO-FLOWER, and LVO-BULK.

The improved electrochemical performance in LVO-ROD is attributed to its unique structure. Firstly, it has the smallest particle size that reduces the Li-ion diffusion length (Table 4.1). As seen in Figure 4.9, the particle size of single-crystal LVO-ROD is about 50–100 nm in diameter and 100-500 nm in length, which are all less than the dimensions of flower–shaped LVO-FLOWER (0.5-1 µm for primary particle size) and bulk-shaped LVO-BULK (~7 µm). Secondly, it is porous and provides the largest specific surface area that facilitates electrolyte diffusion.

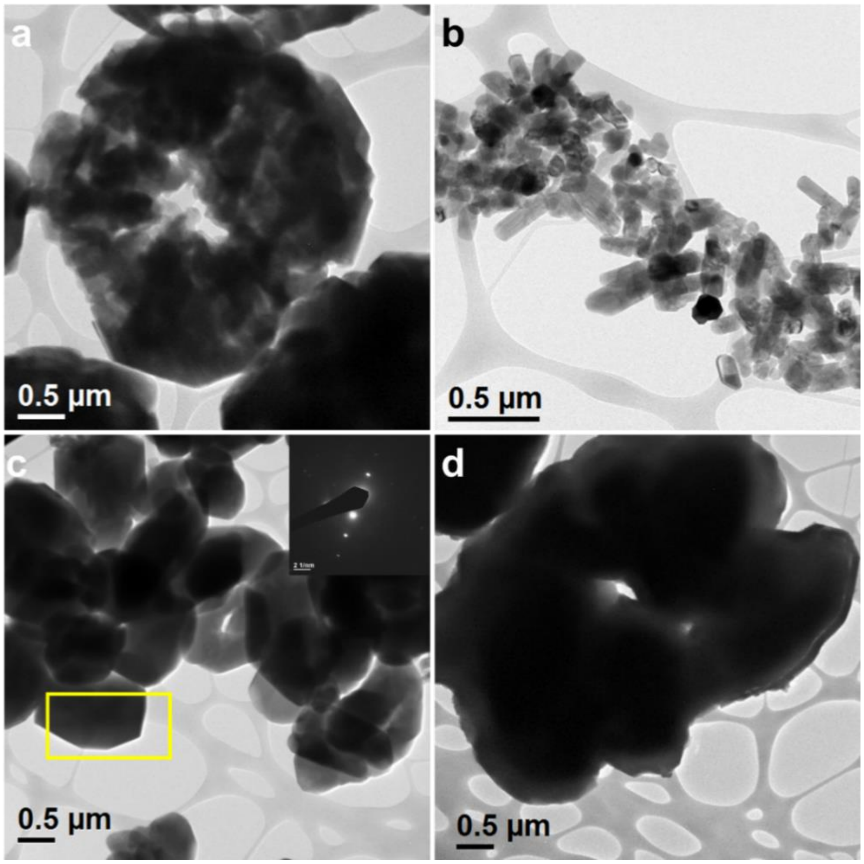

Figure 4.9 TEM images of (a) LVO-SPHERE, (b) LVO-ROD, (c) LVO-FLOWER, (d) LVO-BULK.

BET results (Figure 4.10 & Table 4.1) reveal that the specific surface area decrease in the sequential order of LVO-ROD > LVO-SPHERE > LVO-FLOWER > LVO-BULK, which is consistent with the trend of electrochemical performance. In addition, both LVO-SPHERE and LVO-ROD possess mesopores with the pore size distribution around 40 nm. LVO-ROD has the highest pore volume among the samples. LVO-SPHERE has a spherical-assembly structure. The relatively lower capacity compared to LVO-ROD probably due to its structure being less porous than LVO-ROD. In contrast, LVO-FLOWER has a wide pore size distribution between 50 and 120 nm. All these factors allow the electrochemical performance of LVO-ROD above others.

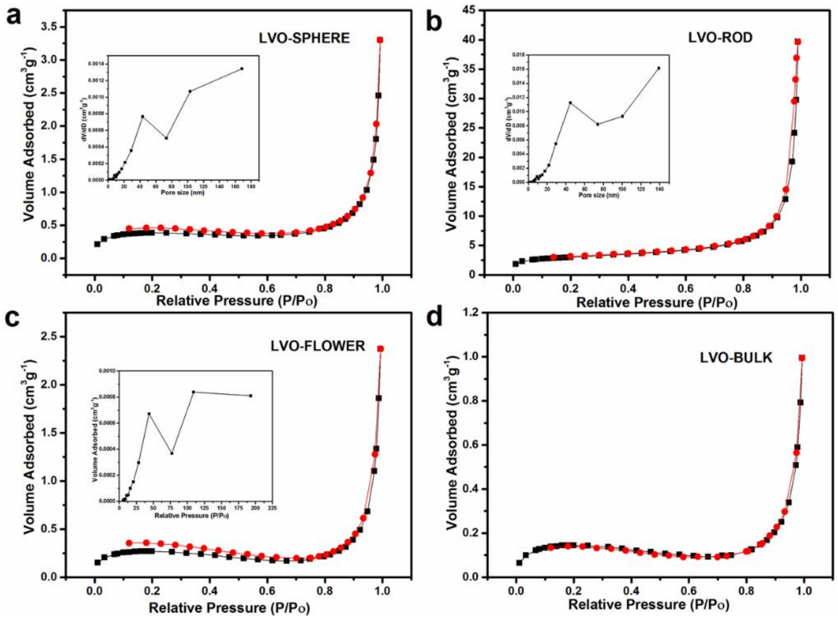

Figure 4.10 N2 adsorption-desorption isotherms of (a) LVO-SPHERE, (b) LVO-ROD, (c) LVO-LVO-FLOWER, (d) LVO-BULK.

EIS measurements and CV testing were carried out to shed more light on the kinetic properties of various LVO-based electrodes. In Figure 4.11, each EIS curve consists of a semicircle and an inclined line. R_1 in high frequency can be assigned to electrolyte resistance. While each semicircle comprises two compressed semicircles: resistance of SEI film (R_f) in the high frequency, and resistance of charge-transfer (R_{ct}) in the middle frequency [22, 47]. The Warburg impedance in low frequency is related to Li ion diffusion within the particles. Based on the fitted results from equivalent circuit model, the R_{ct} of LVO-SPHERE, LVO-ROD, LVO-FLOWER, and LVO-BULK are turned out to be 340, 76, 350 and 260 Ω, respectively (Table 4.3).

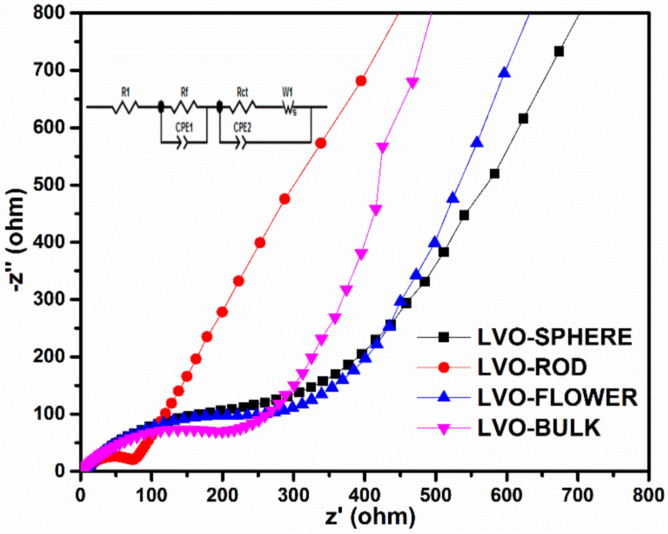

Figure 4.11 EIS spectra collected after 3 cycles of CV scanning.

Table 4.3 Equivalent circuit parameters and apparent Li ion diffusion coefficient calculated from CV rates

Sample	R_1 (Ω)	R_f (Ω)	R_{ct} (Ω)	D_{Li+} (cm^2s^{-1})
LVO-SPHERE	2.5	5.1	340	2.622×10^{-12}
LVO-ROD	2.4 2.8 $^{(100th\ cyc)}$	4.6 $15.5^{(100th\ cyc)}$	76 $180^{(100th\ cyc)}$	3.722×10^{-12}
LVO-FLOWER	2.6	7.8	350	4.114×10^{-13}
LVO-BULK	2.3	10.2	260	1.084×10^{-12}
C@LVO-ROD	2.7 $^{(100th\ cyc)}$	$10.1^{(100th\ cyc)}$	$110^{(100th\ cyc)}$	4.815×10^{-11}

LVO-ROD exhibits lowest R_{ct}, indicating a fastest charge-transfer process. This is further supported by CV testing under different sweep rates (Figure 4.12). The redox peak separation (voltage difference between anodic peak and cathode peak) increases gradually with sweep rate, implying the increasing polarization. The apparent lithium diffusion coefficient in various LVO-based electrodes can be calculated by the classical Randles-Sevchik equation:

$$I_p=(2.69x10^5)n^{3/2}AD_0^{1/2}C_0v^{1/2} \quad (1)$$

where I_p is the peak current, A the apparent surface area, D_0 the diffusion coefficient and ν the CV scanning rate and C_0 is the maximum Li^+ concentration (9.8×10^{-3} mol cm^{-3}).

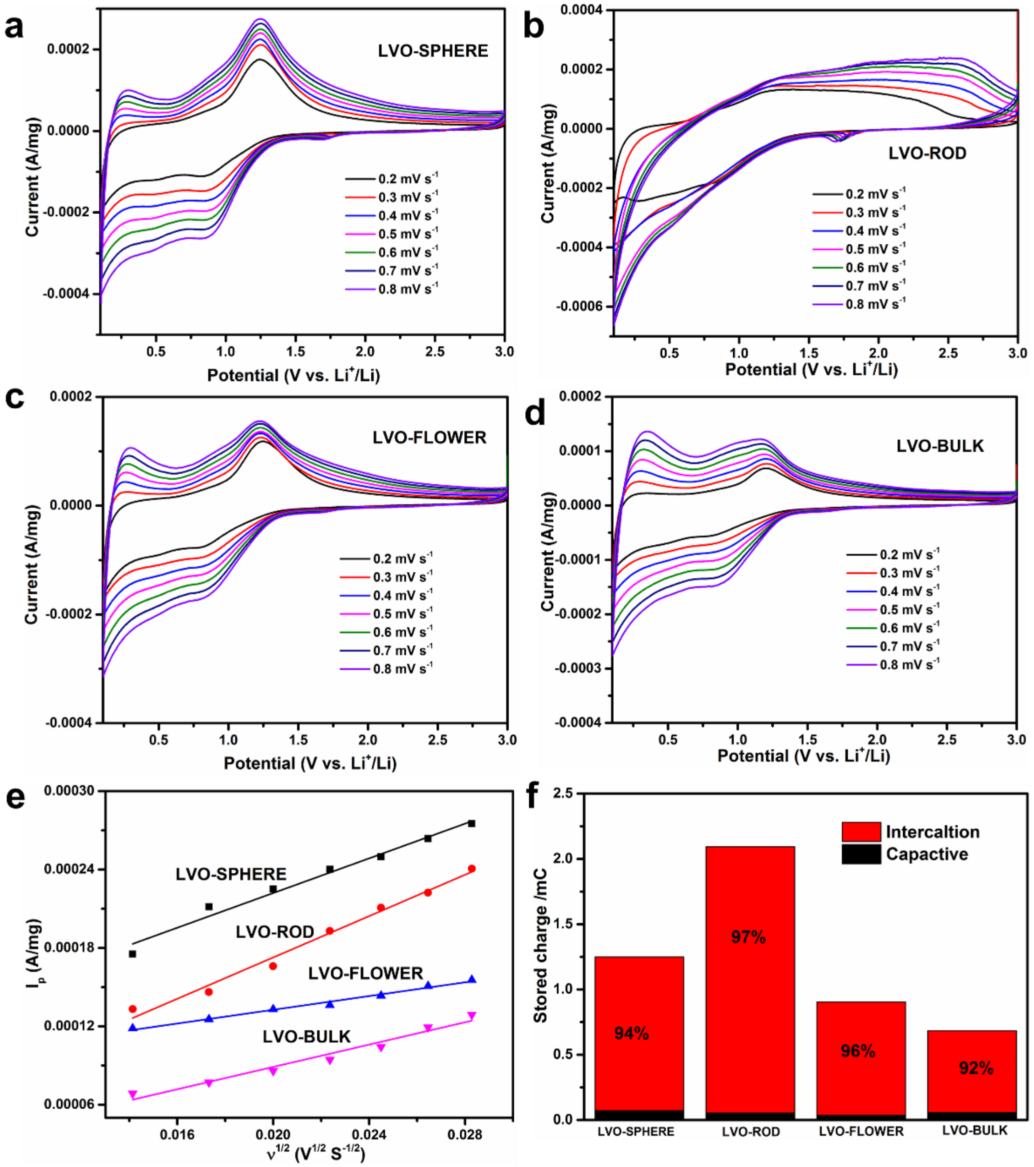

Figure 4.12 CV curves of (a) LVO-SPHERE; (b) LVO-ROD; (c) LVO-FLOWER; (d) LVO-BULK at different scan rates between 0.01 to 3.00 V; (e) Dependence of oxidation peak current on the square root of scan rate. (f) Bar chart showing total stored charge with percentage contribution from capacitive and intercalation at 0.2 mV/s for all samples with stored charge calculated by integrating the CV area according to the equation: $Q = \int \left(\frac{i}{v}\right) dV$ [48].

Figure 4.12e shows the linear relationship between the oxidation peaks Ip and the square root of the scan rate from 0.2 to 0.8 mV $s^{-1/2}$. The diffusion coefficient is calculated to be

3.722 x 10^{-12} cm^2 s^{-1} for LVO-ROD, which is higher than those of LVO-SPHERE, LVO-FLOWER, and LVO-BULK (Table 4.3). This enhanced kinetic contributes to the better performance of LVO-ROD. To further investigate the effect of different morphologies on the electrochemical performance, the total charge storage at a certain sweep rate was quantified on the basis of separating the specific contribution from the capacitive and diffusion-controlled charge at a fixed voltage [49]. The results (Figure 4.12) reveal that the LVO-ROD exhibits the highest intercalation effects contribution ratio (~97%), probably due to its good crystallinity and enhanced ion diffusion.

4.4 Conclusions

Spherical-assembly LVO-SPHERE, flower shape LVO-FLOWER, single-crystal LVO-ROD nanorods, and bulk LVO-BULK were prepared via a solvothermal synthesis method in different alcohols. The effect of LVO morphologies on the electrochemical performance was systematically investigated. The single-crystal LVO-ROD nanorods are found to be advantageous due to the unique 1D structure that is porous and has a small particle size. Therefore, the short lithium ion diffusion length and the large specific surface area facilitate high electron pathway. Further improvement in electrochemical performance was achieved by the surface carbon coating that allows the increase of the electronic conductivity and the suppression of the pulverization caused by volume change in LVO nanoparticles upon cycling. In addition, the findings from the present work promote a better understanding of the morphology controlled Lithium-ion storage in LVO, and provide insight for high-performance LVO-based electrode design.

References

[1] L. Croguennec, M.R. Palacin, J. Am. Chem. Soc., 137 (2015) 3140-3156.

[2] V. Aravindan, Y.S. Lee, S. Madhavi, Adv. Energy Mater., 5 (2015) 1402225.

[3] H.-K. Kim, S.-M. Bak, K.-B. Kim, Electrochem. Commun., 12 (2010) 1768-1771.

[4] L. Zhao, Y.S. Hu, H. Li, Z. Wang, L. Chen, Adv. Mater., 23 (2011) 1385-1388.

[5] L. Yu, H.B. Wu, X.W. Lou, Adv. Mater., 25 (2013) 2296-2300.

[6] E. Kang, Y.S. Jung, G.H. Kim, J. Chun, U. Wiesner, A.C. Dillon, J.K. Kim, J. Lee, Adv. Funct. Mater., 21 (2011) 4349-4357.

[7] J. Liu, K. Song, P.A. Van Aken, J. Maier, Y. Yu, Nano Letters, 14 (2014) 2597-2603.

[8] R.A. Armstrong, C. Lyness, P.M. Panchmatia, S.M. Islam, P.G. Bruce, Nat. Mater., 10 (2011) 223-229.

[9] R. Malini, U. Uma, T. Sheela, M. Ganesan, N.G. Renganathan, Ionics, 15 (2009) 301-307.

[10] P.G. Bruce, B. Scrosati, J.M. Tarascon, Angew. Chem. Int. Ed., 47 (2008) 2930-2946.

[11] H. Li, X. Liu, T. Zhai, D. Li, H. Zhou, Adv. Energy Mater., 3 (2013) 428-432.

[12] A. Manthiram, J. Phys. Chem. Lett., 2 (2011) 176-184.

[13] J. Lee, J. Moon, O.B. Chae, J. Lee, J. Ryu, M. Cho, K. Cho, S.M. Oh, Chem. Mater., 28 (2016) 5314-5320.

[14] H. Li, X. Liu, T. Zhai, D. Li, H. Zhou, Adv. Energy Mater., 3 (2013) 428-432.

[15] Z. Liang, Z. Lin, Y. Zhao, Y. Dong, Q. Kuang, X. Lin, X. Liu, D. Yan, J. Power Sources, 274 (2015) 345-354.

[16] X. Song, M. Jia, R. Chen, J. Mater. Process. Technol., 120 (2002) 21-25.

[17] K. Gaur, A.J. Pathak, H.B. Lal, J. Mater. Sci., 23 (1988) 4257-4262.

[18] E.M. Dompablo, P. Tartaj, M.J. Amarilla, U. Amador, Chem. Mater., 28 (2016) 5643–5651.

[19] S. Ni, J. Zhang, J. Ma, X. Yang, L. Zhang, X. Li, H. Zeng, Adv. Mater. Interfaces, 3 (2016) 1500340.

[20] C. Liao, Q. Zhang, T. Zhai, H. Li, H. Zhou, Energy Storage Mater., 7 (2017) 17-31.

[21] C. Zhang, H. Song, C. Liu, Y. Liu, C. Zhang, X. Nan, G. Cao, Adv. Funct. Mater., 25 (2015) 3497-3504.

[22] C. Zhang, C. Liu, X. Nan, H. Song, Y. Liu, C. Zhang, G. Cao, ACS Appl. Mater. Interfaces, 8 (2015) 680-688.

[23] S. Ni, X. Lv, J. Ma, X. Yang, L. Zhang, J. Power Sources, 248 (2014) 122-129.

[24] W.T. Kim, Y.U. Jeong, Y.J. Lee, Y.J. Kim, J.H. Song, J. Power Sources., 244 (2013) 557-560.

[25] Y. Shi, J.-Z.Z. Wang, S.-L.L. Chou, D. Wexler, H.-J.J. Li, K. Ozawa, H.-K.K. Liu, Y.-P.P. Wu, Nano Lett., 13 (2013) 4715-4720.

[26] J. Liu, P.J. Lu, S. Liang, J. Liu, W. Wang, M. Lei, S. Tang, Q. Yang, Nano Energy, 12 (2015) 709-724.

[27] Y. Dong, Y. Zhao, H. Duan, P. Singh, Q. Kuang, H. Peng, J. Power Sources, 319 (2016) 104-110.

[28] S. Hu, Y. Song, S. Yuan, H. Liu, Q. Xu, Y. Wang, J. Power Sources, 303 (2016) 333-339.

[29] J. Zhang, S. Ni, T. Kang, J. Tang, X. Yang, L. Zhang, J. Mater. Chem. A, 4 (2016) 14101-14105.

[30] D. Zhao, M. Cao, ACS Appl. Mater. Interfaces, 7 (2015) 25084–25093.

[31] Q. Li, J. Sheng, Q. Wei, Q. An, X. Wei, P. Zhang, L. Mai, Nanoscale, 6 (2014) 11072-11077.

[32] C. Zhang, H. Song, C. Liu, Y. Liu, C. Zhang, X. Nan, G. Cao, Advanced Functional Materials, 25 (2015) 3497-3504.

[33] S. Ni, X. Lv, J. Ma, X. Yang, L. Zhang, Electrochim. Acta, 130 (2014) 800-804.

[34] S. Ni, J. Zhang, J. Ma, X. Yang, L. Zhang, J. Mater. Chem. A, 3 (2015) 17951-17955.

[35] G. Wang, J. Roos, D. Brinkmann, M. Pasquali, G. Pistoia, J. Phys. Chem. Solids, 54 (1993) 851-855.

[36] D.J. Kim, B.E. Jun, C.S. Kim, H.K. Kim, J.N. Kim, Y.H. Hwang, J. Appl. Phys., 93 (2003) 1697-1700.

[37] P. Goel, M. Arora, RSC Adv., 5 (2015) 29741-29747.

[38] J. Liu, Z. Chen, S. Chen, B. Zhang, J. Wang, H. Wang, B. Tian, M. Chen, X. Fan, Y. Huang, T.C. Sum, J. Lin, Z.X. Shen, ACS Nano, 11 (2017) 6911-6920.

[39] N.V. Kosova, D.O. Rezepova, A.B. Slobodyuk, Electrochim. Acta, 167 (2015) 75-83.

[40] L. Shao, K. Wu, X. Lin, M. Shui, R. Ma, D. Wang, Ceram. Int., 40 (2014) 6115-6125.

[41] X. Zhou, G. Wu, J. Wu, H. Yang, J. Wang, G. Gao, J. Mater. Chem. A, 1 (2013) 15459-15468.

[42] P. Pookmanee, S. Kojinok, R. Puntharod, J. Ferroelectrics, 456 (2013) 45-54.

[43] E. Pohjalainen, T. Rauhala, M. Valkeapää, J. Kallioinen, T. Kallio, J. Phys. Chem. C, 119 (2015) 2277-2283.

[44] M. Ma, H. Wang, S. Liang, S. Guo, Y. Zhang, X. Du, Electrochim. Acta 256 (2017) 110-118.

[45] M. Ma, H. Wang, M. Niu, L. Su, X. Fan, J. Deng, Y. Zhang, X. Du, RSC Adv., 6 (2016) 43316-43321.

[46] L. Shen, H. Lv, S. Chen, P. Kopold, P.A. van Aken, X. Wu, J. Maier, Y. Yu, Adv. Mater., 29 (2017) 1700142.

[47] Y. Yang, J. Li, D. Chen, J. Zhao, J. Electrochem. Soc., 164 (2017) A6001-A6006.

[48] (!!! INVALID CITATION !!!).

[49] J. Liu, J. Wang, C. Xu, H. Jiang, C. Li, L. Zhang, J. Lin, Z.X. Shen, Adv.Sci., (2017) 1700322.

Chapter 5

Carbon-coated Li_3VO_4 microspheres

In this work, morphology controllable orthorhombic Li_3VO_4 *has been synthesized by tuning the solvent composition (volume ratios of ethanol to deionized water) in a solvothermal approach. The resulting* Li_3VO_4 *samples with various morphologies (nanorod-shaped particle, self-assembled hierarchical microsphere, cube-like particle, sheet-like structure) show different electrochemical performances when employed as anodes for Li-ion battery applications. The* Li_3VO_4 *with the self-assembled hierarchical microsphere morphology (volume ratio of ethanol to deionized water at 15:15) exhibits the best electrochemical performance. Furthermore, the subsequent carbon coating process on the microsphere sample has significantly improved the capacities at both low (350 to 430 mAh* g^{-1} *at 100 mA* g^{-1}*) and high current (180 to 350 mAh* g^{-1} *at 2 A* g^{-1}*) conditions with excellent cycling stability as well.*

*This section is published in Yang, G et al. International Journal of Hydrogen Energy 2017, 42, 22167-22174.

5.1 Introduction

Lithium-ion batteries (LIBs) are considered as promising energy storage devices for various applications ranging from portable consumer electronics to electric vehicles because of the high energy density and decent power capability [1, 2]. However, the current commercial graphitic anode has a relatively low specific capacity (372 mAh g^{-1}) and a low voltage plateau (< 0.1 V *vs.* Li^+/Li); the low voltage could cause Li-plating upon operation at high current, which is one major setback for graphitic materials. Therefore, intense research is on to find a better alternative to graphite. Conversion and alloy type materials are well-known alternatives because of their high specific capacities [3-5]. However, conversion type materials exhibit large voltage hysteresis, volume variation, relatively higher redox potential and poor cycling stability [6, 7]. Alloy type materials suffer from huge volume change during charging/discharging process and poor cyclability; for instance, Si has a volume change of more than 300% during cycling [8, 9], which generates high mechanical stress that eventually causes the active material to detach from the current collector, leading to the drastic capacity fading [10]. Thus, intercalation type materials are still ideal candidates owing to the negligible volume change, which ensures structural integrity, good reversibility, and high coulombic efficiency of the electrode. Besides graphite, $Li_4Ti_5O_{12}$ is another intercalation type material known for its low volume change and high reversibility. However, the high insertion potential (about 1.5 V vs. Li^+/Li) and low capacity (~150 mAh g^{-1}) of $Li_4Ti_5O_{12}$ restrict its application [11-13].

Recently, Li_3VO_4 (denoted as LVO) anode with β-polymorph has been reported as a promising insertion type material to replace graphite and $Li_4Ti_5O_{12}$. It can accommodate up to two moles of Li, corresponding to a theoretical capacity of 395 mAh g^{-1}, which is higher than that of $Li_4Ti_5O_{12}$ [14]. Besides its high capacity, LVO also has an appropriate voltage window (0.5–0.8 V vs. Li^+/Li), which avoids the safety issue associated with the formation of Li dendrites and guarantees high voltage of the full cell [15, 16]. Thus, these advantages make LVO a promising anode material among the currently studied materials and extensive research has been conducted on this material [16-21]. To obtain the electrochemical performance of LVO, it is widely accepted that controlling the morphology (i.e., particle size, shape, and dimensionality of LVO) can be feasible. For instance, Li *et al.* prepared a hollow shell-controlled LVO *via* a self-template method, where the thickness of LVO shell can be controlled by adjusting the volume ratio of water and ethylene glycol. The thickness of the shell could affect the final electrochemical activity [22]. Recently, Tartaj *et al.* reported an aerosol spray approach to produce LVO colloidal aggregates with different morphology (spheres and platelet-like) using different reactants, where the spheres outperform the platelets in terms of electrochemical capabilities [19]. This clearly suggests that the electrochemical response of LVO is strongly dependent on morphology. Therefore, morphology control is very important to achieve high performance.

Apart from the controlling the morphology, improving the electronic conductivity of LVO is another approach of improving electrochemical performance [23-25]. Many methods like wrapping with graphene nanosheets and coating with conductive Ni have been proven effective in improving the electrochemical performance of LVO [23-28]; however, these methods are difficult to realize when it comes to reality. Conventional carbon coating is still one of the most widely used methods because of its low cost and high effectiveness [29].

In the present work, we report a facile solvothermal approach to yield LVO using mixed solvents of deionized water (DIW) and absolute ethanol (EtOH). The morphology of LVO greatly changes while tuning the volume ratio of EtOH/DIW. nanorod-shaped particle, self-assembled hierarchical microsphere, cube-like particle, sheet-like structure are obtained when the volume ratios of EtOH to DIW range from 30:0, 20:10, 15:15, 10:20 to 0:30. The Li-storage properties are studied in half-cell assembly, and the sample with self-assembled hierarchical microsphere (volume ratio of EtOH to DIW water at 15-15) demonstrates the best performance. The structural characteristics and morphology of the carbon coated and carbon-free 15-15 samples were characterized using XRD, field emission scanning electron microscopy (FE-SEM) and high-resolution transmission electron microscopy (HR-TEM). The electrochemical performance of the carbon-free 15-15 and carbon coated 15-15 in the potential range of 0.1–3.0 V was also systematically investigated and described in detail.

5.2 Experimental section

5.2.1 Synthesis of Li_3VO_4

The details are seen in Chapter 3.5.

5.2.2 Materials characterization

The crystal structure and microstructures were examined by powder X-ray diffraction (XRD, Bruker D8 with Cu Kα radiation), SEM, JEOL JSM-7600, Japan and high-resolution Transmission electron microscopy (HR-TEM, JEOL JEM-2100F) at the electron beam energy of 200 kV, respectively. Raman spectra was obtained with a WITecCRM200 Raman system (WITec, Germany) with a laser wavelength of 532 nm (2.33 eV). The galvanostatic charge–discharge cycling test was conducted at 25 °C between 0.1 and 3.0 V *vs.* Li under various current densities with Neware battery testing system (Neware, BTS-5V10mA, China). Cyclic voltammetry (CV) was performed by using an electrochemical workstation (Autolab, PGSTAT302N) with a scan rate of 0.2 mV s^{-1} over 0.1 to 3.0 V *vs.* Li^+/Li) applied to the test cells.

5.2.3 Electrochemical Characterization

All the electrochemical studies of LVO were examined in CR2016 - coin cells. The electrodes were prepared by mixing 70 wt. % active materials, 20 wt. % Super P (Timcal) and 10 wt. % binder (PVDF Kynar) in N-methyl-pyrrolidinone (NMP, Sigma Aldrich) to form a homogeneous slurry and coated on Cu foil by the doctor blade technique. The electrode was subsequently dried at 60 °C for 2 h and 120 °C for 10 h in a vacuum oven before being assembled into a coin cell in an Ar-filled glovebox (MBraun, Germany) with oxygen and water content less than 1 ppm. The mass loading was about 0.8–1 mg cm^{-2}. Lithium metal was served as a counter and reference electrode in half-cell configuration. Celgard 2400 was used as a separator and filled with 1 M solution of $LiPF_6$ dissolved in ethylene carbonate/diethylene carbonate (EC:DEC = 1:1 by volume, Charslton

Technologies Pte. Ltd.) was used as the electrolyte. The specific capacity for carbon-coated composite was calculated based on the total weight including LVO and amorphous carbon.

5.3 Results and discussion

5.3.1 Synthesis and characterization of LVO with various morphologies

The morphologies of as-synthesized LVO samples at various EtOH/DI water ratio of 30:0, 20:10, 15:15, 10:20 and 0:30 were examined using FE-SEM with the results shown in Figure 5.1. As can be seen, when 30 mL ethanol is used as solvent without DIW, spherical particles with size around 1 µm are formed (Figure 5.1a). The obtained particles appear nanorod-like rods with the addition of EtOH/DIW at a volume ratio of 20:10 (Figure 5.1b). Self-assembled hierarchical microspheres, consisting of many small primary particles, are produced when the EtOH/DIW ratio is reduced to 15:15 (Figure 5.1c and d). Lowing EtOH/DIW ratio down to 10:20 results in the formation of cubic-like LVO particles with the size of around 4 µm (Figure 5.1e). LVO particles become super large with sheet-like structure when the EtOH/DIW ratio is further reduced to 0:30 (Figure 5.1f). Apparently, the particle size increases with the increase of the content of DIW except for the first sample. Since the first sample was prepared using 30 ml EtOH as a solvent, the phase is not pure. Further discussion of this is carried out in the XRD section. Meanwhile, it is proved that there are several morphologies of LVO and is dependent on the solvent and volume ratio. The different volume ratio of the solvents provides different polarities and saturated vapor pressures, which enables the formation of these diverse morphologies. The amount of individual nucleus formation, the amalgamation, and the direction of preferential growth of the nucleus are largely affected by the solvents. Solvents with a high degree of supersaturation favor multi-dimensional growth because they are most affected by the polarity and solubility, whilst anisotropic low dimensional growth is favored at low supersaturation [30, 31]. Solvent polarity and metal salts' solubility in solvent are affected by mixing different amount of alcohol and water as solvent. This is proved by the fact that the bulk LVO can be produced in pure DIW.

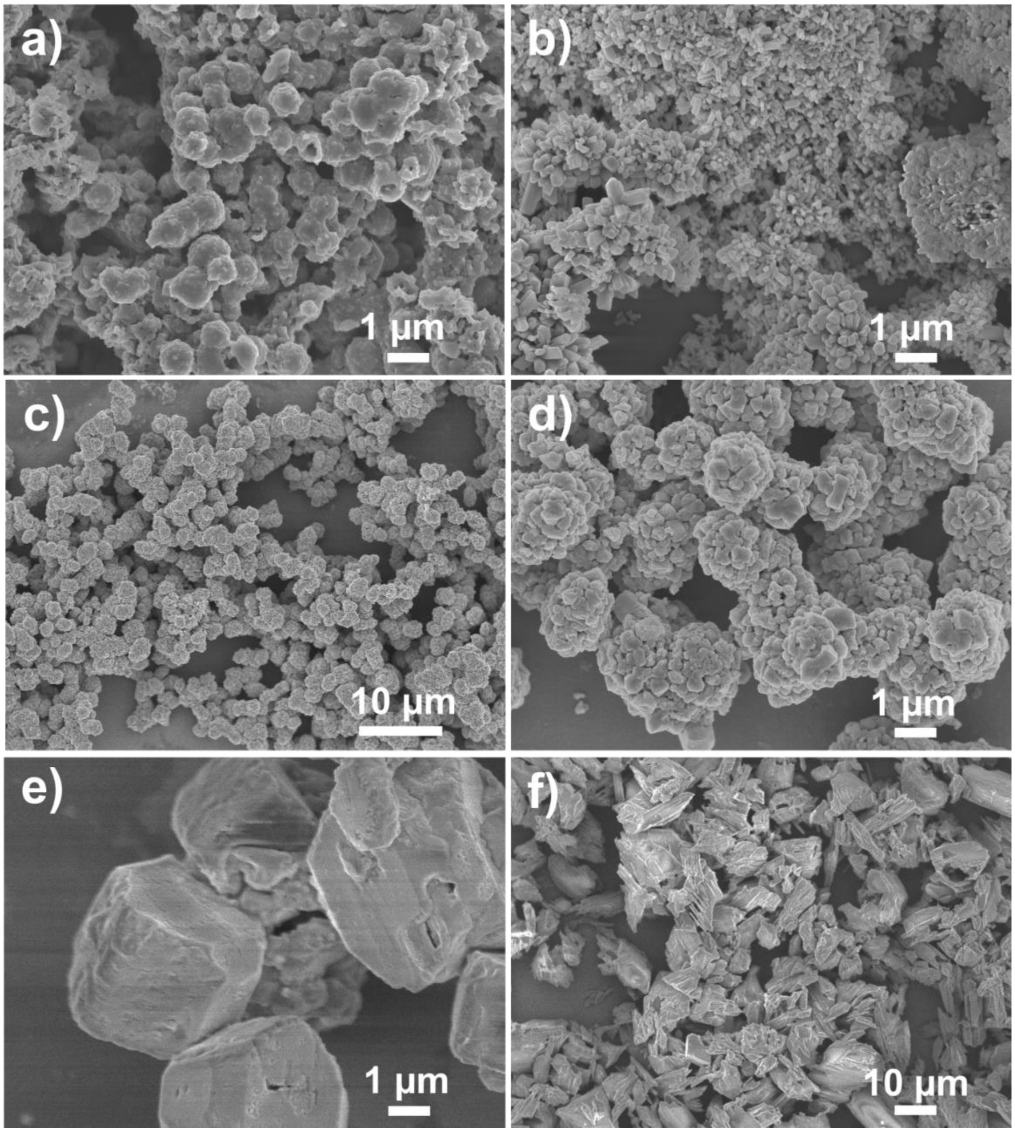

Figure 5.1 SEM images of Li$_3$VO$_4$ at: a) 30-0 (V:Li=2:6 volume ratio of EtOH:DI water=30:0) ; b)20-10 (V:Li=2:6 the volume ratio of EtOH:DIW=20:10); c,d) 15-15 (V:Li=2:6 volume ratio of EtOH:DIW=15:15) at different magnification; e) 10-20 (V:Li=2:6 the volume ratio of EtOH:DIW=10:20); f) 0-30 (V:Li=2:6 the volume ratio of EtOH:DIW=0:30). The total volume of EtOH and DIW is 30 mL.

Figure 5.2 shows the XRD patterns of LVO prepared at different EtOH/DIW ratios. The reaction temperature and time are set at 180 °C and 4 h, respectively. Samples prepared at EtOH/DIW volume ratios of 20:10, 15:15, 10:20, and 0:30 are identified to be pure phase LVO, and all the sharp reflections in XRD patterns are generated from Li$_3$VO$_4$ orthorhombic phase with lattice constants a = 6.319 Å, b= 5.448 Å, and c =4.940 Å (JCPDS

NO. 38-1247). However, a secondary phase of $LiVO_3$ presents when the ratio of EtOH/DIW is 30:0. This may be due to NH_4VO_3 that does not fully dissolved in absolute ethanol even at 180 °C. With the increase of ethanol content, the intensity of overall peaks is depressed, indicating the reduction of crystallinity.

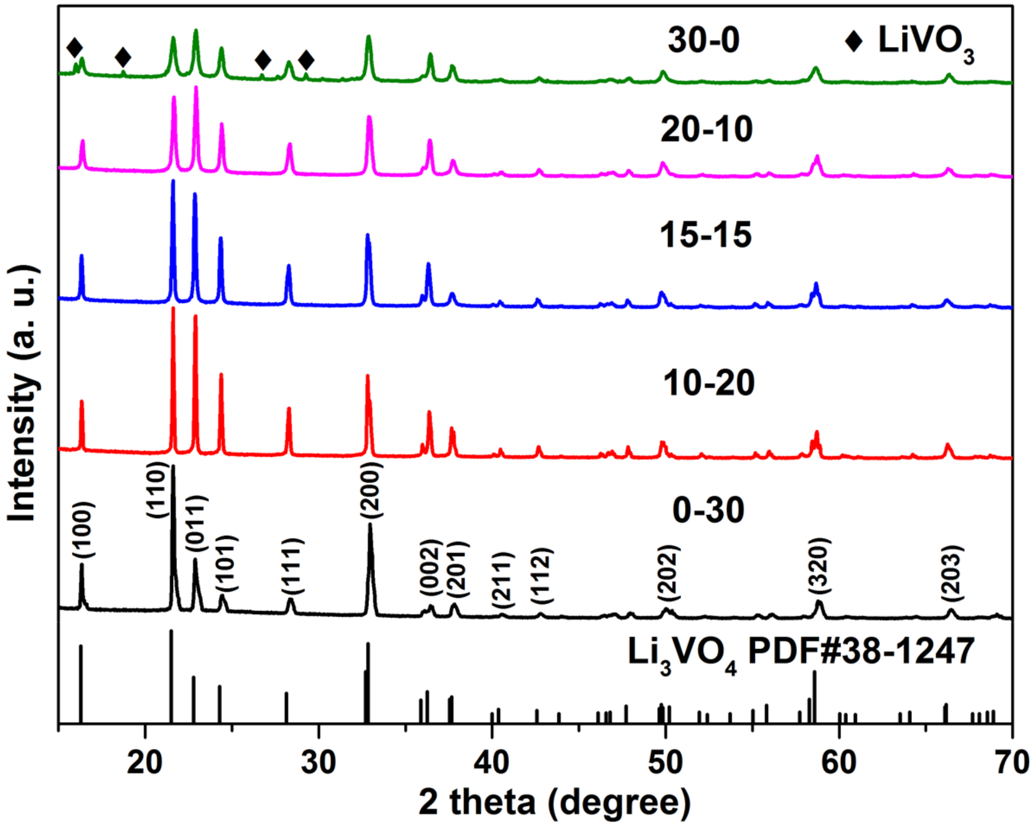

Figure 5.2 XRD patterns of the LVO particles synthesized at 0-30, 10-20, 15-15, 20-10 and 30-0 (the volume ratio of EtOH and deionized water (DIW)).

Since LVO is soluble in DIW (seen Figure 5.3), methanol was used to wash away the excess LiOH. It is worth noting that LiOH has a much higher solubility (9.76 g/100 g > 2.36 g/100 g) in methanol than in ethanol. The morphology after washing with DIW and methanol was imaged in an SEM and is shown in Figure 5.3c-d, where 4 µm-sized particles are etched and appear as flake-like shapes within only 1 min of washing period followed by sonication of 1 min. The dissolution of LVO in DIW has been also reported previously [22, 25].

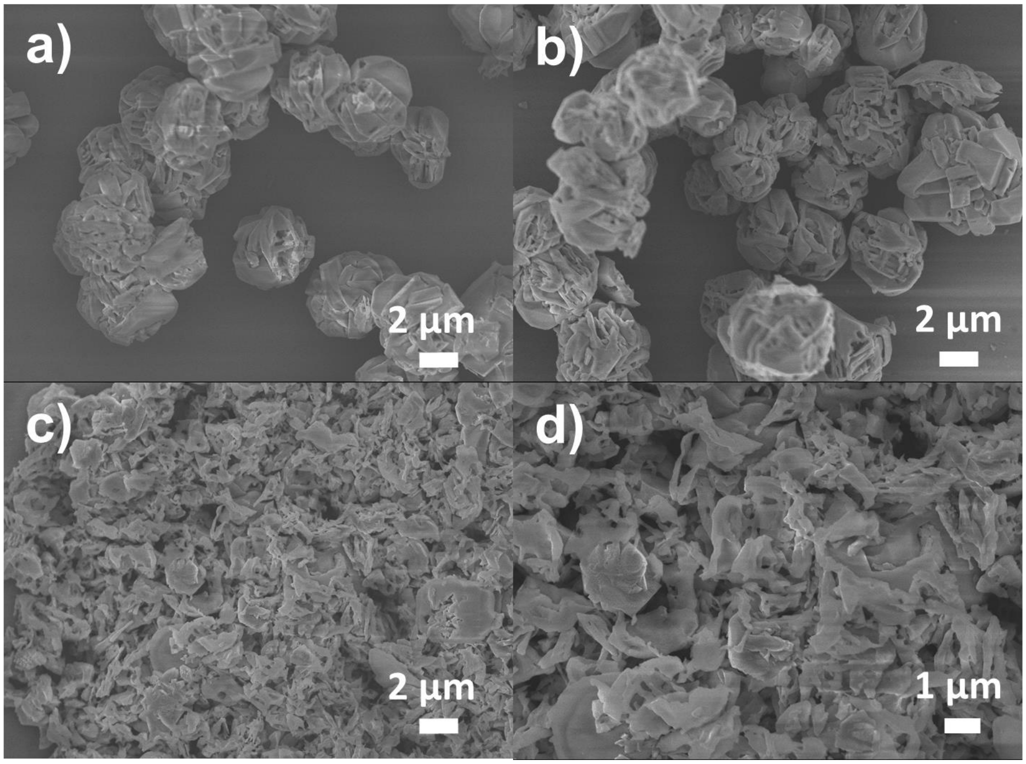

Figure 5.3 SEM images of the as-synthesized LVO (EtOH:DI water 0:30, Li/V=36:2) through solvothermal synthesis and washed with Methanol and DI water: a) As-prepared LVO; b) Washed with methanol for 1 min and sonication for 1 min; c)Washed with DI water for 1 min and sonication for 1 min; d) High magnification of image C.

5.3.2 Comparison of electrochemical performance of LVO Microsphere with other morphologies

The lithium storage performance of samples as anode materials for LIBs was evaluated by half-cells. Cyclic voltammetry (CV) of the EtOH/DIW ratio of 15-15 for the first three cycles was performed at a scan rate of 0.2 mV s^{-1} in the voltage range of 0.1–3 V, as shown in Figure 4.8a. Figure 5.3b-e shows the CVs of other samples with the different EtOH/DIW ratios, i.e., 0-30, 10-20, 20-10, and 30-0. The 1st cycle is apparently different from the subsequent two cycles for all 5 samples, which is usually ascribed to the occurrence of side reaction on the electrode surfaces and interfaces and the formation of SEI (solid electrolyte interface) film. The two reduction peaks around 0.87 V and 0.54 V after the first cycle are attributed to the insertion of lithium ions to Li_3VO_4. As a result, V^{5+} is reduced to V^{3+} [15, 32]. Also, the broader oxidation peak around 1.35 V in all cycles is related to the desertion of lithium ions from Li_3VO_4, i.e., the oxidation of V^{3+} to V^{5+}.

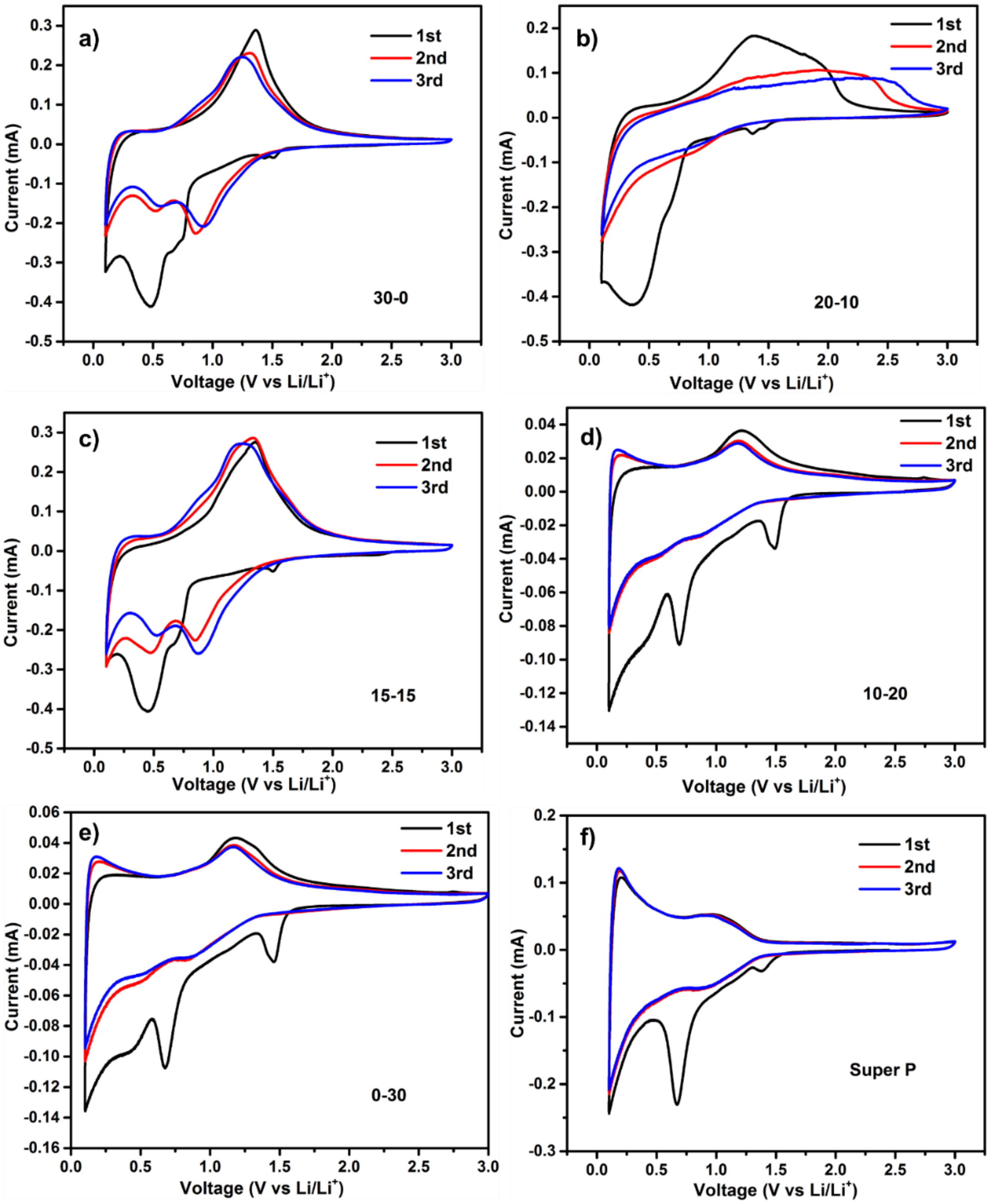

Figure 5.4 First three Cyclic voltammetry (CVs) of LVO: a) 30-0 (LVO prepared from Li:V=2:6, V_{EtOH}:V_{water}=30:0); b) 20-10 (LVO prepared from Li:V=2:6, V_{EtOH}:V_{water}=20:10); c) 15-15 (LVO prepared from Li:V=2:6, V_{EtOH}:V_{water}=15:15); d) 10-20 (LVO prepared from Li:V=2:6, V_{EtOH}:V_{water}=10:20); e) 0-30 (LVO prepared from Li:V=2:6, V_{EtOH}:V_{water}=0:30); f) Super P in the first three cycles at a scanning rate of 0.2 mV s^{-1} in the voltage range from 0.1 to 3 V.

It is noteworthy that the oxidation peaks from the first to third cycles almost overlap, indicating the high reversibility. More importantly, both samples with the EtOH/DIW ratios of 15-15 and 30-0 have a current that is about 10 times higher than that of the samples with EtOH/DIW ratios of the 10-20 and 0-30. The cathodic peak at around 1.5 V is related to conductive carbon Super P, which can be observed in Figure 5.4f, where the CV of Super P is scanned. Figure 5.5 shows the typical galvanostatic discharge–charge curves of two samples with EtOH/DIW ratios of 15-15 and 30-0 at a current density of 100 mA g^{-1} between 3.0 to 0.2 V. The sample with the EtOH/DIW ratio of 15-15 has a higher capacity and a relatively longer plateau from the 2^{nd} cycle onwards than the sample with the EtOH/DIW ratio of 30-0, which is consistent with the CV measurements.

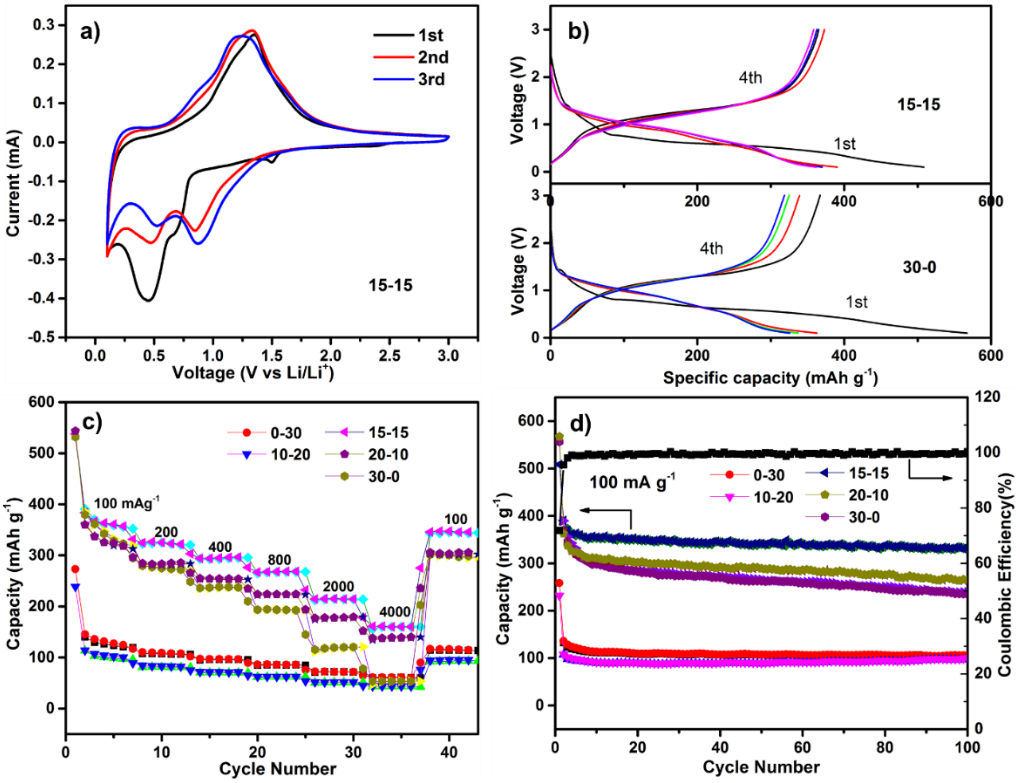

Figure 5.5 (a) First three CV cycles of 15-15; (b) Galvanostatic discharge–charge profiles of 15-15 and 30-0 for the first four cycles at a current rate of 0.1 A g^{-1} in the voltage range of 0.1–3.0 V vs. Li^+/Li; (c) Rate performance of 0-30, 10-20, 15-15, 20-10 and 30-0 (the volume ratio of EtOH and DIW) at varying current densities from 0.1 to 4 A g^{-1} in the voltage range of 0.1–3.0 V vs. Li^+/Li; (d) Cycling performance of 0-30, 10-20, 15-15, 20-10 and 30-0 at 100 mA g^{-1}.

The rate performance of 0-30, 10-20, 15-15, 20-10 and 30-0 samples were evaluated by charge-discharge at various current densities from 100 to 4000 mA g^{-1} (Figure 5.5C). With the increase of current density, the capacity drops due to the higher polarization and the electrochemical reaction performed only by the surface of the active material. In comparison, 15-15 exhibits the best performance among all the samples prepared from volume ratio of EtOH and DIW. This result is consistent with the CVs results (Figure 5.5a) and cycling performance in Figure 5.5d. It is noted that the capacity is restored to the initial value when the current density is abruptly reduced to 100 mA g^{-1} after the high current discharge–charge measurements, indicating high reversibility. Cycling performance is another critical factor for anode materials in the practical applications. Figure 5.5d shows the cycling performance at a moderate current density of 100 mA g^{-1} for 100 cycles. Sample 15-15 shows the highest capacity and stability among all the samples tested.

5.4.1 Carbon coating effect on electrochemical performance of LVO microspheres

To improve the performance of 15-15, carbon coating process was conducted using PVP as carbon source and EtOH as a solvent. From Figure 5.6a and Figure 5.6c, the low magnification TEM images of both 15-15 and C 15-15 demonstrate that the microsphere particles are clustered as a number of small particles. HR-TEM images (Figure 5.6b and d) indicated that the microspheres are polycrystalline clearly covered by amorphous carbon (Figure 5.6d).

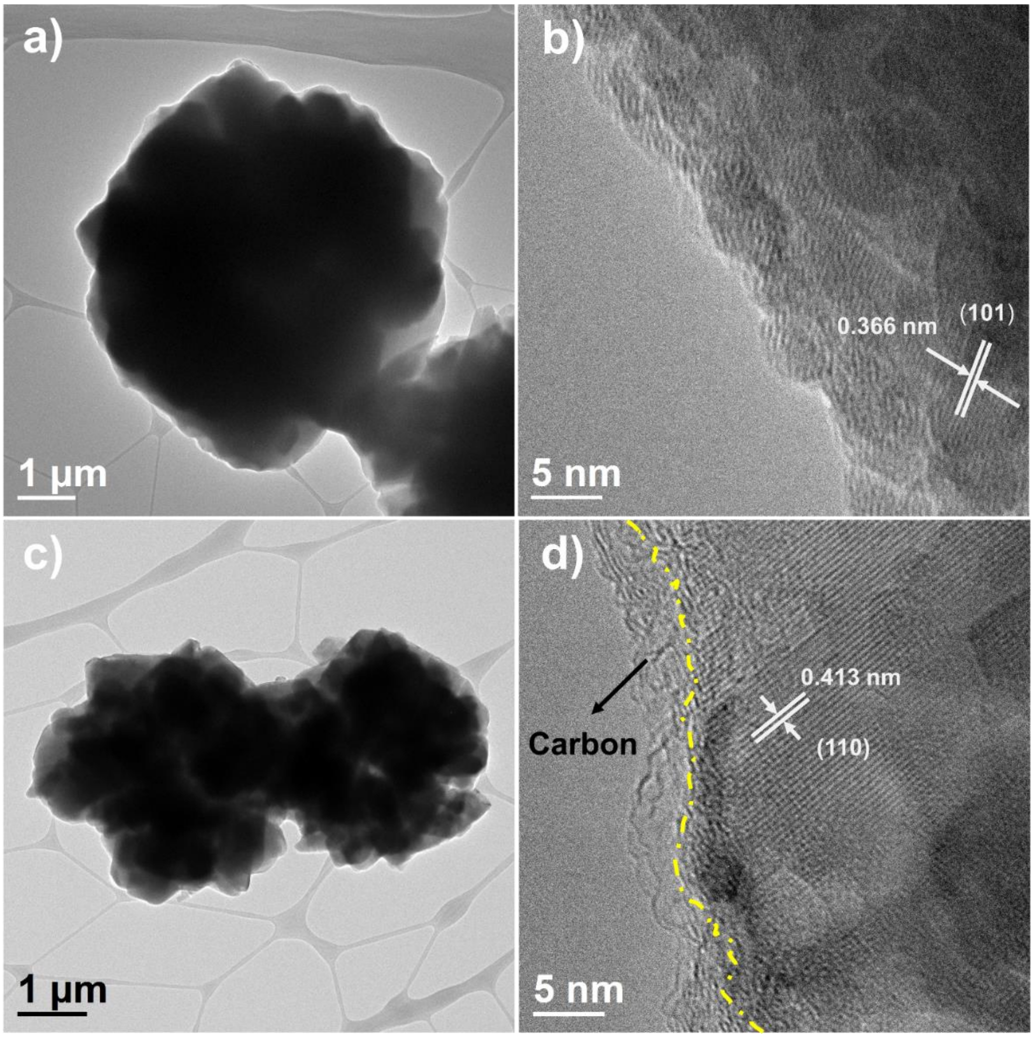

Figure 5.6 TEM images confirm the carbon coating. (a and b) TEM and HR-TEM images of the pristine 15-15 before carbon coating; (c and d) TEM and HR-TEM images of the carbon-coated 15-15 (C 15-15).

Figure 5.7a shows the XRD patterns for 15-15 before and after carbon coating. Figure 5.7b is the Raman spectrum of the products, which shows a weak peak at 824 cm^{-1} associated with the vibration of Li_3VO_4 crystal lattice and two strong peaks at 1358 and 1601 cm^{-1} that correspond to the disorder (D-band) and graphitic (C-band) phases of carbon, respectively [33]. These results indicate that Li_3VO_4/C composite architectures were successfully synthesized.

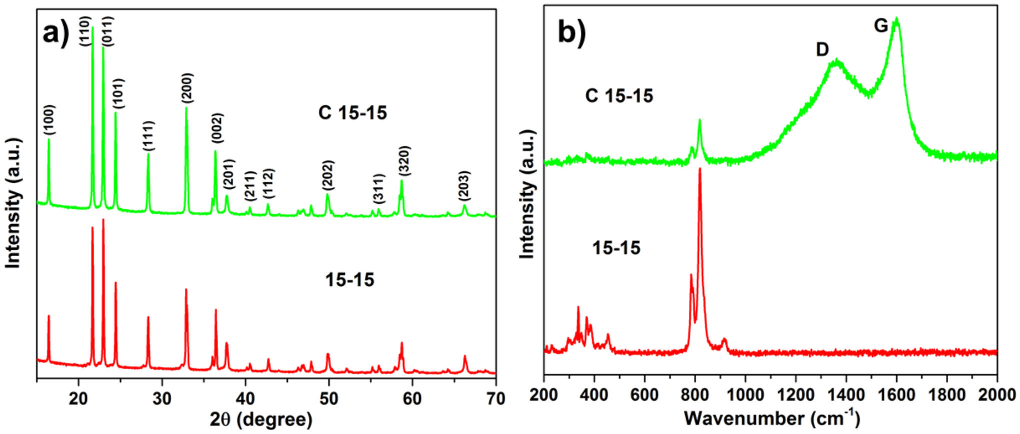

Figure 5.7 (a) XRD patterns for coated and uncoated 15-15; (b) Raman spectra of the coated and carbon free 15-15.

Thermal analysis was employed to study the composition of the C 15-15 in the air. Figure 5.8 shows the TG of the C-coated 15-15. The weight loss below 200 °C can be ascribed to the elimination of absorbed waters, and the weight in temperature region 200–800 °C corresponds to the burning of carbon. Thus, the weight of carbon can be estimated to be 14 wt. % in the C 15-15.

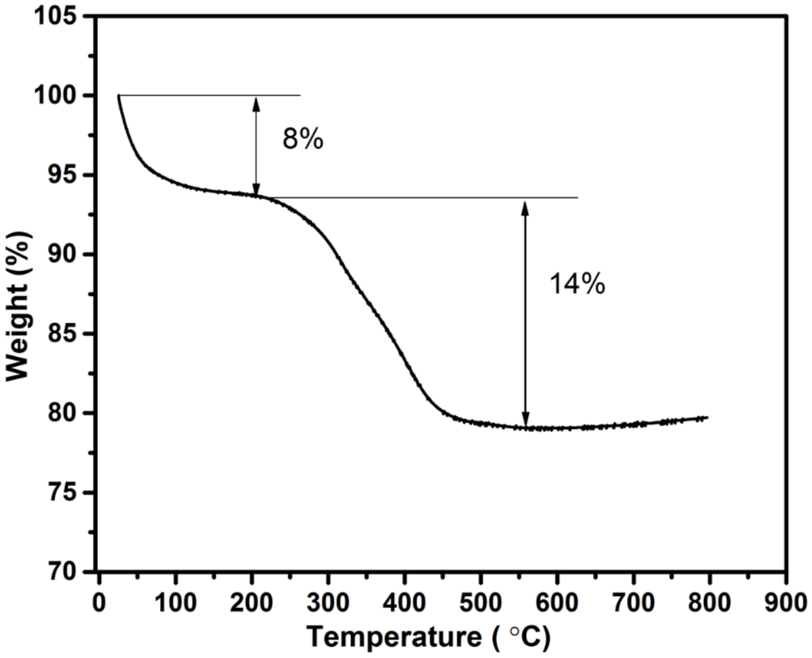

Figure 5.8 TGA curves of C 15-15(carbon coated Li_3VO_4 at a volume ratio of EtOH:DI at 15-15).

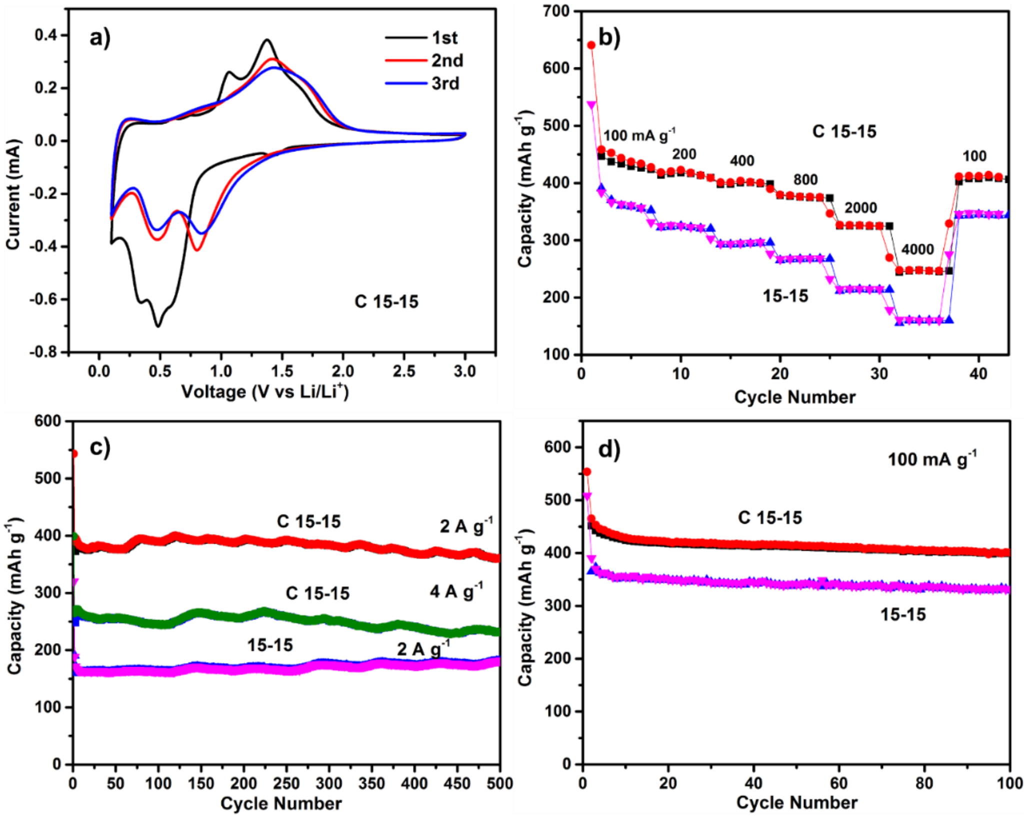

Figure 5.9 (a) First three CV cycles of carbon coated 15-15 (C 15-15); (b) Rate performance of 15-15 and C 15-15 at varied current densities from 0.1 to 4 A g^{-1} in the voltage range of 0.1–3.0 V vs Li^+/Li; (c) Cycling performance of C 15-15 and 15-15 at 2 and 4 A g^{-1}; (d) Cycling performance of 15-15 and C 15-15 at 100 mA g^{-1}.

The electrochemical performance of 15-15 and carbon coated 15-15 are further investigated. Figure 5.9a shows the CV curves of C 15-15, where the main reduction peak is visible at about 0.5 V and two oxidation peaks at about 1.07 and 1.35 V. The 1.07 V oxidation peak disappears after the 1st cycles, which is similar to previous reports [15, 34]. The almost overlapping 2nd and 3rd CV cycles indicate good cycling stability. Additionally, C 15-15 has a slightly higher current density on the CV curves, which was verified by EIS measurements. The impedance of the C 15-15 and 15-15 electrodes after 3 CV cycles were evaluated and the typical Nyquist plots are displayed in Figure 5.10. The EIS spectra consists of a medium-to-high-frequency compressed semicircle, describing the charge transfer resistance (Rct) and a low-frequency tail corresponding to the Warburg impedance related to the Li^+ ions diffusion within the particles. As clearly seen, C 15-15 has a semicircle with a smaller diameter compared to that of 15-15, indicating the lower Rct for C 15-15 electrode. The rate performance is also evaluated and the capacities are measured to be 430, 420, 400, 380, 324, and 250 mAh g^{-1} at rates of 100, 200, 400, 800, 2000, and 4000 mA g^{-1}, respectively (Figure 5.9b). When the current density finally returns to 100 mA g^{-1}, the charge capacity recovers to 430 mAh g^{-1}, indicating the excellent rate capability of the C 15-15. Compared with the 15-15, C 15-15 shows higher capacities at various rates. Moreover, for C 15-15, at the current densities of 100 mA g^{-1}, discharge capacity of 430 mAh g^{-1} is maintained after 100 cycles, higher than 350 mAh g^{-1} of bare 15-15 (Figure 5.9d). Even at a higher current density of 2 A g^{-1}, the C 15-15 electrode delivers a capacity as high as 350 mA g^{-1}, which is much higher than 180 mAh g^{-1} of 15-15 at the same current density of 2 A g^{-1}. In addition, when a current density of 4 A g^{-1} is used, C 15-15 still can have a capacity of 230 mAh g^{-1} even after 500 cycles. This result supports the fact that carbon coated 15-15 could successfully enhance electronic/ionic transport within the anode, thus resulting in improved electrochemical kinetics.

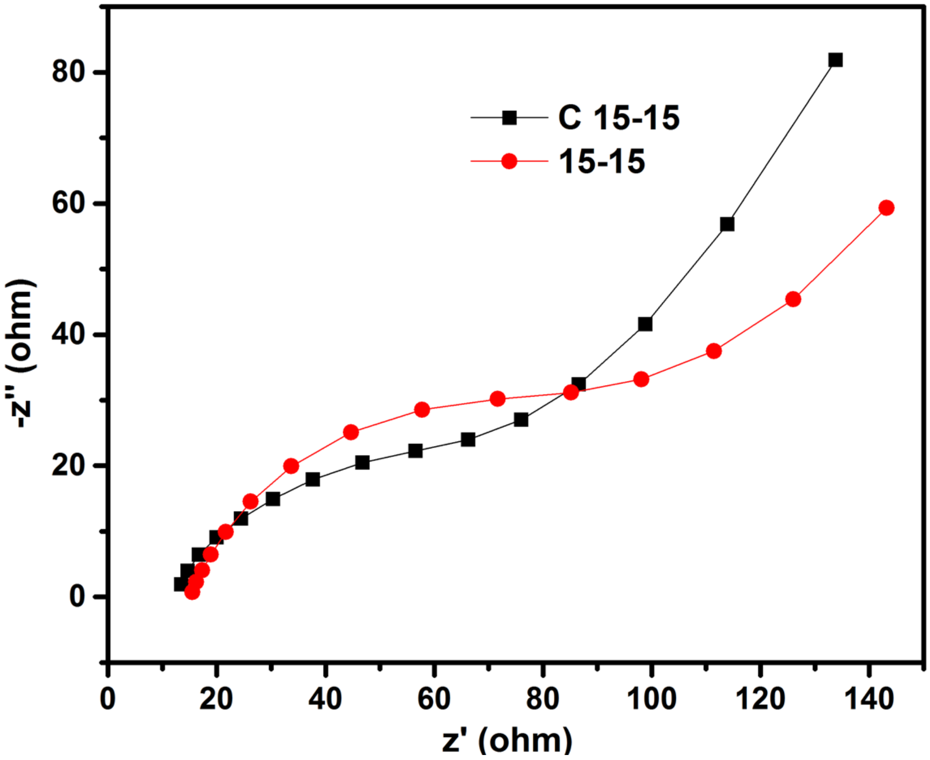

Figure 5.10 The typical Nyquist plots of C 15-15 and 15-15 after 3 cycles of CV.

5.4.2 Investigation carbon coating effect on nanorod LVO

To further boost the electrochemical performance of LVO-ROD, carbon coating was conducted by using PVP as a carbon source. The bare LVO-RODs appear in rod-shaped particles (Figure 5.11a), and they are aggregated upon high-temperature carbonization process (Figure 5.11b). An amorphous carbon layer with a non-uniform thickness is observed on the surface of LVO particle (Figure 5.11c). The presence of carbon layer is further supported by Raman spectra (Figure 5.11d), in which the characteristic D and G band peaks of graphite are clearly detected, in addition to the peaks that are related to LVO-ROD. Element mappings show the homogenous distribution of carbon on LVO, forming C@LVO-ROD composites (Figure 5.11g-j). Thermal analysis was carried out to determine the content of the C@LVO-ROD (Figure 5.11e). The weight loss below 200 °C is attributed to the elimination of absorbed water, and the weight loss in temperature region 200 – 800 °C is associated with the escape of carbon. The weight of carbon was therefore estimated to be 6.5 wt. % in the C@LVO-ROD. These particles are identified as orthorhombic Li_3VO_4, on the basis of a fast-Fourier transform (FFT) analysis (inset of the Figure 5.11c). The lattice fringes are measured to be 0.39 nm and 0.22 nm, corresponding to the d-spacing of the (101) and (012) planes, respectively. Similar XRD patterns were obtained for the bare LVO-ROD and C@LVO-ROD (Figure 5.11f), suggesting that the introduction of carbon does not change the crystal structure and compositions of LVO. The carbon coating forms a 3D conductive network giving rise to improved electrical conductivity. Moreover, it could suppress the pulverization related to the volume change in LVO nanoparticles upon cycling to some extent, also be beneficial for structural integrity and stability.

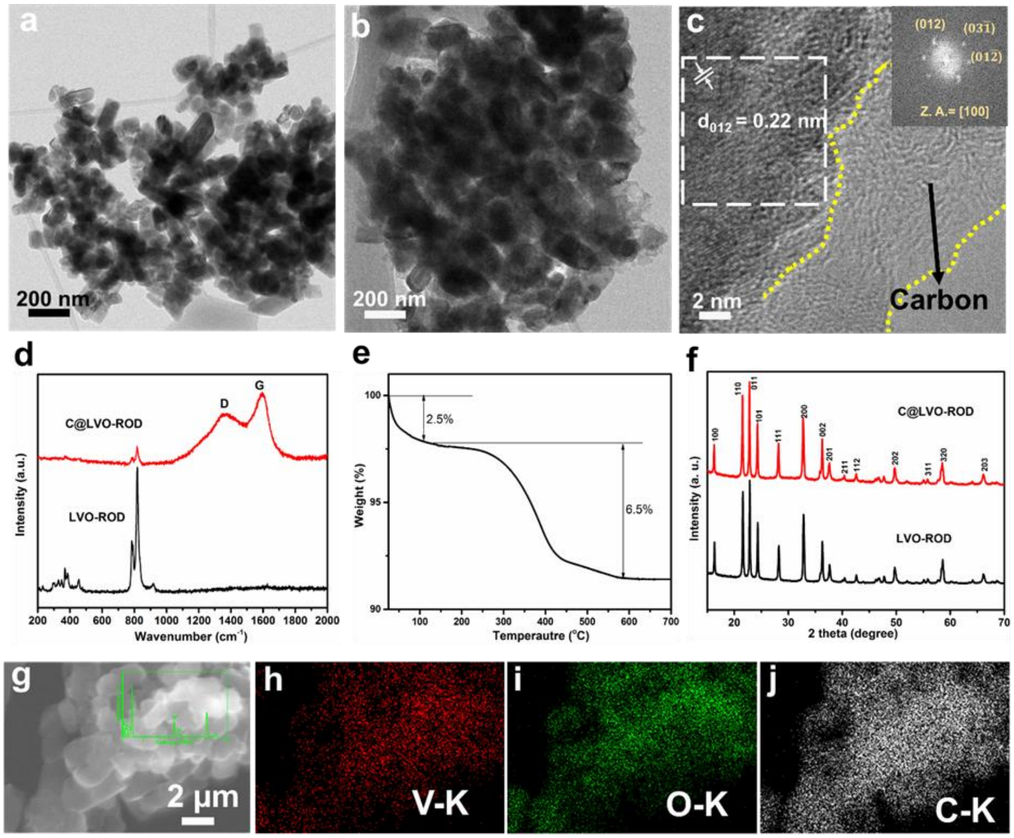

Figure 5.11 Carbon coating characterization. (a, b) TEM images of LVO-ROD and C@LVO-ROD, (c) HRTEM images of the carbon-coated LVO-ROD (C@LVO-ROD), Inset: FFT image of C@LVO-ROD; (d) Raman spectra of the LVO-ROD and C@LVO-ROD, e) TGA curves of C@LVO-ROD; f) XRD patterns for LVO-ROD and C@LVO-ROD; g, h, i, j) SEM image and elemental mapping images of V, O, and C for C@LVO-ROD and inset in g shows the EDX spectrum.

The electrochemical performance of carbon-coated sample (C@LVO-ROD) was tested and compared with the bare sample. The C@LVO-ROD delivers specific capacities of 460, 440, 410, 365, 305, and 250 mAh g^{-1} at rates of 100, 200, 400, 800, 2000, and 4000 mA g^{-1}, respectively (Figure 5.12). Moreover, a discharge capacity of 420 mAh g^{-1} is still retained upon reducing the current density back to 100 mA g^{-1}, indicating the excellent reversibility. C@LVO-ROD shows higher capacities than those of LVO-ROD at all current rates. The improved cycling performance was also demonstrated by C@LVO-ROD (Figure 5.12b-d). A capacity of 430 mAh g^{-1} (at 100 mA g^{-1}) is maintained even after 100 cycles, higher than 234 mAh g^{-1} of bare LVO-ROD. This obtained capacity of 430 mA g^{-1} corresponds to an uptake of 2.2 Li^+ for LVO. In previous literature, a reversible capacity of 250 mAg^{-1} was obtained with the voltage down to 0.1 V, where ultrasonic spray pyrolysis synthesis method was adopted [35]. Here a superior capacity of 430 mA g^{-1} was obtained in our case. This probably due to the conductive coated carbon, which could compensate the intrinsic poor electronic conductivity ($<10^{-10}$ S m^{-1}). Another previous paper reported that 3 Li (corresponds to a capacity of 592 mA g^{-1}) can be inserted at 0.14 V vs Li/Li^+ [36]. In contrast, Katsuhiko Naoi et al. stated that a total number of 2 Li per LVO can be inserted at 0.1 V vs Li/Li^+ and the result is proved by in operando XRD and XAFS [20]. Thus, the exact number of Li which can be accommodated at 0.1 V is still debatable, but high extrinsic/intrinsic conductivity, low current rate for Li diffusion and low voltage are always necessary to achieve higher capacity. Apart from that, long-term cycling at 200 mA g^{-1} is conducted on LVO-ROD and C@LVO-ROD. Obviously, C@LVO-ROD demonstrates much better performance compared to bare LVO-ROD (Figure 5.13).

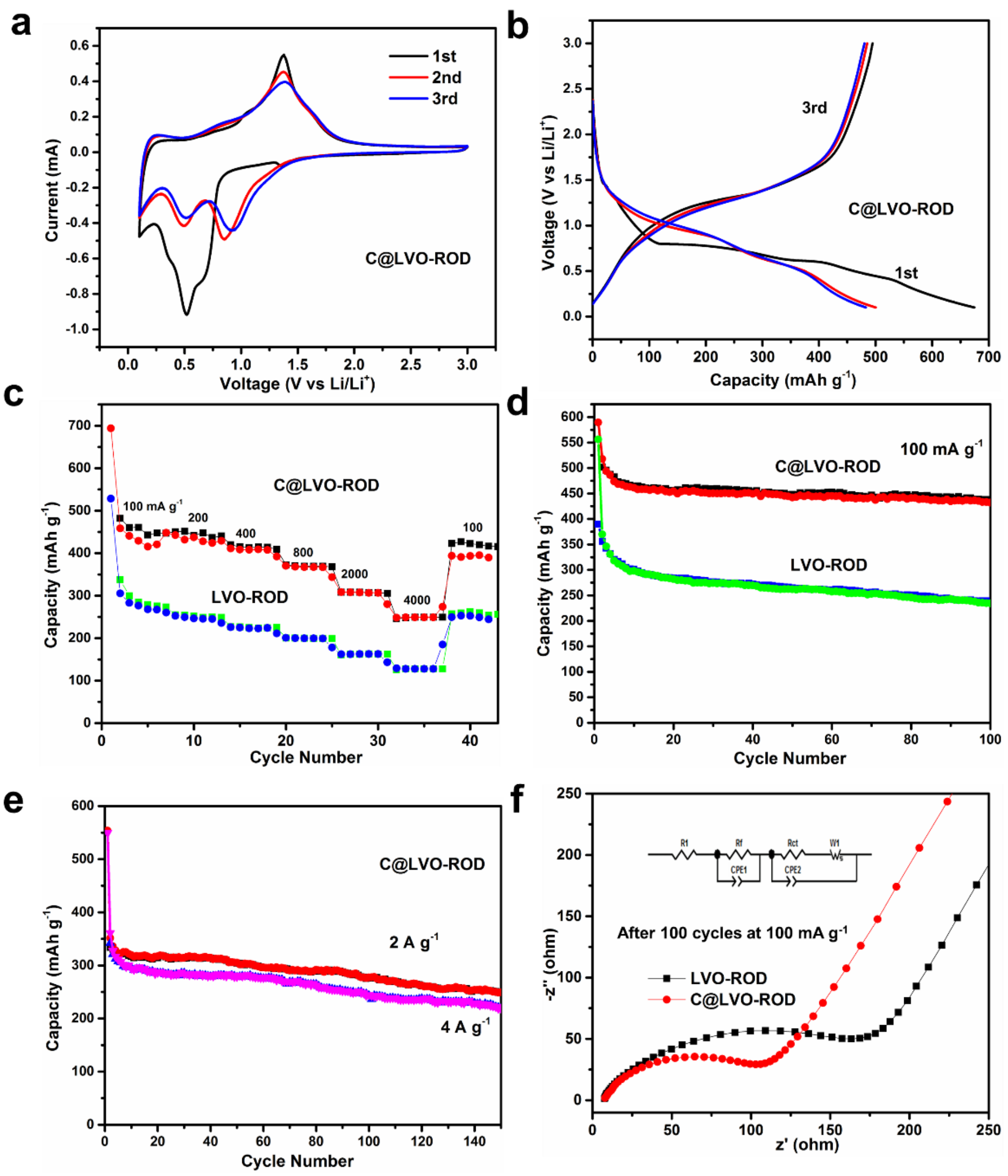

Figure 5.12 Lithium storage behavior. (a) First three CV cycles of C@LVO-ROD, (b) Galvanostatic discharge-charge profiles of C@LVO-ROD for the first four cycles at a current rate of 0.1 A g^{-1} in the voltage range of 0.1-3.0 V vs Li/Li^+, (c) Rate performance of LVO-ROD and C@LVO-ROD at varying current densities from 0.1 to 4 A g^{-1} in the voltage range of 0.1-3.0 V vs Li/Li^+, (d) Cycling performance of C@LVO-ROD and LVO-ROD at 0.1 A g^{-1}, (e)Cycling performance of C@LVO-ROD at 2 and 4 A g^{-1} for 150 cycles, (f) EIS spectra of LVO-ROD and C@LVO-ROD after 100 cycles at a current density of 0.1 A g^{-1}.

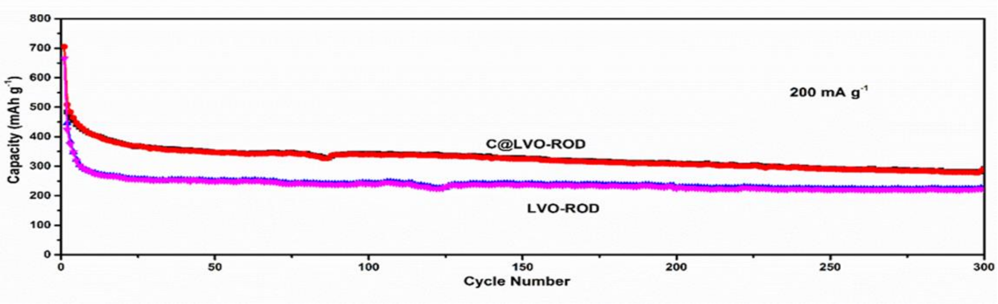

Figure 5.13 Cycling performance of C@LVO-ROD and LVO-ROD at 200 mA g^{-1}.

Based on Randles-Sevchik equation, the apparent Li^+ ions diffusion coefficient of C@LVO-ROD was calculated to be 4.815 x 10^{-11} cm^2 s^{-1}, which is much higher than that of LVO-ROD (3.722 x 10^{-12} cm^2 s^{-1}) (Figure 5.14 and Table 4.3). The impedances of the two samples after 100 cycles were evaluated using EIS measurements and the typical Nyquist plots are fitted by using equivalent circuit model [37-39]. The simulated parameters are shown in Figure 5.12f. As can be seen, the charge transfer resistance (Rct) of C@LVO-ROD is found to be 110 Ω, which is lower than that of the bare LVO-ROD electrode of 180 Ω. Benefiting from these, C@LVO-ROD electrode delivers capacities as high as 250 at 2 A g^{-1} and 220 mAh g^{-1} at 4 A g^{-1} event after 150 cycles. These values are comparable with those of other reported LVO in the literature (summarized in Appendix Table S3).

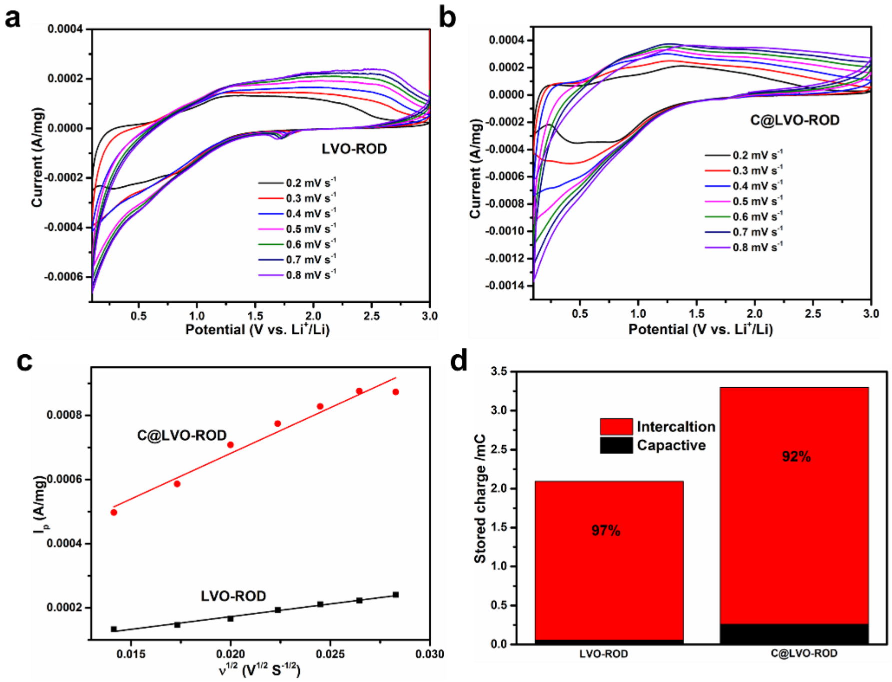

Figure 5.14 (a) Dependence of oxidation peak current on the square root of scan rate, (b) Bar chart showing total stored charge with percentage contribution from capacitive and intercalation at 0.2 mV/s for LVO-ROD and C@LVO-ROD.

5.5 Conclusion

In summary, Li_3VO_4 samples with different morphologies have been synthesized via a solvothermal method with different volume ratios of EtOH and DIW. Their electrochemical performances as anode materials for LIB were investigated. The sample with EtOH and DIW volume ratio of 15-15 was found to show the best performance among all the samples prepared. In addition, the carbon coating process on 15-15 greatly improves its capacities from 350 to 430 mAh g^{-1} at 100 mA g^{-1} and 180 to 350 mAh g^{-1} at 2 A g^{-1}. These results can be attributed to the formation of conductive carbon coating network on the LVO microsphere surface. These properties make C 15-15 a promising anode material for lithium ion batteries application.

References

[1] L. Croguennec, M.R. Palacin, J. Am. Chem. Soc., 137 (2015) 3140-3156.

[2] V. Aravindan, Y.S. Lee, S. Madhavi, Adv. Energy Mater., 5 (2015) 1402225.

[3] C. Yuan, H. Wu, Y. Xie, X.W.D. Lou, Angew Chem Int Ed, 53 (2014) 1488-1504.

[4] X.l. Huang, R.z. Wang, D. Xu, Z.l. Wang, H.g. Wang, J.j. Xu, Z. Wu, Q.c. Liu, Y. Zhang, X.b. Zhang, Adv Funct Mater, 23 (2013) 4345-4353.

[5] D. Ma, Z. Cao, H. Wang, X. Huang, L. Wang, Energy Environ. Sci., 5 (2012) 8538-8542.

[6] H.K. Liu, Z.P. Guo, J.Z. Wang, J. Mater. Chem., 20 (2010) 10055-10057.

[7] L. Liu, L. Sun, J. Liu, X. Xiao, Z. Hu, X. Cao, B. Wang, Int J Hydrogen Energy, 39 (2014) 11258-11266.

[8] E.M. Erickson, C. Ghanty, D. Aurbach, J. Phys. Chem. Lett., 5 (2014) 3313-3324.

[9] H. Tao, L. Xiong, S. Zhu, X. Yang, L. Zhang, Int. J. Hydrogen Energy., 41 (2016) 21268-21277.

[10] A.L. Michan, M. Leskes, C.P. Grey, Chem. Mater., 28 (2016) 385-398.

[11] Z. Yang, D. Choi, S. Kerisit, K.M. Rosso, D. Wang, J. Zhang, G. Graff, J. Liu, J. Power Sources, 192 (2009) 588-598.

[12] H. Zhang, Y. Chen, J. Li, C. He, Y. Chen, Int. J. Hydrogen Energy, 39 (2014) 16096-16102.

[13] T.F. Yi, S.Y. Yang, Y.R. Zhu, Y. Xie, R.S. Zhu, Int. J. Hydrogen Energy, 40 (2015) 8571-8578.

[14] C. Zhang, H. Song, C. Liu, Y. Liu, C. Zhang, X. Nan, G. Cao, Adv. Funct. Mater., 25 (2015) 3497-3504.

[15] Z. Liang, Z. Lin, Y. Zhao, Y. Dong, Q. Kuang, X. Lin, X. Liu, D. Yan, J. Power Sources, 274 (2015) 345-354.

[16] S. Ni, J. Zhang, J. Ma, X. Yang, L. Zhang, X. Li, H. Zeng, Adv. Mater. Interfaces, 3 (2016) 1500340.

[17] S. Hu, Y. Song, S. Yuan, H. Liu, Q. Xu, Y. Wang, J. Power Sources, 303 (2016) 333-339.

[18] J. Meng, Z. Liu, C. Niu, X. Xu, X. Liu, G. Zhang, J. Mater. Chem. A, 4 (2016) 4893-4899.

[19] P. Tartaj, J.M. Amarilla, M.B. Vazquez-Santos, Chem. Mater., 28 (2016) 986-993.

[20] E. Iwama, N. Kawabata, N. Nishio, K. Kisu, J. Miyamoto, W. Naoi, P. Rozier, P. Simon, K. Naoi, ACS Nano, 10 (2016) 5398-5404.

[21] J. Zhang, S. Ni, J. Ma, X. Yang, L. Zhang, J. Power Sources, 301 (2016) 41-46.

[22] Q. Li, Q. Wei, Q. Wang, W. Luo, Q. An, Y. Xu, J. Mater. Chem. A, 3 (2015) 18839-18842.

[23] Y. Shi, J.Z. Wang, S.L. Chou, D. Wexler, H.J. Li, K. Ozawa, H.K. Liu, Y.P. Wu, Nano Lett., 13 (2013) 4715-4720.

[24] Y. Shi, J. Gao, H.D. Abruña, H.J. Li, H.K. Liu, D. Wexler, J.Z. Wang, Y. Wu, Chem. Eur. J., 20 (2014) 5608-5612.

[25] Q. Li, J. Sheng, Q. Wei, Q. An, X. Wei, P. Zhang, L. Mai, Nanoscale, 6 (2014) 11072-11077.

[26] S. Ni, X. Lv, J. Ma, X. Yang, L. Zhang, Electrochim. Acta, 130 (2014) 800-804.

[27] S. Ni, X. Lv, J. Ma, X. Yang, L. Zhang, J. Power Sources, 248 (2014) 122-129.

[28] J. Liu, P.J. Lu, S. Liang, J. Liu, W. Wang, M. Lei, S. Tang, Q. Yang, Nano Energy, 12 (2015) 709-724.

[29] H. Li, H. Zhou, Chem. Commun., 48 (2012) 1201-1217.

[30] Y. Zhang, M. Ma, J. Yang, C. Sun, H. Su, W. Huang, Nanoscale, 6 (2014) 9824-9830.

[31] Y. Xia, P. Yang, Y. Sun, Y. Wu, B. Mayers, B. Gates, Y. Yin, F. Kim, H. Yan, Adv. Mater., 15 (2003) 353-389.

[32] H. Li, X. Liu, T. Zhai, D. Li, H. Zhou, Adv. Energy Mater., 3 (2013) 428-432.

[33] Z. Jian, M. Zheng, Y. Liang, X. Zhang, S. Gheytani, Y. Lan, Y. Shi, Y. Yao, Chem. Commun., 51 (2015) 229-231.

[34] C. Zhang, C. Liu, X. Nan, H. Song, Y. Liu, C. Zhang, G. Cao, ACS Appl. Mater. Interfaces, 8 (2015) 680-688.

[35] W.T. Kim, B.K. Min, H.C. Choi, Y.J. Lee, Y.U. Jeong, J. Electrochem. Soc, 161 (2014) A1302-A1305.

[36] E.M. Dompablo, P. Tartaj, M.J. Amarilla, U. Amador, Chem. Mater., 28 (2016) 5643–5651.

[37] X. Sun, C. Yan, Y. Chen, W. Si, J. Deng, S. Oswald, L. Liu, O.G. Schmidt, Adv. Energy Mater., 4 (2014) 1300912.

[38] X. Sun, G.P. Hao, X. Lu, L. Xi, B. Liu, W. Si, C. Ma, J. Mater. Chem. A, 4 (2016) 10166-10173.

[39] X. Sun, W. Si, X. Liu, J. Deng, L. Xi, L. Liu, C. Yan, O.G. Schmidt, Nano Energy, 9 (2014) 168-175.

Chapter 6

Urchin-like VS_4 Anode for High-performance Lithium Ion Storage

In this work, VS_4 *anode materials with controllable morphologies from hierarchical microflower, octopus-like structure, sea grass-like structure, to urchin-like structure have been successfully synthesized via a facile solvothermal synthesis method using different alcohols as solvents. Their structures and electrochemical properties with various morphologies are systematically investigated, and the structure-property relationship is established. Experimental results reveal the significant dependence of physical features such as the morphology, crystallite size, and specific surface area on the* Li^+ *ion storage in* VS_4*. According to this study, electrochemical performance degrades in the order of urchin-like* VS_4 > *octopus-like* VS_4 > *sea grass-like* VS_4 > *flower-like* VS_4*. Amongst them, urchin-like* VS_4 *demonstrates the best electrochemical performance benefiting from its peculiar structure which possesses a large surface area that accommodates the volume change to a certain extent, and single-crystal thorns which provide fast electron transportation.*

---

*This is chapter is published in Yang, G, et al. ACS Applied Materials & Interfaces 2018.

6.1 Introduction

Li-ion batteries are one of the critical energy storage devices because of their high energy density, long cycle life, and lightweight [1, 2]. However, for the application of electric vehicles and hybrid electric vehicles, the current commercially used anode material (graphite) is inadequate in satisfying the requirements due to the shortage of high specific capacity, safety, cyclability, and rate performance. Thus, increasing efforts have been made to search for high capacity materials, such as Si, Sn, transitional metal oxide, etc [3-6]. Recently, transition metal sulfides, such as MoS_2, Sb_2S_3, Co_9S_8, etc. came into light owing to their high capacity and relatively high electronic conductivity, which translated to significant improvement in charge transportation and rate performance [7-11]. In addition, the diverse crystal structures of these transition metal sulfides open up great opportunities for the design of high-performance electrodes for Li-ion batteries [12].

Recently, VS_4 has attracted much attention due to its low cost and high theoretical capacity of 1196 mAh g^{-1}, compared to its analogue VS_2 (466 mAh g^{-1}) [13]. The higher capacity has been attributed to the higher sulfur content since the sulfur acts as an active participant in the electrochemical reaction [14]. In addition, the one-dimensional chain-like crystal structure of VS_4 provides more potential storage sites for alkali ions. Furthermore, the charge-transfer kinetics is facilitated by the weak bonding between the chains [15]. Although VS_4 is quite attractive, the underlying Li^+ ion storage mechanism in VS_4 is still unclear. Initially, Cho et al [13]. proposed that lithiation of VS_4 becomes Li_2S and vanadium metal. After which, vanadium metal remains inert while the electrochemical reaction occurs between S and Li_2S during subsequent cycles, with the process similar to Li-S battery. However, due to the X-ray amorphous nature of intermediates and products during the conversion reaction of VS_4 and limitations of the XRD, the reaction mechanism could not be fully verified. To further clarify the Li storage mechanism in VS_4, more advanced tools (NMR, PDF, and XANES) were employed by Grey and coworkers [16]. Unlike previous findings, they discovered that the metastable intermediate $Li_{3+x}VS_4$ is formed during lithiation process. It translates back to VS_4 upon charging. This is different from the previous findings, provoking the debate about the underlying mechanism. Further work has also shown the effect of compositing with different carbon or conductive polymer on the electrochemical performance of VS_4, basically to improve the electronic conductivity and suppress the dissolution of polysulfides. For example, VS_4 nanoparticles embedded carbon coated MWCNTs delivers a reversible capacity of 922 mAh g^{-1} at 0.5 A g^{-1} when used as an anode for Li-ion batteries and shows excellent performance in Na-ion batteries [12]. 3D VS_4/graphene through the hydrothermal method delivers a reversible discharge capacity 1044 mAh g^{-1} at 0.2 A g^{-1} when used as anode material for Li-ion batteries [17]. In addition, VS_4 compositing with different substrates (graphene oxide, CNT, pyrene, graphite, TiO_2, and Au nanoparticles) was also prepared via a hydrothermal method [15]. VS_4/graphene delivers a 630 mAh g^{-1} at a high rate of 10 A g^{-1} [16]. Mai et al. also prepared VS_4 on reduced graphene oxide layer for Na-ion batteries [18]. VS_4 coated with different conductive polymers such as PEDOT, PPY, and PANI, were also prepared and showed improved performance due to the enhanced electronic conductivity and lower dissolution of polysulfides [14]. Although significant progress has been made, several limitations such as difficulty in controlled synthesis, and lack of understanding in the effect of morphologies on electrochemical performance, Li^+ ion storage, and kinetic behaviors in VS_4, greatly impede its wide applications.

In this work, a series of VS_4 with controlled morphologies from hierarchical microflower, octopus-like structure, sea grass-like structure, to urchin-like structure were developed via a facile solvothermal synthesis method using different alcohols. The morphologies and structures of these four samples were examined and their effects on the electrochemical performance anode were also investigated. The results reveal that the Li^+ storage behavior is strongly dependent on the crystallite size and morphology of VS_4. Specifically, the urchin structure with single-crystal long thorns shows the best cycling and rate performance. The enhanced electrochemical performance can be attributed to 1) long single-crystal thorns that ensure the fast electron and ion transport; 2) peculiar urchin-like structure that provides a large surface area facilitating Li^+ ion diffusion and the abundant porosity accommodating the volume change upon cycling. Moreover, the formation of solid electrolyte interface (SEI) on urchin-like VS_4 and the kinetics of lithium-ion diffusion were systematically investigated using EIS.

6.2 Experimental section

6.2.1 Synthesis of VS_4

The details are seen in Chapter 3.5.

6.2.2 Materials Characterization

The powder X-ray diffraction patterns were collected by Bruker D8 Advance using Cu Kα radiation. The morphologies of synthesized samples were characterized by scanning electron microscopy (SEM, JEOL JSM-7600, Japan) and high-resolution Transmission electron microscopy (HRTEM, JEOL JEM-2100F). Raman spectra were obtained using a WITecCRM200 Raman system (WITec, Germany) with a laser wavelength of 532 nm. Fourier transform infrared spectroscopy (FTIR) was carried out on the samples in KBr pellets using a Perkin Elmer Spectrum GX at a resolution of 1 cm^{-1}. The Brunauer-Emmett-Teller (BET) specific surface areas were measured by using the Micromeritics ASAP Tristar II 3020.

6.2.3 Electrochemical Characterization

Electrochemical performances of VS_4 were evaluated by assembling 2016 coin cell in an argon-filled glovebox (MBraun, Germany) with oxygen and water content less than 1 ppm. The electrodes were prepared by mixing 70 wt. % active materials, 10 wt. % binder (PVDF Kynar), and 20 wt. % Super P (Timcal) in a weight ratio of 7:1:2 in N-methyl-pyrrolidinone (NMP, Sigma Aldrich). The typical electrode was dried at 60 °C in a vacuum oven overnight before being assembled into a coin cell in the glovebox. The mass loading is about 0.8 mg cm^{-1}. Lithium pellet was served as a counter electrode and Celgard 2400 as the separator. The electrolyte was composed of a 1 M solution of $LiPF_6$ dissolved in ethylene carbonate/diethylene carbonate (EC: DEC = 1:1 by volume, Charslton Technologies Pte. Ltd). Electrochemical impedance spectroscopy (EIS) and cyclic voltammetry (CV) measurements were performed using Solartron Instrument. The frequency of EIS measurement was carried out from 100 KHz to 0.01 Hz with an AC signal of 10 mV in amplitude.

6.3 Results and discussion

VS_4 materials with various morphologies (Figure 6.1) from hierarchical microflower, octopus-like structure, sea grass-like structure, to urchin-like structure were synthesized. Flower-VS_4 consisting of a hierarchical porous fluffy flower spheres with a core size around 1~2 μm were clearly identified (Figure 6.1a and a1). Octopus-VS_4 (Figure 6.1b and 1b1) delivers an octopus-like structure with a core size ~300 nm and tentacles with tapering diameter ~100 nm. In contrast, the sea grass-VS_4 (Figure 6.1c and 1c1) has a sea grass-like structure, in which the core is not obvious, with leaf length ~1 μm. Both tentacle/leaf lengths of octopus-VS_4 and leaf length of sea grass-VS_4 are shorter than the thorn lengths of urchin-VS_4 (Figure 6.1d1). The detailed morphology of urchin-VS_4 (Figure 6.1d1) reveals that the thorns have a diameter of 50~100 nm, and the thorns of one urchin-like hierarchical nanospheres bundle with other thorns from neighboring urchin nanospheres to form an interconnected network. Viewed under a higher magnification, flower-VS_4 (Figure 6.1a2) demonstrates a core surrounded by myriads of short nanowires or nanosheets on the surface. In contrast, octopus-VS_4 (Figure 6.1b2) demonstrates tentacles structure with a tapering diameter. Sea grass-VS_4 (Figure 6.1c2) shows a porous leaf-like structure with a diameter of approximately 100 nm. The thorns of urchin-VS_4 are uniform and longer in length. More detailed morphologies properties were listed in Table 7.1. The structures of flower-VS_4, octopus-VS_4, sea grass-VS_4, and urchin-VS_4 (Figure 6.1a3, 1b3, 1c3 and 1d3) were further characterized by HRTEM images, and different degree of crystallinity have been identified. The lattice fringes and FFT of all four products corroborate the pure phase of VS_4. Flower-VS_4 consists of both amorphous phase and crystalline phase. The crystallite size is around 10 nm in length and 5 nm in width. Similarly, sea grass-VS_4 also has both an amorphous phase and a crystalline phase. The crystallite size is around 40 nm in length, which is much longer than that of flower-VS_4. While octopus-VS_4 and urchin-VS_4 deliver an even higher crystallinity compared to these of flower-VS_4 and sea grass-VS_4 from the HRTEM images. In a further comparison, urchin-VS_4 with much more uniform single-crystal thorns demonstrates the highest crystallinity among them. Uniform lattice fringes with the width of 0.52 nm of one thorn have been identified from SAED pattern, which correspond to the d-spacing of the (020) plane of VS_4. Moreover, the distinct periodic dots in SAED patterns suggest its single-crystal feature. Therefore, crystallinity of the samples descends in the order of urchin-VS_4 > octopus-VS_4 > sea grass-VS_4 > flower-VS_4.

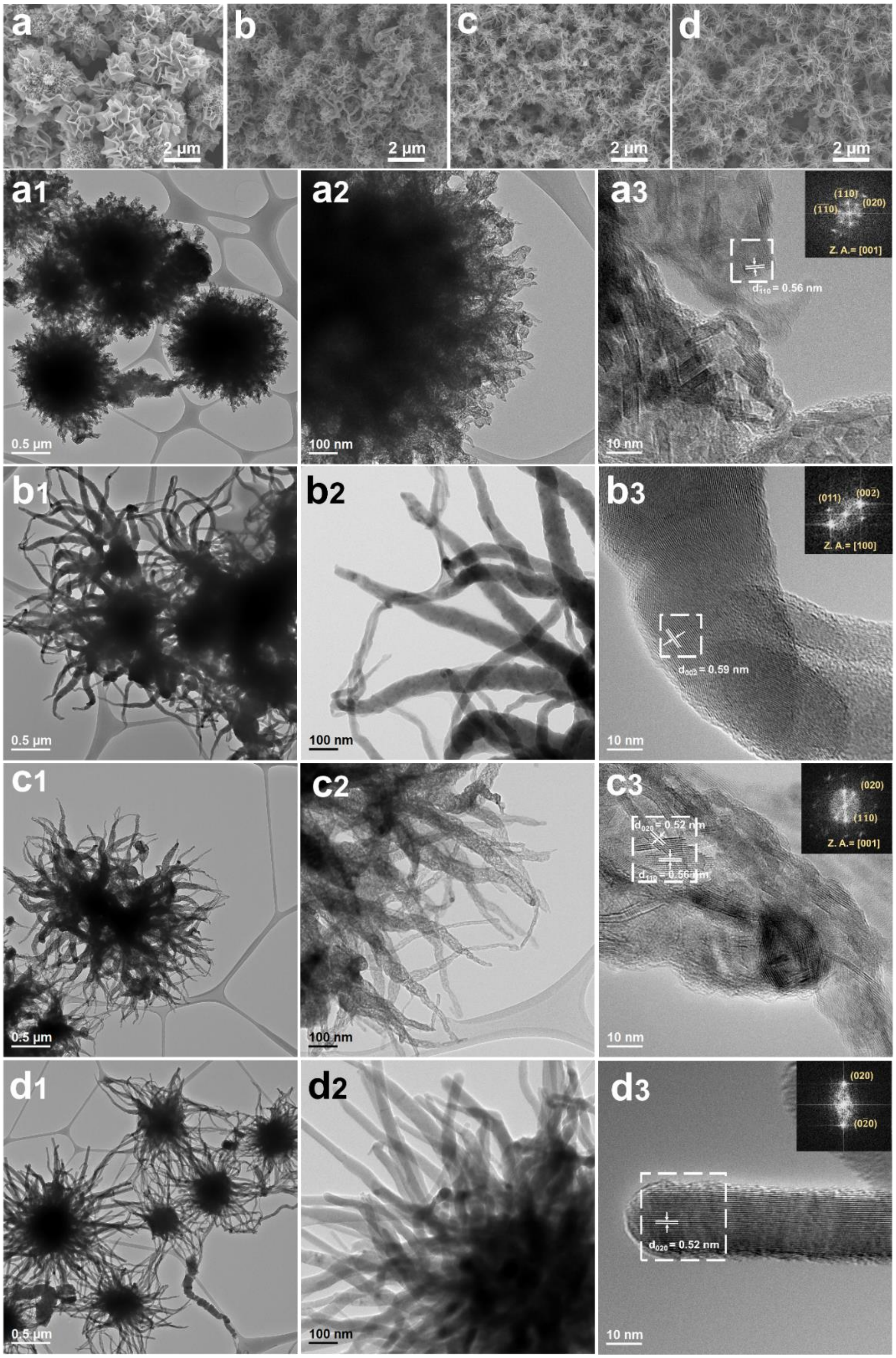

Figure 6.1 SEM, TEM and HRTEM images of (a, a1, a2, and a3) flower-VS_4; (b, b1, b2, and b3) octopus-VS_4; (c, c1, c2, and c3); sea grass-VS_4, and (d, d1, d2, and d3) urchin-VS_4.

TEM and their corresponding EDX elemental mapping images of S and V (Figure 6.2) corroborate the uniform distribution of element V and S across the urchin. The stoichiometric S/V ratio is determined to be 4, giving the stoichiometric formula of VS_4.

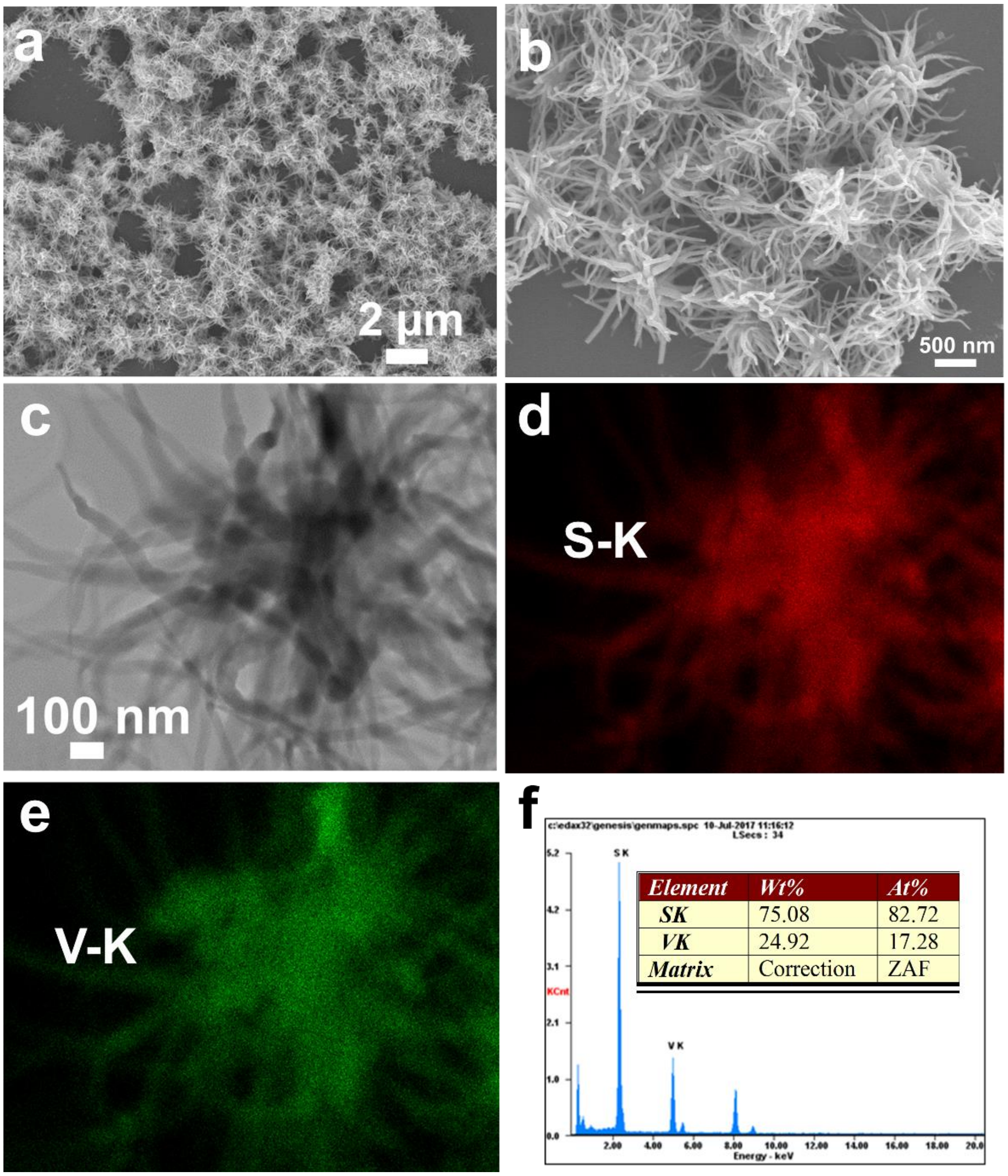

Element	*Wt%*	*At%*
SK	75.08	82.72
VK	24.92	17.28
Matrix	Correction	ZAF

Figure 6.2 SEM images and elemental mapping of urchin-like VS_4.

Powder-XRD results reveal that all samples are composed of pure VS_4 phase (JCPDS NO. 72-1294) (Figure 6.3), agreeing well with HRTEM analysis. More structural and/or element information were collected from Raman (Figure 6.3b) and FTIR characterizations (Figure 6.3c). The peaks around 190 and 279 cm^{-1} in the Raman spectra are attributed to the stretching and bending modes of V-S (Figure 6.3b) [15, 17-19]. In FTIR spectra, the bands at 550 and 980 cm^{-1} are characteristic of doubly bonded/bridged S^{2-} (V-S-S) and terminal S stretching of VS_4 (Figure 6.3c) [14, 15, 20]. Apart from the signals of VS_4, a band of amorphous carbon is also observed at 1400 cm^{-1} [21]. Other bands around 1200 and 1631 cm^{-1} arise from the C-O-R vibrations and residual moisture present in the samples during solvothermal synthesis [14, 21].

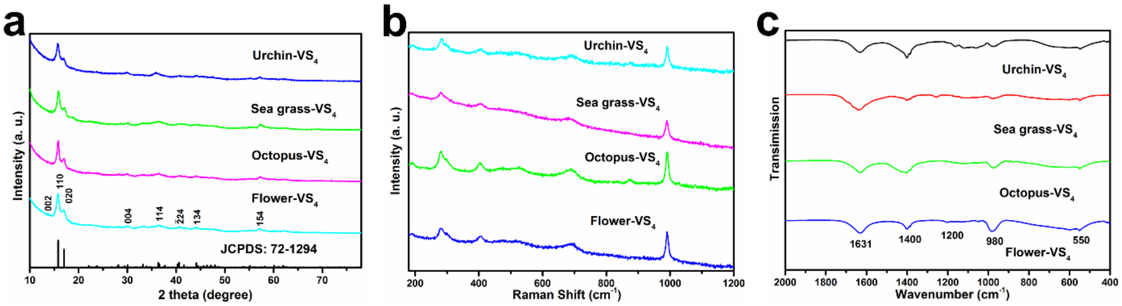

Figure 6.3 (a) XRD patterns, (b) Raman spectra and (c) FTIR spectra of flower-VS_4, octopus-VS_4, sea grass-VS_4, and urchin-VS_4.

Table 6.1 VS_4 morphologies, BET surface area, and pore volume.

Sample	Morphologies	$S_{BET}(m^2g^{-1})$	Pore volume (cm^3g^{-1})
Flower-VS_4	Sheet or small nanowires	6.644	0.0614
Octopus-VS_4	Tentacles length ~1 µm	3.717	0.0231
Sea grass-VS_4	Leaves length ~800 nm	5.596	0.0262
Urchin-VS_4	Thorns length~2 µm	5.885	0.0280

The electrochemical performance of flower-VS_4, octopus-VS_4, sea grass-VS_4, and urchin-VS_4 was evaluated and compared. Typical cyclic voltammogram (CV) curves of urchin-VS_4 electrode for the first five cycles are illustrated in FigFigure 6.4a. In the first cathodic scan, a peak at 1.61 V indicates the lithiation process from VS_4 to $Li_{3+x}VS_4$ [16]. It is noted that there is another peak around 0.64 V which is attributed to the formation of solid-electrolyte interface (SEI), decomposition of the electrolyte, and the reduction of $Li_{3+x}VS_4$ to Li_2S and V [13, 16]. In the delithiation process, two anodic peaks at 1.91 V and 2.38 V were observed which correspond to the delithiation of Li_2S and the formation of VS_4 or $Li_{3+x}VS_4$, respectively [16]. Subsequent cycles reveal a shift in cathodic peaks toward the positive. Such could be attributed to the compositional change and structure rearrangements [12, 22, 23]. The second anodic curves were quite similar to the first cycle. From the second cycle onwards, the curves are very close and almost identical, indicating the good cycling stability for the lithiation/delithiation processes. In contrast, curves become smaller with the increasing cycling numbers for samples flower-VS_4, octopus-VS_4, and sea grass-VS_4 (Figure 6.4). This implies poor cycling stability probably attributed to plausible structure degradation. These results further highlight the advantages of urchin-like structure of VS_4.

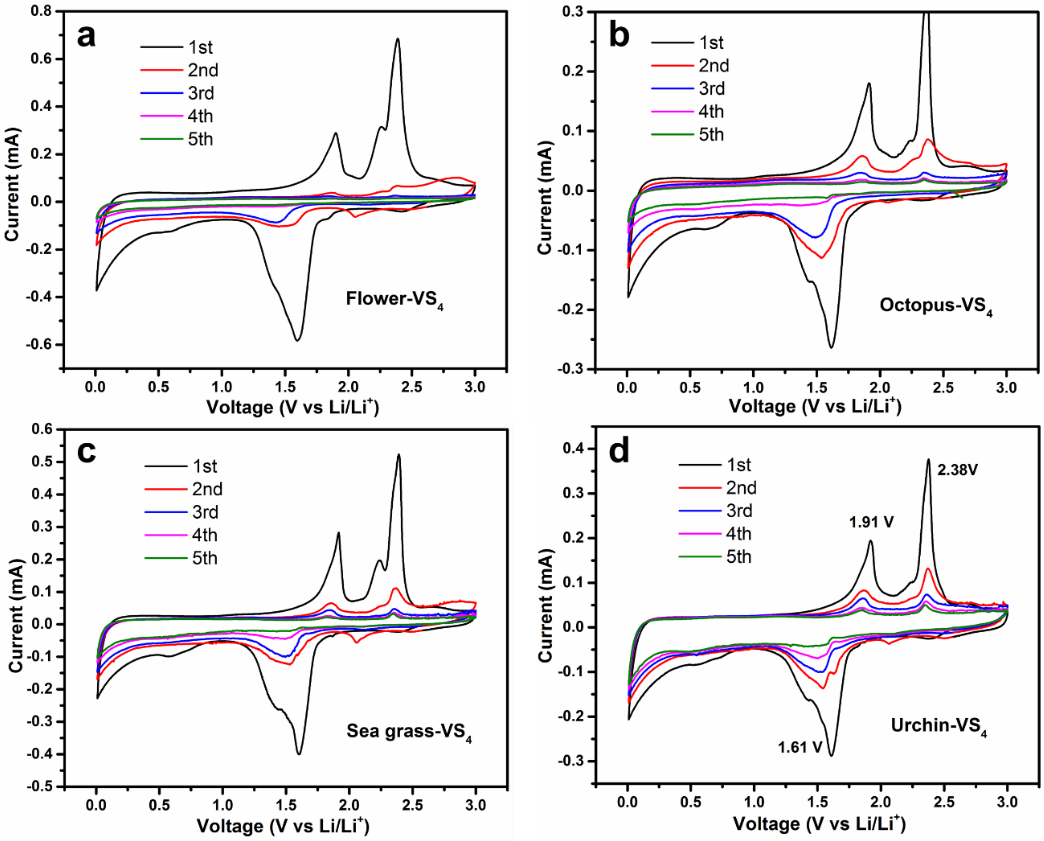

Figure 6.4 First five CVs of: (a) flower-VS_4; (b) octopus-VS_4; (c) sea grass-VS_4; (d) urchin-like VS_4 with a scan rate of 0.2 mV s^{-1} in the voltage range of 0.01-3.00 V vs Li/Li^+.

In good agreement with the CV curves (Figure 6.5), representative galvanostatic discharge/charge profiles show an obvious plateau at 1.85 V and two shallow plateaus at

1.5 V and 0.8 V. The first discharge capacity is 1305 mAh $g^{-1,}$ and the first charge capacity is 847 mAh g^{-1}, giving rise to an initial coulombic efficiency of 65%. This value for flower-VS_4, octopus-VS_4, and sea grass-VS_4 is 73%, 69%, and 74%, respectively, suggesting a serve side reaction [24, 25]. After the first cycles, specific capacities of flower-VS_4, octopus-VS_4, and sea grass-VS_4 drop rapidly compared to that of urchin-VS_4. The rate capability of flower-VS_4, octopus-VS_4, sea grass-VS_4, and urchin-VS_4 was evaluated by charge-discharge at various current rates from 0.1 A g^{-1} to 2 A g^{-1} (Figure 6.6). Urchin-VS_4 delivers a high specific capacity of 500 mAh g^{-1} at 0.1 A g^{-1}. It decreases to 400, 250, 150 and 60 mAh g^{-1}, as the current densities increase to 0.2, 0.5, 1 and 2 A g^{-1}, respectively. As the current density returns to 0.1 A g^{-1}, the capacity recovers to 480 mAh g^{-1}. Note that all values of specific capacities for urchin-VS_4 are higher than those of flower-VS_4, octopus-VS_4, and sea grass-VS_4, corroborating its good rate capability. Moreover, good cycling stability has been demonstrated for urchin-VS_4 in which a specific capacity of 490 mAh g^{-1} is delivered even after 100 cycles. In contrast, the specific capacities of flower-VS_4, octopus-VS_4, and sea grass-VS_4 after 100 cycles are 81, 230, and 145 mAh g^{-1}, respectively.

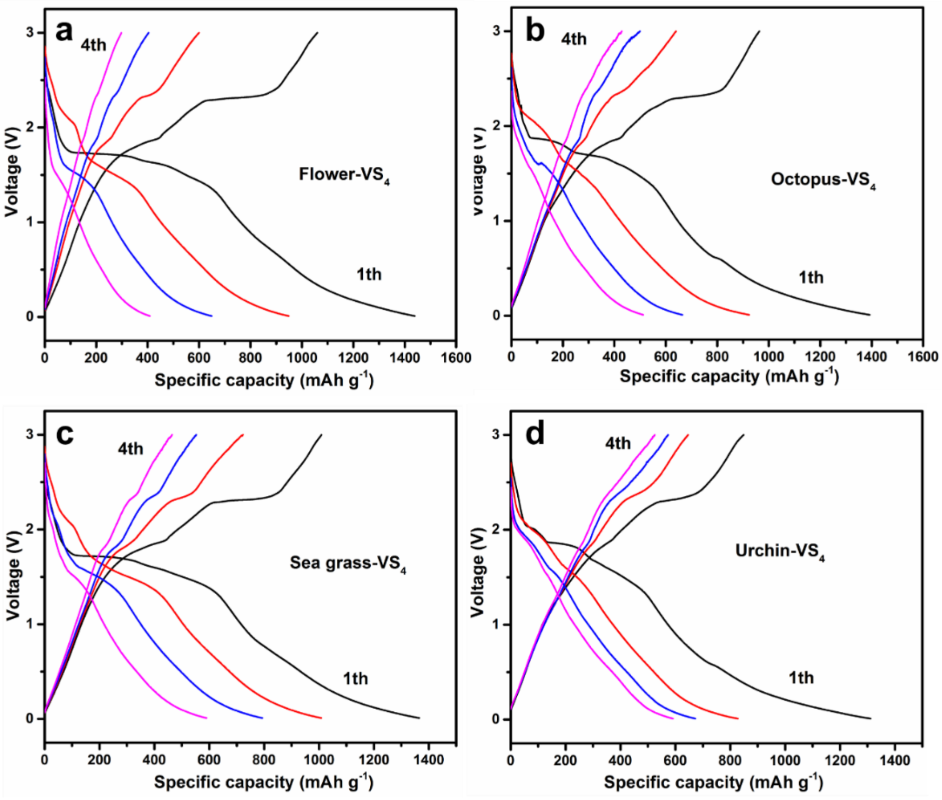

Figure 6.5 First three galvanostatic discharge-charge profiles at a current rate of 0.1 A g^{-1} in the voltage range of 0.1-3 V vs Li/Li^+ for: (a) flower-VS_4; (b) octopus-VS_4; (c) sea grass-VS_4; (d) urchin-like VS_4.

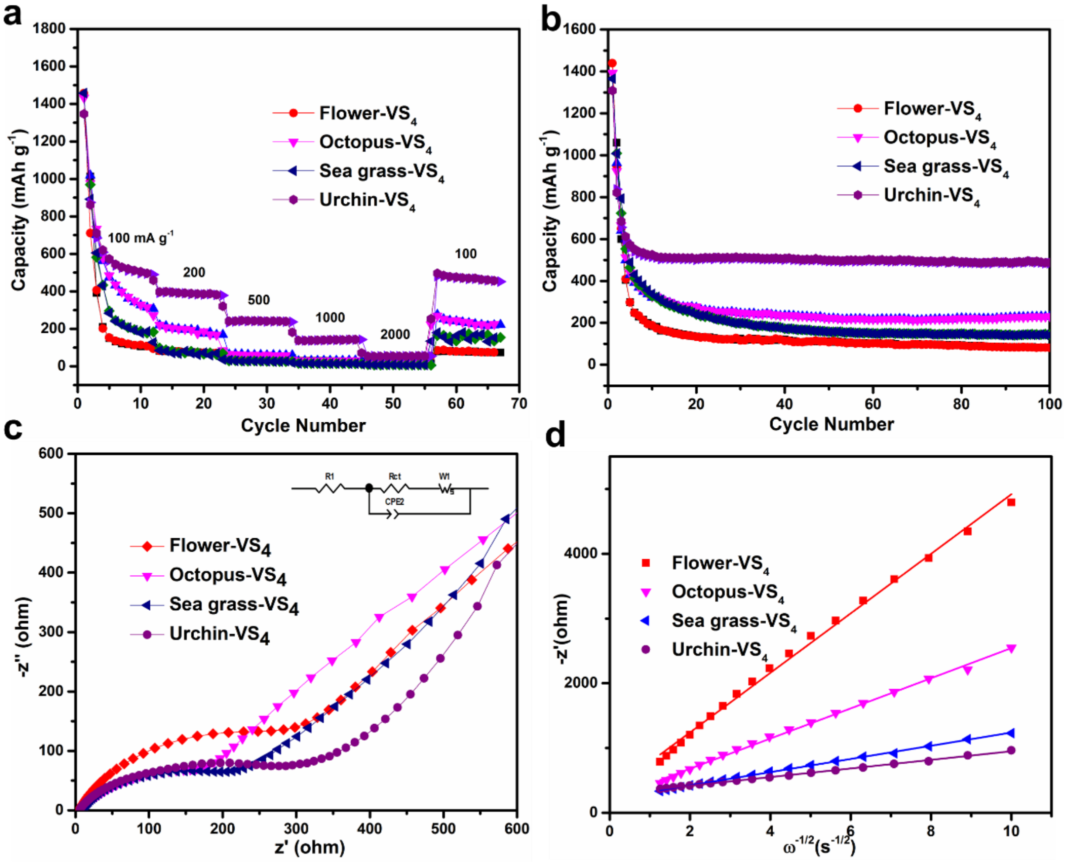

Figure 6.6 (a) First five CV cycles of urchin-VS_4 at sweep rate of 0.1 mV s^{-1}; (b) Galvanostatic discharge/charge profiles of urchin-VS_4 for the first four cycles at a current rate of 0.1 A g^{-1} in the voltage range of 0.01-3.00 V vs Li^+/Li; (c) Rate performance of flower-VS_4, octopus-VS_4, sea grass-VS_4, and urchin-VS_4 at varied current densities from 0.1 to 2 A g^{-1} in the voltage range of 0.01-3.00 V vs Li^+/Li; (d) Cycling performance of flower-VS_4, octopus-VS_4, sea grass-VS_4, and urchin-VS_4 at 0.1 A g^{-1}; (e) EIS spectra of electrodes after 5 CV cycles with a scan rate of 0.1 mV s^{-1}. The inset shows the equivalent circuit model and the resistance data from fitting EIS; (f) Linear fitting of z' vs $\omega^{-1/2}$ relationship.

It is worth noting that the capacity degrades in the sequential order of urchin-VS_4 > octopus-VS_4 > sea grass-VS_4 > flower-VS_4 (Figure 6.6a-b), which is consistent with crystallinity mentioned previously (observed in Figure 6.1). Higher crystallinity provides a larger capacity and stable cycling. This is in good agreement with previous reports which states that too small crystallite size may not result in good electrochemical performance. For instances, Shen et al [26]. prepared $Li_4Ti_5O_{12}$ with different nanocrystal sizes. They found that 6 nm size particles have a poor rate capability compared to the 9 nm size particles. They attributed the poor performance to the amorphous phase composed of disordered atoms for 6 nm particles which makes the lithium ions difficult to diffuse into the particle core. A similar study also reported that the low crystallinity sample TiO_2 contains a considerable amount of defect sites hindering Li-ion diffusion [27]. Furthermore, urchin-VS_4 also has the second largest surface area and pore volume (Table 6.1 & Figure 6.7). The large surface area might increase the interface of the active material and electrolyte, thus facilitating the Li^+ ion transport. Moreover, its mesoporous structure is believed to favor ion diffusion and allow an easy permeability of electrolyte [28, 29]. Urchin-VS_4 demonstrates 3D structures with many long nanowires emanating from the core. The nanowires also provide shortened diffusion length and large interfacial area of active material and electrolyte. The large volume change during charging and discharging can also be alleviated by the porosity [30-43]. Thus, the best cycling and capacity retention performance of urchin-VS_4 among all the samples is attributed to its peculiar nanostructure with the large surface area and high crystallinity, which facilitate the ion diffusion and electron transport.

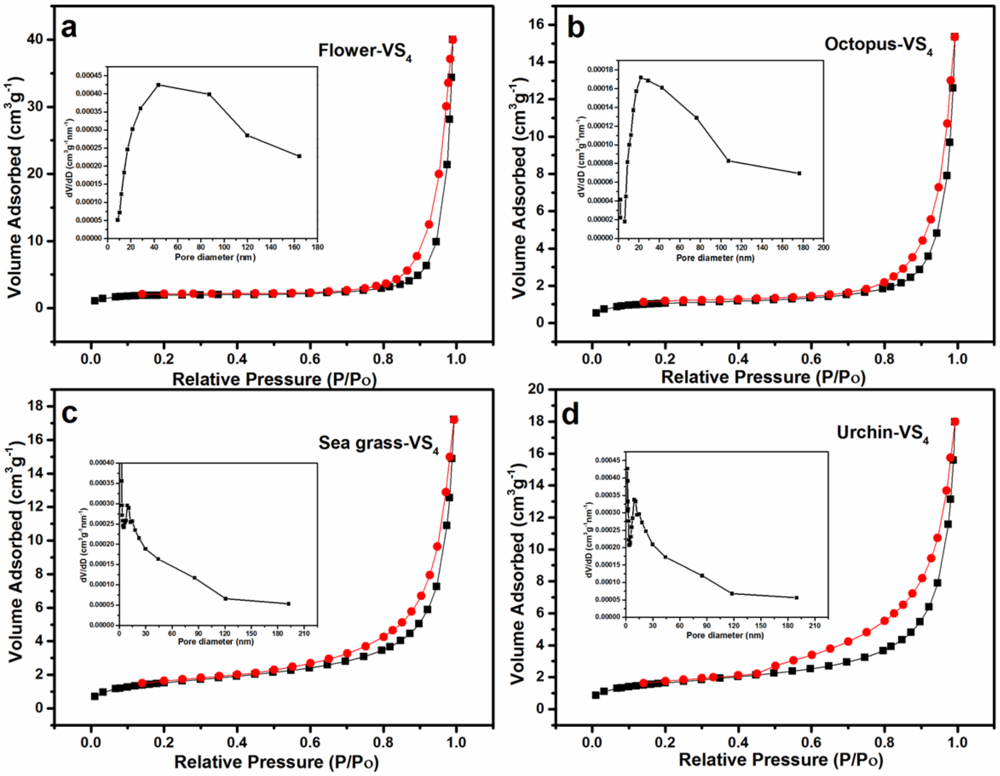

Figure 6.7 The Nitrogen-adsorption-desorption isotherms of the (a) flower-VS_4, (b) octopus-VS_4, (c) sea grass-VS_4, and (d) urchin-like VS_4. The insets are their corresponding pore size distribution.

The impedances of all four samples after 5 CV cycles were evaluated using EIS measurements and the typical Nyquist plots are fitted by using equivalent circuit model (Figure 6.6c). The simulated parameters are shown in Table 2. As seen, the charge transfer resistance (Rct) of flower-VS_4, octopus-VS_4, sea grass-VS_4, and urchin-VS_4 is found to be 273, 181, 213 and 327 Ω, respectively. The higher Rct value for urchin-VS_4 could be attributed to the side reactions between electrode and electrolytes since it has a relatively higher surface area [44, 45]. However, urchin-VS_4 displays the highest diffusion coefficient (D_{Li+}) of 3.15246 x 10^{-17} (Figure 6.6d and Table 6.2). This could be ascribed to the high crystallinity of urchin-VS_4 that facilitates fast electron and ionic transport.

Table 6.2 Equivalent circuit parameters and apparent Li ion diffusion coefficient calculated from EIS and CV rates.

Sample	**R_1 (Ω)**	**R_{ct} (Ω)**	**D_{Li+} (cm^2s^{-1}) from EIS**	**D_{Li+} (cm^2s^{-1}) from CV**
Flower-VS_4	5.279	272.9	6.59443×10^{-19}	7.68579×10^{-15}
Octopus-VS_4	7.884	181.3	2.56739×10^{-18}	1.82601×10^{-14}
Sea grass-VS_4	7.43	213.1	1.34254×10^{-17}	1.48008×10^{-14}
Urchin-VS_4	3.317	327.6	3.15246×10^{-17}	1.57853×10^{-13}

The kinetic properties for urchin-VS_4 are further supported by CV testing at different sweep rates (Figure 6.8). The reduction peaks shift to lower potential range, and oxidation peaks shift to the higher potential range. This is due to the high polarization with increasing sweep rates [46]. Figure 6.8e shows the relationship between reduction peak current I_p and the square root of the scan root $v^{1/2}$. The linear relation indicates that reaction is a Li-ion diffusion controlled. Based on the Randles-sevcik equation [47]:

$$I_p = (2.69 \times 10^5)n^{3/2}AD_0^{1/2}C_0v^{1/2} \qquad (1)$$

where I_p is the peak current, A is the apparent surface area, D_0 is the diffusion coefficient, C_0 is the maximum Li^+ concentration, and v is the CV scanning rate. The diffusion coefficient was calculated to be 1.57853×10^{-13} cm^2 s^{-1} for urchin-VS_4, which is higher than those of octopus-VS_4 (1.82601×10^{-14} cm^2 s^{-1}), sea grass-VS_4 (1.48008×10^{-14} cm^2 s^{-1}), and flower-VS_4 (7.68579×10^{-15} cm^2 s^{-1}) (Table 6.2). The enhanced kinetics may explain the better performance of urchin-VS_4. To further investigate the effect of different morphologies on the electrochemical performance, the total charge storage at a certain sweep rate was also quantified by separating the specific contribution from the capacitive and diffusion-controlled charge at a fixed voltage [48]. The results (Figure 6.8f) reveal that urchin-VS_4 exhibited an intercalation effects contribution ratio (~96%), which is equal or higher than that of octopus-VS_4 (96%), sea grass-VS_4 (88%), and flower-VS_4 (89%). This can be attributed to its high crystallinity and enhanced ion diffusion.

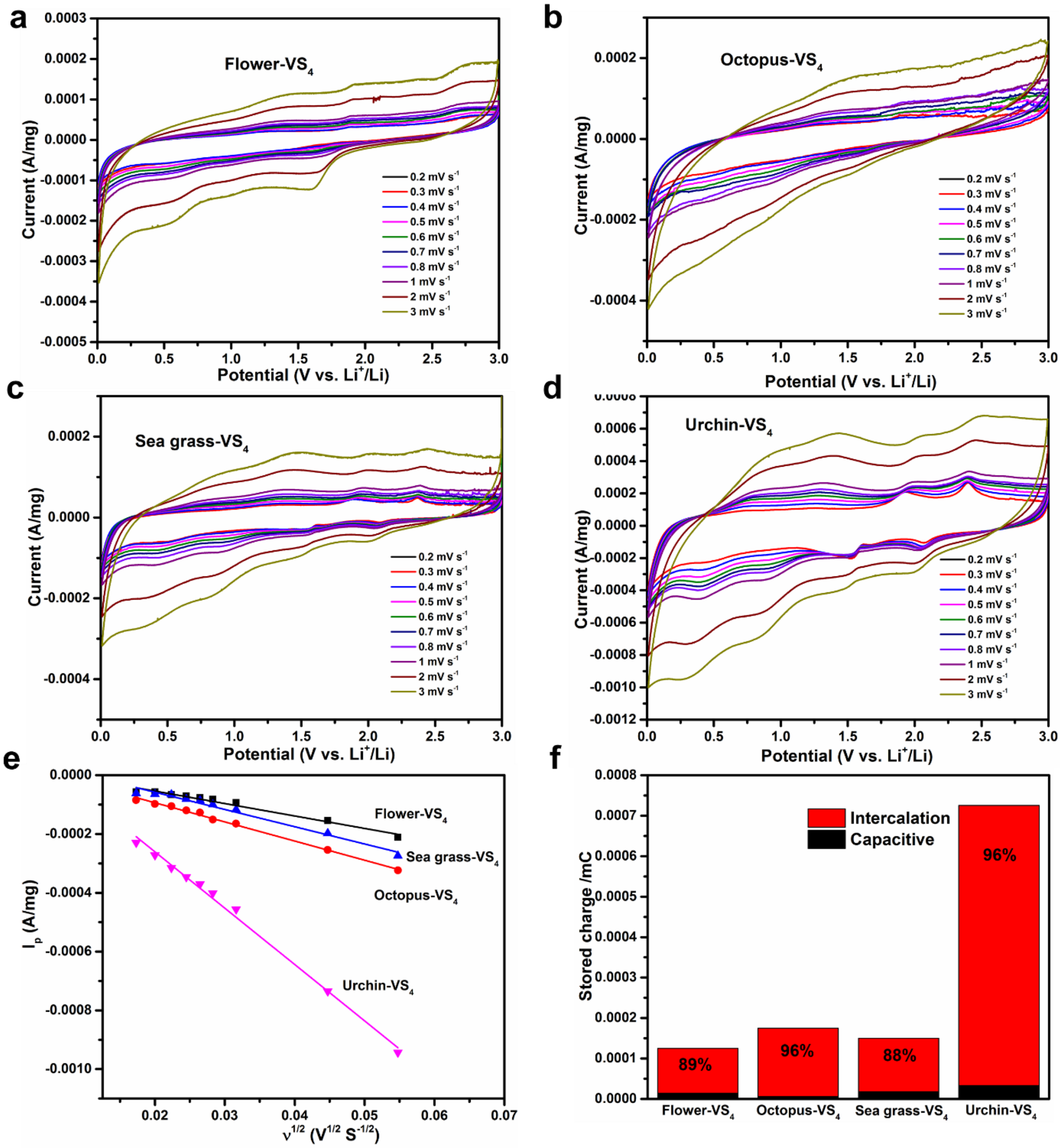

Figure 6.8 CV curves of (a) flower-VS_4; (b) octopus-VS_4; (c) sea grass-VS_4; (d) urchin-VS_4 at different scan rates between 0.01 to 3.00 V; (e) Dependence of reduction peak current on the square root of scan rate. (f) Bar chart showing total stored charge with percentage contribution from capacitive and intercalation at 0.3 mV/s for all samples with stored charge calculated by integrating the CV area according to the equation: $Q = \int \left(\frac{i}{v}\right) dV$. [49]

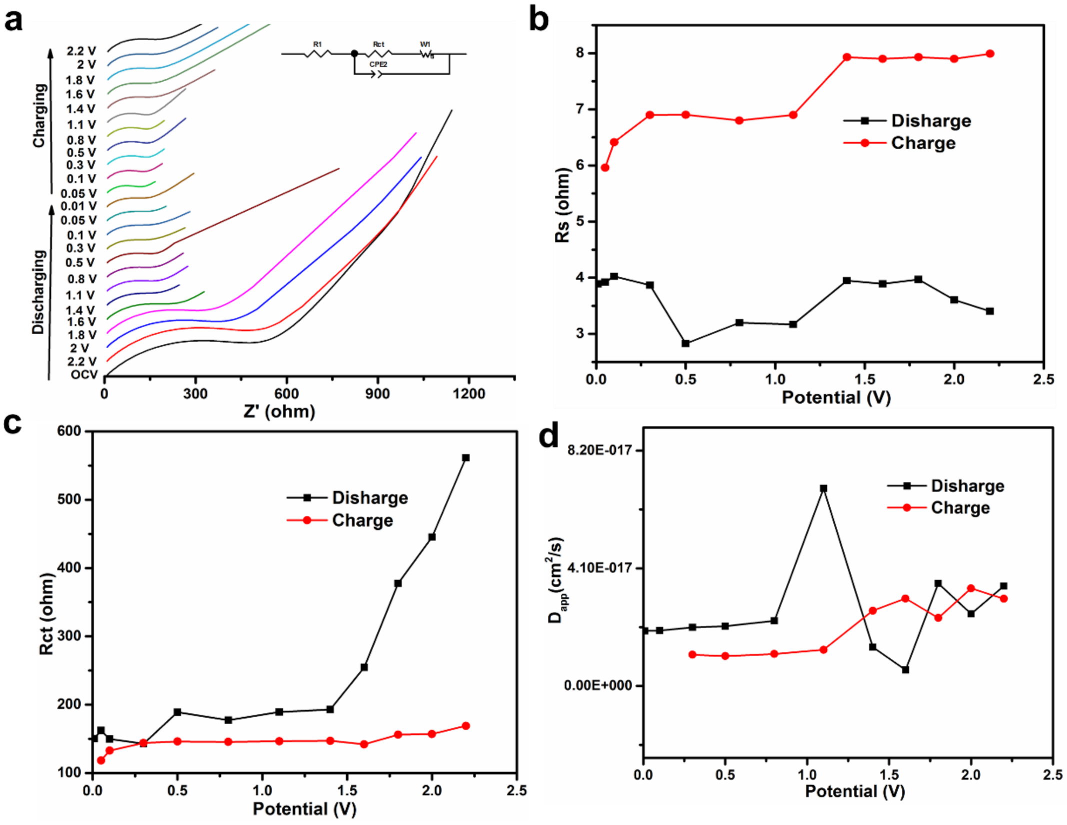

Figure 6.9 (a) EIS profiles of urchin-VS_4 at the first discharge and charge. (b) Variation trend of Rs and (c) Rct during the first discharge and charge. (d) Diffusion coefficients of Li calculated from EIS vs potential.

To gain more insight into lithium storage behaviors, including formation of SEI and kinetics of lithium-ion diffusion during the initial discharging and charging process, EIS profiles at different discharge/charge potential were recorded to evaluate the tendencies of electronic conductivity (R_s), charge transfer resistance (R_{ct}), and apparent Li diffusion coefficients (D_{app}) (Figure 6.9). The changing in R_s during the initial discharging and charging was shown in Figure 6.9b, where the R_s increases initially until 1.8 V. This is probably due to the decomposition of the electrolyte. It then decreases at around 1.4 V, resulting from phase transition upon lithiation that increases the electronic conductivity. Another increase in R_s starts at around 0.5 V due to the SEI formation. Note that R_s upon charging is generally higher than that of the discharge process. This is reasonable as the electronic insulating SEI formed during the 1st discharge process reduced the electronic conductivity. The variation tendency of R_{ct} is shown in Figure 6.9c. During the discharge process, the R_{ct} decreases rapidly and becomes stable at around 1.6 V due to initial intercalation of Li^+ ions [50]. In the charging process, R_{ct} increases slightly because of Li^+ ion deinsertion. The D_{aap} values (Figure 6.9d) derived from EIS analysis ranges from 5.5888 x 10^{-18} cm^2 s^{-1} to 6.88601 x 10^{-17} cm^2 s^{-1} upon discharging and charging, respectively, over the potential range of 0.01-2.25 V. The relative larger D_{app} values during discharging than charging below 1.5 V imply that insertion process is more favorable than extraction process. All these, together, demonstrate the practical feasibility of VS_4 anode.

6.4 Conclusion

VS_4 with controlled morphologies from hierarchical microflower, octopus-like structure, sea grass-like structure, to urchin-like structure were prepared via a facile solvothermal synthesis in different alcohols. The effect of morphologies, surface area, and crystallite size on the electrochemical performance was systematically investigated. The urchin-like VS_4 with long single-crystal thorns is found to be advantageous due to its unique structure that provides a large surface area for Li^+ ion transportation, high crystallinity that ensures fast electron transportation, and porosity that accommodates the volume change upon cycling. Kinetic parameters derived from EIS spectra and sweep rate dependent CV curves such as charge transfer resistances and Li^+ ion apparent diffusion coefficients both support this claim well. In addition, EIS experiment was performed during the first discharge-charge process to study the formation of the solid electrolyte interface (SEI) on urchin-like VS_4 and the kinetics of lithium-ion diffusion. These findings from this work promote a better fundamental understanding of the Li^+ storage behavior in VS_4 as well as other vanadium-based materials. It also provides invaluable guidance for morphology-controlled synthesis to tailor optimal electrochemical performance.

References

[1] M. Armand, J.M.M. Tarascon, Nature, 451 (2008) 652-657.

[2] M. Winter, J.O. Besenhard, M.E. Spahr, P. Novák, Adv. Mater., 10 (1998) 725-763.

[3] A. Casimir, H. Zhang, O. Ogoke, J.C. Amine, J. Lu, G. Wu, Nano Energy, 27 (2016) 359-376.

[4] G. Derrien, J. Hassoun, S. Panero, Adv. Mater., 19 (2007) 2336–2340.

[5] X. Sun, G.P. Hao, X. Lu, L. Xi, B. Liu, W. Si, C. Ma, J. Mater. Chem. A, 4 (2016) 10166-10173.

[6] J. Liu, W. Zhou, L. Lai, H. Yang, S. Lim, Y. Zhen, T. Yu, Z. Shen, J. Lin, Nano Energy, 2 (2013) 726-732.

[7] K. Bindumadhavan, S.K. Srivastava, Chem. Commun., 49 (2013) 1823-1825

[8] J. Xiao, L. Wan, S. Yang, F. Xiao, S. Wang, Nano Lett., 14 (2014) 831–838.

[9] H. Chen, J. Jiang, L. Zhang, H. Wan, T. Qi, D. Xia, Nanoscale, 5 (2013) 8879-8883

[10] H. Wang, H. Jiang, Y. Hu, P. Sáha, Q. Cheng, C. Li, Chem. Eng. Sci., 174 (2017) 104-111.

[11] Z. Deng, H. Jiang, Y. Hu, Y. Liu, L. Zhang, H. Liu, C. Li, Adv. Mater., 29 (2017) 1603020.

[12] Y. Zhou, J. Tian, H. Xu, J. Yang, Y. Qian, Energy Storage Mater., 6 (2017) 149-156.

[13] X. Xu, S. Jeong, C. Rout, P. Oh, M. Ko, H. Kim, M. Kim, R. Cao, H. Shin, J. Cho, J. Mater. Chem. A, 2 (2014) 10847-10853.

[14] Y. Zhou, Y. Li, J. Yang, J. Tian, H. Xu, J. Yang, W. Fan, ACS Appl. Mater. Interfaces, 8 (2016) 18797-18805.

[15] C. Rout, B.-H. Kim, X. Xu, J. Yang, H. Jeong, D. Odkhuu, N. Park, J. Cho, H. Shin, J. Am. Chem. Soc., 135 (2013) 8720-8725.

[16] S. Britto, M. Leskes, X. Hua, C.-A. Hébert, H. Shin, S. Clarke, O. Borkiewicz, K.W. Chapman, R. Seshadri, J. Cho, C.P. Grey, J. Am. Chem. Soc., 137 (2015) 8499-8508.

[17] Q. Li, Y. Chen, J. He, F. Fu, J. Lin, W. Zhang, J. Alloys Compd., 685 (2016) 294-299.

[18] R. Sun, Q. Wei, Q. Li, W. Luo, Q. An, J. Sheng, D. Wang, W. Chen, L. Mai, ACS Appl. Mater. Interfaces, 7 (2015) 20902–20908.

[19] W.F. Hillebrand, J. Am. Chem. Soc., 29 (1907) 1019-1029.

[20] W. Fang, H. Zhao, Y. Xie, J. Fang, J. Xu, Z. Chen, ACS Appl. Mater. Interfaces, 7 (2015) 13044-13052.

[21] C. Zhang, H. Song, C. Liu, Y. Liu, C. Zhang, X. Nan, G. Cao, Advanced Functional Materials, 25 (2015) 3497-3504.

[22] Z. Zheng, Y. Wang, A. Zhang, T. Zhang, F. Cheng, J. Power Sources, 198 (2012) 229-235.

[23] C.T. Cherian, J. Sundaramurthy, M. Kalaivani, J. Mater. Chem., 22 (2012) 12198-12204.

[24] S. Laruelle, S. Grugeon, P. Poizot, M. Dolle, J. Electrochem. Soc., 149 (2002) A627-A634.

[25] G. Binotto, D. Larcher, A.S. Prakash, Chem. Mater., 19 (2007) 3032–3040.

[26] Y. Shen, J.R. Eltzholtz, B.B. Iversen, Chem. Mater., 25 (2013) 5023–5030.

[27] J.W. Kang, D.H. Kim, V. Mathew, J.S. Lim, J. Electrochem. Soc., 158 (2011) A59-A62.

[28] F.M. Balcı, Ö. Kudu, E. Yılmaz, Chem. Eur. J., 22 (2016) 18873–18880.

[29] J. Hu, C.F. Sun, E. Gillette, Z. Gui, Y.H. Wang, S.B. Lee, Nanoscale, 8 (2016) 12958-12969.

[30] C. Wang, D. Higgins, F. Wang, D. Li, R. Liu, G. Xia, N. Li, Nano Energy, 9 (2014) 334-344.

[31] L. Liu, L. Mou, J. Yu, S. Chen, RSC Adv., 7 (2017) 2637-2643.

[32] H. Cao, X. Zhou, C. Zheng, Z. Liu, ACS Appl. Mater. Interfaces, 7 (2015).

[33] Y. Fu, H. Jiang, Y. Hu, L. Zhang, C. Li, J. Power Sources, 261 (2014) 306-310.

[34] J. Shu, R. Ma, L. Shao, M. Shui, L. Hou, K. Wu, Y. Chen, RSC Adv., 3 (2013) 372-376

[35] T. Zhang, H. Yue, H. Qiu, Y. Wei, C. Wang, G. Chen, Nanotechnology, 28 (2017) 10.

[36] G. Huang, S. Xu, Z. Xu, H. Sun, L. Li, ACS Appl. Mater. Interfaces, 6 (2014) 21325–21334.

[37] Y. Dong, D. Li, C. Gao, Y. Liu, J. Zhang, J. Mater. Chem. A, 5 (2017) 8087-8094

[38] X.Q. Zhang, Y.C. Zhao, C.G. Wang, X. Li, J.D. Liu, J. Mater. Sci., 51 (2016) 9296–9305.

[39] J. Liang, K. Xi, G. Tan, S. Chen, T. Zhao, P.R. Coxon, Nano Energy, 27 (2016) 457-465.

[40] K. Zhang, M. Park, L. Zhou, G.H. Lee, W. Li, Adv. Funct. Mater., 26 (2016) 6728–6735.

[41] X. Wu, J. Guo, M.J. McDonald, S. Li, B. Xu, Y. Yang, Electrochim. Acta 163 (2015) 93-101.

[42] D. Li, C. Feng, H.K. Liu, Z. Guo, Sci Rep., 5 (2015) 11326.

[43] A.K. Mondal, D. Su, Y. Wang, S. Chen, Q. Liu, J. Alloys Compd., 582 (2014) 522-527.

[44] Y.B. He, M. Liu, Z.D. Huang, B. Zhang, Y. Yu, B. Li, J. Power Sources, 239 (2013) 269-276.

[45] J. Cui, C. Qing, Q. Zhang, C. Su, X. Wang, Y.-B. Ionics, Ionics, 20 (2014) 23-28.

[46] Z. Chen, J. Wang, D. Chao, T. Baikie, L. Bai, S. Chen, Y. Zhao, T. Sum, J. Lin, Z. Shen, Sci. Rep., 6 (2016) 25771.

[47] J. Liu, Z. Chen, W. Xuan, S. Chen, B. Zhang, J. Wang, H. Wang, B. Tian, M. Chen, X. Fan, Y. Huang, T. Sum, J. Lin, Z. Shen, ACS Nano, 11 (2017) 6911–6920.

[48] J. Liu, J. Wang, C. Xu, H. Jiang, C. Li, L. Zhang, J. Lin, Z.X. Shen, Adv.Sci., (2017) 1700322.

[49] (!!! INVALID CITATION !!!).

[50] L.L. Zhou, S.-Y. Shen, X.-X. Peng, L.N. Wu, Q. Wang, C.-H. Shen, T.-T. Tu, L. Huang, J.-T. Li, S.-G. Sun, ACS Appl. Mater. Interfaces, 8 (2016) 23739-23745.

Chapter 7

In-situ grown VS_4 Nanowire on Reduced Graphene Oxide as Anode for High-performance Lithium Ion Storage

VS_4 has emerged as promising anode material for LIBs due to its unique one-dimensional chain structure, high sulfur content, and excellent electrochemical performance. Despite its advantages, not much work has been done on this material due to the highly difficult and complicated synthesis procedure. As such, successful fabrication of VS_4 with peculiar morphologies on rGO can be deemed as a hopeful construction. Herein, in-situ grown 1D (one-dimensional) VS_4 nanowires on rGO were demonstrated via a facile solvothermal synthesis procedure. A series of rGO with VS_4 (VS_4, 5rGO@VS_4, 15rGO@VS_4, and 35rGO@VS_4) were synthesized and compared in terms of their rate capability and cycling stability. In this study, samples prepared are comprehensively characterized by which various structure-property relationships were also established.

7.1 Introduction

Rechargeable Li-ion batteries have been considered as one of the promising energy storage candidates for applications from portable devices to electric vehicles. This is because rechargeable Li-ion batteries possess high energy density, long cycle life, and lightweight [1, 2]. Nevertheless, the conventional commercial graphite has a low specific capacity and safety issue, which hinders its application in next-generation Li-ion batteries. Thus, seeking high capacity anode materials to replace current graphite is an urgent task [3-6]. Transition metal sulfides, such as MoS_2, Sb_2S_3, Co_9S_8, etc. have received wide interest because of the relatively good high capacity and relatively high electronic conductivity to their oxide counterparts, which promotes better charge transportation and rate performance [7-12]. Among the transitional metal sulfides, patronite VS_4 has been regarded as potential anode material owing to its low cost and high theoretical capacity of 1196 mAh g^{-1} [13]. It possesses a linear chain-like structure with two S_2^{2-} moieties between the V centers, which provides high capacity due to the more potential storage sites for alkali ions [14]. The large interchain V-V distance (> 0.61 nm) lead to slight interactions between the neighboring chains. Such interactions not only facilitate the alkali ions intercalation but also its rate capability [15]. However, similar to other metal sulfides, the low electrical conductivity and excessive volume change during discharging/charging limit VS_4 for widespread applications. To solve these problems, intensive research has been ongoing to incorporate VS_4 with other electrical conductive substrates, such as conductive polymer, graphene, carbon, etc [12-14, 16-18]. However, to the best of our knowledge, fabrication of graphene-supported VS_4 with carefully crafted morphological control is uncommon.

Graphene, a monolayer of carbon atoms with a two-dimensional sheet, has drawn intensive attention in Li-ion batteries due to the high electrical conductivity, mechanical stability, and large surface area. These properties endow graphene as an ideal single-atom thick substrate for the growth of functional nanomaterials (usually active high-capacity compounds). These nanomaterials not only increase the overall capacity of the graphene-based composites but also prevent the restacking of few-layer graphene. Meanwhile, graphene can increase the electrical conductivity and provide an elastic buffer space to accommodate the volume change of the supported active material. Moreover, the graphene can immobilize the active material during repetitive cycling and prevent their agglomeration. Many studies have shown that graphene-supported nanocomposites demonstrate excellent performance, especially for active material with special structures, such as 0D nanoparticles, 1D nanowires or nanorods, 2D nanosheet or nanoplates, and 3D flowers. For example, growth of NiO nanosheets and nanoparticles on graphene nanosheets has been carried out through a facile hydrothermal method. Such an arrangement exhibits superior electrochemical performances compared to pure NiO nanosheets [19]. The authors attributed its better performance to the synergetic effect between graphene nanosheet and NiO sheets, where NiO nanosheets separate graphene nanosheets and prevent agglomeration while graphene provides large surface area and electrical conductivity. Fe_2O_3 on graphene sheets nanocomposites were prepared by microwave-assisted hydrothermal technique [20]. The nanorice Fe_2O_3/graphene exhibited a larger reversible capacity as well as good cycling performance, whereby its improved performance is ascribed to the increased electrical conductivity and mechanical stability. Other reports concerning graphene-supported active material with various structures, such as nanopillar Sn/graphene [21], Sn@CNT nanorods/graphene [22], Sn@carbon nanocables/graphene [23], 1D Co_3S_4 nanotubes/graphene [24], et al. also have demonstrated their advantages and good electrochemical performance. Although great progress has been achieved so far, synthesizing VS_4 with peculiar morphologies like 1D nanowire on graphene directly is still challenging.

We herein develop a novel one-step strategy to direct synthesize one-dimensional VS_4 nanowire on graphene. The hybrids possess several advantages: First, one-dimensional VS_4 nanowires can provide the high electron pathway. Second, VS_4 nanowire enables effect electrolyte transportation, active-site accessibility, and good electron transportation between nanowires and graphene. Third, the one-dimensional structure and two-dimensional graphene can accommodate the volume change in lithium insertion and extraction processes. Fourth, a one-step fabrication procedure is simple with no toxic chemical like hydrazine commonly used to reduce graphene oxide. To our knowledge, this is the first time that VS_4 nanowires directly grow on graphene by such a facile hydrothermal method.

7.2 Experimental section

7.2.1 Synthesis of VS_4

The details are seen in Chapter 3.5.

7.2.2 Materials Characterization

The powder X-ray diffraction patterns were collected by Bruker D8 Advance using Cu Kα radiation. The morphologies of synthesized samples were characterized by scanning electron microscopy (SEM, JEOL JSM-7600, Japan) and high-resolution Transmission electron microscopy (HRTEM, JEOL JEM-2100F). Raman spectra were obtained using a Raman system (Renishaw) with a laser wavelength of 532 nm. Fourier transform infrared spectroscopy (FTIR) was carried out on the samples in KBr pellets using a Perkin Elmer Spectrum GX at a resolution of 1 cm^{-1}. The Brunauer-Emmett-Teller (BET) specific surface areas were measured by using the Micromeritics ASAP Tristar II 3020.

7.2.3 Electrochemical Characterization

Electrochemical performances of VS_4 were evaluated by assembling 2016 coin cell in an argon-filled glovebox (MBraun, Germany) with oxygen and water content less than 1 ppm. The electrodes were prepared by mixing 70 wt. % active materials, 10 wt. % binder (PVDF Kynar), and 20 wt. % Super P (Timcal) in a weight ratio of 7:1:2 in N-methyl-pyrrolidinone (NMP, Sigma Aldrich). The typical electrode was dried at 60 °C in a vacuum oven overnight before being assembled into a coin cell in the glovebox. The mass loading is ca.

0.8 mg cm^{-1}. Lithium pellet was served as a counter electrode and Celgard 2400 as the separator. The electrolyte was composed of a 1 M solution of $LiPF_6$ dissolved in ethylene carbonate/diethylene carbonate (EC: DEC = 1:1 by volume, Charslton Technologies Pte. Ltd). Electrochemical impedance spectroscopy (EIS) and cyclic voltammetry (CV) measurements were performed using Solartron Instrument. The frequency of EIS measurement was carried out from 100 KHz to 0.01 Hz with an AC signal of 10 mV in amplitude.

7.3 Results and discussion

Reduced graphene oxide loaded VS_4 nanocomposites with various amount of rGO were synthesized and characterized using SEM and TEM (Figure 7.1). Without the addition of GO, urchin-like VS_4 was obtained (Figure 7.1a-a3). The detailed morphology of urchin-VS_4 (Figure 7.1a1-a_2) reveals the presence of thorns with a diameter of 50~100 nm. Adjacent thorns of neighboring urchin-like nanospheres bundle together to form an interconnected network. The thorns of urchin-VS_4 are uniform. With 5 wt% GO added, the urchin shaped VS_4 changes in morphology whereby nanowires are fabricated on the surface of GO. Further addition of GO results in a reduction in nanowires density, as seen in Figure 7.1b-d. TEM images represented by Figure 7.1b2-d2 also show good consistency with the SEM images obtained. Morphological characterization also show a decrease in diameter of nanowire with the addition of GO from ca. 80 nm to ca. 40 nm. The structures of VS_4, 5rGO@VS_4, 15rGO@VS_4, and 35rGO@VS_4 (Figure 7.1a3, b3, c3, and d3) were further characterized by HRTEM images, and 1D VS_4 nanowires have been identified. The lattice fringes and FFT of all four products corroborate the pure phase of VS_4. Uniform lattice fringes with the width of 0.52 nm of one thorn have been identified from SAED pattern, which corresponds to the d-spacing of the (020) plane of VS_4. TEM and their corresponding EDX elemental mapping images of S and V (Figure 7.2) corroborate the uniform distribution of element V and S across the nanowires. More detailed morphologies properties were listed in Table 7.1.

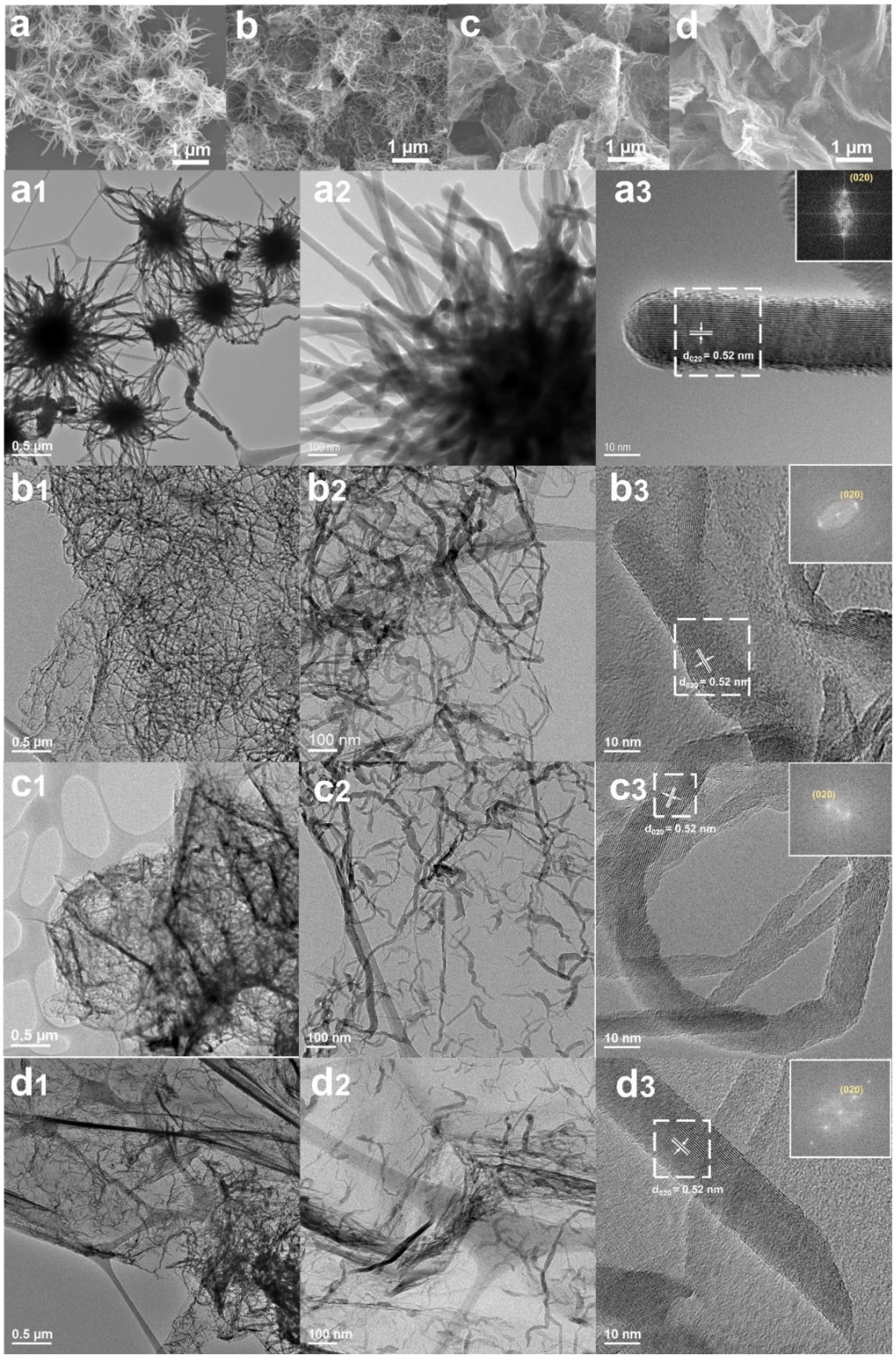

Figure 7.1 SEM, TEM and HRTEM images of (a, a1, a2, and a3) VS_4; (b, b1, b2, and b3) 5rGO@VS_4; (c, c1, c2, and c3) 15rGO@VS_4, and (d, d1, d2, and d3) 35rGO@VS_4.

Table 7.1 VS_4 morphologies, BET surface area, and pore volume

Sample	Morphologies	S_{BET} (m^2g^{-1})	Pore volume (cm^3g^{-1})
VS_4	Sea-urchin structure with long nanowires	5.8	0.027
5rGO@VS_4	Nanowires grown on rGO	13.6	0.089
15rGO@VS_4	Nanowires grown on rGO	19.2	0.108
35rGO@VS_4	Nanowires grown on rGO	16.7	0.140

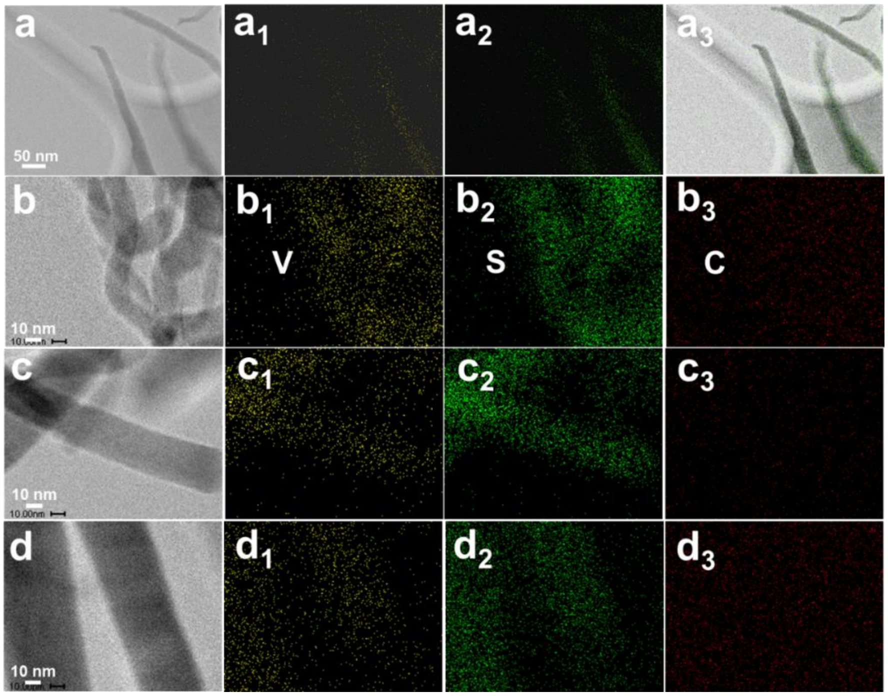

Figure 7.2 SEM images and the corresponding EDS elemental mapping of (a, a1, a2, a3) V, S and combination for VS_4 and V, S, and C for (b, b1, b2, and b3) 5rGO@VS_4; (c, c1, c2, and c3) 15rGO@VS_4, and (d, d1, d2, and d3) 35rGO@VS_4.

Powder-XRD results reveal pure VS_4 phase (JCPDS NO. 72-1294) (Figure 7.3a) for as-prepared samples, agreeing well with HRTEM analysis. More structural and/or element information were collected using Raman (Figure 7.3b) and FTIR characterizations (Figure 7.3c). The peaks around 190 and 279 cm^{-1} in the Raman spectra are attributed to the stretching (A_1) and bending (B_1) modes of V-S (Figure 7.3b) [15, 17, 18, 25]. The peaks at around 1340 and 1580 cm^{-1} are associated with the D and G bands of graphene. It can be observed that the peak of VS_4 becomes weaker with the increasing amount of rGO, while the graphene bands increase in prominence. In the FTIR spectra, bands at 550 and 980 cm^{-1} are characteristic of doubly bonded/bridged S^{2-} (V-S-S) and terminal S stretching of VS_4 (Figure 7.3c) [14, 15, 26]. Apart from the signals of VS_4, a band of amorphous carbon is also observed at 1400 cm^{-1} [27]. However, 5rGO@VS_4, 15rGO@VS_4, and 50rGO@VS_4 samples also reveal the presence of a broad peak around 550 cm^{-1} and a weak peak at 1400 cm^{-1}. Such weak peaks of VS_4 may be due to the FTIR signal blocking from rGO. Other bands around 1200 and 1631 cm^{-1} arise from the C-O-R vibrations and residual moisture present in the samples during solvothermal synthesis [14, 27]. To determine the carbon content and evaluate the thermal stability of VS_4/graphene nanocomposites, rGO, pure VS_4, and VS_4 with series of rGO were analyzed by TGA in synthetic air. A small amount of weight loss observed below 200 °C is attributed to the desorption of moisture. While VS_4 decomposes with two steps, the step of 200-250 °C indicates the reaction of VS_4 with O_2, and the second step of 300~350 °C is associated with the reaction between sulfur compounds with O_2. In good agreement with other literature, oxidation decomposition is observed at 400-530 °C [28]. Thus, the rGO content in the nanocomposites of 5rGO@VS_4, 15rGO@VS_4, and 50rGO@VS_4, can be estimated around to be 5, 15, 35% based on the weight loss over 400~530 °C. After 550 °C, a slight weight gain is seen, which is caused by oxidization of vanadium oxide [12].

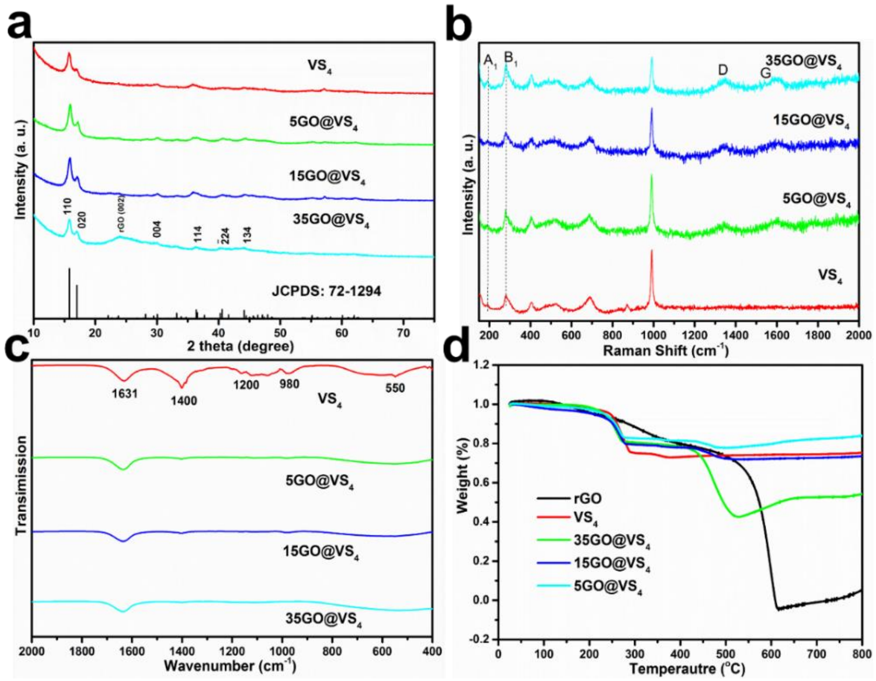

Figure 7.3 (a) XRD patterns, (b) Raman spectra and (c) FTIR spectra (d) TG of VS_4, 5rGO@VS_4, 15rGO@VS_4, and 35rGO@VS_4.

In addition to morphology and surface chemistry, BET specific surface area and pore volume are critical factors for energy storage. The BET and pore size distribution of VS_4, 5rGO@VS_4, 15rGO@VS_4, and 35rGO@VS_4 are exhibited in Figure 7.4 and Table 7.1. The Nitrogen-adsorption-desorption isotherms are characteristic of Type IV adsorption isotherms with the Type H3 hysteresis loop, revealing the presence of slit-shaped pores. The nanocomposites generally displayed a higher specific surface area compared to pure VS_4. This can be attributed to the presence of rGO. However, there is a decrease in surface area when rGO increases to 35%, which could be due to the agglomeration of rGO when an excess amount of rGO are added during the hydrothermal reaction. The large pore volume of 15rGO@VS_4 can also act as buffering spaces for volume changes of VS_4 nanowires. As such, larger pore volume not only facilitates facile diffusion of the electrolyte but also improve lithium ion insertion and extraction during cycling [29, 30].

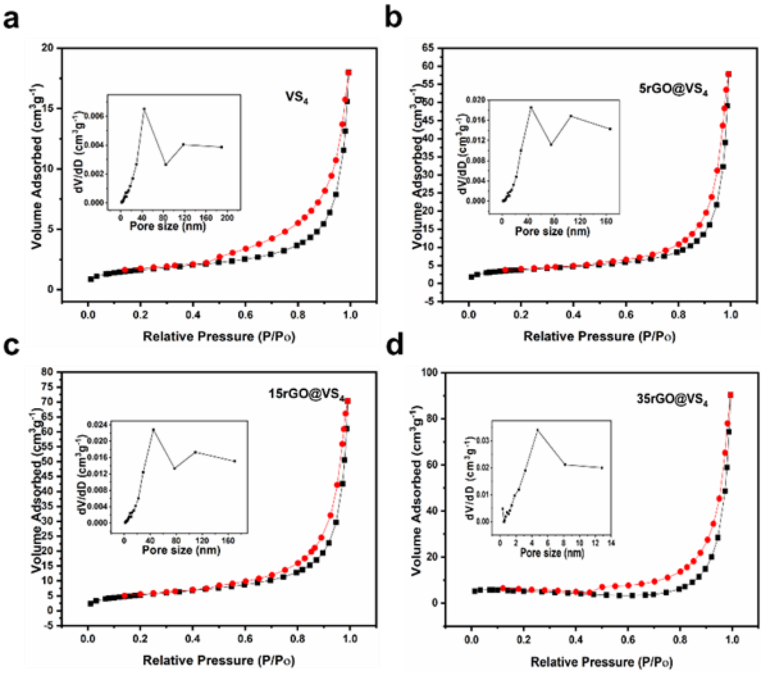

Figure 7.4 The Nitrogen-adsorption-desorption isotherms of the VS_4, 5rGO@VS_4, 15rGO@VS_4, and 35rGO@VS_4. The insets are their corresponding pore size distribution.

The electrochemical performances of VS_4, 5rGO@VS_4, 15rGO@VS_4, and 35rGO@VS_4 were evaluated and compared. Typical cyclic voltammogram (CV) curves of the 15rGO@VS_4 electrode for the first five cycles are illustrated in Figure 7.5. In the first cathodic scan, a peak at 1.61 V indicates the lithiation process from VS_4 to $Li_{3+x}VS_4$ [16]. It is noted that there is another peak around 0.64 V which is attributed to the formation of solid-electrolyte interface (SEI), decomposition of the electrolyte, and the reduction of $Li_{3+x}VS_4$ to Li_2S and V [13, 16]. In the delithiation process, two anodic peaks at 1.91 V and 2.38 V can be seen which correspond to the delithiation of Li_2S and the formation of VS_4 or $Li_{3+x}VS_4$, respectively [16]. Subsequent cycles reveal a shift in cathodic peaks toward the positive. Such could be attributed to the compositional change and structure rearrangements [12, 31, 32]. The second anodic curves were quite similar to the first cycle. From the second cycle onwards, the curves are very close and almost identical, indicating the good cycling stability for the lithiation/delithiation processes. In contrast, curves become smaller with increasing cycling numbers for samples 5rGO@VS_4, 15rGO@VS_4, and 35rGO@VS_4 (Figure 7.5). This implies the suitable amount of rGO probably is important for cycling. The peak currents of nanocomposites are generally higher than those of pure VS_4. Among them, 15rGO@VS_4 shows the highest peak current, thus indicating its highest capacity and best performance. Such a result is also in good agreement with the tested electrochemical performance which will be discussed later.

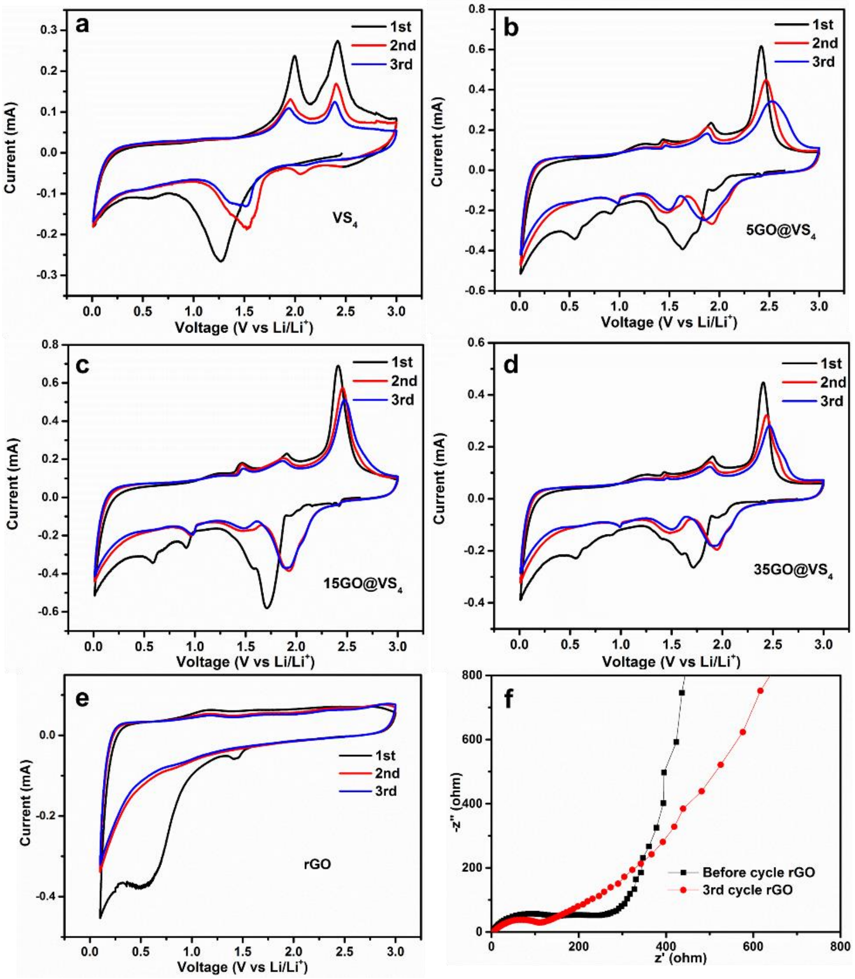

Figure 7.5 First five CVs of 5rGO@VS_4, 15rGO@VS_4, and 35rGO@VS_4 and (e) rGO as well as the EIS before cycle and after 3 cycles of CV scanning with a scan rate of 0.2 mV s^{-1} in the voltage range of 0.01-3.00 V vs Li/Li^+.

Meanwhile, in good agreement with the CV curves (Figure 7.5 and Figure 7.6), representative galvanostatic discharge/charge profiles show an obvious plateau at 1.85 V and two shallow plateaus at 1.5 V and 0.8 V. The first discharge capacity for 15rGO@VS_4 is 1481 mAh g^{-1} and the first charge capacity is 1060 mAh g^{-1}, giving rise to an initial coulombic efficiency of 71.6%. This value for VS_4, 5rGO@VS_4, and 35rGO@VS_4 is 64.8%, 66.4%, and 67.2%, respectively, suggesting a serve side reaction [33, 34]. After the first cycles, the specific capacity of pure VS_4 drops rapidly. However, the stability of VS_4/rGO nanocomposites is much improved, implying the benefits of the adding rGO.

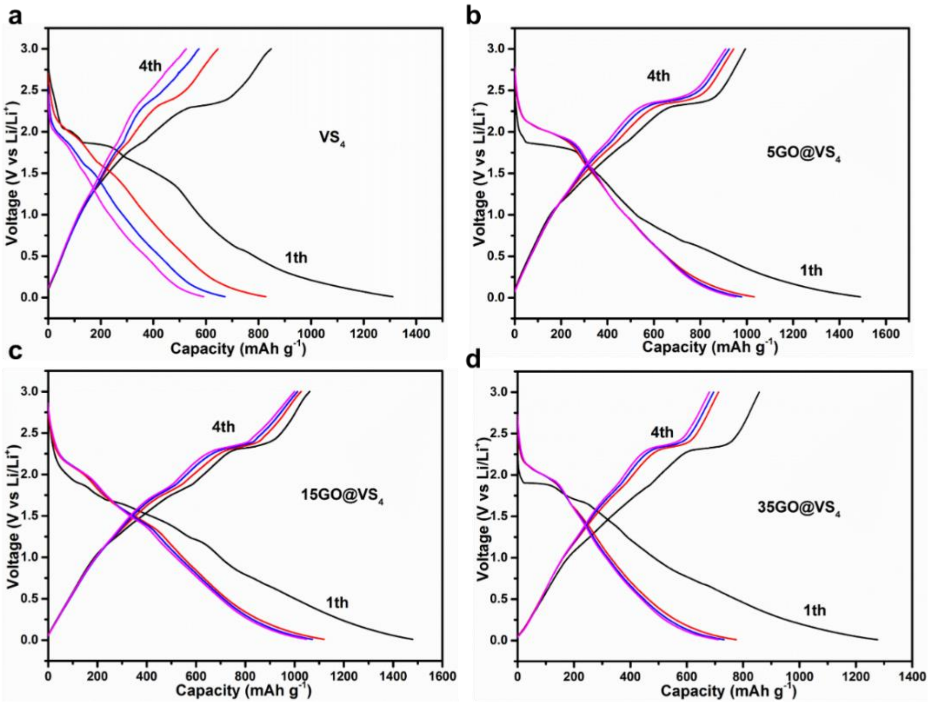

Figure 7.6 First three galvanostatic discharge-charge profiles at a current rate of 0.1 A g^{-1} in the voltage range of 0.01-3 V vs Li/Li^+ for: (a) VS4; (b) 5rGO@VS_4; (c) 15rGO@VS_4, and (d) 35rGO@VS_4.

The rate capability of VS_4, 5rGO@VS_4, 15rGO@VS_4, and 35rGO@VS_4 was evaluated by charge-discharge at various current rates from 0.1 A g^{-1} to 2 A g^{-1}. 15rGO@VS_4 delivers a high specific capacity of 1013 mAh g^{-1} at 0.1 A g^{-1}. It decreases to 960, 893, 793 and 616 mAh g^{-1}, as the current densities increase to 0.2, 0.5, 1 and 2 A g^{-1}, respectively. As the current density returns to 0.1 A g^{-1}, the capacity recovers to 1095 mAh g^{-1}. Note that all values of specific capacities for 15rGO@VS_4 are higher than those of VS_4, 5rGO@VS_4, and 35rGO@VS_4, corroborating its good rate capability. Moreover, good cycling stability has been demonstrated for 15rGO@VS_4 in which a specific capacity of 1126 mAh g^{-1} is delivered even after 100 cycles. In contrast, the specific capacities of VS_4, 5rGO@VS_4, and 35rGO@VS_4 after 100 cycles are 483, 680, and 976 mAh g^{-1}, respectively. It is worth noting that the capacity degrades in the sequential order of 15rGO@VS_4 > 5rGO@VS_4 > 35rGO@VS_4 > VS_4 (Figure 7.7), which is consistent with CV and galvanostatic discharge/charge mentioned previously (observed in Figure 7.7). In addition, the cycling performance of 5rGO@VS_4, 15rGO@VS_4, and 35rGO@VS_4 nanocomposite at a high current rate is explored. As depicted in Figure 7.7g, the reversible capacity of 15rGO@VS_4 is retained at 330 mAh g^{-1} at the current of 2 A g^{-1}, which is higher than those of 5rGO@VS_4 and 35rGO@VS_4 after 2000 cycles. Hence, the electrochemical performance of the composite was associated with the GO/VS_4 ratio (i. e. graphene content). The composite with a VS_4/rGO ratio of 15 (a.k.a 15rGO@VS_4) displayed the best result in terms of capacity retention and rate capability. The rGO could provide the structure stability and electrical conductivity, while VS_4 could contribute the total capacity. The effect of VS_4/rGO would be greater than the effect of each of them, or sum of the individuals. This phenomenon could be a synergic effect, according to previous reports [35, 36]. Moreover, 15rGO@VS_4 has the largest surface area compared to VS_4, 5rGO@VS_4, and 35rGO@VS_4, which together with its mesoporous structure is believed to favor ion diffusion and allow an easy permeability of electrolyte, contributing to its excellent electrochemical performance [37, 38].

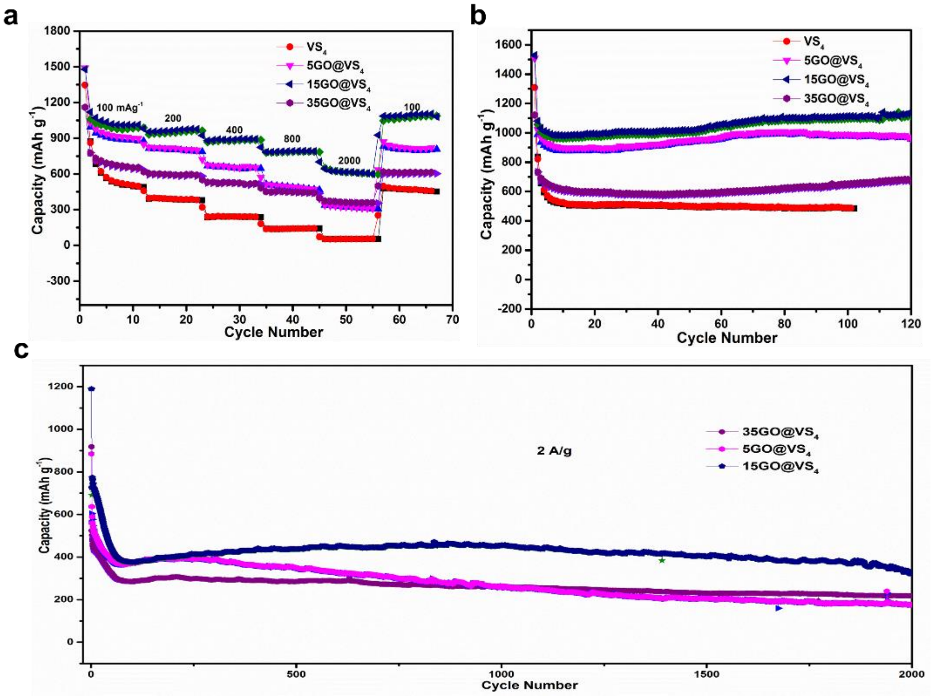

Figure 7.7 (a) Rate performance of VS_4, 5rGO@VS_4, 15rGO@VS_4, and 35rGO@VS_4 at varied current densities from 0.1 to 2 A g^{-1} in the voltage range of 0.01-3.00 V vs Li^+/Li; (b) Cycling performance of VS_4, 5rGO@VS_4, 15rGO@VS_4, and 35rGO@VS_4 at 0.1 A g^{-1} (g) Long cycling performance of 5rGO@VS_4, 15rGO@VS_4, and 35rGO@VS_4 at a high current rate of 2 A g^{-1}.

The kinetic properties for 15rGO@VS_4 are further supported by CV testing at different sweep rates (Figure 7.8a-d). The reduction peaks shift to the lower potential range, and oxidation peaks shift to the higher potential range. This is due to the high polarization with increasing sweep rates [39]. Figure 7.8e shows the relationship between reduction peak current I_p and the square root of the scan root $\nu^{1/2}$. The linear relation indicates that reaction is a Li-ion diffusion controlled. Based on the Randles-sevcik equation [40]:

$$I_p = (2.69 \times 10^5)n^{3/2}AD_0^{1/2}C_0\nu^{1/2} \qquad (1)$$

where I_p is the peak current, A is the apparent surface area, D_0 is the diffusion coefficient, C_0 is the maximum Li^+ concentration, and ν is the CV scanning rate. The diffusion coefficient was calculated to be 1.694 x 10^{-12} cm^2 s^{-1} for 15rGO@VS_4, which is higher than those of VS_4 (1.578 x 10^{-13}), 5rGO@VS_4 (4.948 x 10^{-13}), and 35rGO@VS_4 (2.680 x 10^{-13}). The enhanced kinetics may explain the better performance of 15rGO@VS_4. To further investigate the effect of different morphologies on the electrochemical performance, the total charge storage at a certain sweep rate was also quantified by separating the specific contribution from the capacitive and diffusion-controlled charge at a fixed voltage [41]. Results obtained (Figure 7.8f) reveal that 15rGO@VS_4 exhibited an intercalation effects contribution ratio (~76%), which is equal or higher than that of VS_4 (92%), 5rGO@VS_4 (81%), and 35rGO@VS_4 (62%). It is observed that the intercalation effect contribution ratio decreases with the increasing amount of rGO. This is reasonable because rGO normally contribute the capacitive charge. Suitable amount of intercalation and capacitive charge contribution renders 15rGO@VS_4 the highest rate and cycling performance.

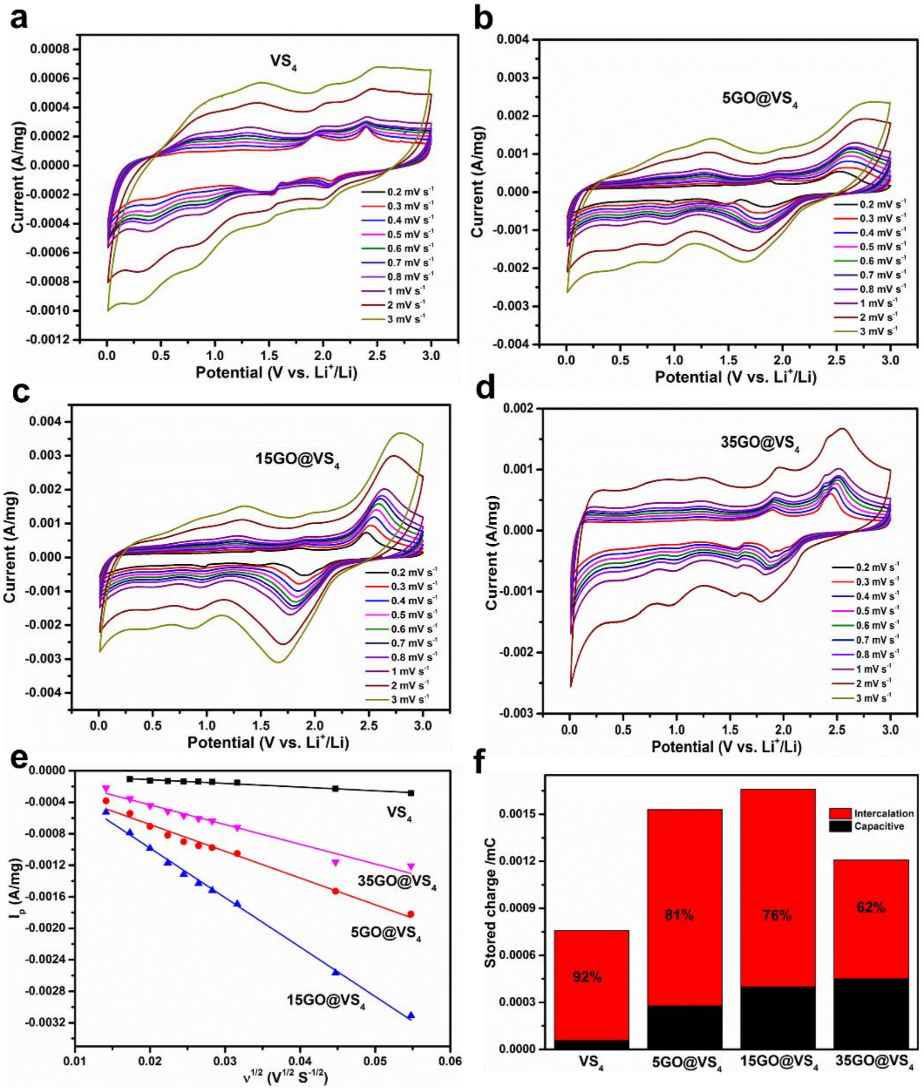

Figure 7.8 CV curves for (a) VS_4; (b) 5rGO@VS_4; (c) 15rGO@VS_4, and (d) 35rGO@VS_4 at a series of scan rates between 0.01 to 3V. (e) Dependence of reduction peak current on the square root of scan rate. ; (f) Linear fitting of z' vs $\omega^{-1/2}$ relationship. (f) Bar chart showing total stored charge with percentage contribution from capacitive and intercalation at 0.3 mV/s for all samples with stored charge calculated by integrating the CV area according to the equation: $Q = \int \left(\frac{i}{v}\right) dV$ [42].

To gain more insight into lithium storage behaviors, such as kinetics of lithium-ion diffusion, EIS measurements after a series of cycles were conducted (Figure 7.9). R_s is the resistance due to the electrolyte, separator and electrical contact resistance, while the semicircle represents the SEI films and charge-transfer resistance R_{ct} [29, 43]. Excluding the EIS for the OCV, the Rct decreases with the cycling number and such is probably due to the activation of active material. From 5rGO@VS$_4$, 15rGO@VS$_4$, to 35rGO@VS$_4$, the semicircle diameter reduces with increasing amount of rGO. This is reasonable as the inert rGO protect the VS$_4$ active material from excessive contacting with electrolyte and generating more SEI. Meanwhile, the electrical conductive rGO enhance the overall electrical conductivity of nanocomposites, resulting in lower charge-transfer resistance. It is worth noting the R_s of VS$_4$ is higher compared to the nanocomposites. Results mentioned abovee confirm the advantages of compositing with rGO.

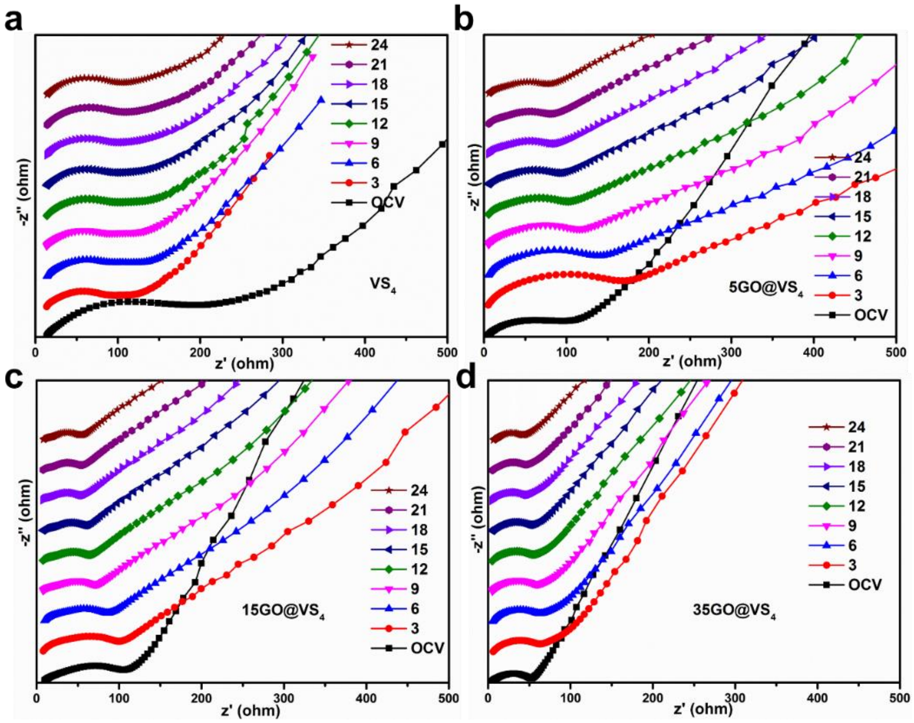

Figure 7.9 EIS profiles of (a) VS$_4$, (b) 5rGO@VS$_4$, (c) 15rGO@VS$_4$, and (d) 35rGO@VS$_4$ after a series of cycles (OCV, 3, 6, 9, 12, 15, 18, 21, and 24).

7.4 Conclusion

VS_4 nanowires are successfully grown on rGO via in-situ facile solvothermal synthesis approach. Different amount of rGO compositing with VS4 (i. e. VS_4, 5rGO@VS_4, 15rGO@VS_4, and 35rGO@VS_4) were compared and investigated in terms of their electrochemical performance and the physical structures. VS_4 in-situ grown on rGO has proven to enhance the electrochemical performance of pure VS_4 whereby it exceeds the performances from literature. In addition, 15rGO@VS_4 is found to have the best rate capability and cycling performance, even at a high current rate of 2 Ag-1. This could attribute its suitable amount of rGO being added, high surface area, larger pore volume, and VS_4 nanowires structure, in which Li+ insertion/extraction, as well as the accessibility of electrolyte, are enhanced. Kinetic parameters such as apparent diffusion coefficient derived from sweep rate dependent CV curves further support the results obtained previously. Moreover, EIS curves of VS_4, 5rGO@VS_4, 15rGO@VS_4, and 35rGO@VS_4 after various cycles are compared and studied. The advantages of compositing with rGO are revealed and highlighted. Our work not only provides a facile way to synthesize VS_4 in-situ grown on rGO, but also promotes a better understanding of Li^+ storage behavior in VS_4, which could be applied to many other vanadium-based materials.

References

[1] M. Armand, J.M.M. Tarascon, Nature, 451 (2008) 652-657.

[2] M. Winter, J.O. Besenhard, M.E. Spahr, P. Novák, Adv. Mater., 10 (1998) 725-763.

[3] A. Casimir, H. Zhang, O. Ogoke, J.C. Amine, J. Lu, G. Wu, Nano Energy, 27 (2016) 359-376.

[4] G. Derrien, J. Hassoun, S. Panero, Adv. Mater., 19 (2007) 2336–2340.

[5] X. Sun, G.P. Hao, X. Lu, L. Xi, B. Liu, W. Si, C. Ma, J. Mater. Chem. A, 4 (2016) 10166-10173.

[6] J. Liu, W. Zhou, L. Lai, H. Yang, S. Lim, Y. Zhen, T. Yu, Z. Shen, J. Lin, Nano Energy, 2 (2013) 726-732.

[7] K. Bindumadhavan, S.K. Srivastava, Chem. Commun., 49 (2013) 1823-1825

[8] J. Xiao, L. Wan, S. Yang, F. Xiao, S. Wang, Nano Lett., 14 (2014) 831–838.

[9] H. Chen, J. Jiang, L. Zhang, H. Wan, T. Qi, D. Xia, Nanoscale, 5 (2013) 8879-8883

[10] H. Wang, H. Jiang, Y. Hu, P. Sáha, Q. Cheng, C. Li, Chem. Eng. Sci., 174 (2017) 104-111.

[11] Z. Deng, H. Jiang, Y. Hu, Y. Liu, L. Zhang, H. Liu, C. Li, Adv. Mater., 29 (2017) 1603020.

[12] Y. Zhou, J. Tian, H. Xu, J. Yang, Y. Qian, Energy Storage Mater., 6 (2017) 149-156.

[13] X. Xu, S. Jeong, C. Rout, P. Oh, M. Ko, H. Kim, M. Kim, R. Cao, H. Shin, J. Cho, J. Mater. Chem. A, 2 (2014) 10847-10853.

[14] Y. Zhou, Y. Li, J. Yang, J. Tian, H. Xu, J. Yang, W. Fan, ACS Appl. Mater. Interfaces, 8 (2016) 18797-18805.

[15] C. Rout, B.-H. Kim, X. Xu, J. Yang, H. Jeong, D. Odkhuu, N. Park, J. Cho, H. Shin, J. Am. Chem. Soc., 135 (2013) 8720-8725.

[16] S. Britto, M. Leskes, X. Hua, C.-A. Hébert, H. Shin, S. Clarke, O. Borkiewicz, K.W. Chapman, R. Seshadri, J. Cho, C.P. Grey, J. Am. Chem. Soc., 137 (2015) 8499-8508.

[17] Q. Li, Y. Chen, J. He, F. Fu, J. Lin, W. Zhang, J. Alloys Compd., 685 (2016) 294-299.

[18] R. Sun, Q. Wei, Q. Li, W. Luo, Q. An, J. Sheng, D. Wang, W. Chen, L. Mai, ACS Appl. Mater. Interfaces, 7 (2015) 20902–20908.

[19] Y. Zou, Y. Wang, Nanoscale, 3 (2011) 2615-2620.

[20] Y. Zou, J. Kan, Y. Wang, The Journal of Physical Chemistry C, 115 (2011) 20747-20753.

[21] L. Ji, Z. Tan, T. Kuykendall, E.J. An, Y. Fu, V. Battaglia, Y. Zhang, Energy & Environmental Science, 4 (2011) 3611-3616.

[22] Y. Zou, Y. Wang, Acs Nano, 5 (2011) 8108-8114.

[23] B. Luo, B. Wang, M. Liang, J. Ning, X. Li, L. Zhi, Advanced Materials, 24 (2012) 1405-1409.

[24] N. Mahmood, C. Zhang, J. Jiang, F. Liu, Y. Hou, Chemistry-A European Journal, 19 (2013) 5183-5190.

[25] W.F. Hillebrand, J. Am. Chem. Soc., 29 (1907) 1019-1029.

[26] W. Fang, H. Zhao, Y. Xie, J. Fang, J. Xu, Z. Chen, ACS Appl. Mater. Interfaces, 7 (2015) 13044-13052.

[27] C. Zhang, H. Song, C. Liu, Y. Liu, C. Zhang, X. Nan, G. Cao, Advanced Functional Materials, 25 (2015) 3497-3504.

[28] W. Guo, D. Wu, International Journal of Hydrogen Energy, 39 (2014) 16832-16840.

[29] X. Lu, F. Yang, Y. Wang, X. Geng, P. Xiao, Journal of Alloys and Compounds, 636 (2015) 202-210.

[30] X. Li, X. Zhang, Y. Zhao, D. Feng, Z. Su, Y. Zhang, Electrochimica Acta, 191 (2016) 215-222.

[31] Z. Zheng, Y. Wang, A. Zhang, T. Zhang, F. Cheng, J. Power Sources, 198 (2012) 229-235.

[32] C.T. Cherian, J. Sundaramurthy, M. Kalaivani, J. Mater. Chem., 22 (2012) 12198-12204.

[33] S. Laruelle, S. Grugeon, P. Poizot, M. Dolle, J. Electrochem. Soc., 149 (2002) A627-A634.

[34] G. Binotto, D. Larcher, A.S. Prakash, Chem. Mater., 19 (2007) 3032–3040.

[35] Z.-S. Wu, W. Ren, L. Wen, L. Gao, J. Zhao, Z. Chen, G. Zhou, F. Li, H.-M. Cheng, ACS nano, 4 (2010) 3187-3194.

[36] X. Wang, X. Zhou, K. Yao, J. Zhang, Z. Liu, Carbon, 49 (2011) 133-139.

[37] F.M. Balcı, Ö. Kudu, E. Yılmaz, Chem. Eur. J., 22 (2016) 18873–18880.

[38] J. Hu, C.F. Sun, E. Gillette, Z. Gui, Y.H. Wang, S.B. Lee, Nanoscale, 8 (2016) 12958-12969.

[39] Z. Chen, J. Wang, D. Chao, T. Baikie, L. Bai, S. Chen, Y. Zhao, T. Sum, J. Lin, Z. Shen, Sci. Rep., 6 (2016) 25771.

[40] J. Liu, Z. Chen, W. Xuan, S. Chen, B. Zhang, J. Wang, H. Wang, B. Tian, M. Chen, X. Fan, Y. Huang, T. Sum, J. Lin, Z. Shen, ACS Nano, 11 (2017) 6911–6920.

[41] J. Liu, J. Wang, C. Xu, H. Jiang, C. Li, L. Zhang, J. Lin, Z.X. Shen, Adv.Sci., (2017) 1700322.

[42] P. Yu, C. Li, X. Guo, J. Phys. Chem. C, 118 (2014) 10616-10624.

[43] E. Barsoukov, J.R. Macdonald, Impedance spectroscopy: theory, experiment, and applications, John Wiley & Sons, 2005.

Chapter 8

Discussion and Future work

In this chapter, the threads running through each part of the thesis are drawn together: the findings in Chapter 4-6 are summarized to prove the true/false of the hypotheses and the main conclusions are drawn. Furthermore, the key findings and contributions of PhD work are highlighted. After that, the opportunities and strategies for future are proposed with some reconnaissance work which did not warrant a complete chapter.

8.1 Conclusions

Li_3VO_4 has been researched since 2013 for a lithium-ion battery application. This is due to its safe operating voltage (0.5-1.0 V vs. Li/Li^+) and larger capacity compared to commercial graphite. Until now, not much research work has been conducted on the morphologies effect on the electrochemical performance for LIB application. In this thesis, morphologies effect of LVO in lithium storage was investigated. Facile carbon coating strategy was developed to improve the electrical conductivity and electrochemical performance. Apart from vanadium oxide, VS_4 with various morphologies were successfully synthesized and investigated systematically.

Firstly, the influence of LVO morphologies on the corresponding electrochemical performance is studied in chapter 4. A range of morphologies (e.g., single-crystal nanorods, spherical-assembly, flower shape, and bulk-shape) has been designed via solvothermal approach. Comprehensive characterization equipment like XRD, Raman, BET, SEM, and FTIR were utilized, and electrochemical performance was tested. Experimental results show that morphology has a big impact on lithium storage behavior. Specifically, Li^+ ion storage has a decrement in the order of nanorods, sphere, flower, and bulk. Possible reasons behind the superior performance of LVO nanorods were investigated. Such excellent performance could be attributed to its unique hierarchical one-dimensional nanorod structure, high specific surface area, small particle size, and high crystallinity. Furthermore, the calculated lithium-ion diffusion coefficient of LVO nanorod is the highest, which further confirm its excellent performance. However, the cycling stability of LVO nanorods is inferior, especially at the high current rate. This could be due to the aggregation of adjacent nanorods during cycling. Despite the addition of carbon coating, stability is barely improved. On the other hand, the sphere morphology displayed excellent cycling stability. Thus, combination of the advantages of sphere structure with nanorod structure could be plausible to improve the stability while maintaining the high capacity.

To take advantage of the positive attributes of both nanorod and sphere structure, hierarchical LVO microspheres were fabricated through a simple solvothermal method with the following carbon coating process as seen in chapter 5. It is verified that the hierarchical LVO microspheres demonstrate a better electrochemical performance compared to that of nanorods in both low and high current densities. This could be attributed to its hierarchical structure, which allows better tolerance to volumetric change as well as ameliorates the agglomeration during cycling. Furthermore, the carbon coating on the hierarchical microspheres enhances the extrinsic electrical conductivity of LVO, thus reducing the charge transfer resistance which is evident in by the EIS result.

Due to the high demand for the electric automotive and electric energy storage system, anode material with higher capacity is desirable. Vanadium-based sulfide material, specifically VS_4, was investigated due to its high theoretical specific capacity of 1196 mAh/g. Till today, little research has been conducted on this material due to the challenges associated with VS_4 fabrication. In chapter 6, VS_4 anode materials with controllable morphologies from hierarchical microflower, octopus-like structure, sea grass-like structure, to the urchin-like structure have been successfully synthesized using different alcohols as solvents. Their structures and electrochemical properties with various morphologies were systematically investigated, and the structure-property relationship was established. Experimental results reveal Li^+ ion storage in VS_4 is highly dependent on physical features such as the morphology, crystallite size, and specific surface area. According to this study, electrochemical performance degrades in the order of urchin-like VS_4 > octopus-like VS_4 > sea grass-like VS_4 > flower-like VS_4. Amongst them, urchin-like VS_4 demonstrates the best electrochemical performance benefiting from its peculiar structure, which possesses large surface area to accommodate high volume change to a certain extent, and single-crystal thorns that provide fast electron transportation. Kinetic parameters derived from EIS spectra and sweep rate dependent CV curves, such as charge transfer resistances, Li^+ ion apparent diffusion coefficients and stored charge ratio of capacitive and intercalation contributions, are in good agreement with this claim. In addition, EIS experiment was performed during the first discharge-charge process to study the formation of the solid electrolyte interface (SEI) on urchin-like VS_4 and the kinetics of lithium-ion diffusion. This study also provides invaluable guidance for morphology-controlled synthesis tailored for optimal electrochemical performance.

To further improve the electrochemical performance of VS_4, incorporating VS_4 with rGO was conducted. As mentioned earlier, the growth of active material with special morphologies on rGO could improve the electrochemical performance much more compared to that of mechanically mixed rGO and VS_4. However, it is challenging to grow VS_4 with peculiar morphologies on rGO, until now it has been rarely reported. Here, the growth of VS_4 nanowires directly on rGO was demonstrated. In comparison to pristine VS_4, rGO@VS_4 shows much improved performance in terms of capacity and rate performance. A series of VS_4 nanocomposites (5, 15, and 35 wt% rGO) were synthesized and compared. It is found that 15 wt% rGO@VS_4 shows the best performance. These prepared samples are fully characterized and kinetic parameters like charge transfer resistance and lithium ion diffusion coefficients are calculated. The detailed explanation is given.

8.2 Significant Contributions

Based on the studies carried out in the thesis, several novel findings and outcomes have been made and are summarized in the sections below.

Firstly, morphology and electrochemical performance relationship have rarely been studied on LVO. In chapter 4 and 5, LVO with various morphologies have been synthesized and compared using comprehensive characterization tools. Their kinetic parameters like lithium ion diffusion coefficients and charge transfer resistance have been calculated from various CV rates and EIS spectra. New morphologies like single-crystal nanorods and hierarchical microspheres have been successfully synthesized via a simple solvothermal method. Carbon coating on nanorods and hierarchical microspheres further enhance the electrochemical performance.

Secondly, VS_4 with new morphologies like urchin-like has been synthesized via a facile solvothermal method. Understanding in the effect of morphologies on electrochemical performance, Li^+ ion storage, and kinetic behaviors in VS_4 has been studied in chapter 6.

Thirdly, a facile synthesis approach of VS_4 nanowires in-situ grown on rGO has been successfully demonstrated. Different amounts of rGO loading in VS_4 nanocomposite are synthesized and investigated. This is the first time reported.

8.3 Reconnaissance Results and Future works

8.3.1 Doping LVO with various transitional metal elements (Ti^{4+}, Mo^{6+}, W^{6+}, et.al)

Cr doped Li_3VO_4 was prepared by solid-state synthesis using Cr_2O_3 as Cr source and followed by calcination [1]. The Li vacancies generated by Cr doping contributed to its high conductivity, and no impurity phases were shown with the Cr doping up to 10%. However, this Cr doped Li_3VO_4 was not tested in Lithium-ion battery, which can be part of my plan. $LiSnVO_4$ was synthesized by sol-gel technique and exhibited irreversible discharge capacity of 1270 mAh g^{-1} at first cycle, followed by a reversible capacity of 211 mAh g^{-1} [2]. $LiSnVO_4$ was also reported using solid-state reaction and delivered a capacity of 700mAh g^{-1} at a low current rate of 50 mA g^{-1}. Both $LiCuVO_4$ and $LiSnVO_4$ had low first coulombic efficiency because metallic Cu and Sn were produced, which revealed the same mechanism as conversion reaction; after the 1st discharge, the $LiSnVO_4$/or $LiCuVO_4$ converts to Li_3VO_4 and the subsequent mechanism followed that of Li_3VO_4 [3]. However, the alloying mechanism of Sn is also involved in $LiSnVO_4$. Since the doping on Li_3VO_4 is still insufficient, doping with transition metals can be conducted to improve the intrinsic electronic and ionic conductivities of Li_3VO_4.

Different Ti doping LVO by solid-state reaction

Rietveld refinement method is used to gain a better understanding of the crystal structure of LVO. Figure 8.1 shows the observed, calculated and error XRD patterns for $Li_{3+x}Ti_xV_{3-x}O_4$ (x=0, 0.01, 0.03, and 0.05). The experimental result matches well with the calculated XRD pattern and no impurity peaks are visible approving that Ti atoms have successfully doped inside LVO.

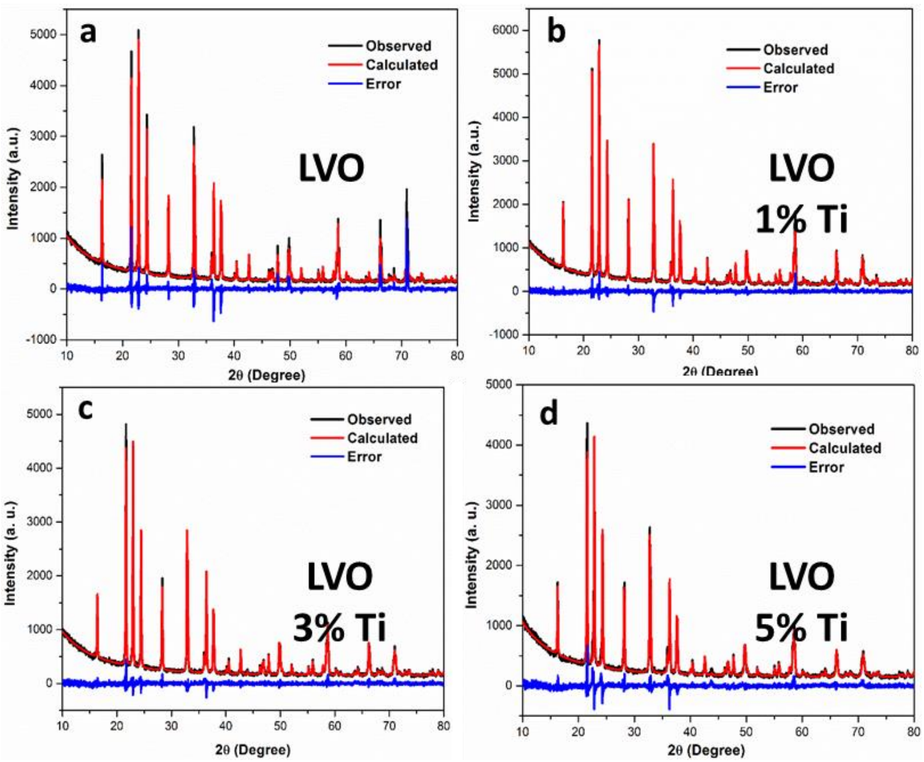

Figure 8.1 Final observed, calculated, and error profiles with Rietveld refinements for a) Li_3VO_4; b) $Li_{3.01}Ti_{0.01}V_{0.99}O_4$; c) $Li_{3.03}Ti_{0.03}V_{0.97}O_4$ d) $Li_{3.05}Ti_{0.05}V_{0.95}O_4$.

Mo^{6+} doped LVO and W^{6+} doped LVO

Mo^{6+} doped LVO and W^{6+} doped LVO were also conducted by the solid-state method (Figure 8.2). In order to minimize the doped Li_3VO_4 particle size, ammonium metatungstate hydrate and ammonium molybdate tetrhydrate were used as dopant precursors in solid-state reaction, respectively. However, small ammount of impurity is identified in LVO 3%Mo, LVO 5%Mo, LVO 3%W and LVO 5%W. According to the XRD database, they are molybdate oxide or tungsten oxide. The sol-gel method is suggested to be used in future as this method allows the mixture of chemicals at an atomic level leading to a small particle size.

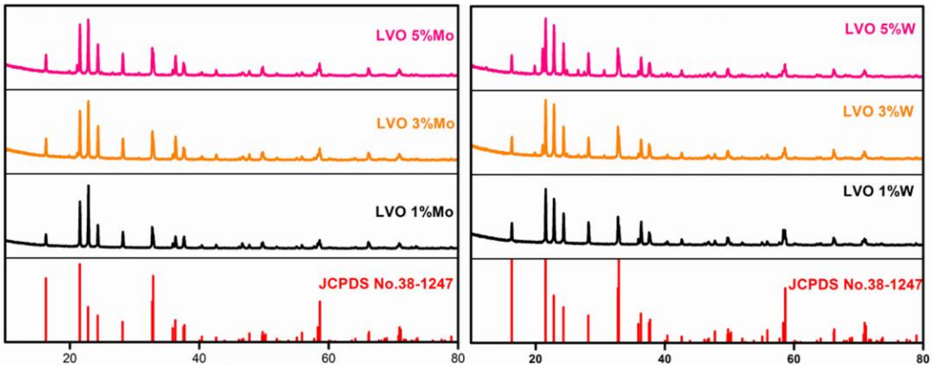

Figure 8.2 Mo^{6+} doped LVO and W^{6+} doped LVO.

Select proper dopant and optimize the doping process for LVO.

The α-V_2O_5, similar to Li_3VO_4, has a layered structure with distorted close-packed oxygen. This intrinsic layered structure contributes to the fast capacity fading. Heteroatoms such as Cr, Al, Sn, and Cu have been reported to improve the cycling properties of α-V_2O_5 by doping into the lattice. However, only very few 3d transition metal ions have been applied as dopants in Li_3VO_4 so far. Doping Li_3VO_4 with elements such as Ti^{4+}, W^{6+}, Mo^{6+}, Nb^{5+} may yield similar effects to that of α-V_2O_5 since they have the similar crystal structure. It is well known that doping can not only alter Li ion diffusion coefficient by distorting lattice structure arrangement, but also increase electronic conductivity by introducing additional electrons or holes. Moreover, dopants may hinder the normal growth of crystals resulting in the reduction of particle size. Doping is a part of my future study, and the impacts of doping on the cycling performance, working potential and the rate capability of LVO will be investigated based on the criteria for the selection of suitable dopants as following:

1) The dopant ion should have 3d band electrons to provide free carriers, which is crucial for high electronic conductivity.
2) Design the dopant ion out of the pathway for Li ion diffusion. Otherwise, the rate performance will drop.
3) The redox potential of dopant ion should be lower than the main ions. For example, LTO has a Ti^{+4}/Ti^{+3} at 1.5 V (vs Li/Li^+) and if it is doped with Fe^{2+}/Fe^{3+} (2.2 V), Fe^{2+}/Fe^{3+} will happen first because its relatively higher redox reaction potential.

8.3.2 Annealing of urchin-like VS_4 to further enhance electrochemical performance

Urchin-like VS_4 in chapter 6 has the best electrochemical performance as anode material for LIB. However, still, there is room to improve. Herein, to further enhance the electrochemical performance for urchin-VS_4, annealing strategy is applied on this material to further increase its crystallinity since the low crystallinity is suspected to be the cause that restricts the material to achieve high capacity. The annealed VS_4 is shown in Figure 8.3. As can be seen, the morphologies have changed from urchin-like to particle shape with around 100-200 nm size.

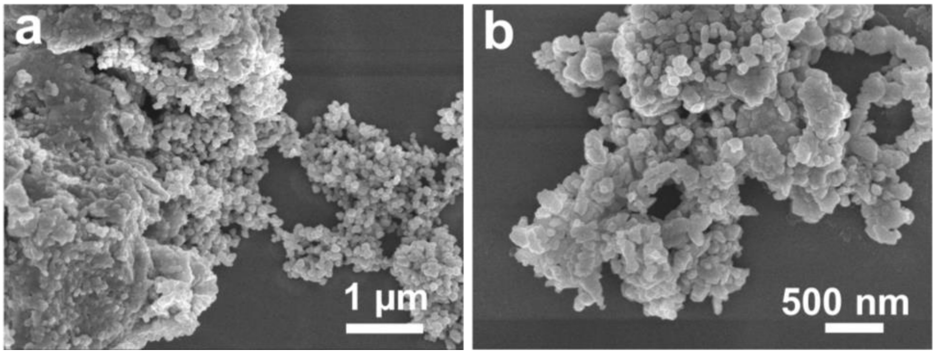

Figure 8.3 SEM images of B-VS4 after annealing at 350 C for 30 mins.

The phase of the annealed sample is characterized by XRD (Figure 8.4) and shows that other phases V_3S_5 and S appear after the annealing process. This is due to the easy decomposition nature of VS_4.

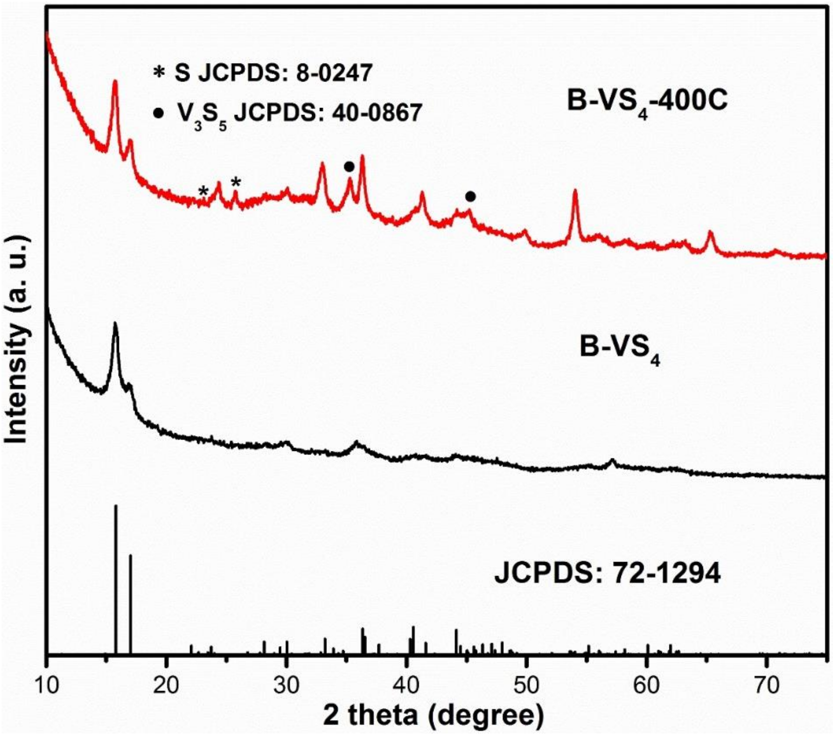

Figure 8.4 XRD patterns of the B-VS_4 and annealed VS_4 at 350 C at 30 mins.

Rate performance and cycling performance were tested to further check its electrochemical performance (Figure 8.5). The rate and cycling performance improved significantly after annealing. Further cauterizations need to be done to clarify the reasons that making the performance improved.

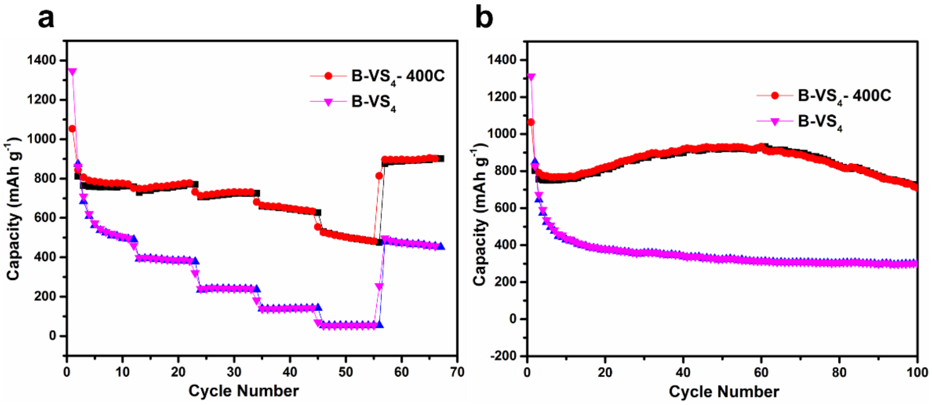

Figure 8.5 (a) rate performance and (b) cycling performance of B-VS_4 and annealed VS_4 at 350 C at 30 mins.

References

[1] V. Massarotti, D. Capsoni, M. Bini, P. Mustarelli, G. Chiodelli, C.B. Azzoni, P. Galinetto, M.C. Mozzati, The journal of physical chemistry. B, 109 (2005) 14845-14851.

[2] L.P. Teo, M.H. Buraidah, A.K. Arof, Ionics, (2015) 2393-2399.

[3] M. Li, X. Yang, C. Wang, N. Chen, F. Hu, X. Bie, Y. Wei, F. Du, G. Chen, J. Mater. Chem. A, (2015) 586-592.

List of publications

1. **Yang, G**.; Zhang, B.; Feng, J.; Lu, Y.; Wang, Z.; Aravindan, V.; Aravind, M.; Liu, J.; Srinivasan, M.; Shen, Z.; Huang, Y., Morphology controlled lithium storage in Li_3VO_4 anodes. ***Journal of Materials Chemistry A*** **2018,** *6*, 456-463.

2. **Yang, G**.; Feng, J.; Zhang, B.; Aravindan, V.; Peng, D.; Cao, X.; Yu, H.; Madhavi, S.; Huang, Y., Solvothermal synthesis of Li_3VO_4: Morphology control and electrochemical performance as anode for lithium-ion batteries. ***International Journal of Hydrogen Energy*** **2017,** *42*, 22167-22174.

3. **Yang, G.**; Zhang, B.; Feng, J.; Wang, H; Ma, M.; Huang, K; Liu, J; Madhavi, S.; Shen, Z.; Huang, Y., High crystallinity urchin-like VS_4 anode for high-performance lithium ion storage. **ACS Applied Materials & Interfaces** 2018.

4. Zhang, B.#; **Yang, G**.**#**; Li, C.; Huang, K.; Wu, J.; Hao, S.; Feng, J.; Peng, D.; Huang, Y., Phase controllable fabrication of zinc cobalt sulfide hollow polyhedra as high-performance electrocatalysts for the hydrogen evolution reaction. ***Nanoscale*** **2018**. (**Co-first author**)

3. Zhang, B.; Chen, B.; Wu, J.; Hao, S.; **Yang, G**.; Cao, X.; Jing, L.; Zhu, M.; Tsang, S. H.; Teo, E. H. T., The Electrochemical Response of Single Crystalline Copper Nanowires to Atmospheric Air and Aqueous Solution. ***Small*** **2017,** *13*.

4. Muthiah, A.; Baikie, T.; Ulaganathan, M.; Copley, M.; **Yang, G**.; Aravindan, V.; Srinivasan, M., Structural, Thermal, and Electrochemical Studies of Novel $Li_2Co_xMn_{1-x}(SO_4)_2$ Bimetallic Sulfates. ***The Journal of Physical Chemistry C*** **2017,** *121*, 24971-24978.

5. 7. Yao, X.; Wang, D.; Zhao, X.; Ma, S.; Bassi, P. S.; **Yang, G**.; Chen, W.; Chen, Z.; Sritharan, T., Scale-Up of $BiVO_4$ Photoanode for Water Splitting in a

Photoelectrochemical Cell: Issues and Challenges. **Energy Technology 2018**, 6, 100-109.

6. 8. Huang K, Peng D, Zhang B, Cao X, Hao S, **Yang G**, et al. Three dimension (3D) hierarchical electrode (Au/rGO/CoPt 3) for electrooxidation of ethanol in fuel cells. International Journal of Hydrogen Energy. 2018

APPENDIX-I

Morphological and carbon coating effect on LVO nanorod

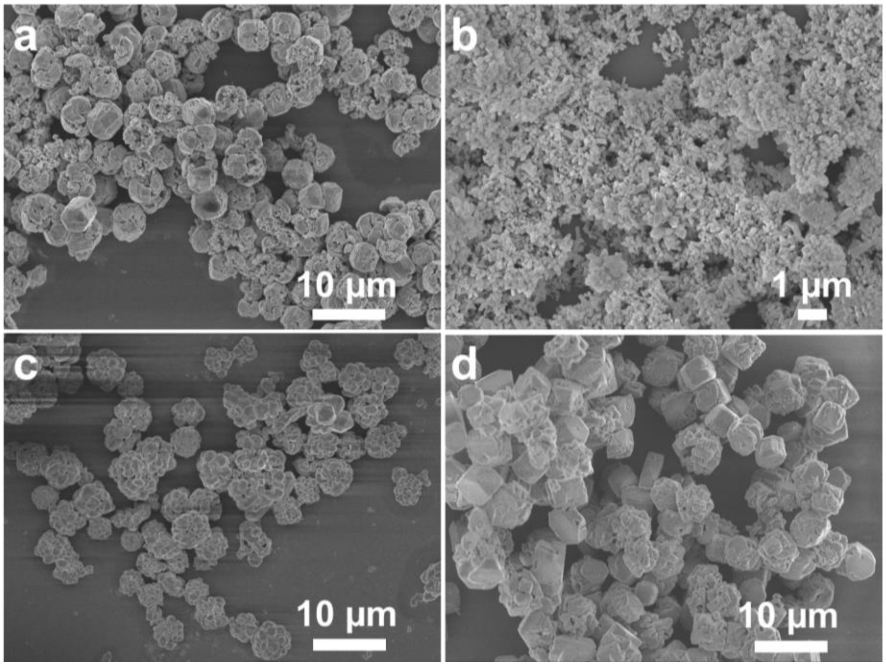

Figure A.1 SEM images of LVO of (a) LVO-SPHERE, (b) LVO-ROD, (c) LVO-FLOWER, (d) LVO-BULK.

Table A. 1 FTIR peaks and their assignments

Peaks	Band assignment	Reference
3433	ν(OH) water	[1]
2344	CO_2	[2]
1637	δ(OH)	[1]
1420	Amorphous carbon	[1]
851	ν_s(V-O)	[3]
806	ν_{as}(V-O)	[3]
466	ν_s(V-O-V)	[1]

ν: stretching; δ: bending.

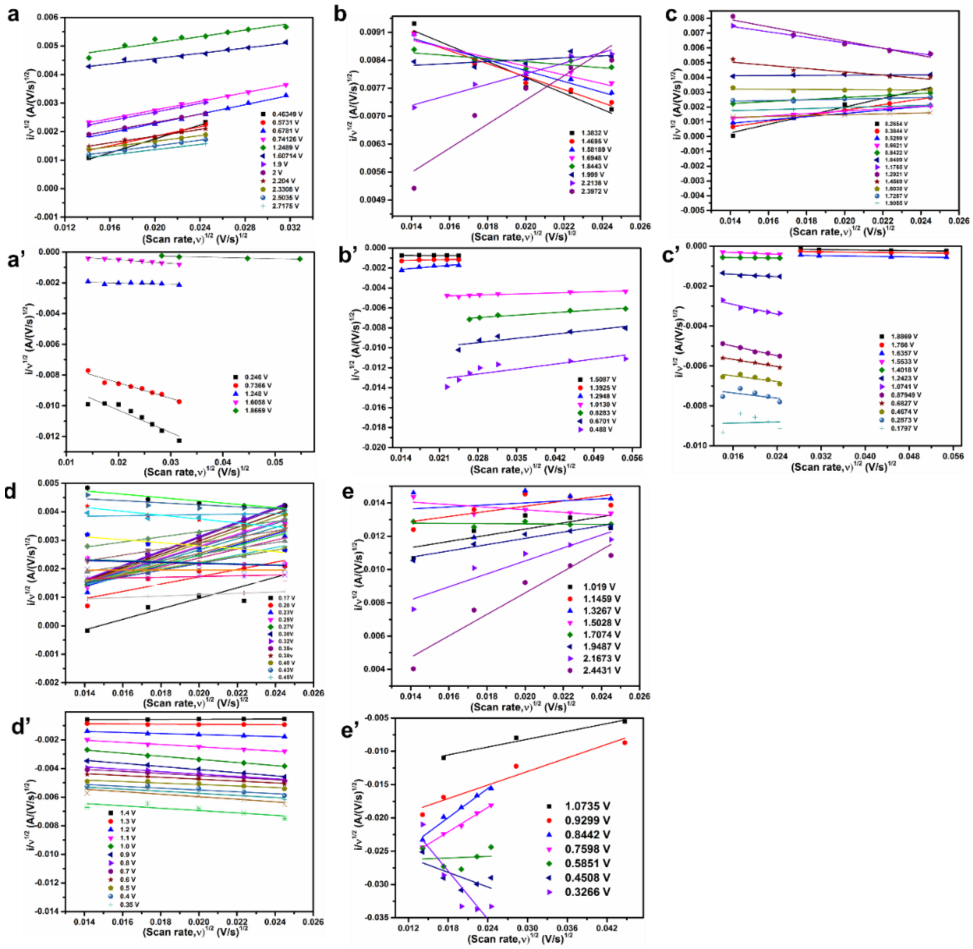

Figure A. 2 (a, a'), (b, b'), (c, c'), (d, d') and (e, e') are the plots of $v^{1/2}$ vs $i/v^{1/2}$ for LVO-SPHERE, LVO-ROD, LVO-FLOWER, LVO-BULK, and C@LVO-ROD at both anodic and cathodic scan. The plots are used for calculating constants k_1 and k_2 at different potentials of the cathodic scan and anodic scan.

The total current at a fixed potential can be described using the following equation: I(V) = K1v + K2v1/2, where K1v and K2v1/2 represent the capacitive contribution and intercalation contribution, respectively. K1 and k2 can be obtained from the slope and y-axis intercept of the straight line: i(V)/v1/2 = k1v1/2 + k2, as shown in Figure S9. Thus, the contribution from capacitive and intercalation can be calculated and each component contribution at scan rate of 0.2 mV/s is shown in Figure S8f.[4, 5]

Table A. 2 Summary of the electrochemical performance of Li_3VO_4 from literature

Material	**Current (mA g^{-1})** **1C ≈ 394 mA g^{-1}**	**Reversible capacity** **mAh g^{-1}/cycle no.**	**Ref.**
Li_3VO_4	20 mA g^{-1}	283/25	[6]
Li_3VO_4	0.25 C	396/100	[7]
Li_3VO_4/C	1 C	394/100	[8]
Li_3VO_4	0.2 C	164/100 197/100	[9]
Li_3VO_4/graphene	20 mA g^{-1}	378/50	[10]
Li_3VO_4/C	0.8 C	363/40	[11]
Li_3VO_4/graphite	156 mA g^{-1}	468/100	[12]
Li_3VO_4/CNTs	2000 mA g^{-1}	250/2000	[13]
Li_3VO_4/graphene	0.2 C	453/200	[14]
Li_3VO_4/graphene	5 C	163/5000	[15]
Li_3VO_4/Ni	0.3 C	378/100	[16]
Li_3VO_4/C	20 mA g^{-1}	245/50	[17]
Li_3VO_4	0.1 C	311/50	[18]
Li_3VO_4/C	0.1 C	401/50	[19]
Li_3VO_4/C-Ni	1800 mA g^{-1}	325/2000	[20]
Li_3VO_4/3D graphene	2 A g^{-1}	Li_3VO_4/3D GN 356/200 Li_3VO_4+3D GN 144/200	[21]
Li_3VO_4/c	150 mA g^{-1}	542/300	[22]
Li_3VO_4/N-C	150 mA g^{-1}	544/800	[23]
Li_3VO_4/C	2 A g^{-1}	280/500	[24]
Li_3VO_4/graphite	100 mA g^{-1}	360/200	[25]

Li_3VO_4/C hollow sphere	800 mA g^{-1}	LVO/C 400/100 LVO 204/100	[26]
Li_3VO_4/C/CNTs	4 A g^{-1}	272/500	[27]
Li_3VO_4/C/rGO	2 A g^{-1}	LVO/C/rGO 387/200 LVO/C 305/200	[28]
Li_3VO_4@C nanofiber	40 mA g^{-1}	Fiber 394/100 Power 318/100	[29]
Mo^{6+} doped Li_3VO_4	2950 mA g^{-1}	Mo^{6+}-Li_3VO_4 439/200 Bare Li_3VO_4 166/200	[30]
Oxygen-deficient Li_3VO_4	1 A g^{-1}	244/500	[31]
C@ Li_3VO_4-ROD	100 mA g^{-1} 2 A g^{-1} 4 A g^{-1}	430/100 250/150 220/150	This work

References

[1] Q. Li, Q. Wei, J. Sheng, M. Yan, L. Zhou, W. Luo, R. Sun, L. Mai, Adv. Sci., 2 (2015) 1500284.

[2] P. Goel, M. Arora, RSC Adv., 5 (2015) 29741-29747.

[3] N.V. Kosova, D.O. Rezepova, A.B. Slobodyuk, Electrochim. Acta, 167 (2015) 75-83.

[4] M. Sathiya, A.S. Prakash, K. Ramesha, J.M. Tarascon, A.K. Shukla, J. Am. Chem. Soc. , 133 (2011) 16291-16299.

[5] J. Wang, J. Polleux, J. Lim, B. Dunn, J. Phys. Chem. C, 111 (2007) 14925-14931.

[6] H. Li, X. Liu, T. Zhai, D. Li, H. Zhou, Adv. Energy Mater., 3 (2013) 428-432.

[7] S. Ni, X. Lv, J. Ma, X. Yang, L. Zhang, J. Power Sources, 248 (2014) 122-129.

[8] Z. Liang, Z. Lin, Y. Zhao, Y. Dong, Q. Kuang, X. Lin, X. Liu, D. Yan, J. Power Sources, 274 (2015) 345-354.

[9] W.T. Kim, Y.U. Jeong, Y.J. Lee, Y.J. Kim, J.H. Song, J. Power Sources., 244 (2013) 557-560.

[10] Y. Shi, J.Z. Wang, S.L. Chou, D. Wexler, H.J. Li, K. Ozawa, H.K. Liu, Y.P. Wu, Nano Lett., 13 (2013) 4715-4720.

[11] Z. Liang, Y. Zhao, L. Ouyang, Y. Dong, Q. Kuang, X. Lin, X. Liu, D. Yan, J. Power Sources, 252 (2014) 244-247.

[12] S. Ni, X. Lv, J. Zhang, J. Ma, X. Yang, L. Zhang, Electrochim. Acta, 145 (2014) 327-334.

[13] Q. Li, J. Sheng, Q. Wei, Q. An, X. Wei, P. Zhang, L. Mai, Nanoscale, 6 (2014) 11072-11077.

[14] J. Liu, P.J. Lu, S. Liang, J. Liu, W. Wang, M. Lei, S. Tang, Q. Yang, Nano Energy, 12 (2015) 709-724.

[15] Z. Jian, M. Zheng, Y. Liang, X. Zhang, S. Gheytani, Y. Lan, Y. Shi, Y. Yao, Chem. Commun., 51 (2015) 229-231.

[16] S. Ni, X. Lv, J. Ma, X. Yang, L. Zhang, Electrochim. Acta, 130 (2014) 800-804.

[17] G. Shao, L. Gan, Y. Ma, H. Li, T. Zhai, J. Mater. Chem. A, 3 (2015) 11253-11260.

[18] C. Du, J. Wu, J. Liu, M. Yang, Q. Xu, Z. Tang, X. Zhang, Electrochim. Acta, 152 (2015) 473-479.

[19] C. Zhang, H. Song, C. Liu, Y. Liu, C. Zhang, X. Nan, G. Cao, Adv. Funct. Mater., 25 (2015) 3497-3504.

[20] J. Zhang, S. Ni, T. Kang, J. Tang, X. Yang, L. Zhang, J. Mater. Chem. A, 4 (2016) 14101-14105.

[21] X. Jin, B. Lei, J. Wang, Z. Chen, K. Xie, F. Wu, J. Alloys Compd., 686 (2016) 227-234.

[22] S. Ni, J. Zhang, J. Ma, X. Yang, L. Zhang, X. Li, H. Zeng, Adv. Mater. Interfaces, 3 (2016) 1500340.

[23] J. Zhang, S. Ni, J. Ma, X. Yang, L. Zhang, J. Power Sources, 301 (2016) 41-46.

[24] P. Tartaj, J.M. Amarilla, M.B. Vazquez-Santos, Chem. Mater., 28 (2016) 986-993.

[25] S. Hu, Y. Song, S. Yuan, H. Liu, Q. Xu, Y. Wang, J. Power Sources, 303 (2016) 333-339.

[26] Y. Yang, J. Li, X. He, J. Wang, D. Sun, J. Zhao, J. Mater. Chem. A, 4 (2016) 7165-7168.

[27] Y. Yang, J. Li, D. Chen, J. Zhao, J. Electrochem. Soc., 164 (2017) A6001-A6006.

[28] Y. Yang, J. Li, J. Huang, J. Huang, J. Zeng, J. Zhao, Electrochimica Acta, 247 (2017) 771-778.

[29] R. Qin, G. Shao, J. Hou, Z. Zheng, T. Zhai, H. Li, Sci. Bull., 62 (2017) 1081-1088.

[30] Y. Dong, H. Duan, K.-s. Park, Y. Zhao, ACS Appl. Mater. Interfaces, 9 (2017) 27688–27696.

[31] K. Wang, C. Zhang, H. Fu, C. Liu, Z. Li, W. Ma, X. Lu, G. Cao, Chem. Eur. J., 23 (2017) 5368–5374.

APPENDIX-II

Morphological control and urchin-like VS_4

Table A. 3 FTIR peaks and their assignments

Peaks	**Band assignment**	**Reference**
1631	δ(OH)	[1]
1400	Amorphous carbon	[1]
1200	C-O-R	**[2]**
980	S^{2-}(V-S-V)	**[2-4]**
550	Terminal S stretching	**[2-4]**

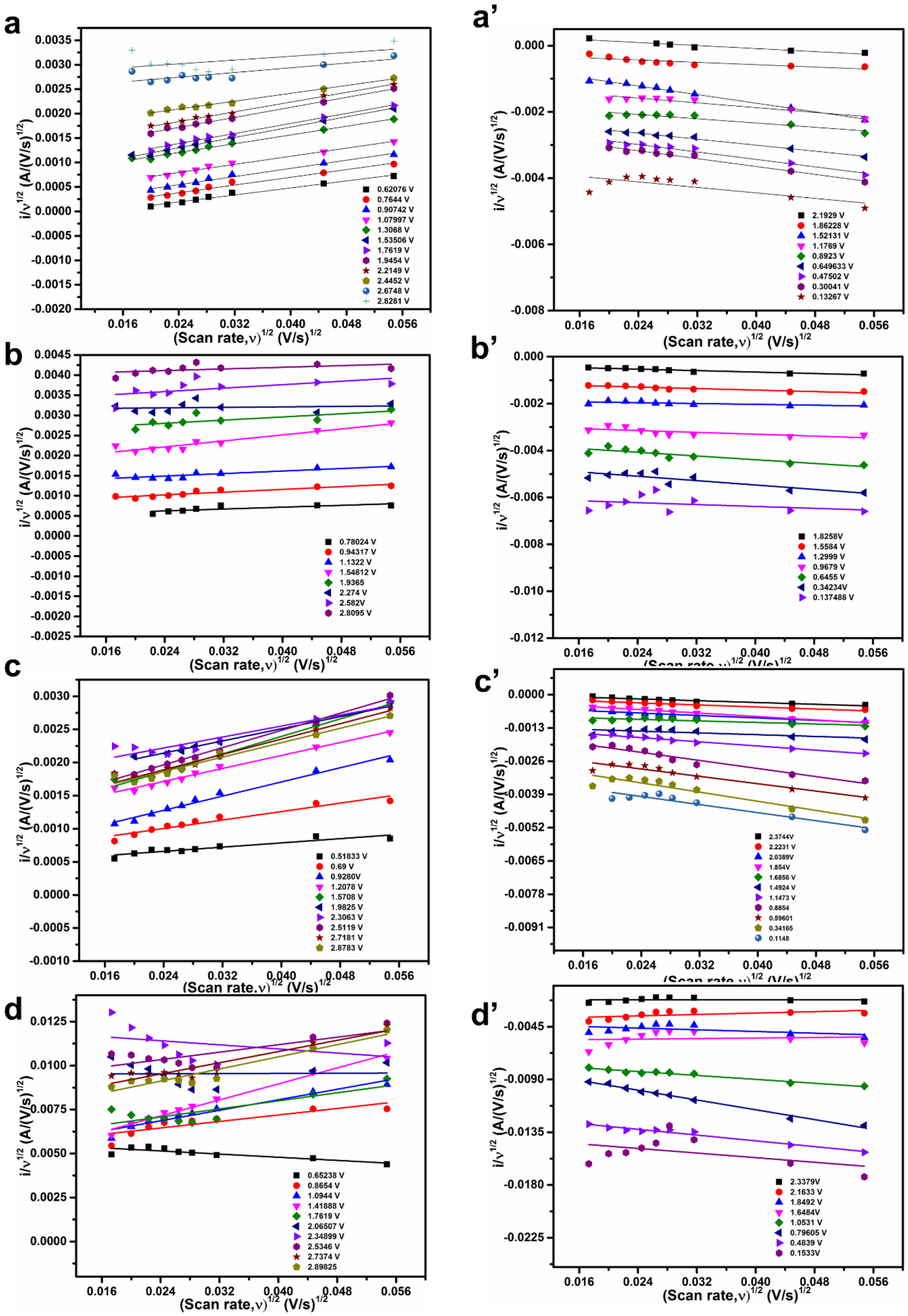

Figure A. 3 (a, a’), (b, b’), (c, c’) and (d, d’) are the plots of ν1/2 vs i/ν1/2 for flower-VS_4, octopus-VS_4, sea grass-VS_4 and urchin-like VS_4 at both anodic and cathodic scan. The plots are used for calculating constants k_1 and k_2 at different potentials of the cathodic scan and anodic scan.

The total current at a fixed potential can be described using the following equation: $I(V) = k_1\nu + k_2\nu^{1/2}$, where $k_1\nu$ and $k_2\nu^{1/2}$ represent the capacitive contribution and intercalation contribution, respectively. k_1 and k_2 can be obtained from the slope and y-axis intercept of the straight line: $i(V)/\nu^{1/2} = k_1\nu^{1/2} + k_2$, as shown in Fig. S5. Thus, the contribution from capacitive and intercalation can be calculated and each component contribution at scan rate of 0.2 mV/s.

References

[1] Q. Li, Q. Wei, J. Sheng, M. Yan, L. Zhou, W. Luo, R. Sun, L. Mai, Adv. Sci., 2 (2015) 1500284.

[2] Y. Zhou, Y. Li, J. Yang, J. Tian, H. Xu, J. Yang, W. Fan, ACS Appl. Mater. Interfaces, 8 (2016) 18797-18805.

[3] W. Fang, H. Zhao, Y. Xie, J. Fang, J. Xu, Z. Chen, ACS Appl. Mater. Interfaces, 7 (2015) 13044-13052.

[4] G. Lui, G. Jiang, A. Duan, J. Broughton, J. Zhang, M.W. Fowler, A. Yu, Industrial & Engineering Chemistry Research, 54 (2015) 2682-2689.

APPENDIX-III

VS_4 nanowires grown on rGO

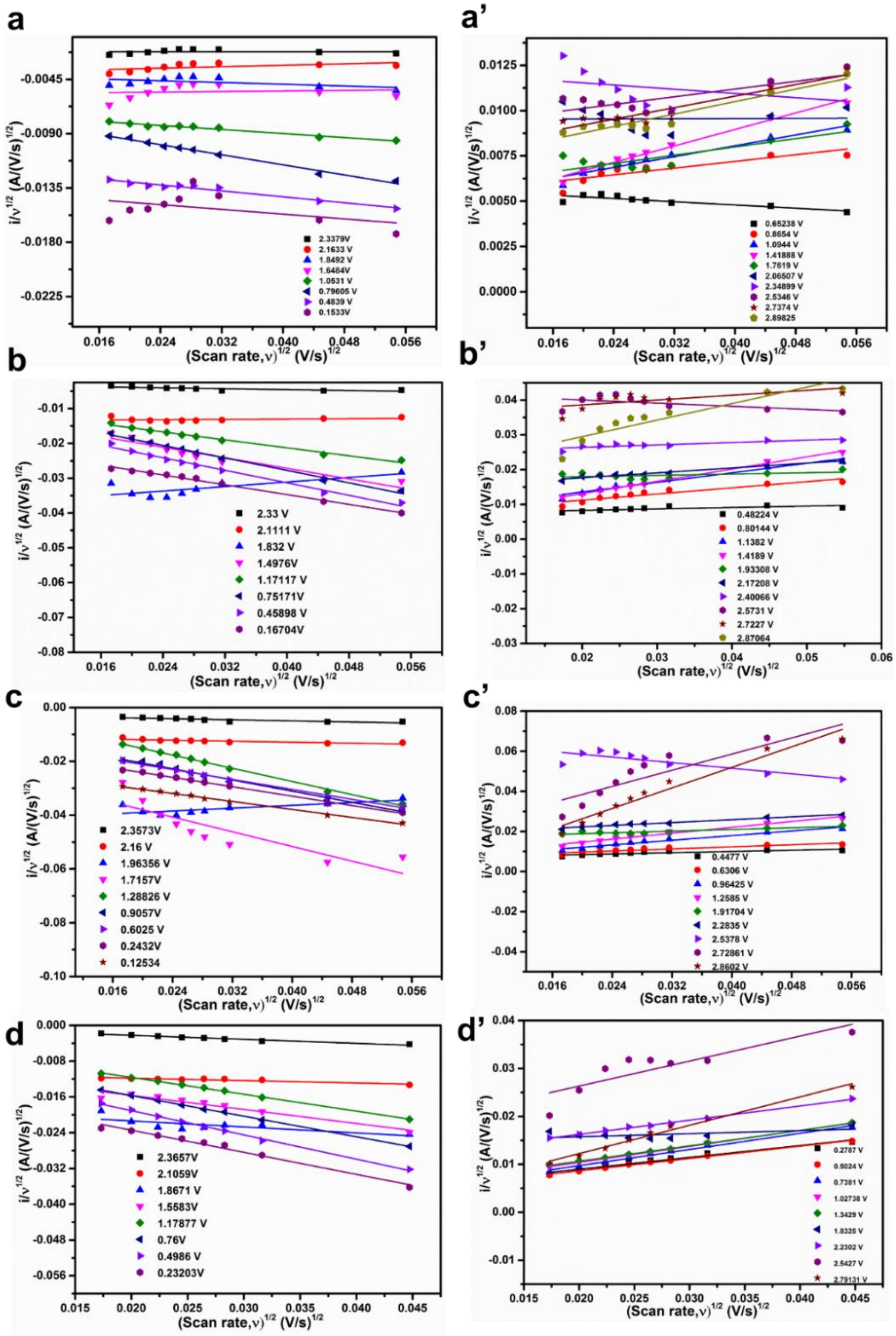

Figure A. 4 (a, a'), (b, b'), (c, c') and (d, d') are the plots of $\nu^{1/2}$ vs $i/\nu^{1/2}$ for VS_4, 5rGO@VS_4, 15rGO@VS_4, and 35rGO@VS_4 at both anodic and cathodic scan. The plots are used for calculating constants k_1 and k_2 at different potentials of the cathodic scan and anodic scan.